Innovative Crossed-Field Devices for the Generation of High Power Microwaves

by

Drew Anthony Packard

A dissertation submitted in partial fulfillment
of the requirements for the degree of
Doctor of Philosophy
(Nuclear Engineering and Radiological Sciences)
in the University of Michigan
2021

Doctoral Committee:

Professor Ronald M. Gilgenbach, Co-Chair
Professor Yue Ying Lau, Co-Chair
Professor Brian E. Gilchrist
Associate Research Scientist Nicholas M. Jordan
Associate Professor Ryan D. McBride

Drew Anthony Packard

drupac@umich.edu

ORCID iD: 0000-0002-7763-3434

Dedication

This dissertation is dedicated to my partner and best friend, Kiera, who has been there for me at every step.

Acknowledgements

Since I was a child, it has been a dream of mine to attend the University of Michigan. I was fortunate to be accepted after graduating high school, and even more fortunate that upon completion of undergraduate studies I was offered the opportunity to pursue a graduate degree. My gratitude extends to every person on this long journey that has made a difference.

Professor Gilgenbach provided the opportunity to get my foot in the door, and he has since been a constant presence in my academic life. His impact goes far beyond the career advice and experimental techniques passed down. My life would be extremely different had he not hired me as a young undergraduate to help around the lab, and I cannot thank him enough for his understanding guidance, patience, and trust.

Professor Lau taught me the most physics over the years, across multiple courses, the many hours in his office after classes, and research discussions. His presence at lab get-togethers outside of work and at conferences is always sure to come with an indispensable piece of wisdom. The theoretical backbone of this dissertation would not have been possible without the heavy lifting by Professor Lau. I cannot overstate how lucky I am to have worked so closely with these two pillars of plasma physics.

The other members of the committee, Dr. Jordan, Professor McBride, and Professor Gilchrist were very helpful in shaping this dissertation into a sensible and worthwhile document, and were invaluable in guiding this research along a successfully trajectory. Thank you all for your input and advice, especially to Dr. Jordan for fielding all of my naïve experimental questions as these experiments were devised.

Of course, any graduate school experience is shaped heavily by your surrounding peers. To the generation of graduate students before me- Drs. Sonal Patel, David Simon, Patrick Wong, Adam Steiner, David Yager-Elorriaga, Matt Weis Geoff Greening, and Steve Exelby- thank you all for setting an excellent example. To David Yager-Elorriaga, Geoff, and Steve, the knowledge you bestowed to me was indelible and vital. To those who I didn't overlap with during school but managed to get to know over the years- Drs. Brad Hoff, Matthew Gomez, Matthew Franzi, Will

White, Ian Rittersdorf, David French, Jacob Zier, and Professor Peng Zhang- thank you for your wisdom and perspective. It is easy to get lost in the circle of continuous education over the years, but you all helped to keep my perspective directed to important matters when school inevitably ends. In particular, thank you to Brad for bringing me to visit AFRL and for the continuous guidance over the years.

Being a member of this lab was made effortless by the good relationships and friendships we managed to build. Attending conferences with fellow students was always a joy because it was like going on an adventure with all of your best friends, and I will miss our camaraderie. Thank you to Stephanie Miller, Chris Swenson, Stephen Langellotti, George Dowhan, Akash Shah, Trevor Smith, Sunny Tummala, Brendan Sporer, Jeff Woolstrum, Nick Ramey, Emma Guerin, Anna Cooleybeck, Julio Diaz, Juan Riquezes, Dr. Paul Campbell, Dr. Foivos Antoulinakis, Dr. Steve Exelby, and Dr. Abhijit Jassem for the unforgettable experiences in and out of the lab. We put together the greatest volleyball team in the history of this lab, without question. To my good friend Paul, I will miss rooming with you at conferences and our weekly trips to the Syrian bakery, and Stephanie, I look forward to our inevitable voyage to Vegas. It will be a long time before the next pair of MELBA operators can defeat Steve and me in a tag-team weightlifting competition (mostly because of Steve). One of my favorite trips to this day was to Yosemite with Abhi and Foivos in 2018.

A pivotal inflection point in my life was over the duration of the internships I spent at L3-Communications (now L3Harris) as an undergraduate. It is very possible that I never would have developed such a strong interest in electron beams and microwaves without working directly with magnetrons so early in my career. Thank you to Dr. Carter Armstrong for taking a chance on me. Dr. Richard Kowalczyk provided an excellent education in microwave engineering and vacuum electronics over the months that we worked together, and has since been a reliable and invaluable sounding board as I have navigated the pitfalls of graduate school. The rest of those that I worked with at San Carlos- Dr. Dave Whaley, Dr. Thomas Hargreaves, Dr. Brandon Weatherford, Dr. Richard True, Mark Kirshner, Lad Turek, Chris Walz, Clark Meadows, Ann Sy, Ramon Duggal, Blake Griffin, Andrew Zubyk, and everyone else- I can only hope that I will have colleagues in the future as helpful and insightful.

Finally, I give thanks to my family. Thank you to my grandparents Don and Jan for expecting nothing less of me than becoming a doctor, Rena and Craig for your unending love and

support, and to my parents Brad and Tina for instilling the confidence and perseverance necessary to make it here. To my brothers Seth and Sean, thank you for always pushing me to be at my best. Of course, I would not have been capable of making it through the long days and weeks of schoolwork over the years without looking forward to seeing Kiera at the end of it all; she makes everything worthwhile. I also cannot forget my cat Ellie, who provided support by knocking things off my desk and laying on my keyboard and mousepad for the months I spent writing this dissertation.

This research was supported by the Office of Naval Research (ONR) under grant numbers N00014-16-1-2353, N00014-18-1-2499, N00014-19-1-2262, the Air Force Office of Scientific Research (AFOSR) under grant No. FA9550-20-1-0409, L3Harris Electron Devices Division, the Air Force Research Laboratory (AFRL) for their ICEPIC support, and the Directed Energy Professional Society (DEPS) through the Directed Energy Professional Society Graduate Scholarship.

Table of Contents

List of Tables

List of Figures

List of Appendices

Abstract

Modern High Power Microwave (HPM) initiatives pursue challenges in fundamental science, such as fusion research and particle accelerators, as well as industrial applications and homeland security. RADAR, telecommunications, and counter-IED (improvised explosive device) measures also rely on HPM. Crossed-field devices, like the magnetron and magnetically insulated line oscillator (MILO), are a subclass of microwave sources capable of delivering HPM. This dissertation describes the theory, simulation, and design processes applied to produce novel contributions in two separate projects, one a relativistic magnetron and the other a MILO.

The magnetron is an inherently narrowband source, which is undesirable for applications such as counter-IED technologies. Past Recirculating Planar Magnetron (RPM) concepts have proven multispectral microwave generation in magnetrons, and the Harmonic-RPM was designed to expand and further understand these capabilities. In the innovative configuration of this dissertation, the HRPM implements a 1 GHz, L-Band Oscillator (LBO) and a 2 GHz, S-Band Oscillator (SBO) on the same side of the planar cathode, both that are made frequency-agile by leveraging the novel phenomenon of harmonic frequency locking. An experimental investigation of harmonic frequency locking between the LBO and SBO demonstrated the LBO can be used to control the SBO frequency and phase through harmonic beam content, and the SBO responds to this excitation at varying degrees depending on its quality factor. In the low quality factor experiment, the HRPM was driven at 255 ± 19 kV, 1.23 ± 0.32 kA, producing microwave bursts up to 40 MW with shot-averaged pulse duration of 77 ± 17 ns at 7.3 ± 2.4% total efficiency. When the HRPM was properly tuned to excite the SBO on resonance in the low quality factor experiment, the shot-averaged SBO power was 28 ± 9 MW at 2.102 GHz ± 1.5 MHz. Harmonic frequency locking enabled tuning of the SBO over a range of 33 MHz in this experiment, corresponding to 1.6% tunability. By reversing electron rotation direction by the magnetic field, it was shown that the SBO was no longer influenced by the harmonic content of the LBO-modulated beam.

The MILO is a variant of the magnetron, differentiating itself in its method of producing the magnetic field for synchronous interaction. The magnetron uses permanent magnets or pulsed

solenoidal coils, whereas the MILO magnetic field is established by large, pulsed currents along the central axis of the device. The vast majority of MILO devices in the literature operate at a low impedance (V/I) of roughly 10 Ω and typically 50-60 kA, resulting in efficiencies commonly in the single digits of percent. The MILO investigated in this dissertation was the first to demonstrate oscillations at less than 10 kA currents, at -240 kV for an impedance of 25-30 Ω. Microwave bursts were observed up to 25 MW at 1.5% efficiency with shot-averaged frequency and pulse duration of 993 ± 7 MHz and 118 ± 43 ns, respectively. The shot-averaged output power was highly irreproducible at 10 ± 7 MW, and is significantly lower than simulation estimates. These experiments were compared with a contemporary theoretical treatment of Brillouin flow in the coaxial MILO geometry, which revealed consistent device operation in a unique condition near the Hull cutoff condition.

Chapter 1 Introduction

A brief history of high power microwave devices is given in this chapter, along with an overview of the field at large. The two devices of interest in this dissertation are the magnetron and magnetically insulated line oscillator. There is a dedicated section to each of these microwave sources, discussing their advantages and disadvantages.

1.1 High Power Microwaves

Until World War II, applications of the microwave spectrum were limited to lower power technologies such as communications. Development of the cavity magnetron [1] took place in the early 20th century, beginning with Gerdien [2] and Hull [3] in the 1910s, who described cylindrical, coaxial diodes with a magnetic field applied on the common axis. Variations ensued across the globe over decades, culminating with the work by Boot and Randall at Birmingham University in 1940 [4] when they introduced a cavity magnetron prototype with peak power of 15 kW at 3 GHz, well exceeding the goal of 1 kW at this wavelength. This invention was a disruptive breakthrough, enabling the detection of Axis air forces and submarines from more considerable distances. Shortly after that, Winston Churchill approved the "Tizard mission," which delivered this prototype to the U.S. for industrialization in high-resolution radar systems central to the Allied war effort in Europe.

After World War II, applications for the microwave spectrum arose that demanded the generation of higher power. The typical application was for heating, such as in the microwave oven [5], [6]. Modern pulsed power technology began in the 1960s [7], [8], enabling the compression of large amounts of energy into small time scales. For microwave devices, the advent of pulsed power gave access to the relativistic regime, and the first high power microwave (HPM) devices [9]–[11] were demonstrated in the 1970s [12]–[14]. HPM commonly refers to devices that produce bursts of high peak power for 10-100 ns, on the order of MW to GW depending on the applied voltage, in the range of 1 GHz to 100 GHz. A race to generate the highest possible peak power transpired in the 1980s and 1990s. Over these decades of research, a vibrant community formed around HPM, requiring an interdisciplinary knowledge of conventional microwave vacuum electronics and engineering, pulsed power, and plasma physics.

HPM has garnered more focus on applications over the last two decades, primarily in the defense sector. The U.S. Army has deployed multiple systems, including the Active Denial System, Max Power, and Phaser, intended for crowd dispersal, the remote detonation of improvised explosive devices (IEDs), and neutralization of unmanned aerial vehicles, respectively [15], [16]. The Counter-electronics High Powered Microwave Advanced Missile Project (CHAMP) is another HPM system mounted to a missile that can disable electronics and computer systems from a distance without harming physical structures or people [17]. Other examples include fundamental science in accelerators [18], neutralization of aerosols [19], and space-borne missions such as space-to-earth energy transfer and the search for extraterrestrial intelligence (SETI) [20], among others.

Various technologies can generate HPM [21], each with its strengths and weaknesses. Many of these sources are classified as "linear beam devices" or "crossed-field devices" [22], [23]. Crossed-field devices are marked by orthogonal electric and magnetic fields, whereas electrons in linear beam devices are typically transported along an axis in an annular or pencil beam. This dissertation focuses on two crossed-field devices, one of which is a relativistic magnetron and the other the magnetically insulated line oscillator (MILO) [9], [10], [24]–[26]. The magnetron and MILO are both oscillators, whereas the crossed-field amplifier (CFA) [27] is a variant of the magnetron that amplifies rather than oscillates. Examples of linear beam devices include the relativistic klystron amplifier (RKA) [28], [29], relativistic backward wave oscillator (RBWO) [30], [31], and relativistic traveling wave tube (TWT) [32]. Other beam-based devices include the gyrotron [33], free electron laser [34], and vircator [35]. HPM can also be generated with beamless methods, such as ultra-wideband (UWB) sources [36], nonlinear transmission lines (NLTL) [37], and solid state systems [38].

1.2 Relativistic Magnetron

As a microwave source, the magnetron is appealing for fielded applications because it is uniquely compact, energy-dense, and highly efficient [39]. The basic operating principles of the relativistic magnetron derive from the conventional magnetron, but they are distinguished by the large voltages and currents applied at the input, and thus the drastically increased microwave output power. Conventional magnetrons operate at < 100 kV and approximately 100 A, utilize thermionic or secondary emission cathodes, are limited to microwave generation up to megawatts, and reach efficiencies up to 80-90%. Relativistic magnetrons commonly operate at hundreds of

kilovolts to megavolts and in the kiloampere range by explosive emission cathodes [40], enabling much larger current densities than the conventional magnetron. The high voltages accelerate electrons to velocities at significant fractions of the speed of light, elevating these devices into the relativistic regime. Compared with thermionic or secondary emission cathodes, explosive emission cathodes easily reach the threshold of space-charge limited emission [41], maximizing the amount of electrons available for interaction with the RF wave. Microwave power can thus ascend to GW in relativistic devices, although the efficiency is commonly limited to 20-40% [42]. However, recent works have made significant progress in improving efficiency. The University of New Mexico has investigated a novel axial-diffraction output magnetron with a "transparent cathode," [43], [44] resulting in simulated efficiency at 70% [45]. In experiments, the efficiency reached 63% at 853 MW [46]. Simulations of a magnetron without a physical cathode, with the beam injected externally and confined between a virtual cathode and magnetic mirror, were simulated to operate at up to 92% efficiency [47].

Predating the transparent cathode were innovations at the University of Michigan (UM) known as cathode priming [43] and magnetic priming [48]–[51], which aimed to seed emission on the cathode that would promote electron spoke generation in a particular pattern. Experiments with these techniques resulted in faster start-oscillation, increased microwave pulse lengths, increased mean output power, and reduced starting current. More recently, researchers at UM have investigated and patented the recirculating, planar geometry [27], [52]–[54], illustrated in Figure 1.1. This architecture has now been demonstrated experimentally in several different devices, both magnetron [55], [56], and CFA [57]. The planar geometry enables several advantages to its cylindrical counterpart, including increased cathode area for electron emission, improved heat dissipation, improved magnetic field scaling per number of cavities, greater flexibility in design/fabrication, and compact microwave extraction, among others [52], [58]. The magnetron portion of this dissertation is a continuation of the recirculating planar magnetron (RPM) lineage.

Yet another advantage of the RPM geometry is the physical separation of its two planar drift regions. This geometry enabled the implementation of two different slow-wave structures (SWS), which establish the frequency of oscillations in a magnetron. As a result, the first magnetron designed to oscillate at two discrete frequencies simultaneously was demonstrated in the RPM geometry [56], entitled the Multi-Frequency RPM (MFRPM), and this concept has since received interest elsewhere [59]. In the MFRPM, the resonant frequencies of the two different

SWSs were an octave apart, generated by an L-Band Oscillator (LBO) near 1 GHz and S-Band Oscillator (SBO) near 2 GHz, as shown in Figure 1.1b.

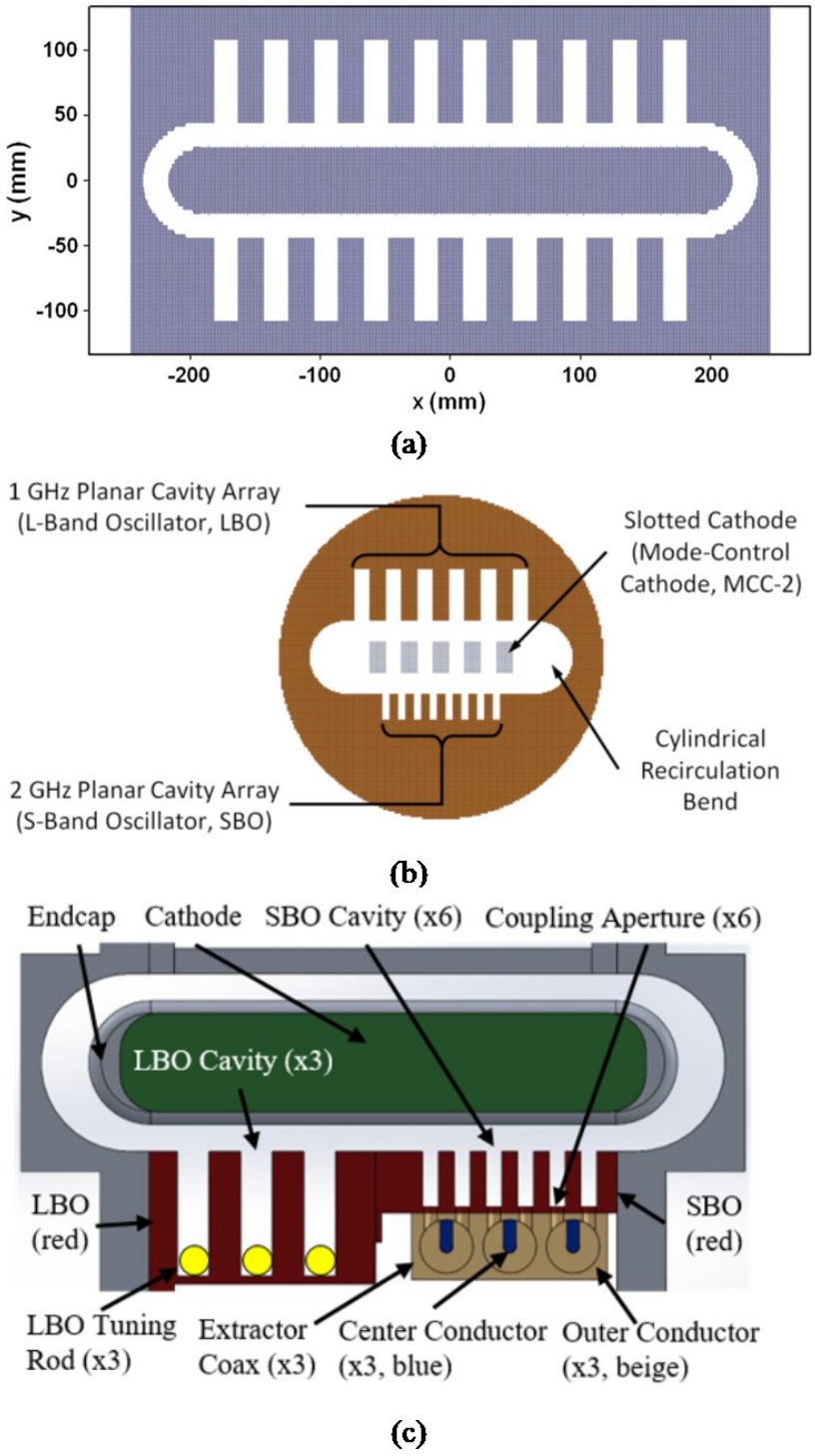

Figure 1.1: (a) Generic RPM with central cathode and surrounding anode, implementing two identical slow-wave structures on opposite sides of the cathode. Reprinted from [58]. (b) MFRPM geometry, implementing two different slow-wave structures on opposite sides of the cathode. Reprinted from [54]. (c) HRPM geometry, implementing two different slow-wave structures on the same side of the cathode. Reprinted from [65].

This work intended to address the inherent limitation of magnetrons as narrowband sources, as they are typically designed to generate a single tone. Other methods have been demonstrated to alter a magnetron's operating frequency, such as selecting different modes [60] or mechanical tuners to modify the mode frequencies [61]. However, these techniques are still limited to operation at a single frequency on the microsecond scale. The approach of utilizing multiple slow-wave structures has previously been applied to MILOs, TWTs, and BWOs [62]–[64]. Wideband generation of HPM is of substantial interest for systems designed to deliver energy to a target, which may couple more strongly to specific bands of the microwave spectrum than others.

The Harmonic Recirculating Planar Magnetron (HRPM) [65] was designed after the conclusion of the MFRPM project, and it was aimed to optimize and expand the multispectral capabilities of the RPM geometry. Visualized in Figure 1.1c, the HRPM places the LBO and SBO adjacent to each other, on the same side of the cathode, while the opposing side of the cathode is left as a smoothbore drift region. In a future prototype, the opposite drift region could be replaced with an additional set of planar oscillators rescaled to operate at different pair of frequencies. Theoretically, other oscillators could be placed adjacent to the LBO and SBO, as well. Therefore, the HRPM is an architecture that potentially allows generation of four or more frequencies simultaneously at MW power levels.

An unanticipated feature of the MFRPM was a novel, locked state known as harmonic frequency locking [66], where the SBO frequency locked to the second harmonic of the LBO frequency. Beyond its multispectral potential, the HRPM was designed to study harmonic frequency locking scientifically. This is why the present LBO was designed with frequency tunability through a mechanical tuner, varying its resonant frequency as the independent variable. The results of these experiments and their effects on the SBO operating frequency will be discussed in detail in Chapter 5.

1.3 Magnetically Insulated Line Oscillator

The MILO is a variant of the magnetron that existed in concept [67] decades prior to its first demonstration in the 1980's. The magnetron and MILO share the standard features of a central cathode, surrounding slow-wave structure, and crossed electric and magnetic fields that establish Brillouin flow (which is the prevalent electron shear flow in a crossed-field geometry [68]–[70]) in the same direction as the propagating electromagnetic wave. The MILO differentiates itself in

the generation of its own magnetic field and lack of beam recirculation. The relativistic magnetron often requires pulsed electromagnets to provide magnetic insulation, which can be very heavy and demand a separate power supply. The primary advantage of the MILO is it completely removes the need for an external magnet system, making it even more compact and lightweight than the magnetron. The injection of very electron high currents into a downstream-diode load establishes the MILO magnetic field that provides self-insulation in the cavity interaction space, as shown in Figure 1.2. It should be noted from Figure 1.2 that the flow of electrons within the cavity region and in the downstream load region serve two very separate purposes. The majority of the input current is collected on the beam dump, establishing insulation in the cavity region. A relatively smaller fraction of the current flows in the cavity region, which is available for energy transfer to microwaves.

As a result of the necessarily large input current, the MILO impedance (V/I) is commonly in the range of 5-15 Ω, operating at voltages in the hundreds of kilovolts to megavolt range and typically 50-60 kA [71]. Microwave powers are commonly on the order of hundreds of MW up to GW, but at low efficiency due to the large load currents. Recent simulation concepts have raised efficiencies to 20-30% [72]–[75], but experimental MILO efficiency has been limited to single digits of percent in many devices. Concepts for improving MILO efficiency are highly sought after to ameliorate this deficiency. The MILO must be designed in tandem with low impedance pulsed power systems, which have historically been achieved with Marx Bank technology, but modern investigations have looked to pair the MILO with the linear transformer driver (LTD) [76], [77] which is better equipped for low impedance operation.

It is assumed the generation of microwaves in a MILO is through the same physical mechanism as in magnetrons. As the RF wave grows from noise, it bunches the electron hub into spokes with the same phase advance per unit cell of the electromagnetic mode. The in-phase electrons are pulled across the gap by the $E_{RF} \times B_{DC}$ drift and transfer their potential energy to the RF wave as they do negative work on the cavity electric field. The stored energy within the cavities can then be extracted and propagated towards an engineered destination.

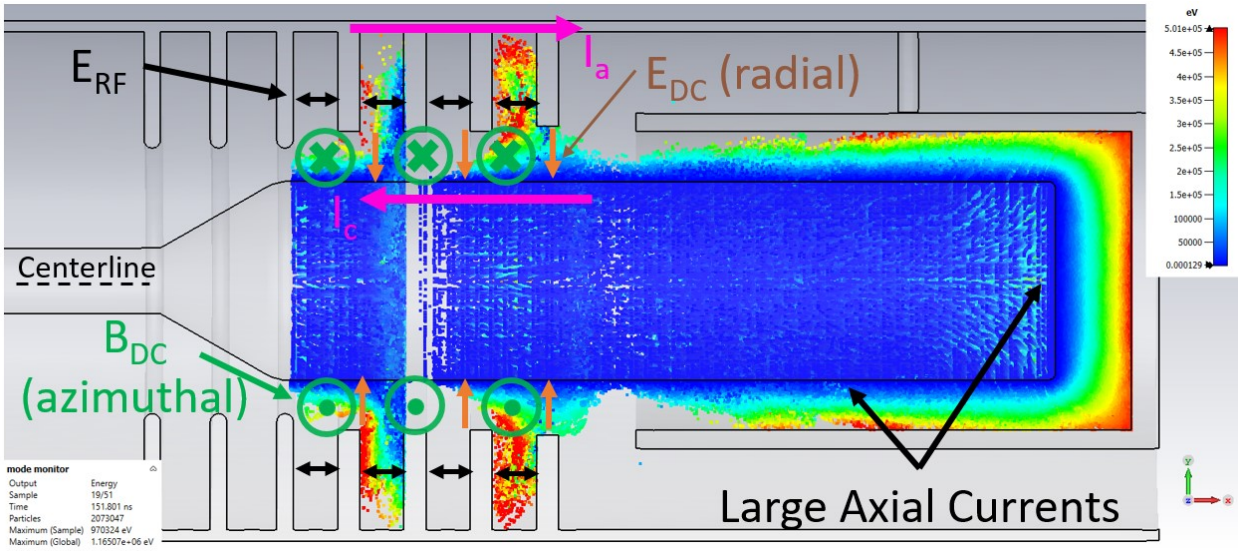

Figure 1.2: Dynamic flow of electrons in a MILO. The collection of large axial currents in the downstream beam dump insulates the electron flow in the cavity region. The cathode current I_c provides the majority of the insulation, rather than the current in the electron hub and spokes in the cavity region I_e (not labeled). The sum of I_e and I_c yields the total injected current, I_a. This figure draws from the work in [77].

The MILO was first demonstrated experimentally in 1988 by Clark et al. [26]. It was further investigated in the U.S. and United Kingdom through the 1990s and into the early 2000s [78]–[82]. Development continued in France [83], India [84], and China [85], [86] into the 2000s and 2010s. Recently, there has been a revival of interest in China and the U.S [77], [87] of which this work is a part. The vast majority of experimental devices operate near 10 Ω impedance, shown in Table 1.1. Investigations of operation at higher impedances such as 20-30 Ω have taken place [9], [88], but are scarce in the literature. Moreover, it appears that experimentation of MILO operation at the *lowest* possible currents has not taken place at all; this would be a desirable goal in investigating the physics and possible operating bounds of this self-insulating device. The MILO presented in this dissertation is the first to operate at less than 10 kA (impedance of 25-30 Ω), to the author's knowledge. The present experiments have elucidated important physical mechanisms in the operation of MILO near the Hull cutoff, which is the minimum magnetic field at which the diode becomes insulated and electrons cease to flow directly from cathode to anode [3].

This dissertation comprises seven chapters that detail the novel contributions made to relativistic magnetrons and MILO's. Chapter 2 discusses a novel theory of crossed-field devices from the Brillouin flow perspective. Chapter 3 outlines the simulation techniques that were applied to design each device. Chapter 4 details the experimental configurations and procedures that were followed in performing the experiments. Chapters 5 and 6 present and discuss the experimental

results and their importance to magnetron and MILO operation, respectively. Both projects are summarized, conclusions are drawn, and suggestions of future work are made in Chapter 7.

Table 1.1: Experimental performance of other MILO devices. The voltage (V), current (I), output power (P_{out}), impedance (Z), efficiency (η), and frequency (f) are listed. Experiments are listed in chronological order as they were published. *Items indicated with asterisk denote estimates from simulation if they were not measured experimentally.

Research Group	**V (kV)**	**I (kA)**	**P_{out} (GW)**	**Z (Ω)**	**η (%)**	**f (GHz)**
Clark et al. [26]	400	50	2*	8	10*	1.4
Calico et al. [78]	500	60	1.5	8.3	5	1.2
Haworth et al. [80]	500	60	1.88	8.3	6.25	1.2
Eastwood et al. [82]	460	26	2.1	18	18	1
Fan et al. [89]	520-540	58-62	2	8.8	6.3	1.73-1.78
Cousin et al. [83]	500	35	0.9	14	6	2.4
Fan et al. [90]	400	50	0.11	8	0.6	9.7
Chen et al. [91]	420	34	0.62	12	4.3	1.26 and 1.45
Wen et al. [92]	539	57	0.089	9.4	0.3	12.5
Fan et al. [86]	460	43	3	11	15	1.4

Chapter 2 Theory of Brillouin Flow

The recent theory by Y.Y. Lau et al. [93] is strongly relevant to the experiments presented in this dissertation. This chapter is dedicated to outlining and contextualizing this theory.

2.1 Overview

The Brillouin flow state is a laminar, axisymmetric flow that the physicist Leon Brillouin developed to describe the operation of crossed-field diodes in equilibrium [68]–[70]. This fluid model assumes that all electrons travel in trajectories parallel to the cathode, with zero flow velocity at the cathode. The multistream model, where electrons are described with individual cycloidal orbits, is the most prominent competing description of the physics of crossed-field diodes [94]. Substantial evidence suggests that the Brillouin flow state is the best description for equilibrium within crossed-field devices before electron spokes are formed. In 1961, Buneman claimed, "double-streaming appears as a possible second-order perturbation to the Brillouin flow" [95]. More recently, it has been shown that the cycloidal flow state is unstable to a small amount of dissipation by current flow in a lossy external circuit [96], a small AC voltage [97], or slight magnetic field misalignment [98]. Simulations using particle-in-cell codes further corroborate the fluid model [99].

This chapter aims to apply the Brillouin flow model to necessary geometries relevant to simulations and experiments described in later chapters. The geometries discussed in Section 2.2 and 2.3, and other vital geometries to HPM and pulsed power, are discussed extensively in [93], and the work presented here follows that manuscript. In this chapter, the planar geometry will be analyzed in Section 2.2, and then the cylindrical geometry with axial flow in Section 2.3, each pictured in Figure 2.1. From these treatments, the critical Hull Cutoff and Buneman-Hartree conditions may be derived in both geometries. This work has been completed previously for the planar geometry. Still, the BH condition has yet to be established for the cylindrical geometry with axial flow, which is the most common configuration of the magnetically insulated line oscillator (MILO). Much of the MILO geometry discussion may be applied to magnetically insulated transmission lines in general [93].

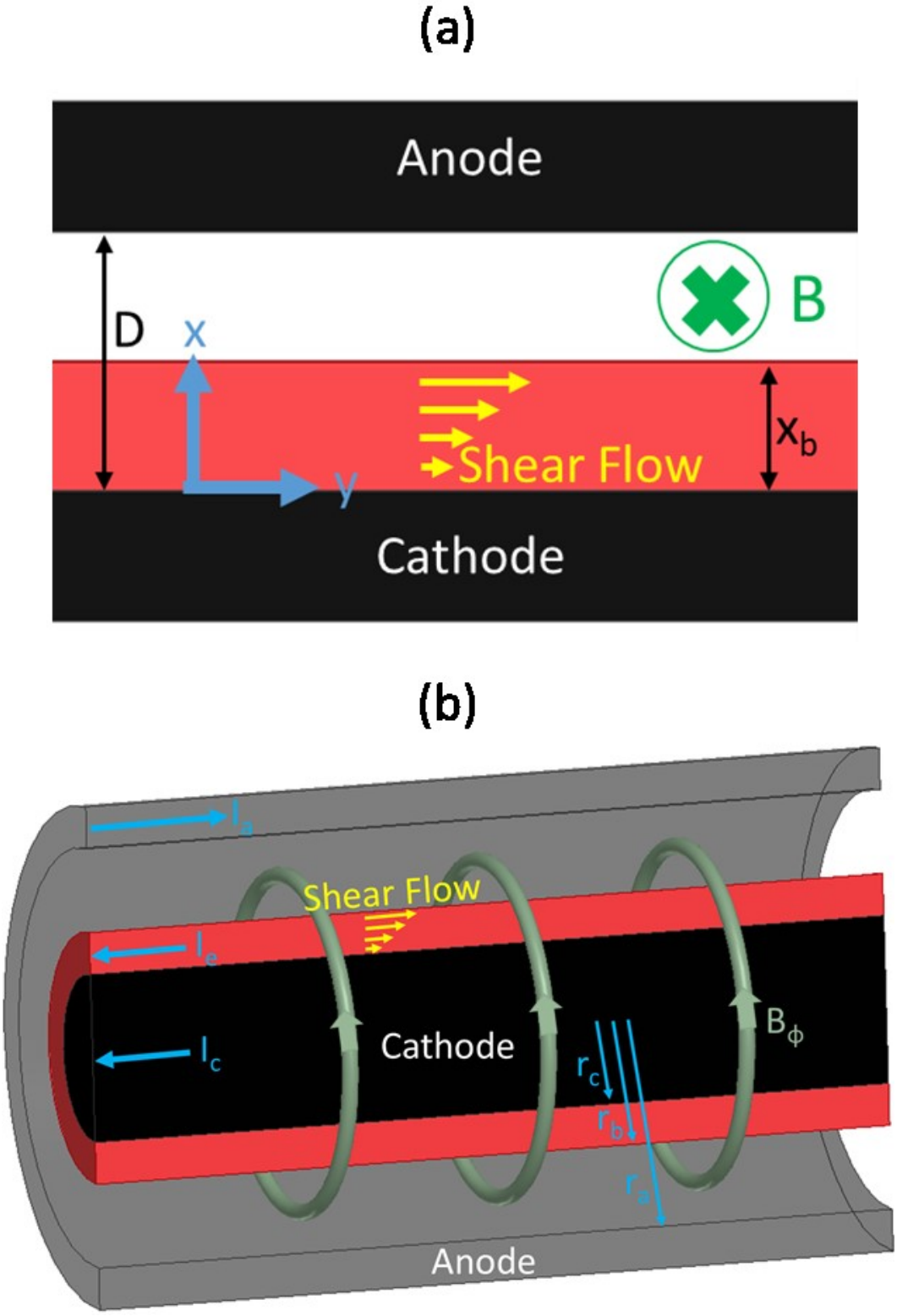

Figure 2.1: The planar (a) and coaxial (b) geometries that will be analytically treated using the Brillouin flow formulation. The electron hub and its velocity shear are depicted in red and yellow, respectively, with magnetic field vectors in green. The insulating magnetic field, in either case, may be applied externally via permanent magnets, or internally through wall currents, or by a hybrid concept where both methods are implemented.

In this theory, the gap voltage (V_a) and the vector potential (A_a) are assumed to be known quantities. The magnetic field in the gap between the anode-cathode (AK gap) is assigned indirectly through the vector potential. By specification of the anode voltage and vector potential, which enter as boundary conditions, the degree of magnetic insulation (which is approximately equivalent to the ratio between the magnetic field and the Hull Cutoff magnetic field) is inherently specified. This choice was necessary to develop a broad theory that may describe the magnetron, whose magnetic field is applied via external magnets, and the MILO, whose magnetic field arises due to internally driven current. *As a result, this theory does not assume how the magnetic field is generated*. It is even possible to apply to a magnetron-MILO hybrid device, which produces some portion of its magnetic field via driven current and the rest via externally applied magnets. In the end, after fully accounting for the electron beam self-magnetic field, it will be shown that all of the Brillouin flow parameters, the Hull Cutoff condition, and the Buneman-Hartree condition depend only on V_a and A_a. Furthermore, all expressions associated with the Brillouin flow have an exact, closed-form solution. The HC and BH conditions for the planar and coaxial vertical flow geometries are identical in terms of V_a and A_a. This approach has been applied to other geometries [93], such as radially convergent flow in a radial transmission line like the linear transformer driver (LTD) [76], and the typical azimuthal flow in cylindrical magnetrons, which has been studied extensively [100]–[102]. However, these geometries are beyond the scope of this thesis and will not be discussed further.

For greater ease of analysis, the governing equations are simplified with nondimensionalization using universal constants, including the electron mass m, elementary charge e, speed of light c, the permittivity of free space ε_0, and the permeability of free space μ_0. The length scale x_s is introduced to complete the nondimensionalization, which may be tailored to accommodate either geometry in Figure 2.1. In terms of these quantities, the scaled parameters of interest are shown in Eqs. 2.1-2.10. The voltage scale V_s, vector potential scale A_s, velocity scale v_s, and current scale I_s all depend solely on universal constants. Meanwhile, the field, current, and density scales are inversely proportional to x_s to the first or second power in addition to the aforementioned universal constants. Equations 2.1-2.10 will be used once the geometry is specified.

$$V_s = voltage\ scale = mc^2/e = 511\ kV \quad (2.1)$$
$$A_s = vector\ potential\ scale = mc/e = 1.706 \times 10^{-3}\ \text{T-m} \quad (2.2)$$
$$v_s = velocity\ scale = c = 3 \times 10^8\ m \quad (2.3)$$
$$I_s = current\ scale = mc/(e\mu_0) = 1.358\ kA \quad (2.4)$$
$$E_s = eletric\ field\ scale = V_s/x_s = mc^2/(ex_s) = (5.11 \times 10^7\ \text{V/m}) * (1\ \text{cm}/x_s) \quad (2.5)$$
$$B_s = magnetic\ field\ scale = A_s/x_s = mc/(ex_s) = 0.1706\ \text{T} * (1\ \text{cm}/x_s) \quad (2.6)$$
$$H_s = magnetization\ scale = B_s/\mu_0 = mc/(ex_s\mu_0) = (1.358\ \text{kA/cm}) * (1\ \text{cm}/x_s) \quad (2.7)$$
$$K_s = surface\ current\ density\ scale = H_s = mc/(ex_s\mu_0) = (1.358\ \text{kA/cm}) * (1\ \text{cm}/x_s) \quad (2.8)$$
$$J_s = current\ density\ scale = I_s/x_s^2 = mc/(e\mu_0 x_s^2) = (1.358\ \text{kA/cm}^2) * (1\ \text{cm}/x_s)^2 \quad (2.9)$$
$$n_s = number\ density\ scale = \epsilon_0 E_s/(\text{e}x_s) = (2.82 \times 10^{11}/\text{cm}^3) * (1\ \text{cm}/x_s)^2 \quad (2.10)$$

With scaled quantities in hand, the dimensionless parameters of interest are given in Eq. 2.11-2.16. The solutions for these parameters within the AK gap are ultimately sought after, and with them, a complete characterization of the Brillouin flow may be prescribed. In the planar geometry, the position within the gap is denoted by $\bar{x}$, whereas the radial position within a coaxial gap is denoted by $\bar{r}$; in these two cases, x_s is set to D and r_a, respectively. The velocity profile is given in terms of β, the familiar normalization for particle velocities to the speed of light.

$$\bar{x} = x/x_s,\ \bar{r} = r/x_s \quad (2.11)$$
$$\bar{\phi} = \phi/V_s,\ \bar{A} = A/A_s \quad (2.12)$$
$$\bar{v} \equiv \beta = v/c,\ \bar{I} = I/I_s \quad (2.13)$$
$$\bar{E} = E/E_s,\ \bar{B} = B/B_s \quad (2.14)$$
$$\bar{H} = H/H_s,\ \bar{K} = K/K_s \quad (2.15)$$
$$\bar{J} = J/J_s,\ \bar{n} = n/n_s \quad (2.16)$$

Shortly, the Brillouin flow equations for the planar gap will be presented (Eq. 2.17-2.26), and their solutions will be derived in full in Section 2.2. The same process will be applied to the coaxial geometry in Section 2.3, wherein there are relatively few, yet subtle, differences. As the full solutions are being derived, it is important to keep in mind that there are merely two free parameters in the Brillouin flow equations once the geometry is specified. Specifically, these are the anode voltage V_a and total magnetic flux A_a, which arise *only* in the boundary conditions, Eq. 2.24 and 2.25. The final solutions to all parameters in Eq. 2.11-2.16 may be traced directly back to V_a and A_a.

Typically, theoretical characterizations of Brillouin flow are undertaken using the magnetic field as the primary field quantity of interest, rather than the vector potential (from which the magnetic field may be determined). This difference in the analysis is undertaken here because it is a more general approach to characterize the multiple devices of interest, specifically the magnetron and magnetically insulated line oscillator (MILO). In a magnetron, the insulating magnetic field is

applied externally, and the DC current is, therefore, a secondary parameter to be derived [103]. Conversely, for a MILO, the magnetic field is generated internally with DC current, so the typical means of Brillouin flow analyses for magnetrons cannot be applied directly. For these reasons, the total magnetic flux is defined a priori to treat both of these crossed-field devices with the same formulation. Therefore, it is no longer necessary to specify how the magnetic field is generated. It could be entirely from an external magnet, driven only by internal currents, or even a combination of both [93].

2.2 Planar Brillouin Flow

First, the planar diode described in Figure 2.1a will be treated. The length scale x_s is set equal to the gap spacing D. Using the dimensionless notation, the Brillouin flow equations are stated in Eqs. 2.17-2.26. By convention, $(\bar{E}, \bar{B}, \bar{\phi}, \bar{A}, \bar{n}, \beta, V_a, A_a)$ are all positive for $0 < \bar{x} < 1$. Because this is a static, non-time varying problem, the electrostatic and magnetostatic fields may be expressed in terms of the scalar and vector potential, respectively, in Eqs. 2.17-2.18. Equations 2.19-2.20 arise from Gauss's law and Ampère's law, where the only terms that survive are the differentials in the x-direction due to the symmetry in the y-direction. The ExB drift of electrons within the hub relates the electric field, magnetic field, and particle velocity in Eq. 2.21. Conservation of energy and canonical momentum for electrons within the hub are upheld in Eqs. 2.22-2.23, where γ is the Lorentz factor. Without loss of generality, the boundary conditions for the scalar potential $\bar{\phi}$ and total magnetic flux per unit length in y $\overline{A_a}$ are explicitly stated in Eqs. 2.24-2.25, regardless of the presence of space charge or how the magnetic field was generated. Finally, Eq. 2.26 states the Brillouin flow assumptions of zero tangential electron flow velocity and zero electric field at the cathode surface. Recall that space charge is present in the Brillouin hub only, and therefore Eqs. 2.21-2.23 are only valid within $0 < \bar{x} < \bar{x}_b$ (Figure 2.1a); the scalar potential, vector potential, and static fields must be treated on a piecewise basis in or out of the hub.

$$\bar{E} = \partial\bar{\phi}/\partial\bar{x} \tag{2.17}$$

$$\bar{B} = \partial\bar{A}/\partial\bar{x} \tag{2.18}$$

$$\partial\bar{E}/\partial\bar{x} = \bar{n} \tag{2.19}$$

$$\partial\bar{B}/\partial\bar{x} = \bar{n}\beta \tag{2.20}$$

$$\bar{E} = \beta\bar{B} \tag{2.21}$$

$$\bar{\phi} = \gamma - 1, \ \gamma = \frac{1}{\sqrt{1-\beta^2}} \tag{2.22a,b}$$

$$\bar{A} = \gamma\beta \tag{2.23}$$
$$\bar{\phi}(cathode) = 0,\ \bar{\phi}(anode) = \bar{V}_a \tag{2.24}$$
$$\bar{A}(cathode) = 0,\ \bar{A}(anode) = \bar{A}_a \tag{2.25}$$
$$\beta(cathode) = 0,\quad \bar{E}(cathode) = 0 \tag{2.26a,b}$$

Equations 2.17-2.26 have previously been solved for the planar geometry in [101], [102]. Following these formulations, the x-coordinate within the hub may be parameterized by,

$$\chi = \chi(\bar{x}),\ \chi(\bar{x}_c) = 0 \tag{2.27a,b}$$

where $\bar{x} = \bar{x}_c = 0$ at the planar cathode. Satisfying the boundary condition Eq. 2.26a, the normalized electron flow velocity within the Brillouin hub is written as,

$$\beta = \tanh(\chi) \tag{2.28}$$

Implementing some basic identities of the hyperbolic trigonometric functions, Eqs. 2.29-2.31 may be derived from Eq. 2.22b, 2.22a, and 2.23, respectively. Defining $\chi' \equiv \partial\chi(\bar{x})/\partial\bar{x}$ and applying the chain rule, Eqs. 2.32-2.34 are retrieved from their original forms, Eqs. 2.17-19.

$$\gamma = \cosh(\chi) \tag{2.29}$$
$$\bar{\phi} = \cosh(\chi) - 1 \tag{2.30}$$
$$\bar{A} = \sinh(\chi) \tag{2.31}$$
$$\bar{E} = \chi'\sinh(\chi) \tag{2.32}$$
$$\bar{B} = \chi'\cosh(\chi) \tag{2.33}$$
$$\bar{n} = \partial[\chi'\sinh(\chi)]/\partial\bar{x} \tag{2.34}$$

Upon substitution of Eq. 2.28, 2.33, 2.34 into Eq. 2.20, the resultant expression collapses into a homogeneous second order linear differential equation, specifically $\frac{\partial^2\chi(\bar{x})}{\partial\bar{x}^2} = 0$. Integrating once,

$$\frac{\partial\chi(\bar{x})}{\partial\bar{x}} = \chi' = \kappa \tag{2.35}$$

where κ is a constant which must be solved directly. Integrating once more and applying the boundary condition from Eq. 2.27b, which eliminates the constant of integration, yields

$$\chi(\bar{x}) = \kappa\bar{x} \tag{2.36}$$

At this point, all that remains is to solve for χ and κ in terms of the boundary conditions $\bar{V}_a$ and $\bar{A}_a$ (Eq. 2.24-2.25). Turning to the vacuum region, $\bar{x}_b < \bar{x} < 1$, where both the electric and magnetic fields are constant, the scalar and vector potential $\bar{\phi}$ and $\bar{A}$ are each a linear function of $\bar{x}$. The additional subscripted terms $\bar{\phi}_b, \overline{A_b}, \bar{E}_b, \overline{A_b}$ (among others) denote their values at the top of the Brillouin hub, and the scalar and vector potential in the vacuum region then read,

$$\bar{\phi}(\bar{x}) = \bar{\phi}_b + \bar{E}_b(\bar{x} - \bar{x}_b) \quad (2.37)$$
$$\bar{A}(\bar{x}) = \bar{A}_b + \bar{B}_b(\bar{x} - \bar{x}_b) \quad (2.38)$$

Taking Eq. 2.37 and 2.38, evaluating them at the anode ($\bar{x} = 1$) and applying Eq. 2.24, 2.25, 2.30-2.33, the following expressions are obtained where the unknowns are χ_b and κ.

$$\bar{V}_a = \cosh(\chi_b) - 1 + \sinh(\chi_b)\kappa(1 - \bar{x}_b) \quad (2.39)$$
$$\bar{A}_a = \sinh(\chi_b) + \cosh(\chi_b)\kappa(1 - \bar{x}_b) \quad (2.40)$$
$$\chi_b = \kappa\bar{x}_b \quad (2.41)$$

Now the goal is to solve for χ_b. From Eq. 2.39 and 2.40, the common factor of $\kappa(1 - \bar{x}_b)$ may be eliminated to arrive at Eq. 2.42, which yields Eq. 2.43 after some rearrangement. Notice that χ_b depends only on the boundary conditions $\bar{V}_a$ and $\bar{A}_a$; this transcendental equation may be solved numerically for χ_b.

$$\frac{\bar{V}_a - \cosh(\chi_b) + 1}{\sinh(\chi_b)} = \frac{\bar{A}_a - \sinh(\chi_b)}{\cosh(\chi_b)} \quad (2.42)$$

$$\bar{A}_a = \sinh(\chi_b) + \coth(\chi_b)\,[\bar{V}_a - \cosh(\chi_b) + 1] \quad (2.43)$$

This numerical solution of χ_b was found to agree with the analytic solution of χ_b, given explicitly in Eq. 2.54 below. Finally, the solution for κ in terms of $\bar{V}_a$ and χ_b may be garnered from Eq. 2.39 and 2.41, and displayed in Eq. 2.44. From this, the solution for $\chi(\bar{x})$ is defined by Eq. 2.36. With solutions for $\chi(\bar{x})$ and κ, all of the Brillouin flow parameters of interest may be solved directly from Eqs. 2.28-2.34.

$$\kappa = \operatorname{csch}(\chi_b)\,(1 + \bar{V}_a) - \coth(\chi_b) + \chi_b \quad (2.44)$$

To obtain the closed-form solution for χ_b, first define the following expressions, Eqs. 2.45-2.46, in terms of the gap voltage.

$$\gamma_a = \bar{V}_a + 1 \equiv 1/\sqrt{1 - \beta_a^2} \quad (2.45)$$
$$\bar{A}_a^{min} = \gamma_a\beta_a \quad (2.46)$$

These expressions define the Hull Cutoff (HC) condition, where the Brillouin hub height approaches the AK gap distance ($\bar{x} \to 1$), at which $\gamma_b = \gamma_a$, i.e., the electron velocity at the top of the Brillouin hub, $\beta_b = \beta_a$, as seen from Eq. 2.22. The minimum magnetic flux per unit length y to achieve insulation, $\bar{A}_a = \bar{A}_a^{min}$, follows from Eq. 2.23. All of these quantities become defined once the gap voltage is specified. *They are independent of the geometries in Figure 2.1.* Solving for γ_a and β_a in terms of $\bar{V}_a$ and substituting into Eq. 2.46 yields Eq. 2.47, which reduces into its

more recognizable form in Eq. 2.48. This relationship relating the magnetic flux to the gap voltage is indeed the Hull Cutoff equation.

$$\bar{A}_a = \sqrt{(\bar{V}_a + 1)^2(1 - (\bar{V}_a + 1)^{-2})} \tag{2.47}$$

$$\bar{A}_a = \sqrt{\bar{V}_a^2 + 2\bar{V}_a} = \gamma_a \beta_a = \bar{A}_a^{min} \tag{2.48}$$

If the gap is insulated ($\bar{A}_a/\bar{A}_a^{min} > 1$), the Buneman-Hartree (BH) condition is met when the edge velocity $\beta(\bar{x}_b) = \beta_b$ is equal to the phase velocity $\beta_{ph} = v_{ph}/c$ of the electromagnetic mode of interest on the slow-wave structure (SWS). Taking Eq. 2.40, multiplied by $\tanh(\chi_b)$, and subtracting this expression from Eq. 2.39 will bring Eq. 2.49 after some arithmetic, which begins to take the form of the familiar BH condition.

$$\bar{V}_a = \bar{A}_a \tanh(\chi_b) - [1 - \tfrac{1}{\cosh(\chi_b)}] \tag{2.49}$$

In a similar fashion to Eq. 2.45, the analogous parameters $\gamma_b, \bar{\phi}_b, \beta_b$ take on their usual meanings in Eq. 2.50 and are evaluated at the top of the Brillouin hub as previously established. By utilizing Eq. 2.28-2.29 to replace the hyperbolic functions and inserting them along with Eq. 2.50 directly into Eq. 2.49, the final BH equation is obtained in Eq. 2.51. This expression is identical to the most commonly used form of the BH condition, derived from the multistream model, but only in the planar geometry [102].

$$\gamma_b = \bar{\phi}_b + 1 \equiv 1/\sqrt{1 - \beta_b^2} \tag{2.50}$$

$$\bar{V}_a = \bar{A}_a \beta_b - [1 - \sqrt{1 - \beta_b^2}] \tag{2.51}$$

As promised, the closed-form solution for χ_b may be solved for β_b in terms of $\bar{V}_a$ and $\bar{A}_a$ using the BH condition. Rearranging, the radical over β_b^2 can be removed by squaring Eq. 2.52. Gathering terms and applying Eq. 2.45-2.46, a quadratic expression for β_b, Eq. 2.53, can be obtained. Finally, by solving the quadratic, the solution for χ_b is given in Eq. 2.54 upon utilization of Eq. 2.28.

$$(\bar{V}_a + \bar{A}_a \beta_b + 1) = \sqrt{1 - \beta_b^2} \tag{2.52}$$

$$\beta_b^2(\bar{A}_a^2 + 1) - 2\bar{A}_a \gamma_a \beta_b + (\bar{A}_a^{min})^2 = 0 \tag{2.53}$$

$$\beta_b = \tanh(\chi_b) = \frac{\gamma_a \bar{A}_a - \sqrt{\bar{A}_a^2 - (\bar{A}_a^{min})^2}}{\bar{A}_a^2 + 1} \tag{2.54}$$

Equation 2.54 gives χ_b analytically in terms of $\bar{A}_a$ and $\bar{V}_a$ upon using Eq. 2.46.

The Hull cutoff condition and BH condition are plotted together in Figure 2.2. The vertical and horizontal red lines indicate the operating point along the BH line at a given ($\bar{V}_a$,$\bar{A}_a$). At this

same horizontal line, a black dashed vertical line at $\bar{A}_a^{min}$ indicates the HC condition for this given voltage, intersecting the parabolic HC curve. $\bar{A}_a^{min}$ is the minimum value of $\bar{A}_a$ to achieve magnetic insulation, at a given anode voltage. The HC and BH curves are tangent at $(\gamma_b - 1, \gamma_b\beta_b)$ [100]. The BH condition assumed velocity synchronism between the fastest electrons in the Brillouin hub and the SWS. At voltages higher than the BH condition for a given $\bar{A}_a$ (but below HC), there exists a resonant layer within the Brillouin hub that is synchronous with the anode phase velocity. This set of curves applies to both the planar geometry and coaxial geometry with axial flow (as it will be shown in Section 2.3), regardless of the aspect ratio or gap distance, and assumes nothing about how the magnetic field is generated. It can be generally applied to the magnetron, MILO, or a hybrid concept in planar or coaxial geometry. Lau et al. [93] show the same HC and BH conditions are also obtained using the single-particle, cycloidal orbit model in both planar and cylindrical configurations in Figure 2.1, regardless of how the magnetic flux is generated.

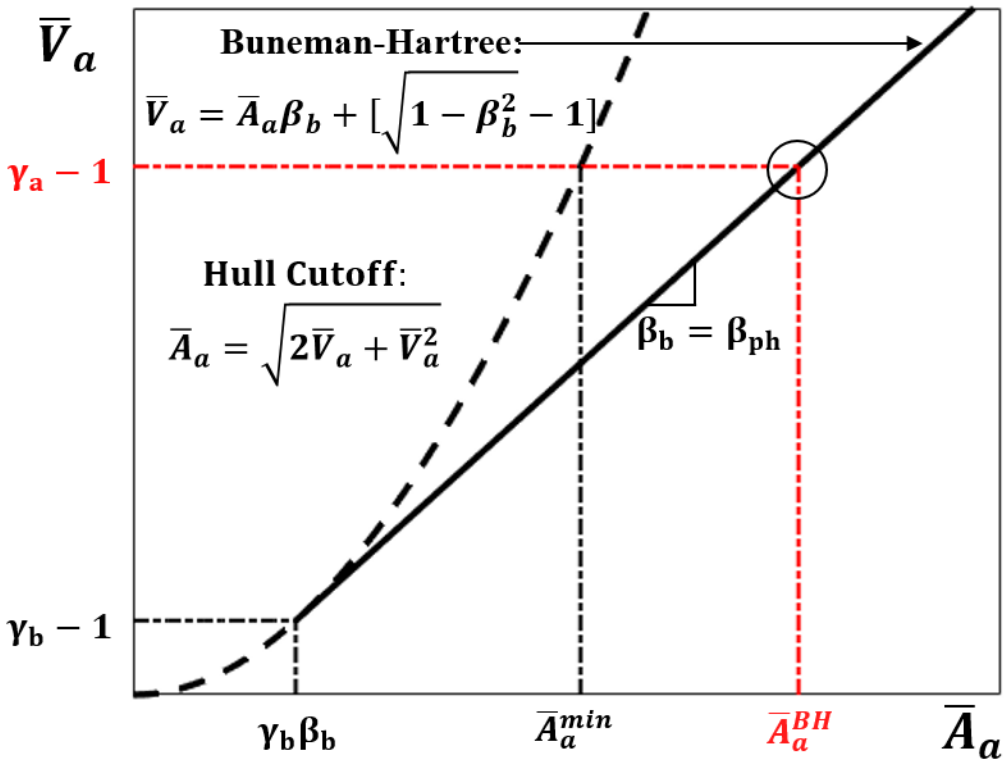

Figure 2.2: The Buneman-Hartree and Hull Cutoff conditions as a function of the normalized gap voltage $\bar{V}_a$ and normalized total magnetic flux $\bar{A}_a$. These expressions were produced using the Brillouin flow model, and assume that the top of the Brillouin hub is synchronous with the anode phase velocity to produce the BH condition. The circled point, intersecting the red lines, is typically the intended point of operation for given $(\bar{A}_a, \bar{V}_a)$. This graph is applicable to both the planar and cylindrical geometries described in Figure 2.1.

With the equations laid out, it is now appropriate to discuss the Brillouin flow properties. Because it is not intuitively straightforward to interpret variations of $\bar{A}_a$, the ratio $\bar{A}_a/\bar{A}_a^{min}$ is defined to capture parameterizations of the magnetic field. The ratio $\bar{A}_a/\bar{A}_a^{min}$ represents the degree of magnetic insulation; with $1 < \bar{A}_a/\bar{A}_a^{min}$, the HC condition has been exceeded, and the diode has become magnetically insulated. In the following figures, the parameter space of $\bar{A}_a/\bar{A}_a^{min}$ and $\bar{V}_a$ will be explored for various quantities of interest that describe the Brillouin flow. First, the quantities χ_b and κ are given in Figure 2.3. Recall that these two parameters can be used to find solutions for all hub quantities of interest, specifically Eq. 2.28-2.34. While χ_b and κ themselves aren't attached to immediate physical meaning, their solutions are what allow the following analysis to proceed. See Eq. 2.36.

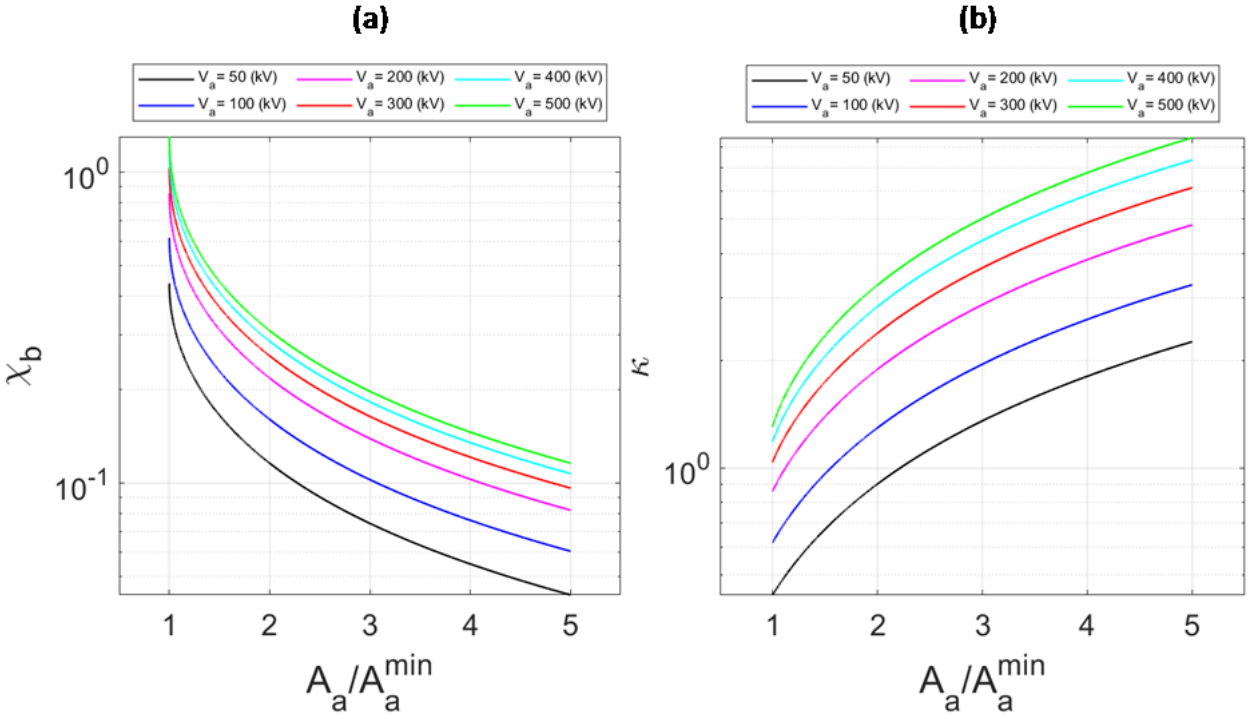

Figure 2.3: The parameters χ_b and κ from which the Brillouin flow properties may be determined, each parameterized as a function of the degree of magnetic insulation $\bar{A}_a/\bar{A}_a^{min}$ and the gap voltage $\bar{V}_a$. (a) The parameter χ_b obtained using the exact expression Eq. 2.54. This can be applied to both planar flow and cylindrical axial flow. (b) The parameter κ obtained using the exact expression Eq. 2.44. This can be applied directly to planar flow (Figure 2.1a). It can also be applied to cylindrical axial flow (Figure 2.1b) via Eq. 2.60 in which $\bar{\kappa} = \kappa/ln(r_a/r_c)$, where r_a/r_c represents the aspect ratio of the coaxial geometry. Thus, the values of χ_b and κ given in this figure can be applied to a coaxial MILO regardless of its aspect ratio.

Figure 2.4 depicts the Brillouin hub height as a function of the degree of insulation and operating voltage, obtained directly from Eq. 2.41. As the magnetic field approaches the Hull cutoff condition, all curves converge upon the correct result where space charge fills the gap. The

hub height is relatively insensitive to the voltage; at fixed $\bar{A}_a/\bar{A}_a^{min}$, the hub height changes by less than a factor of two despite varying the voltage across an order of magnitude. The hub height quickly diminishes as $\bar{A}_a/\bar{A}_a^{min}$ increases, ultimately filling less than 10 % of the gap as the insulation enters the range $2 < \frac{\bar{A}_a}{\bar{A}_a^{min}} < 3$, regardless of voltage. Unexpectedly, the hub height *decreases* as the voltage increases while the degree of insulation is fixed. This implies that for a deeply insulated transmission line such as a MITL, the hub itself carries a small amount of current compared to the cathode current, which is driving the magnetic insulation.

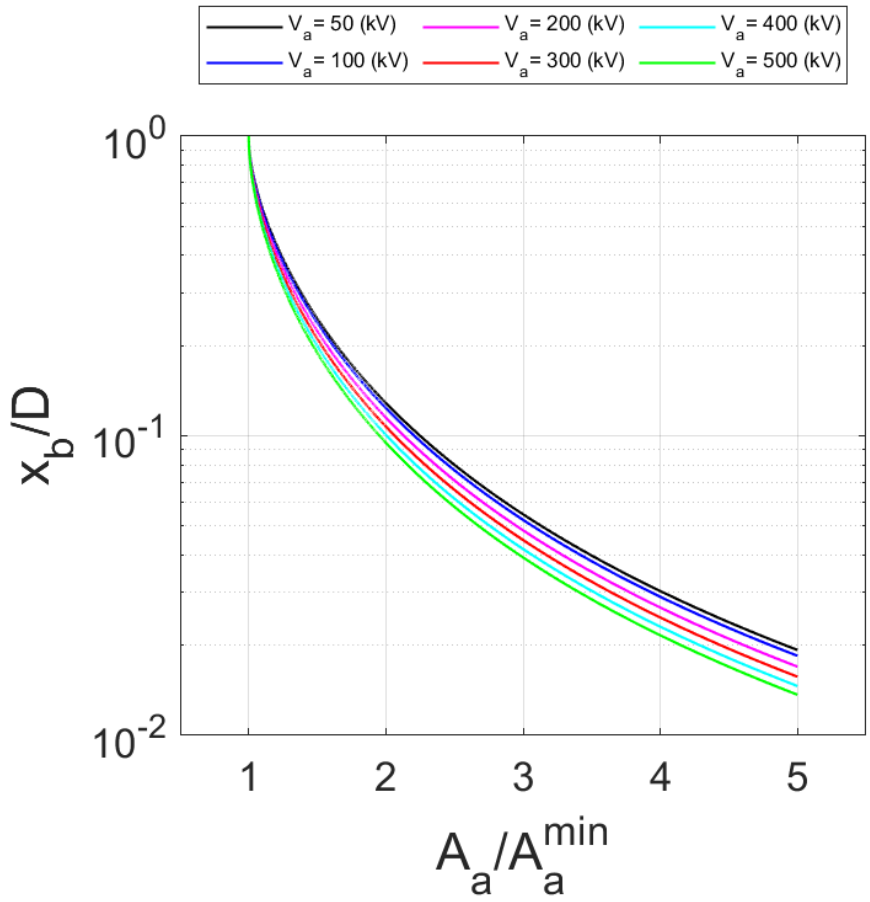

Figure 2.4: Using the expression Eq. 2.41, the normalized height of the Brillouin hub $\bar{x}_b$ for the planar diode (Fig. 1a) is parameterized as a function of the degree of magnetic insulation $\bar{A}_a/\bar{A}_a^{min}$ and across gap voltage. The Brillouin hub height unexpectedly shrinks as the gap voltage increases while holding $\bar{A}_a/\bar{A}_a^{min}$ constant.

The electron velocity at the edge of the Brillouin hub, β_b, is of particular interest because it is key in synchronizing the SWS phase velocity with a Brillouin layer in the hub. If the fastest layer of electrons, represented by β_b, becomes substantially slower than the phase velocity, then it will become increasingly difficult for the electromagnetic mode to couple to and modulate the

beam synchronously throughout the device. For this reason, the region of operation is between the HC and BH lines in Figure 2.2, and not beneath the BH line according to the Brillouin flow model [93]. There are also practical reasons that this would be observed in experiments, however, such as diode plasma gap closure. The expression Eq. 2.54 may be used to calculate β_b directly, and it is shown in Figure 2.5. This valuable expression of β_b, which is only as a function of the degree of insulation and voltage, is valid in both the planar geometry and cylindrical geometry with axial flow, so it may be applied directly to a planar magnetron or coaxial MILO. This dissertation's two devices of interest are a dual-frequency planar magnetron and a cylindrical MILO, which operate at phase velocities of ~0.224c and ~0.3c, respectively, between 200 kV and 300 kV. Thus, it is expected that the magnetron will operate most effectively near $\bar{A}_a/\bar{A}_a^{min} \cong 2$, and the MILO near $\bar{A}_a/\bar{A}_a^{min} \cong 1.5$.

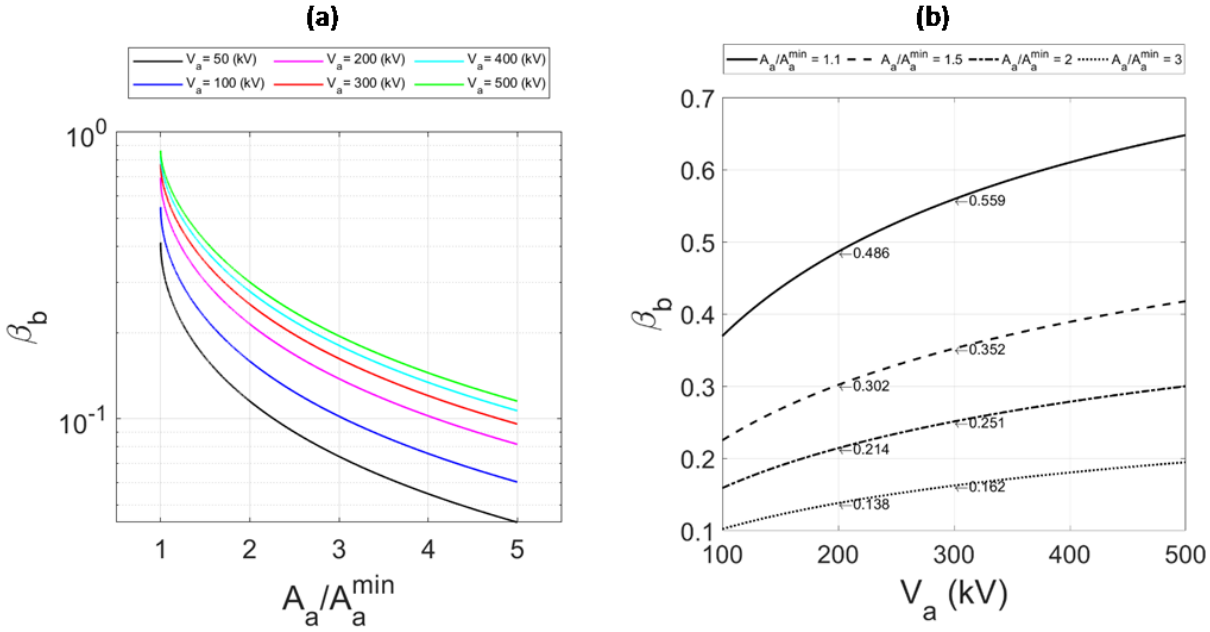

Figure 2.5: The normalized electron velocity at the edge of the Brillouin hub, β_b, calculated from the exact expression Eq. 2.54. For convenience, this information is presented (a) as a function of the degree of insulation $\bar{A}_a/\bar{A}_a^{min}$, the degree of magnetic insulation, at various gap voltages $\bar{V}_a$ and (b) as a function of voltage, at various degrees of insulation. This figure applies to both planar and coaxial geometries in Figure 2.1 and depends only on $\bar{A}_a$ and $\bar{V}_a$.

The electron kinetic energy at the edge of the Brillouin hub, ϕ_b, is given in Figure 2.6 as a function of the degree of insulation for voltages of 50 kV < V_a < 500 kV. By Eq. 2.50, this is an alternative representation of Figure 2.5, but presenting the information in this manner enables greater discussion of the efficiency of magnetrons. Investment of kinetic energy into the Brillouin hub is inherent in crossed-field interaction for synchronization between beam and wave. The

kinetic energy invested in the electrons is therefore unavailable for transfer to the RF wave. In the Brillouin flow model, the total energy of an electron equals zero; therefore, the kinetic energy of an electron equals the magnitude of its potential energy [cf. Eq. 2.22a]. The maximum transferable potential energy from the synchronous layer to the RF wave, which is assumed to be the edge of the hub, is therefore $e(V_a - \phi_b)$, where V_a represents all of the DC potential energy available in an electron that is ultimately collected on the anode. The maximum achievable efficiency is therefore $\eta = 1 - \phi_b/V_a$ [104]. Taking the example of a magnetron operating at 50 kV and $\bar{A}_a/\bar{A}_a^{min} \cong 2$, which is true of many commercial magnetrons, the maximum achievable efficiency is in excess of 90%. This is not realizable in many magnetrons, where often the kinetic energy of electrons impacting the anode exceeds ϕ_b, among other numerous forms of loss. However, some carefully designed magnetrons in fact achieve efficiencies in excess of 90%, and it is this property that in part makes this device efficacious nearly a century after it was invented.

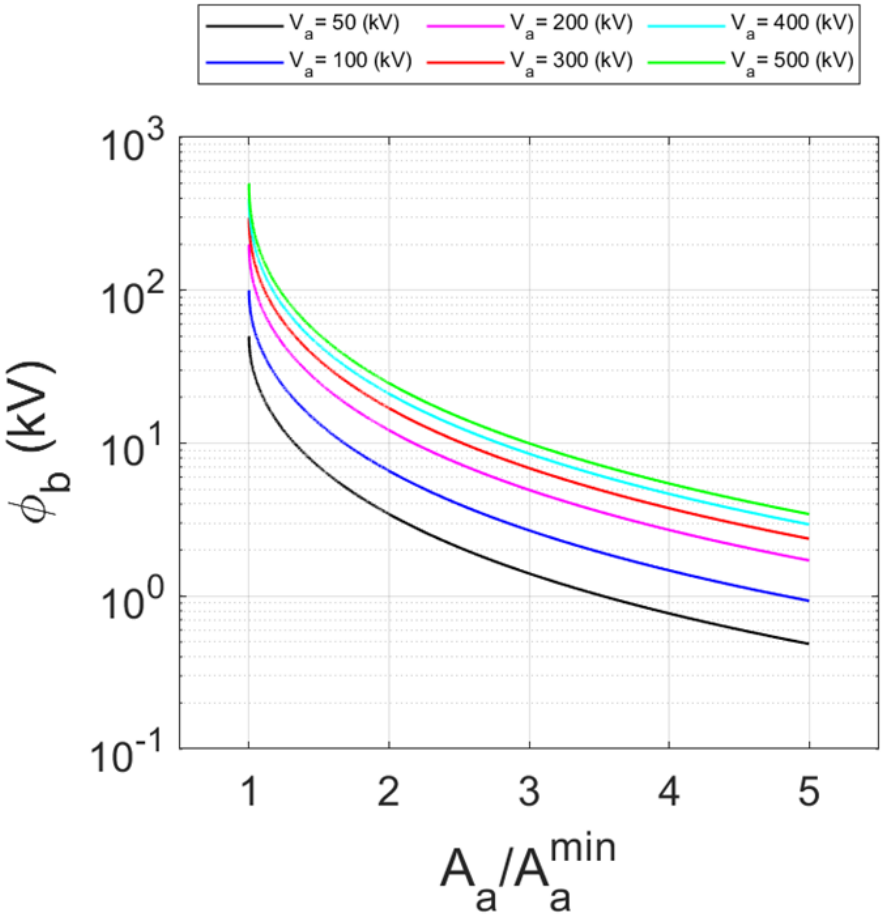

Figure 2.6: The electron kinetic energy at the edge of the Brillouin hub, ϕ_b, as a function of $\bar{A}_a/\bar{A}_a^{min}$, the degree of magnetic insulation, at various gap voltages V_a. This is valid for either geometry in Figure 2.1. The maximum extractable energy from each electron at the hub edge is the difference between V_a and ϕ_b for a given value of $\bar{A}_a/\bar{A}_a^{min}$.

2.3 Coaxial Brillouin Flow

In this section, the same process as in Section 2.2 will be repeated with the same objectives and goals, but now applied to the cylindrical geometry with axial flow as depicted in Figure 2.1b. Here, the flow of current and the vector potential are in the z-direction, the electrostatic field is radial, and the magnetostatic field is azimuthal; once more, the total magnetic flux per unit length, now in the z-direction, is A_a. The gap is held at potential V_a, and the cathode, hub, and anode radii are r_c, r_b, and r_a, respectively. Most importantly, the Buneman-Hartree equation will be derived for the typical MILO geometry from first principles using the Brillouin flow formulation. The length scale x_s is set to the anode radius r_a, and the normalized radius is set equal to $\bar{x}$ by definition to keep the notation consistent with Section 2.2.

$$\bar{r} = r/r_a \equiv \bar{x} \tag{2.55}$$

Many of the equations from Section 2.2 can be applied directly to this problem. Equations 2.17, 2.18, and 2.21-2.34 all remain valid. The Gauss' Law and Ampère's Law, Eqs 2.19-2.20, must be modified for cylindrical coordinates,

$$\frac{1}{\bar{r}}\frac{\partial}{\partial \bar{r}}(\bar{r}\bar{E}) = \bar{n} \tag{2.56}$$

$$\frac{1}{\bar{r}}\frac{\partial}{\partial \bar{r}}(\bar{r}\bar{B}) = \bar{n}\beta \tag{2.57}$$

In searching for a differential equation for $\chi(\bar{r}) = \chi(\bar{x})$, insert Eq. 2.56 into 2.57 and utilize the expressions Eq. 2.28 and 2.33 to replace β and $\bar{B}$. The resultant equation before expansion is given in Eq. 2.58, which reduces to Eq. 2.59 after expanding the derivatives and applying hyperbolic identities and the chain rule. Once more, it is convenient to define $\chi' \equiv \frac{\partial \chi(\bar{r})}{\partial \bar{r}}$, which is now shown to be inversely proportional to $\bar{r}$ (in the planar case, χ' was a constant). Solving Eq. 2.59 yields 2.60, where the boundary condition from Eq. 2.27b is now $\chi(\bar{r}_c) = 0$, and $\bar{\kappa}$ is a constant.

$$\frac{1}{\bar{r}}\frac{\partial}{\partial \bar{r}}(\bar{r}\chi'\cosh(\chi)) = \tanh(\chi)\frac{1}{\bar{r}}\frac{\partial}{\partial \bar{r}}(\bar{r}\chi'\sinh(\chi)) \tag{2.58}$$

$$\frac{\partial}{\partial \bar{r}}\left(\bar{r}\frac{\partial \chi}{\partial \bar{r}}\right) = 0 \tag{2.59}$$

$$\chi(\bar{r}) = \bar{\kappa}\ln(\bar{r}/\bar{r}_c), \quad \chi'(\bar{r}) = \bar{\kappa}/\bar{r} \tag{2.60}$$

Once again, the vacuum field solutions ($\bar{r}_b < \bar{r} < 1$) must be determined. In coaxial geometry, the fields $\bar{E}(\bar{r}) = \partial\bar{\phi}(\bar{r})/\partial\bar{r}$ and $\bar{B}(\bar{r}) = \partial\bar{A}(\bar{r})/\partial\bar{r}$ are inversely proportional to $\bar{r}$, while the scalar potential and magnetic flux are logarithmic functions of $\bar{r}$. The subscripts "b" in

$(\bar{\phi}_b(\chi(\bar{r}=\bar{r_b})), \bar{E}_b(\chi(\bar{r}=\bar{r_b})), \bar{r_b}, \bar{A}_b(\chi(\bar{r}=\bar{r_b})), \bar{B}_b(\chi(\bar{r}=\bar{r_b})))$ denote the values of these parameters at the edge of the Brillouin hub.

$$\bar{\phi}(\bar{r}) = \bar{\phi}_b + \bar{E}_b \bar{r_b} \ln(\bar{r}/\bar{r_b}) \tag{2.61}$$
$$\bar{A}(\bar{r}) = \bar{A}_b + \bar{B}_b \bar{r_b} \ln(\bar{r}/\bar{r_b}) \tag{2.62}$$

In the same manner that produced Eqs. 2.39-2.40, Eqs. 2.61-2.62 are evaluated at the anode radius r_a, and the hyperbolic expressions for $(\bar{\phi}_b, \bar{E}_b, \bar{A}_b, \bar{B}_b)$ are used once again to yield Eqs. 2.63-2.64.

$$\bar{V}_a = \cosh(\chi_b) - 1 + \sinh(\chi_b) \times \bar{\kappa} \ln(1/\bar{r_b}) \tag{2.63}$$
$$\bar{A}_a = \sinh(\chi_b) + \cosh(\chi_b) \times \bar{\kappa} \ln(1/\bar{r_b}) \tag{2.64}$$

By eliminating the common factor of $\bar{\kappa} \ln(1/\bar{r_b})$, the same transcendental expression from the planar analysis, Eqs. 2.42-2.43, may be obtained. *Thus, the solutions for χ_b are indeed the same for the planar geometry and the cylindrical geometry with axial flow*. It also follows that the closed-form solution for χ_b, Eq. 2.54, remains valid, which will be discussed shortly. However, to find complete solutions for the Brillouin profile, it is still necessary to find an expression for $\bar{\kappa}$. First, evaluate $\chi(\bar{r_b})$ using Eq. 2.60 to obtain Eq. 2.65, which may be solved directly for the Brillouin hub height $\bar{r}_b$, given in Eq. 2.66. Direct substitution of Eq. 2.65 into Eq. 2.63 enables the derivation of Eq. 2.67.

$$\bar{\kappa} \ln(\bar{r_b}) = \bar{\kappa} \ln(\bar{r_c}) + \chi_b \tag{2.65}$$
$$\bar{r_b} = \bar{r_c} e^{\chi_b / \bar{\kappa}} \tag{2.66}$$
$$\bar{\kappa} = \frac{1}{ln(r_a/r_c)} \left[\chi_b + \frac{\bar{V}_a - (cosh\chi_b - 1)}{sinh\chi_b}\right] \tag{2.67}$$
$$\bar{\kappa} = \kappa / ln(r_a/r_c) \tag{2.67a}$$

Here, $\bar{\kappa}$ is a constant which depends on the boundary conditions $\bar{V}_a$ and $\bar{A}_a$, by virtue of Eq. 2.54, as well as the aspect ratio of the coax. This difference is in contrast to the planar geometry in Section 2.2, where Eq. 2.44 demonstrates that κ depends only on $\bar{V}_a$ and $\bar{A}_a$. It can be easily shown that $\bar{\kappa} = \kappa / ln(r_a/r_c)$.

With expressions for χ_b and $\bar{\kappa}$ determined, Eq. 2.60 is now fully defined throughout the AK gap. All of the Brillouin flow parameters, Eq. 2.28-2.34, may now be determined, with the hub height given by Eq. 2.66. Now it becomes appropriate to derive the HC and BH conditions. Beginning with the HC condition, where the Brillouin hub height approaches the AK gap distance ($\bar{r} \to 1$), the expressions Eq. 2.45-2.48 and the logic required to produce them all remain valid. Alternatively, because $\bar{r}_b = \bar{r}_a = 1$ at the HC condition, it follows that $\gamma_b = \gamma_a = \bar{V}_a + 1 =$

$cosh\chi_b$. Applying both of these conditions to Eq. 2.64 will yield Eq. 2.68, the same HC condition as Eq. 2.48.

$$\bar{A}_a = \sinh(\chi_b) = \sqrt{(\cosh(\chi_b))^2 - 1} = \sqrt{\bar{V}_a^2 + 2\bar{V}_a} \tag{2.68}$$

Once more, for microwave generation it is assumed that the SWS phase velocity $\beta_{ph} = v_{ph}/c$ at the anode is synchronous with the edge velocity $\beta(\bar{r}_b) = \beta_b$ under sufficient insulation of the AK gap ($\bar{A}_a/\bar{A}_a^{min} > 1$) to produce the BH condition. The BH condition may be found by taking Eq. 2.64, multiplied by $\tanh(\chi_b)$, and subtracting this expression from Eq. 2.63. This arithmetic produces the same result as Eq. 2.49, which may easily be shown to reduce to Eq. 2.51, as explained in Section 2.2. Thus, the BH and HC conditions for the planar geometry and cylindrical geometry with axial flow are identical, and Figure 2.2, therefore, applies to both geometries in Figure 2.1. For convenience, this BH condition is restated here in Eq. 2.69. In section 2.2, it was shown that this equation could be modified to obtain a closed-form solution for χ_b, stated in Eq. 2.54 and restated in Eq. 2.70, which thus applies to the geometry under consideration here in Section 2.3.

$$\bar{V}_a = \bar{A}_a\beta_b - [1 - \sqrt{1 - \beta_b^2}] \tag{2.69}$$

$$\beta_b = \tanh(\chi_b) = \frac{\gamma_a\bar{A}_a - \sqrt{\bar{A}_a^2 - (\bar{A}_a^{min})^2}}{\bar{A}_a^2 + 1} \tag{2.70}$$

Equation 2.69 is the Buneman-Hartree for the cylindrical MILO (Fig. 2.1b), by setting the normalized Brillouin flow speed at the top of the Brillouin hub, β_b, equal to the normalized phase speed of the operating mode there [93], [100].

With all of the Brillouin flow profiles determined for the planar geometry and coaxial geometry with axial flow, it is time to compare and contrast. This comparison is most easily accomplished by considering the direct expressions for the Brillouin flow parameters $(\gamma, \bar{E}, \bar{B}, \bar{\phi}, \bar{A}, \bar{n}, \beta)$, listed in Eq. 2.28-2.34, which apply to both planar and cylindrical axial flow. These expressions are valid within the Brillouin hub, outside of which the vacuum solutions Eq. 2.37-2.38 and 2.61-2.62 must be considered. All of the Brillouin flow properties can be expressed in terms of χ alone, which includes $(\gamma, \bar{\phi}, \bar{A}, \beta)$, or the combination of χ with χ', which includes $(\bar{E}, \bar{B}, \bar{n})$. In planar geometry, $\chi'(\bar{x}) = \kappa$, and in coaxial geometry $\chi'(\bar{r}) = \bar{\kappa}/\bar{r}$, where $\bar{\kappa} = \kappa/ln(r_a/r_c)$. Meanwhile, $\chi(\bar{x}) = \kappa\bar{x}$ for planar and $\chi(\bar{r}) = \bar{\kappa}\ln(\bar{r}/\bar{r_c}) = \kappa[\ln(\bar{r})/\ln(r_a/r_c) + 1]$ for coaxial geometry. These expressions are inherently different from each other, and they arise

due to the difference in the application of the Cartesian and cylindrical coordinate systems. Also as a result of this, the vacuum fields $\bar{E}$ and $\bar{B}$ in Cartesian geometry are uniform, whereas in cylindrical coordinates they are inversely proportional to $\bar{r}$. However, because the expressions for χ_b are identical in both treatments, the parameters which depend only on χ $(\gamma, \bar{\phi}, \bar{A}, \beta)$ are indeed the same *at the edge of the Brillouin hub*. For this exact reason, the edge velocity β_b, electrostatic hub height potential $\bar{\phi}_b$, and, crucially, the Hull Cutoff condition and Buneman-Hartree condition are all the same in both planar flow and cylindrical axial flow.

To further examine the MILO, it is necessary to determine the cathode current I_c, anode current I_a, and electron current I_e, all depicted in Figure 2.1b, and all defined to be positive. The anode current represents the total current delivered to the diode, which includes the sum of the Brillouin hub current I_e and the current driven along the walls of the inner conductor I_c. The explicit relationship between these three paths of current is given in Eq. 2.71.

$$I_e = I_a - I_c = I_c(I_a/I_c - 1) \tag{2.71}$$

Because the current and magnetic field are proportional to each other in this situation, it is helpful to know what the magnetic field is at each location of interest, specifically at the anode and cathode. From Eq. 2.33 and Eq. 2.62, the magnetic field at the cathode (Eq. 2.72) and anode (Eq. 2.73) may be produced. After that, Ampère's Law evaluated at the surface of the cathode yields Eq. 2.74, where Eq. 2.4, 2.6, and Eq. 2.72 have been applied to yield the final equality.

$$\bar{B}_c = \bar{\kappa}/\bar{r}_c \tag{2.72}$$

$$\bar{B}_a = \bar{\kappa}\cosh(\chi_b) \tag{2.73}$$

$$\frac{I_c}{I_s} = \frac{2\pi r_c B_c}{I_s \mu_0} = 2\pi \bar{r}_c \bar{B}_c = 2\pi\bar{\kappa} = 2\pi\kappa/ln(r_a/r_c) \tag{2.74}$$

By reapplying Ampère's Law at the anode surface, the ratio I_a/I_c may be determined explicitly. By virtue of Eq. 2.71, the ratio I_a/I_c may also be produced. With I_c given by Eq. 2.74, both I_a and I_e are now fully defined. Importantly, $I_a : I_c : I_e$ is independent of the aspect ratio. This analysis may be reapplied to a planar MILO/MITL, in which Eq. 2.75 remains valid.

$$I_a : I_c : I_e = \cosh(\chi_b) : 1 : [\cosh(\chi_b) - 1] \tag{2.75}$$

While the ratio between these currents depends only on $\bar{V}_a$ and $\bar{A}_a$, the aspect ratio remains an important tool in MILO design by Eq. 2.74. To meet conditions suitable for operation on MELBA, between roughly 200 kV and 300 kV and near 10 kA, it became necessary to make the cathode much smaller than others commonly utilized in the literature. Figure 2.7 provided the foundation

from which the simulations and experiments in later chapters were built. To keep the AK gap distance relatively small in comparison to the L-Band wavelength and to meet the physical demands of the existing experimental hardware, the cathode radius r_c and anode radius r_a were set to 7 mm and 25 mm, respectively, corresponding to an aspect ratio of $r_a/r_c = 3.6$. At 250 kV, the design goal of operation near 10 kA may be achieved with magnetic insulation in the range $1.1 < \bar{A}_a/\bar{A}_a^{min} < 1.5$.

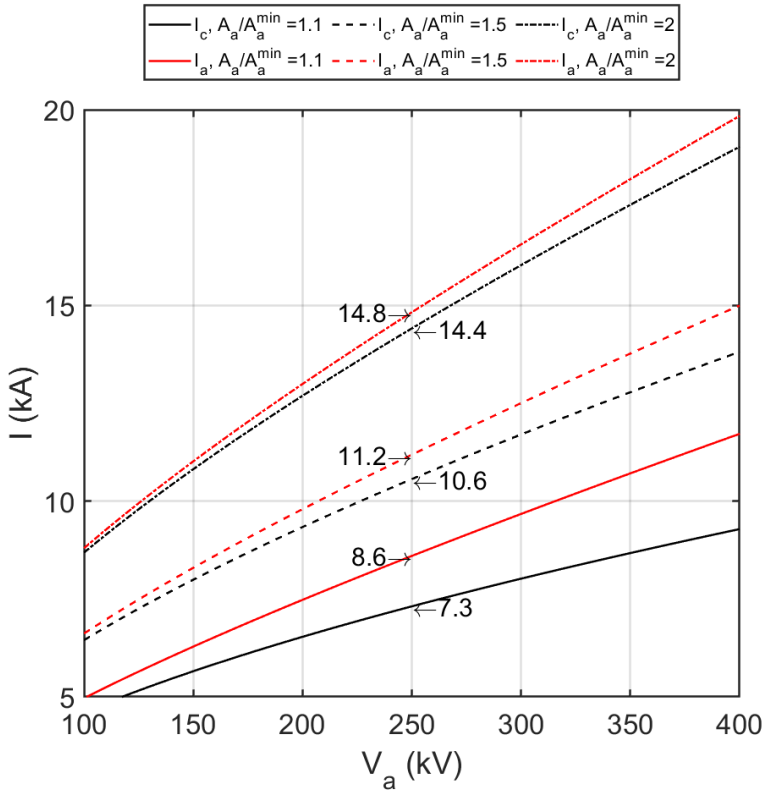

Figure 2.7: The current carried on the cathode surface I_c (Eq. 2.74) and the total current carried on the anode surface I_a (Eq. 2.75) as a function of the voltage and parameterized across several degrees of magnetic insulation for the cylindrical geometry in Figure 2.1b. The aspect ratio is $r_a/r_c = 3.6$, where the cathode radius r_c and anode radius r_a are 7 mm and 25 mm, respectively. The electron hub current is $I_e = I_a - I_c$.

Something else to note from Figure 2.7 is that the electron current is relatively small compared to the cathode current. This is because $I_e/I_c = \cosh(\chi_b) - 1 = \bar{\phi}_b$, and it is evident that the ratio increases as the voltage increases and $\bar{A}_a/\bar{A}_a^{min}$ decreases (see Figure 2.6). It therefore stands to reason that the greater majority of the insulating magnetic field is provided by the wall currents on the cathode, and not by the Brillouin hub itself, which had been suggested previously [26]. This is particularly true for well-insulated diodes and at lower voltages.

In a similar fashion to Figure 2.4, the fraction of the gap distance filled by space charge is shown in Figure 2.8 for an aspect ratio of $r_a/r_c = 3.6$. At Hull cutoff, the gap is completely filled

across all voltages. The hub height then quickly diminishes as the insulation is increased only slightly; at $\bar{A}_a/\bar{A}_a^{min} = 1.1$, the space charge only fills ~40% of the AK gap. At the anticipated operating range of $1.1 < \bar{A}_a/\bar{A}_a^{min} = 1.5$, the hub fills between 12% and 38% of the gap at 250 kV. This behavior depends weakly on the voltage and is broadly similar to the observations made in Figure 2.4. As a result, it is unnecessary to operate far above Hull Cutoff ($A_a/A_a^{min} > 1.5$) to keep electrons from streaming close to the anode, which importantly protects against excessive lifetime damage to the MILO.

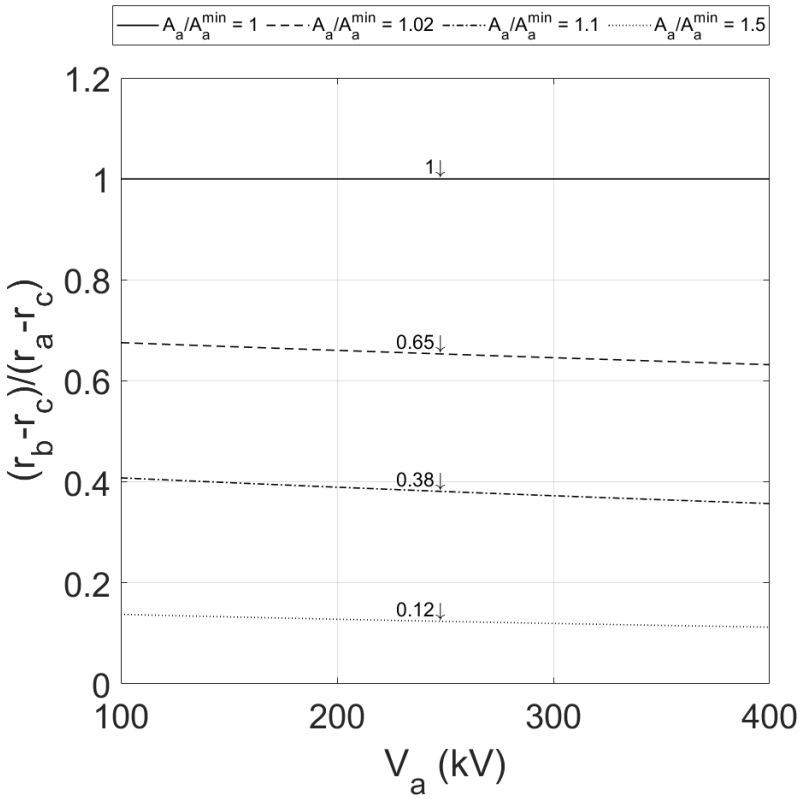

Figure 2.8: The Brillouin hub height r_b, given in Eq. 2.66, represented as the fraction of the coaxial gap width as a function of the voltage and parameterized across several degrees of magnetic insulation for the cylindrical geometry in Figure 2.1b for an aspect ratio of $r_a/r_c = 3.6$. This behavior is weakly dependent on the voltage.

In Figure 2.6, the kinetic energy at the edge of the Brillouin hub was used to comment on the theoretical maximum efficiency of the magnetron. The information presented there may apply to the planar geometry or the cylindrical geometry with axial flow. In Figure 2.9, the same information from Figure 2.6 may be used to ascertain the theoretical maximum efficiency for a MILO. The maximum efficiency is assumed to be $\eta = I_e(V_a - \phi_b)/(I_a V_a) = (1 - \gamma_b^{-1})(1 - \phi_b/V_a)$, where the denominator $(I_a V_a)$ is the total input power supplied by the driver, and the numerator $I_e(V_a - \phi_b)$ is the RF power, assuming that it derives from the potential energy drop

by all electrons in the Brillouin hub, each of which becomes a spoke electron which converts all of its potential energy loss into RF during its journey from the top of the Brillouin hub to the anode. Notice that this is essentially the same expression given in Section 2.2 for magnetron efficiency, but there is another term $I_e/I_a = (1 - \gamma_b^{-1})$ that appears, which significantly reduces the efficiency. As a result, it is more advantageous to operate a MILO at higher voltages and closer to Hull cutoff (Figure 2.9). The efficiency decreases as $\bar{A}_a/\bar{A}_a^{min}$ increases, which is because more current becomes invested in I_a to raise the magnetic field while the electron current doesn't increase enough to compensate. Ultimately, this means the MILO is preemptively inclined to have very low efficiency compared to the magnetron. There may be several ways to ameliorate this issue. It is possible to provide a portion of the magnetic field from an external source or a permanent magnet, thus reducing the current required from the pulsed power to achieve magnetic insulation; this is a significant motivation for the interest in a hybrid between the MILO and magnetron. Another potential method to retrieve spent energy is implementing a depressed collector on the DC beam to retrieve some portion of the electron kinetic energy in that portion of the device, which can be more easily realized in some geometries than others. A similar concept has already been established with the tapered MILO [82].

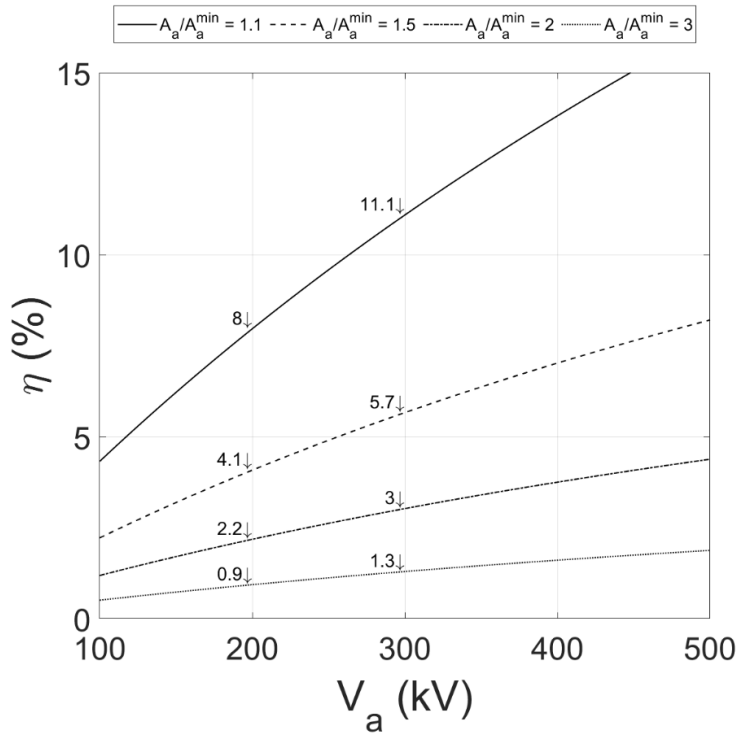

Figure 2.9: Maximum total efficiency η as a function of the voltage and parameterized across several degrees of magnetic insulation for the cylindrical geometry. The efficiency is defined as $\eta = I_e(V_a - \varphi_b)/(I_a V_a)$, where φ_b may be drawn from Figure 2.6 (calculated using Eq. 2.30). By Eq. 2.75, the ratio I_e/I_a is independent of the geometry.

A vital consequence specific to MILO, which was not discussed in this chapter, will be explained in the context of the experiments in Section 6.3. It was found that as the degree of magnetic insulation decreased towards Hull Cutoff, the total current I_a ceases to be a unique function of the flux ratio A_a/A_a^{min}; specifically, the flux ratio becomes a double-valued function of the current. This regime is colloquially referred to as the "v-shaped curve," and it exists regardless of voltage and coaxial aspect ratio [93]. *Within this v-shaped curve, the total current required to insulate the diode is less than the current at Hull cutoff.*

Chapter 3 Simulation and Design

This chapter details the simulation processes, and subsequent design decisions, for the HRPM and MILO projects. Each case follows a similar trajectory. The latent electromagnetic modes within the slow-wave structures (SWSs) are designed to establish synchronism and energy exchange with the electrons streaming by in the Brillouin hub. These simulations utilize a finite difference, frequency-domain solver known as High Frequency Structure Solver (HFSS). Then finite difference, time-domain, three-dimensional simulations are applied to each device using CST-Particle Studio (CST-PS) [105] and ICEPIC [106], which are both particle-in-cell (PIC) codes. These models enable dynamic interaction between electrons and the RF wave in time to make predictions such as output power and current draw.

3.1 Magnetron Frequency Domain Simulations

The HRPM was designed as a multi-frequency resonator that generates two tones simultaneously, one at the second harmonic of the other [65]. This goal was accomplished by placing two planar SWS's adjacent to each other, on the same side of the cathode, unlike previous research by Greening [54], as illustrated in Figure 1.1. This leaves a drift space on the opposite side of the cathode, which in theory could be replaced by a set of oscillators scaled to generate another set of signals, and makes the HRPM a proof-of-concept magnetron prototype that can produce more than two frequencies. The two frequencies chosen for this experiment were near 1 GHz and 2 GHz, and the structures that generate them are the L-Band Oscillator (LBO) and S-Band Oscillator (SBO), respectively.

To enable simultaneous transfer of energy from the electron hub to multiple structures whose desired modes of operation are at different frequencies, each of them must be scaled to equal phase velocities to promote synchronism with the same Brillouin hub velocity. In other words, every structure intended to extract energy from the hub must satisfy the same Buneman-Hartree (BH) Condition [100], which was derived in Chapter 2. The more convenient form for magnetron slow wave structure (SWS) design is given in Eq. 3.1, where relevant parameters are the gap voltage, V_{BH}, magnetic field, B, electron mass, m, speed of light, c, electron charge, e, AK-

gap distance, D, and normalized SWS phase velocity, $v_\theta/c \equiv \beta$. The phase velocity is given in Eq. 3.2, where parameters include the circuit pitch (i.e., periodicity of SWS), P, frequency, f, angular frequency, ω, wavenumber, β_θ, and advancement of the phase in the tangential electric field per unit cell, φ.

$$V_{BH} = \beta BDc - \frac{mc^2}{e}(1 - \sqrt{1-\beta^2}) \tag{3.1}$$

$$v_\theta = {}^{\omega}/_{\beta_\theta} = \frac{2\pi f}{(\varphi/P)} \tag{3.2}$$

The phase velocity was set to roughly 0.23c for the SBO, π-mode frequency between 2.1-2.2 GHz (depending on the experiment), circuit pitch of 0.16 cm, anode-cathode (AK) gap of 2 cm, and gap voltage of -300 kV. At these conditions, the BH magnetic field is 0.227 T. Knowing that the desired LBO frequency is half of the SBO frequency, for operation in the π-mode at the same phase velocity, its circuit pitch must therefore be twice as large as the SBO.

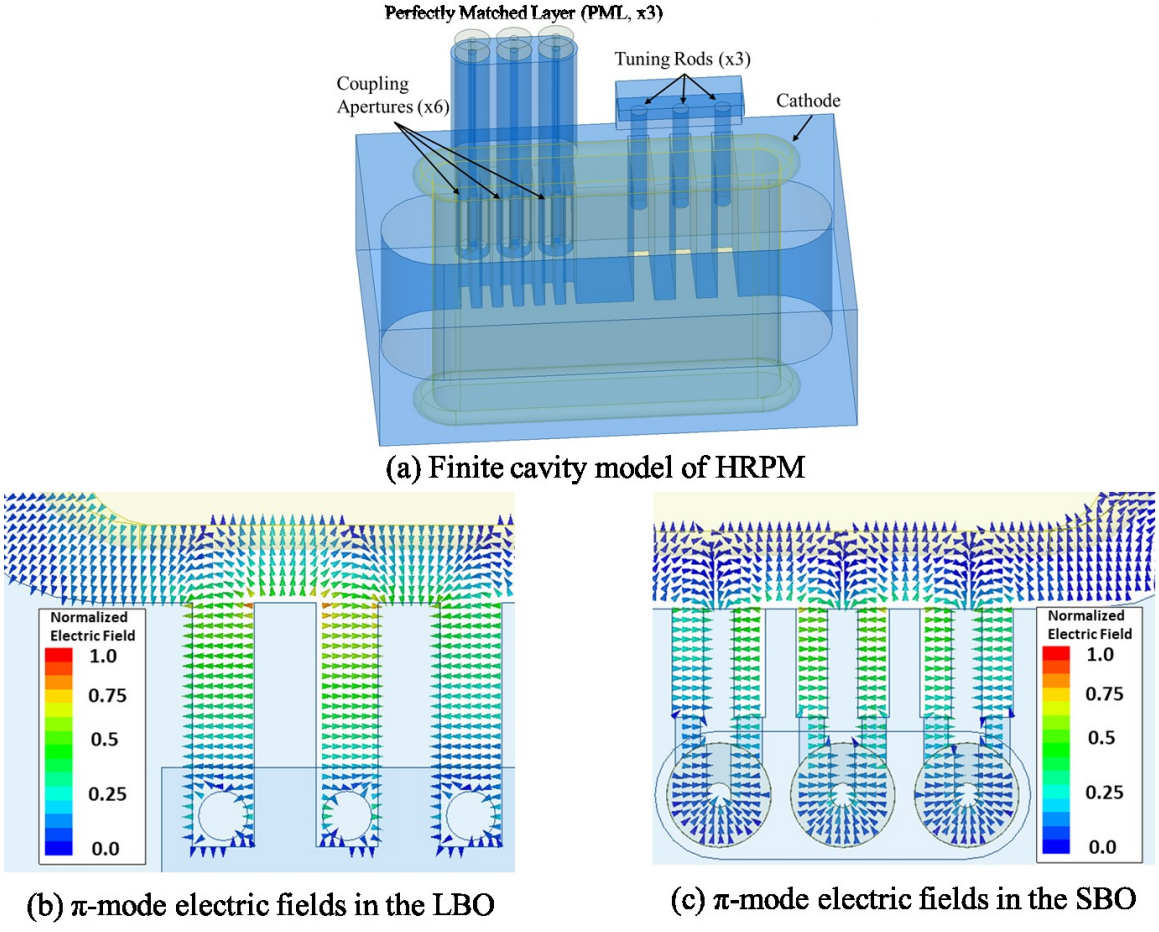

(a) Finite cavity model of HRPM

(b) π-mode electric fields in the LBO

(c) π-mode electric fields in the SBO

Figure 3.1: 3-Dimensional, finite cavity HFSS model of the HRPM, displaying relevant boundary conditions and the fields of the π-mode within both the LBO and SBO. The coupling aperture length h and tuning rod insertion L are both essential independent variables in this study.

With the circuit pitch and frequency determined, two more dimensions of the rectangular cavities must be chosen. The axial length of the vanes was set to 11 cm (along the z-direction of Figure 3.6) to keep consistent with prior experiments [53], [54]. The choice of this parameter is satisfactory for the LBO because it enables generation of an electron hub with large axial length, and the first higher order axial mode (one wavelength variation along the z-direction of Figure 3.6) is separated by a substantial frequency band. The same higher order mode is more problematic for the SBO because it has comparatively smaller separation in frequency with the desired fundamental mode, but it was not observed to pose significant problems in the PIC simulations or experiments.

The choice of the vane height (along the y-direction of Figure 3.6), which largely determines the frequency of the fundamental mode, is where HFSS becomes useful; using the eigenmode solver, the software applies a tetrahedral mesh to the complex geometry and solves Maxwell's equations to determine the resonant modes within a system. The information provided includes the quality factor and resonant frequency, which are of maximum interest in this experiment. While analytic treatments for rectangular SWS's such as these exist [107], it would be very difficult to analytically treat the range of frequencies provided by the tuning stubs by the LBO, or the effect that the Coaxial-All-Cavity-Extractor (CACE) has on the SBO frequency or quality factor. Thus, multiple different models were built to analyze both the SBO and LBO structures.

One of the approaches taken was a finite cavity model, which simulates the anode precisely as it is assembled in the experiment. This model is shown in Figure 3.1, where coaxial-all-cavity-extraction (CACE) [108] is implemented to extract microwave power from the SBO. This scheme is meant to operate in the π-mode, where the cavity fields in adjacent cavities are in opposite directions. Each coaxial line output is terminated with a perfectly matched layer (PML) to absorb the outgoing wave so that the full extractor did not need to be simulated. A surrounding box, which is not pictured, applies a reflecting perfect electrical conductor (PEC) boundary; this choice was made to reduce the complexity of the model rather than simulating the full experimental chamber. Using the eigenmode solver, this model identifies frequency and quality factors for all resonant modes of interest within the model, where modes of interest are defined as those that exist upon the SWS and may couple to the beam.

Another approach applies phase-advance boundary conditions to a unit cell to simulate an infinite cavity model [109], [110]. The LBO model, shown in Figure 3.2, was used to obtain the resonant frequency as a function of the length of the tuning rod, *L*. This approach is helpful because it enables a sweeping examination of the phase difference across the unit cell, which can produce the dispersion relation for a SWS. It is also less computationally expensive to simulate, allowing rapid examination of specific parameters of interest. An equivalent model for the SBO, which is not shown, was also composed to analyze its dispersion relation. With the unit cell model, the LBO and SBO vane heights were set to 6.3 cm and 2.8 cm to meet design constraints mentioned previously.

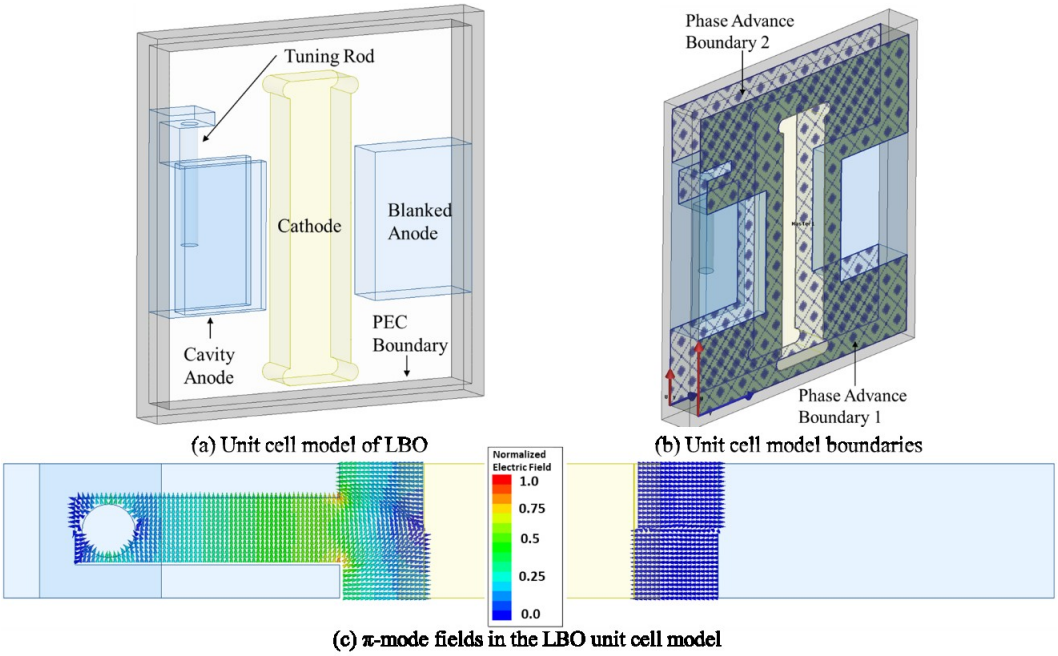

Figure 3.2: Unit cell model of the LBO, labeled by component and boundary conditions and displaying the π-mode fields.

The HRPM was designed to excite the SBO π-mode on resonance with the second harmonic of the LBO resonant frequency [65], which is a decision explained further in Chapter 5. Two independent variables were introduced because of this: the LBO resonant frequency and SBO quality factor. These are controlled by the tuning rods and coupling apertures, respectively, which are pictured in Figure 3.1a and examined in more detail in Chapter 4. The length of the tuning rods, *L*, could be used to shift the LBO frequency on a shot-to-shot basis, and multiple experiments were performed for different values of *h,* the coupling aperture length. The HFSS models were used to design the LBO and SBO with reasonable frequencies across the range of *L* and *h* that were to be examined so that the phase velocity across experiments did not change significantly.

The dispersion relation for each structure is shown in Figure 3.3. The LBO dispersion relation is plotted for several values of L, which is bounded between 0 cm (no tuning rod) and 11 cm (complete insertion into the cavity). The π-mode, which is the absolute maximum for each curve, increases as L is increased. The SBO dispersion relation is plotted for the three values of h (the coupling aperture length) examined in the experiments, along with the dispersion relation if the extractor was nonexistent (h = 0 mm). As the coupling increases between the extractor and the cavities (equivalently, as h increases), the resonant frequency decreases. In each case, the π-mode phase velocity falls close to 0.23c, represented by the solid black line. The black dashed lines correspond to a 5% detune from this design point of 0.23c (±0.0115c). The LBO π-mode across the entire tuning range falls within this cone, as well as the SBO π-mode for the considered range of h. By synchronizing both structures to the same phase velocity, each can interact with the same bunch of electrons as they propagate through the planar region, as dictated by the BH condition.

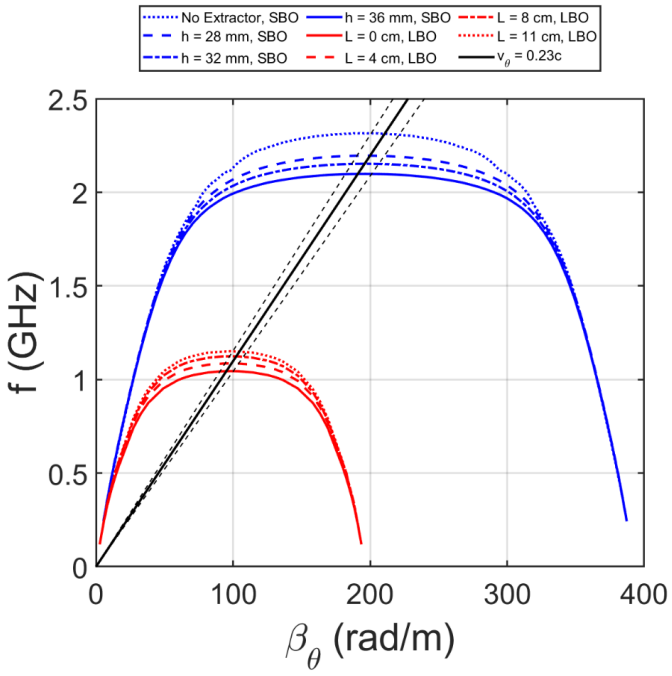

Figure 3.3: Dispersion relations for the LBO and SBO, as a function of the LBO tuner length L and SBO aperture length h, respectively. The π-mode of each structure has a phase velocity of roughly 0.23c.

Figure 3.4 illustrates the SBO and LBO π-mode frequency as a function of h and L, respectively. There is a satisfactory agreement between the finite cavity model, the unit cell model, and experimental cold test in each case. More importantly, the SBO π-mode frequency falls within the second harmonic of the LBO tuning range, regardless of the aperture length, so that the same LBO and tuner may be used throughout all experiments. Due to beam loading [111], it was

expected that the LBO harmonic frequency would decrease more than the SBO frequency, pushing the targeted modes further into the preferred tuning range. This effect was observed in the experiment, which will be discussed more in Chapter 5.

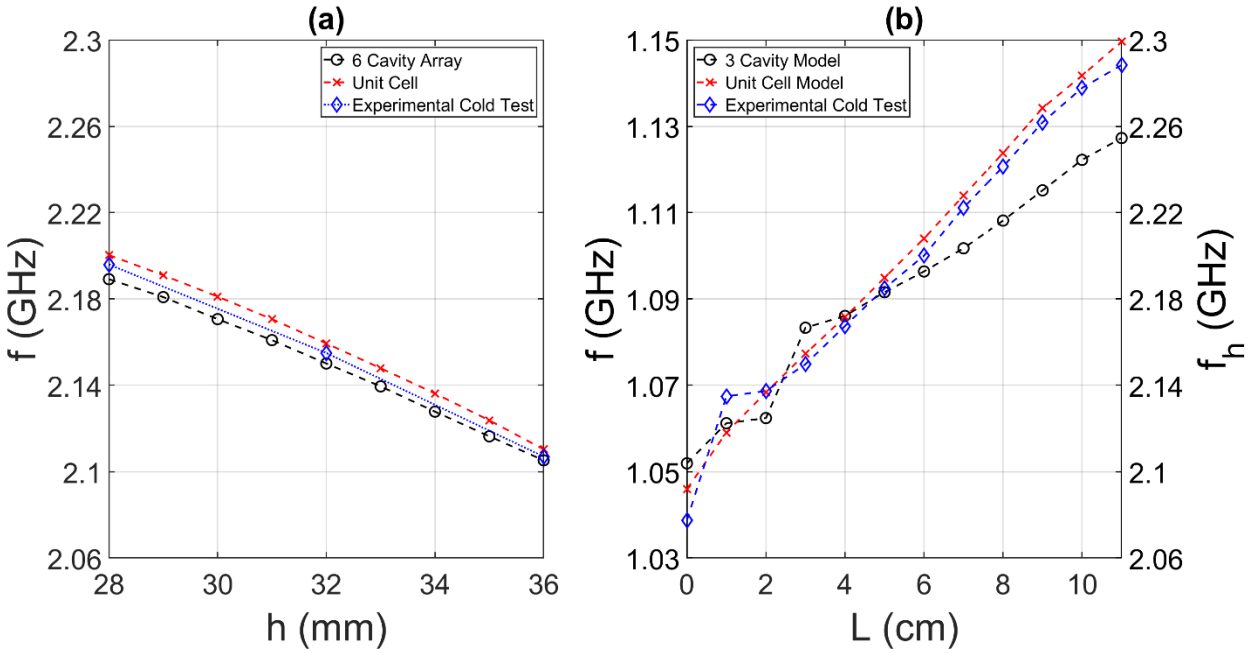

Figure 3.4: (a) SBO frequency as a function of h. (b) LBO frequency as a function of L, with fundamental frequency as the ordinate on the left and second harmonic frequency as the ordinate on the right. Note that the ordinate in (a), corresponding to the SBO π-mode frequency, is identical to the rightmost ordinate in (b), representing the LBO harmonic frequency. These identical axes enable a direct comparison of the SBO π-mode frequency with the LBO harmonic frequency. For example, the SBO π-mode frequency is approximately 2.18 GHz for h = 30 mm. According to (b), the LBO second harmonic frequency is tuned to 2.18 GHz near L = 5 cm.

With the frequency range of both oscillators determined, all that remains is quantifying the SBO quality factor as a function of h. This analysis is summarized in Figure 3.5, for which multiple different models of the SBO were considered. First, there is the straightforward six cavity model, which was shown in Figure 3.1. The predictions retrieved from this model were somewhat unsatisfying, as they demonstrated insufficient agreement with the unit cell model with PEC boundaries. An equivalent ten cavity model was built, which produced a better agreement with the unit cell, likely because it is a better approximation to the infinite cavity model that the unit cell represents. An additional unit cell model was made with finite conductivity, which results in a decrease of the SBO quality factor by some constant. It is typically assumed that for a given mode, the total quality factor Q_t is equal to the parallel-circuit (reciprocal) sum of the external quality factor Q_{ext} and unloaded quality factor Q_u. The external quality factor is introduced by the

extractor, and the unloaded quality arises due to other forms of loss such as finite conductivity or radiation [112].

$$\frac{1}{Q_t} = \frac{1}{Q_u} + \frac{1}{Q_{ext}} \tag{3.3}$$

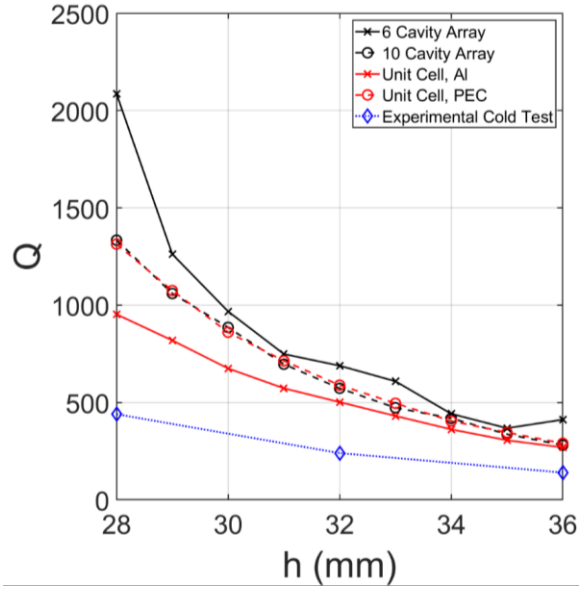

Figure 3.5: SBO π-mode quality factor for several different models, each evaluated as a function of h and compared with experimental measurement from cold test.

However, none of the HFSS models were exceptionally accurate in predicting the experimental measurements of Q_t as a function of h. The finite conductivity unit cell model was the most accurate, and it still overestimated the experimental measurement by roughly a factor of two. It is plausible that this is because the surface conductivity of the anode and extractor are significantly lower than the typical assumption for the conductivity of aluminum [113] (possibly due to aluminum oxide, the thickness of which is comparable to the skin depth of ~1 μm), thus making Q_u much lower in practice compared to what was assumed in the HFSS model. Assuming that Q_{ext} is identical to the quality factor retrieved in the unit cell PEC model, then setting Q_u to 4000 in Eq. 3.2 retrieves the same total quality factor as the unit cell with aluminum finite conductivity. Doing the same calculus, Q_u would need to be roughly 700 to resemble the experimental measurements. Other forms of inaccuracy arise because these projections were made without modeling the full extractor, which is multiple wavelengths long and may introduce more losses. Additionally, these measurements were made in an electrically large test chamber, which could enable radiation losses from the SWS surfaces.

3.2 Magnetron Time Domain Simulations

With both the LBO and SBO designed to satisfy the BH condition on each structure's fundamental π-mode for all experiments of interest, time-domain simulations could be performed to demonstrate the generation of microwave power. Simulations were performed in ICEPIC and CST-PS PIC codes for the Isolated S-Band Oscillator (ISBO), whereas models were only performed in CST-PS for the Isolated L-Band Oscillator (ILBO) and the HRPM.

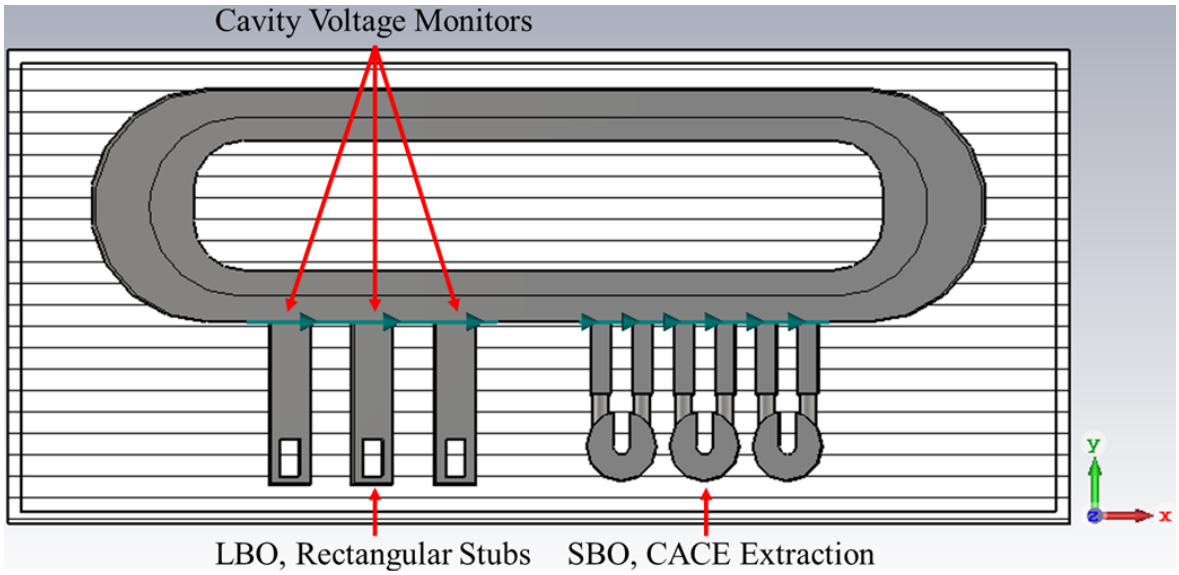

(a) Cross section in XY plane

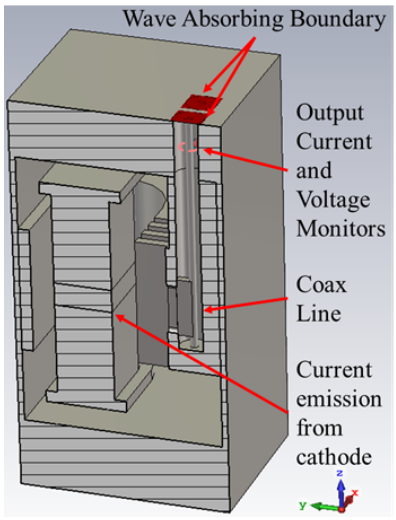

(b) YZ cross section

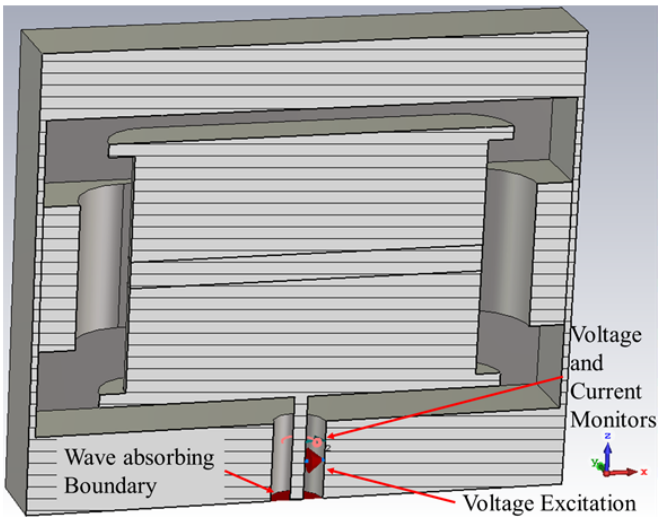

(c) XZ cross section

Figure 3.6: The HRPM CST-PS model detailed by the simulation features and shown in cross sections of three different planes.

Simulation features of the HRPM are detailed in Figure 3.6 in several cross-sections. In the XY plane, the full SWS for each oscillator may be visualized. In the PIC models, the LBO was simulated with rectangular tuning stubs instead of the cylindrical rods designed in the previous section and used in the experiment. This choice was made to avoid stair casing of the round edges due to the box-shaped cells implemented in PIC simulations. The gap between the cylindrical rods and the cavity walls was so small that it became difficult to resolve with an adequate number of mesh cells. Therefore, in the PIC simulations, these cylindrical rods were replaced with rods of a rectangular cross-section. Otherwise, the cavity dimensions and extractor coaxial transmission lines are identical to what was implemented in the experiments.

Other simulation features included cavity voltage monitors, shown in Figure 3.6a, which export the voltage across one cavity throughout the simulation and enable retrieval of oscillation amplitudes, dominant frequencies, and competing frequencies on the SWS. Figure 3.6b illustrates the interior of a coaxial channel, which was terminated by a wave-absorbing boundary. The voltage and current are exported near the port for power analysis. Electron emission is enabled from a central strip on the cathode, 2 cm in length (along the z-direction of Figure 3.6) as in the experiment, via the explosive emission model. In the XZ plane, a voltage excitation is made in coax, sending a ramped voltage pulse with a rise time of 200 ns and a flat top of 300 ns. The voltage and current entering the magnetron are captured slightly downstream of the voltage excitation, and outgoing waves are absorbed at the coaxial port.

3.2.1 Isolated S-Band Oscillator Simulations

The injected current and voltage in the ISBO models are shown in Figure 3.7. ICEPIC and CST form the voltage excitation differently, which results in the differences in Figure 3.7a. In both cases, the injected wave at the excitation will reach the cathode and reflect because the diode is an open circuit before the magnetron begins operation, doubling the voltage as a result. At the voltage port, CST-PS will monitor the reflected wave and adjust its excitation to maintain a constant voltage at the user's specification. Alternatively, ICEPIC does not make this correction, so the user must specify an excitation of roughly half the desired voltage at the cathode. It is for this reason that the applied voltage increases as a function of the magnetic field. As the magnetic field increases, the magnetron draws less current, increasing the impedance and reflecting a more significant portion of the injected voltage wave. Meanwhile, at the same magnetic field, ICEPIC

predicted a higher current, ranging from 300 A to 500 A. Unlike Figure 3.6, the ICEPIC emitting region was the entire face of the cathode (as opposed to a 2 cm stripe). This larger emitting area likely led to the increased emission of current.

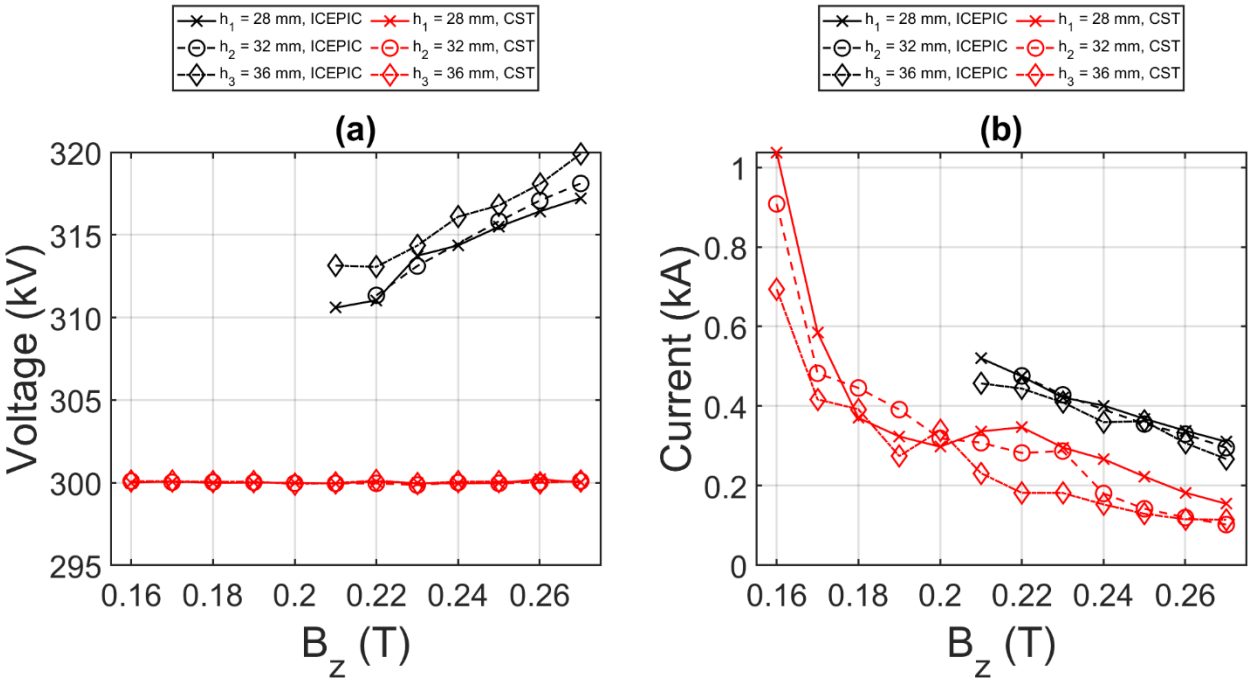

Figure 3.7: (a) Voltage as a function of magnetic field for ICEPIC and CST for several values of h. (b) Current as a function of magnetic field in ICEPIC and CST at several values of h. At -300 kV, the device was predicted to draw current on the order of hundreds of amperes.

The dominant mode of operation and the degree of mode competition are both represented in Figure 3.8. The dominant frequency is displayed in Figure 3.8a, where both codes predict π-mode operation from 0.21 T to 0.27 T. In CST-PS, simulations were extended to lower magnetic fields. There was a transition from π-mode operation to 5π/6 dominance near 0.16 T in the CST-PS models. Figure 3.8b illustrates the prevalence of mode competition; R is the ratio of the competing peak amplitude to the dominant peak amplitude from the Fourier transform of the cavity signals, defined as $R = A_c/A_d$. Low values of R represent minimal mode competition and a signal dominated by a single frequency. Very little mode competition was observed with the π-mode at higher magnetic fields. Both ICEPIC and CST-PS demonstrate an increase in mode competition as the magnetic field is reduced below the BH condition of roughly 0.23 T. The moderate magnetic field range produces substantial mode competition between the π-mode and 5π/6-mode, which is unsurprising because this is the range in-between the BH condition for the two modes. At higher and lower magnetic fields, the π-mode and 5π/6-modes dominate, respectively.

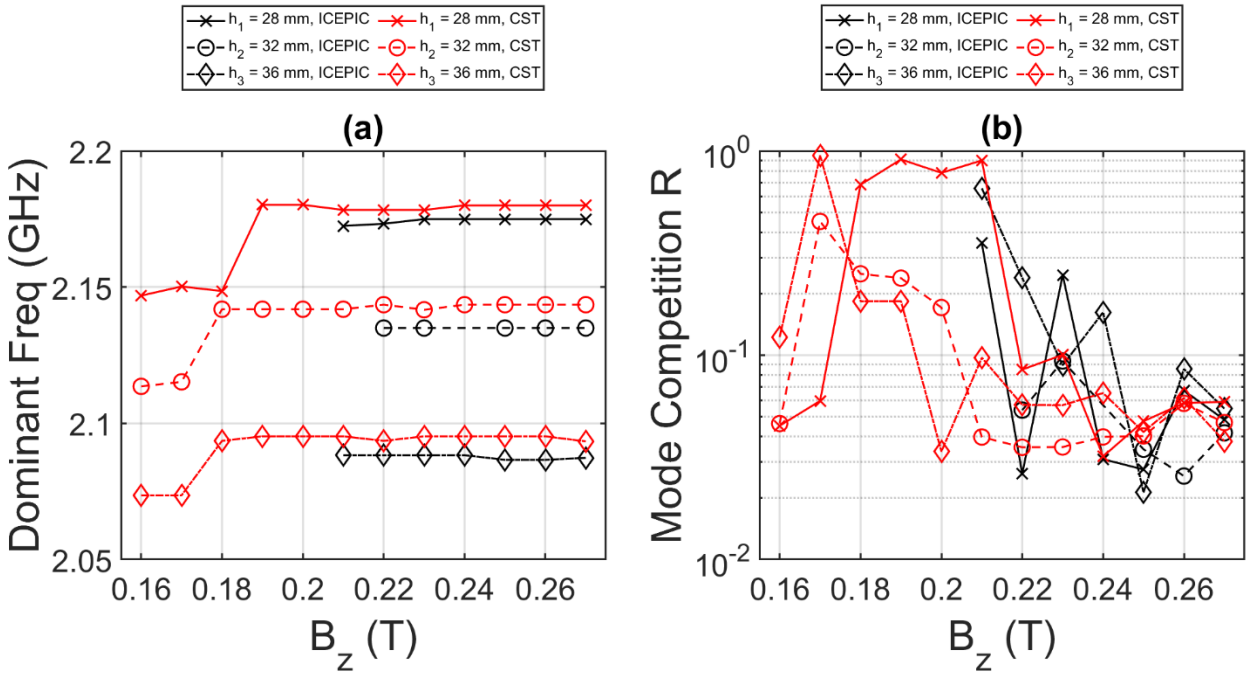

Figure 3.8: (a) Dominant frequency on the slow-wave structure. (b) The ratio of competing peak to dominant peak from SWS Fourier analysis. The π-mode is dominant from 0.22 T to 0.27 T, with relatively little mode competition, in both CST and ICEPIC. Below 0.18 T, the 5π/6 mode is dominant.

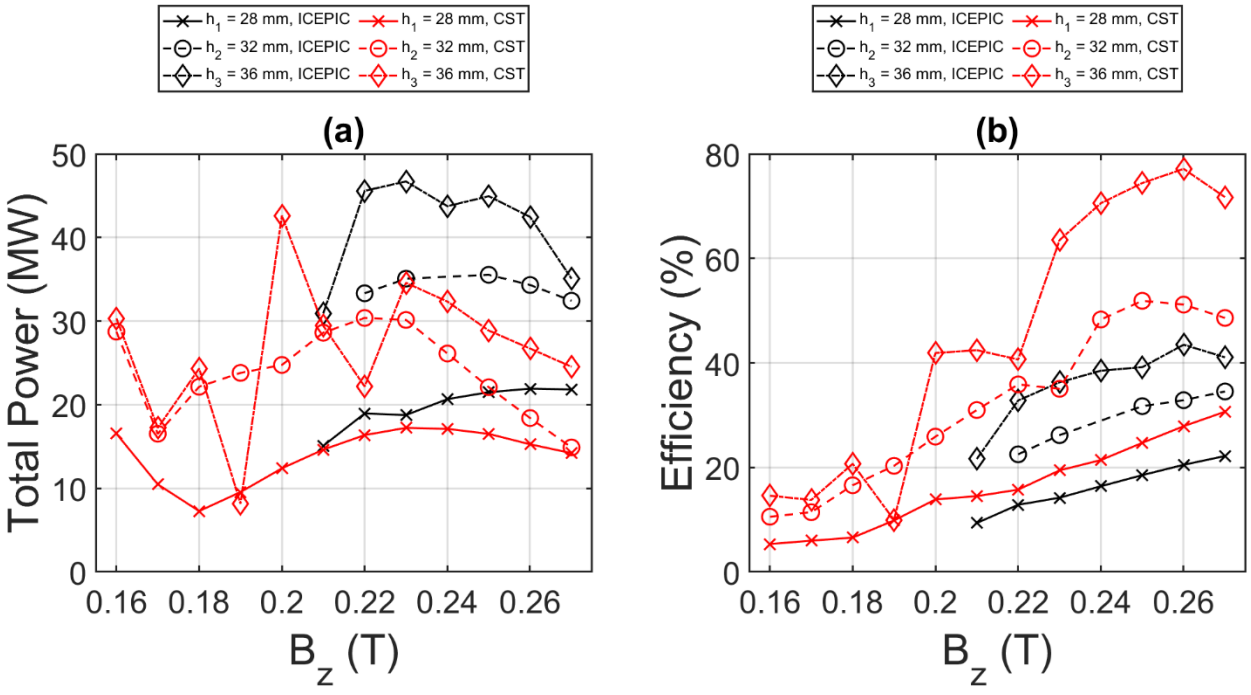

Figure 3.9: (a) Total SBO output power predicted as a function of the magnetic field for multiple values of *h* (coupling aperture length). (b) The instantaneous peak efficiency of microwave generation. Compared with ICEPIC, CST-PS overestimates the efficiency because the current drawn in the CST-PS models was much lower than in ICEPIC.

Total power output from the HRPM is estimated to be on the order of tens of megawatts, as shown in Figure 3.9a. As expected from the quality factor discussion in the prior section, the output power increases by decreasing the external quality factor (equivalently increasing h, the coupling aperture length). In general, the output power is lower in CST-PS than in ICEPIC, yet CST-PS estimates much higher efficiencies than ICEPIC. These are primarily because of the dramatic differences in current drawn outlined in Figure 3.7b. The efficiency estimates from CST-PS are aggressively optimistic and should not be considered as accurate as the ICEPIC prediction. The ICEPIC models were performed with a 1 mm resolution, which is regarded as adequate to resolve devices up to S-Band [114]; a CST-PS convergence study was inconclusive. Output power in the 5π/6-mode is comparable to the π-mode, although the current was substantially higher in the magnetic field range where the 5π/6 mode could be excited.

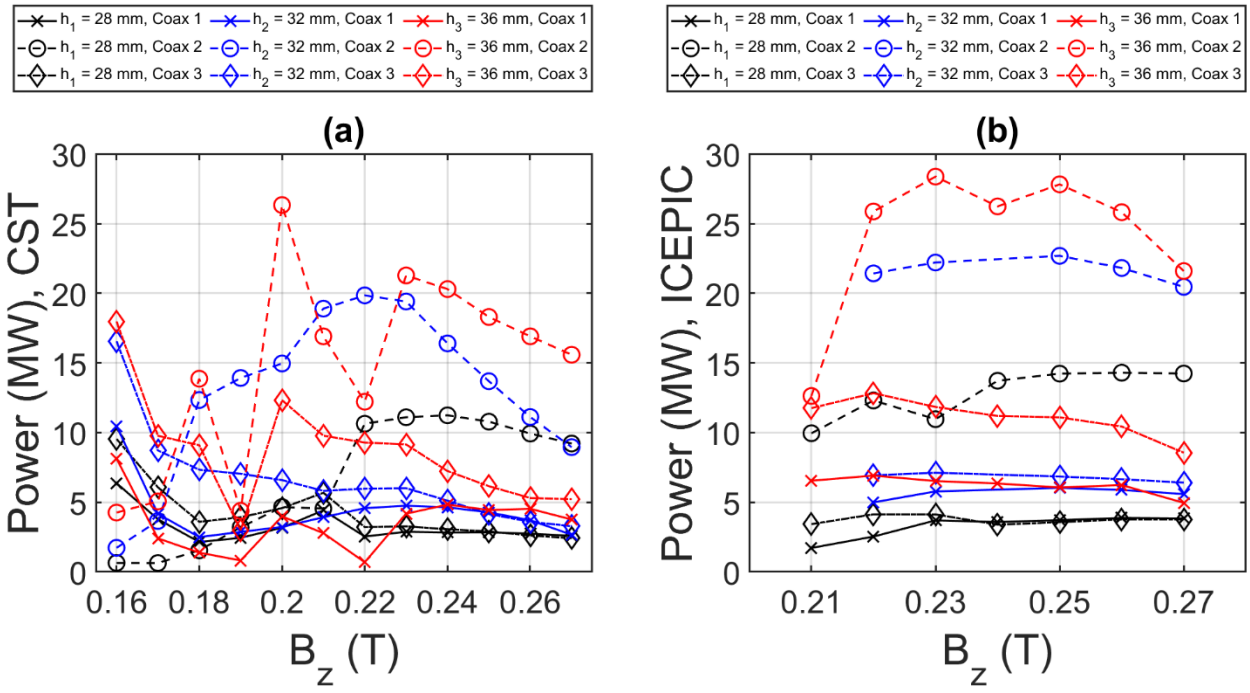

Figure 3.10: Power in each output coax as a function of aperture length h and magnetic field, simulated in CST-PS (a) and ICEPIC (b).

The output power from each coaxial output is illustrated in Figure 3.10. This information is illustrative of the mode of operation and can easily be compared with experiments. In the nomenclature established in the legend, Coax 1, Coax 2, and Coax 3 are the separate coax lines from left to right as shown in Figure 3.6a. The π-mode, specifically in the range of 0.23 T to 0.27 T, demonstrates a very similar profile in both simulation packages. In general, the π-mode generates the highest power in the central Coax 2. For the high (h_1) and moderate (h_2) quality factor

simulations, Coax 1 and Coax 3 generate nearly equivalent power. Dropping the quality factor even lower (h_3), the power extracted in Coax 1 is relatively unchanged from the moderate Q (h_2) simulation, but both Coax 2 and Coax 3 demonstrate increased power. This feature of asymmetric power generation as the quality factor decreased was observed in HRPM experiments, to be described in Chapter 5. Meanwhile, the 5π/6-mode produced very little power in Coax 2, which is expected because its null cavity was located in one of the two central cavities, as identified in HFSS and the PIC models. Because there is no π-phase-shift of the electric field between these two cavities, a TEM wave cannot be excited in the coaxial line, diminishing the power. The power was then distributed primarily into Coax 3.

3.2.2 HRPM Simulations

PIC simulations of the HRPM were generally less successful than the ISBO in terms of their agreement with the experimental results. The geometry presented in Figure 3.6 was only simulated in CST-PS, so the results in Figure 3.11 do not include any information from ICEPIC. These simulations were performed at 0.24 T, where the π-mode demonstrated very little mode competition in models of the ISBO. The independent variable is now L, and the aperture length is h_3.

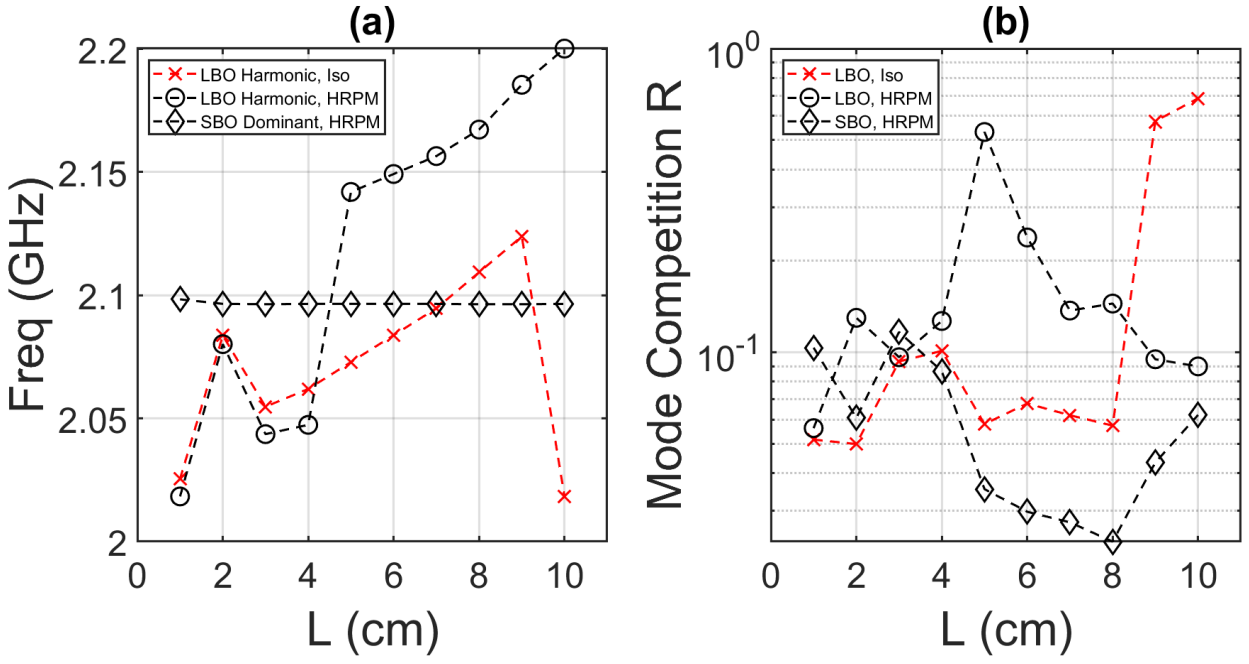

Figure 3.11: (a) LBO and SBO output frequencies from the HRPM model overlaid with the isolated LBO frequency as a function of L. (b) Mode competition in each structure given as a function of L. Harmonic frequency locking is not observed in this model of the HRPM.

Figure 3.11a tracks the dominant frequency of the LBO, in both the ILBO and HRPM models, and the SBO dominant frequency in the HRPM. Notably, the LBO resonates at a drastically different frequency in the HRPM than it does in isolation. The slope of the LBO frequency is mostly the same from $L = 3$ cm $\rightarrow$ 9 cm, but there is a significant jump in the HRPM-LBO frequency between $L = 4$ cm $\rightarrow$ 5 cm. Accompanied by this shift is a sudden increase in mode competition, shown in Figure 3.11b. The SBO continues to resonate in the π-mode at its free-running frequency with very little mode competition, unchanged by the presence of the LBO. Frequency locking is not observed in these simulations. All of this would suggest that it is the SBO that can influence the LBO operating frequency and mode, but these erratic changes in the LBO frequency were not observed in the experiments.

Simulations of the HRPM with correct cavity dimensions and CACE were not performed in ICEPIC. However, previous simulations of a different HRPM prototype were completed, utilizing the SBO extractor from the previous MFRPM design [66]. In this prototype, the SBO π-mode free-running frequency was near 2.3 GHz, with 3 LBO cavities and 6 SBO cavities. Figure 3.12 demonstrates evidence of harmonic frequency locking. The LBO harmonic frequency is proportional to L, and the SBO resonates near the LBO harmonic frequency, shifting away from its free-running frequency. Qualitatively, this behavior has much more in common with the experimental results than the CST-PS models of the device.

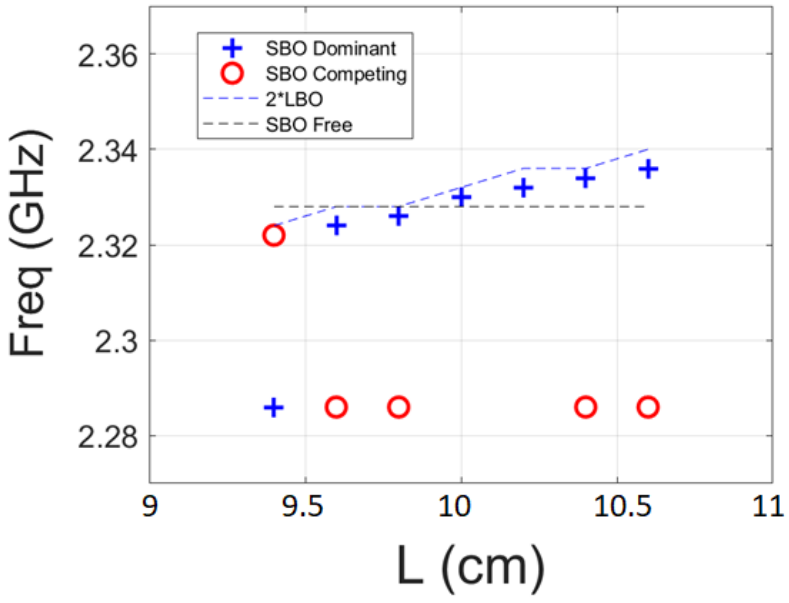

Figure 3.12: Dominant frequency in a preliminary HRPM prototype, with axial extraction through one coaxial line. Evidence of harmonic frequency locking appears as the SBO tracks with the same slope as the LBO harmonic frequency.

3.3 MILO Frequency Domain Simulations

Compared to the multi-frequency concept of the HRPM, intended to operate with frequency agility at multiple different quality factors, the MILO design is relatively straightforward. This cylindrically symmetric device, pictured in Figure 3.13, is designed to resonate at a single frequency and implements an axial extraction scheme similar to past experiments of a GW-class MILO demonstrated at AFRL and elsewhere [77], [80], [83]. However, this device differentiates itself with a mode converter and an axial taper to adapt to waveguide.

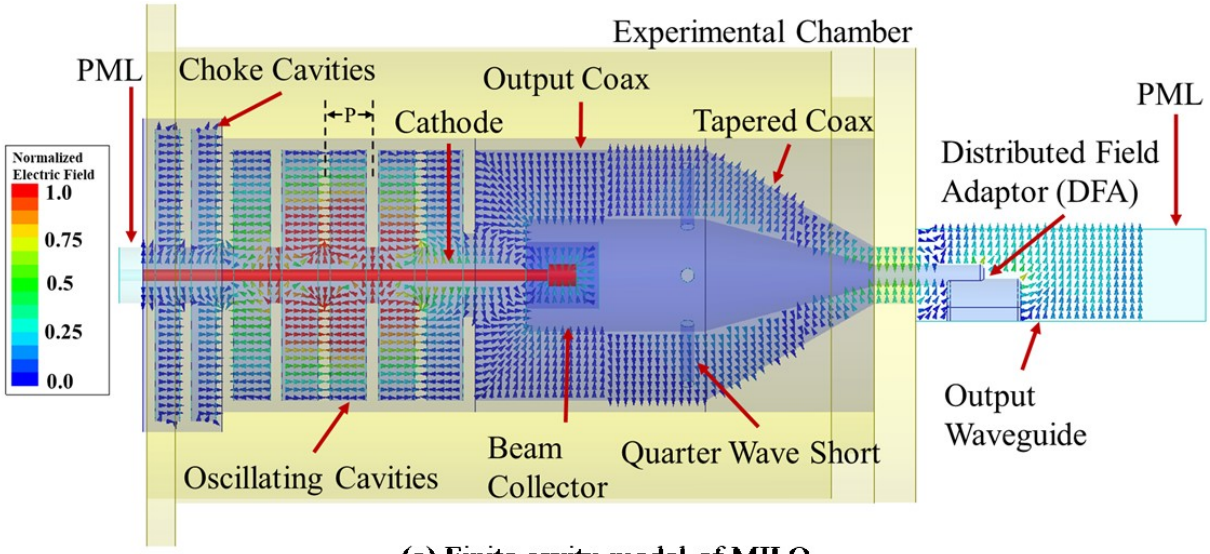

(a) Finite cavity model of MILO

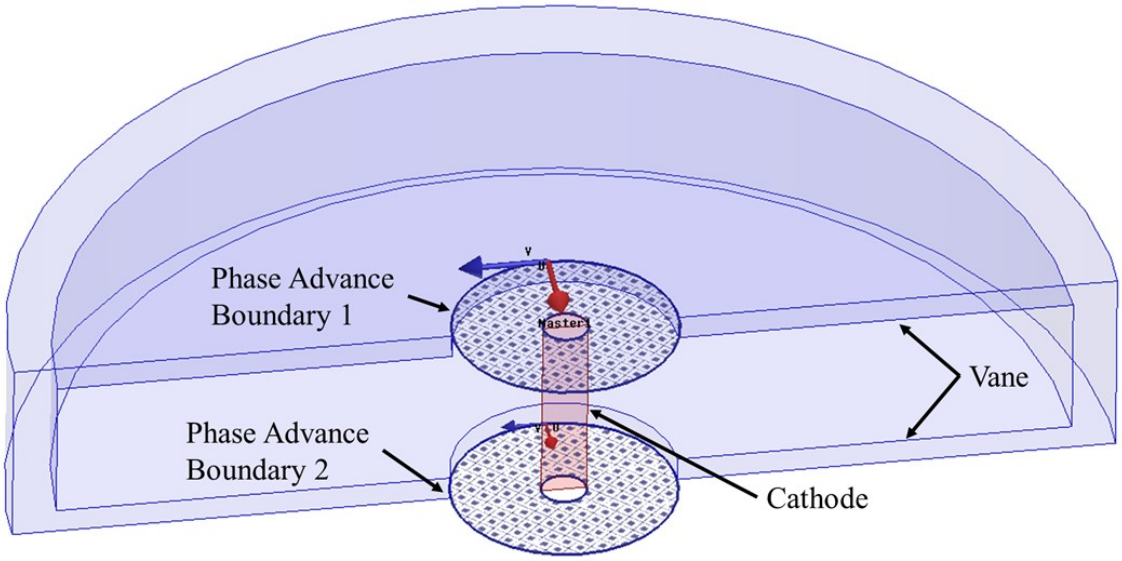

(b) Unit cell model of MILO

Figure 3.13: (a) HFSS model of the full structure, indicating π-mode fields, labeled by component. (b) HFSS model of a unit cell of the slow-wave structure.

The five oscillating cavities were designed for interaction in the π-mode at 1 GHz and an RF phase velocity near 0.3c. Upstream are two choke cavities, which are evanescent to the resonating π-mode, thus reflecting any upstream propagation of the mode in the opposite direction. Downstream of the final vane, a coaxial transmission line (CTL) is formed between the outer radius of the beam collector and the outer wall of the device. The fringing fields of the final vane excite a TEM wave in this coaxial line, propagating downstream. In operation with the beam, substantial currents are collected on the beam collector, grounded through the quarter-wave shorting stubs and the transition from CTL to a waveguide. The quarter-wave shorting stubs provide physical support to the beam collector and are transparent to the RF wave.

Further downstream, the CTL is tapered along a suitable length to adapt to a smaller coaxial cross-section, where the coaxial line is adapted to waveguide through an inline transition [115], [116]. The specific component utilized is a distributed field adaptor (DFA) titled DFA-650c [53]. This transition was made because it is more convenient to make experimental power measurements in waveguide than CTL or circular waveguide, where coupling slots may adversely perturb the field profile. Using the eigenmode solver, parameters such as the outer radius of the beam collector, the distance between the beam collector and the final vane, the inner radius of the final vane, and the length of the tapered coaxial transition were all optimized to minimize the π-mode quality factor. In the geometry built and assembled for experiments, the output quality factor was 315 with PEC boundaries at every surface and 258 with stainless-steel boundaries.

The chief design goal of this project was to achieve operation at less than 10 kA of total current in the range of 200 kV to 300 kV. As discussed in Chapter 2, Eq. 2.74-2.75 were used to produce an anode and cathode aspect ratio that satisfied these demands. It was decided that these operating conditions could be reasonably accommodated with an aspect ratio $r_a/r_c = 3.6$, where the cathode radius r_c was set to 7 mm, and the anode radius r_a was set to 25 mm. The unit cell model, shown in Figure 3.13b, was used to produce the cavity dimensions and dispersion relation for the three different portions of the SWS, given in Figure 3.14. The beamline synchronous with the RF phase velocity of the π-mode is 0.287c. In Chapter 2, Eq. 2.54 was derived to define the edge velocity of the Brillouin hub as a function of the degree of magnetic insulation and operating voltage. Where the edge velocity is greater than the RF phase velocity, some resonant layer exists with which synchronous interaction may be possible. At this voltage and phase velocity, operation

is theoretically realizable if the degree of magnetic insulation is within the range $1.1 < \bar{A}_a/\bar{A}_a^{min} < 1.5$, as shown in Figure 2.5.

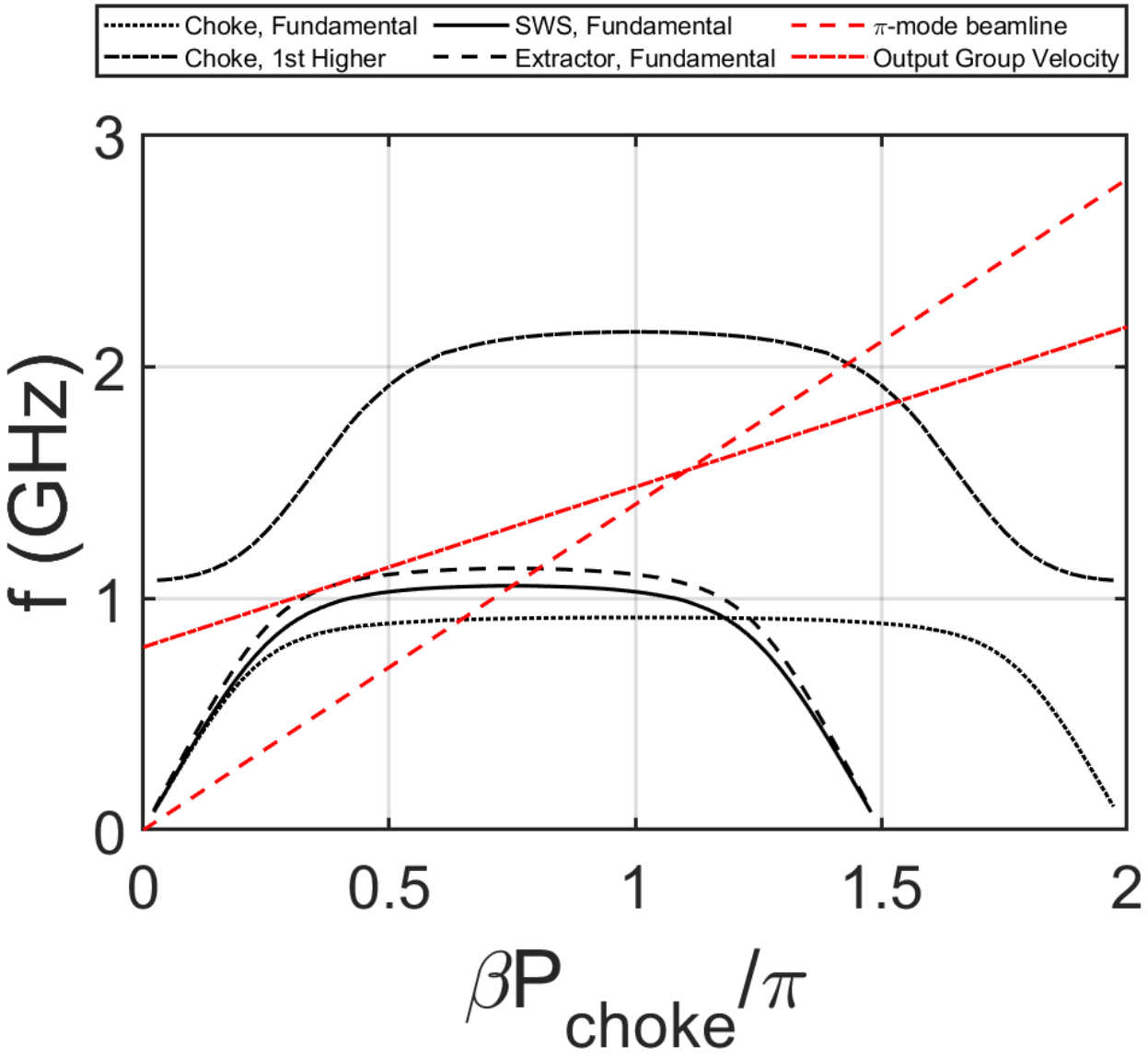

Figure 3.14: Dispersion relation for the MILO structure. In π-mode, the fundamental bandpass of the oscillating cavities is synchronous with a beam velocity of 0.287c. This desired operating mode is located in the forbidden region of the choke structure.

The choke cavities were designed such that the 1 GHz π-mode was in the middle of its forbidden region, which is the unsupported frequency band between the two lowest order modes. If the choke cavity segment is excited in its forbidden region, the electric fields will decay exponentially in the choke, while simultaneously reflecting most of the wave. The final vane has an inner radius slightly larger than the rest of the cavities, which stretches its dispersion relation

vertically. Thus, when it is excited by the π-mode within the oscillating cavities, a wave is launched in the downstream direction, enabling extraction of an increased fraction of the power generation. The frequency of all SWS modes of frequency greater than 800 MHz are listed in Table 3.1.

Table 3.1: Resonant frequency for modes of interest within the cavities, as calculated by HFSS simulations.

Mode Identity	Unit Cell Freq (GHz)	Finite Cavity Model (GHz)
π (choke)	0.916	0.912
2π/5	0.866	0.844
3π/5	0.999	0.969
4π/5	1.039	1.009
π	1.049	1.041

3.4 MILO Time Domain Simulations

Three-dimensional, finite-difference time-domain particle-in-cell simulations of the MILO were conducted in CST-PS (performed by the author) and ICEPIC (performed by Emma Guerin). The CST-PS model of the MILO is shown in Figure 3.15; each feature described in this model was implemented in the ICEPIC model. Voltage monitors across each cavity were implemented to obtain the resonant frequency, and additional voltage monitors tracked the voltage at the input and output. Current monitors were placed at the input, output, and between the SWS and beam collector. Wave absorbing boundaries were set at the input and output to remove reflections.

Voltage was ramped up over 200 ns to a flattop of 200 ns near 230 kV, and electrons were emitted in the blue regions of the cathode through the explosive emission model. Output power was obtained by taking the product of the output voltage and current monitors and then calculating the root mean square (RMS) amplitude throughout the flat top operation. In these simulations, the downstream radius r_d was the independent variable. This variable can manipulate the amount of current emitted by the cathode within the beam collector (which is tracked by the downstream current monitor) and thus controls the magnetic field in the cavity region. Varying r_d is tantamount to altering the magnetic field in a magnetron. The radius of the cathode rod r_c was set to 7 mm.

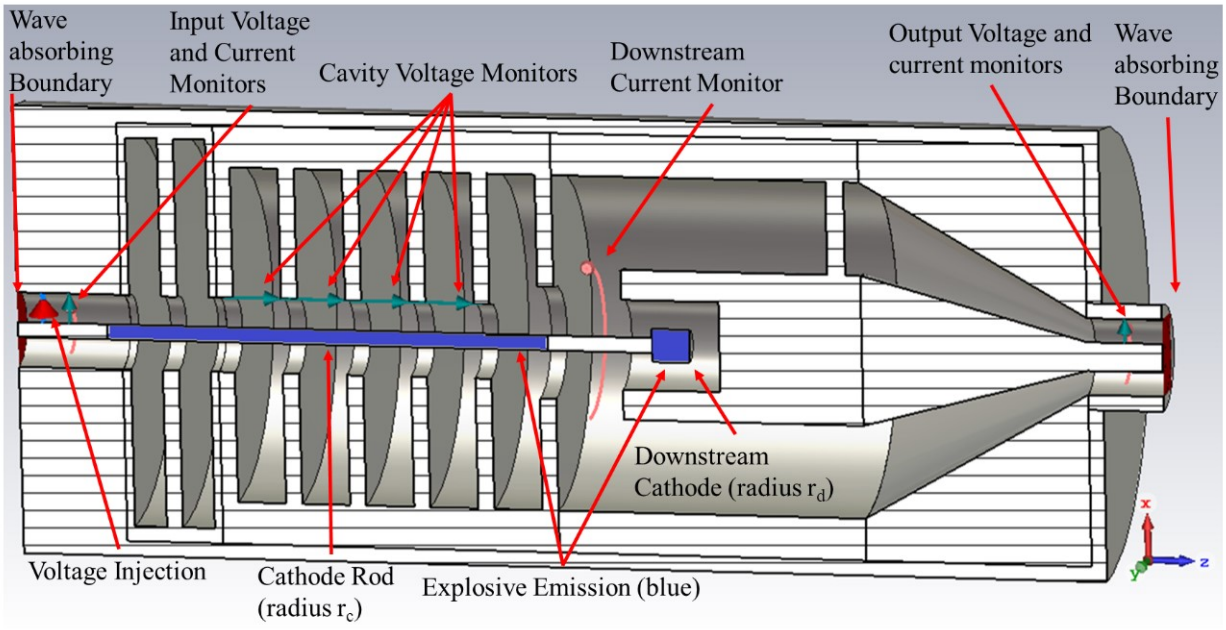

Figure 3.15: MILO CST-PS model detailed with simulation features. An equivalent ICEPIC model was assembled and simulated by Emma Guerin [117].

Operation of the MILO in a steady-state condition is illustrated in Figure 3.16, overlaying particles with the geometry. The downstream cathode would emit early in time compared to the cathode rod. However, the magnetic field generated did not wholly prevent electrons from striking the anode early in the pulse before oscillations began. Resonance in the π-mode was observed, confirmed by the generation of spokes in every other cavity. The RMS voltage was the smallest in the first cavity, resulting in weak spoke formation locally, but grew with cavity number. The largest RMS voltage was in the penultimate cavity, with the final cavity voltage slightly reduced due to its strong coupling to the extractor. Spokes were drawn deep into the cavities 3-5, striking the back walls. The choke cavities were not excited by the beam in the parameter space analyzed in simulation, and no mode competition was observed with higher-order modes or other modes on the fundamental bandpass.

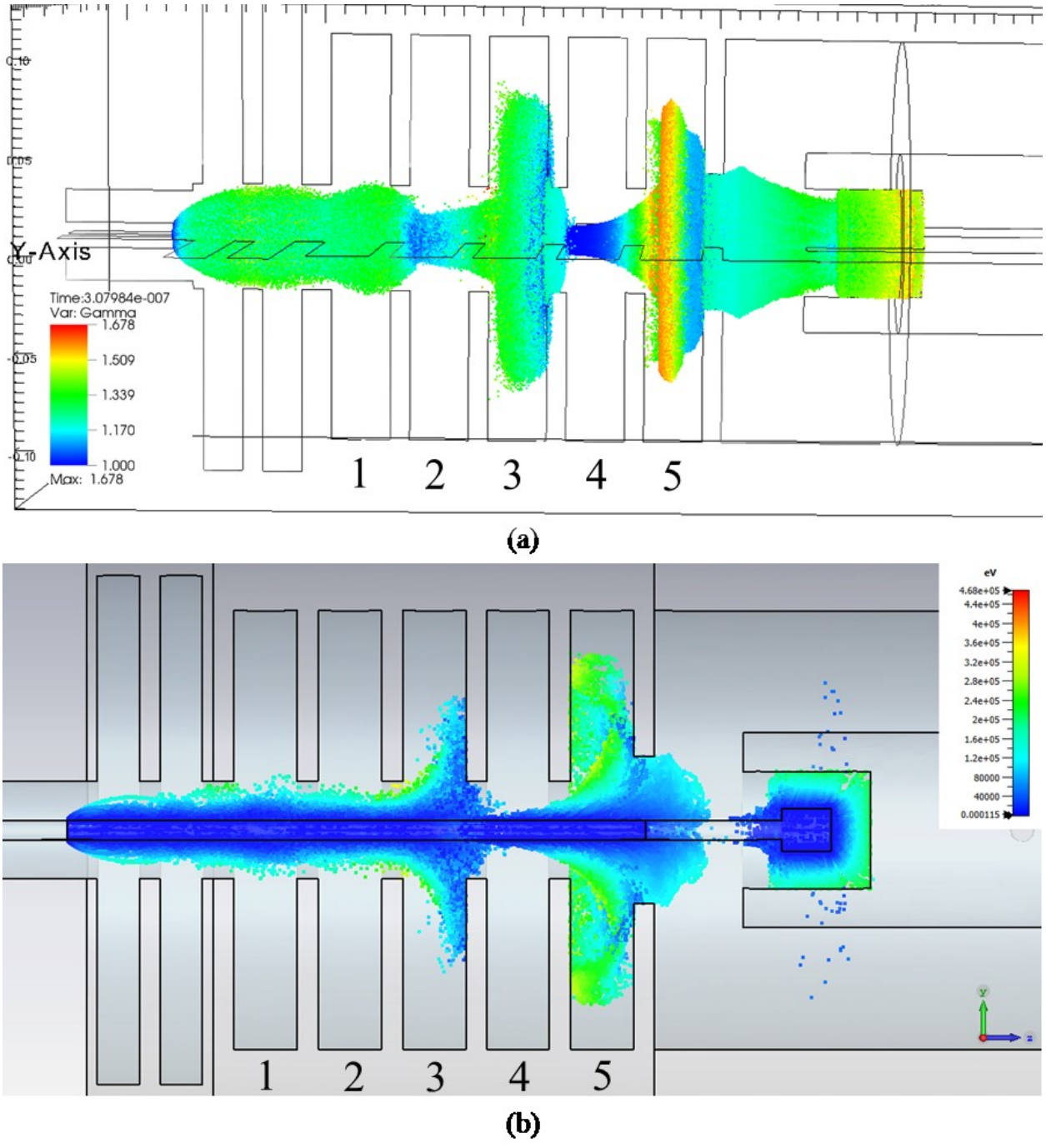

Figure 3.16: Electron spoke formation in MILO model from (a) ICEPIC and (b) CST-PS. The downstream diode establishes the magnetic field needed to insulate the cavities and enables oscillations. The cavities are labeled in sequential order.

The current drawn in various locations of the device is illustrated in Figure 3.17. As r_d was increased, the downstream diode current increased as expected. Once the downstream diode current was raised beyond the Hull cutoff value at r_d = 15 mm, no current was collected on the SWS, indicating that oscillations had ceased. Figure 3.18a confirms this is where the output power

falls to zero. The total current at the input was constant up to r_d = 15 mm, just beneath the Hull cutoff value calculated by the theory. The downstream current increases linearly in this range, but the current collection on the SWS decreases an equal amount as r_d is varied. Thus, in operating the MILO at a fixed voltage, there appears to be a limit in current that can be injected without raising the downstream current beyond Hull cutoff. In other words, the simulations suggest there is a maximum input (total) current that can be injected, and the current available to the SWS is thus strongly affected by the current collected on the downstream diode. The current available to the SWS is thus inextricably tied to the current gathered on the beam collector. If too much is delivered downstream, then the electrons available for interaction with the cavities will be limited. Optimizing r_d for power generation yields r_d = 10 - 12 mm as the preferred range, with output power estimated in the range of 70-80 MW.

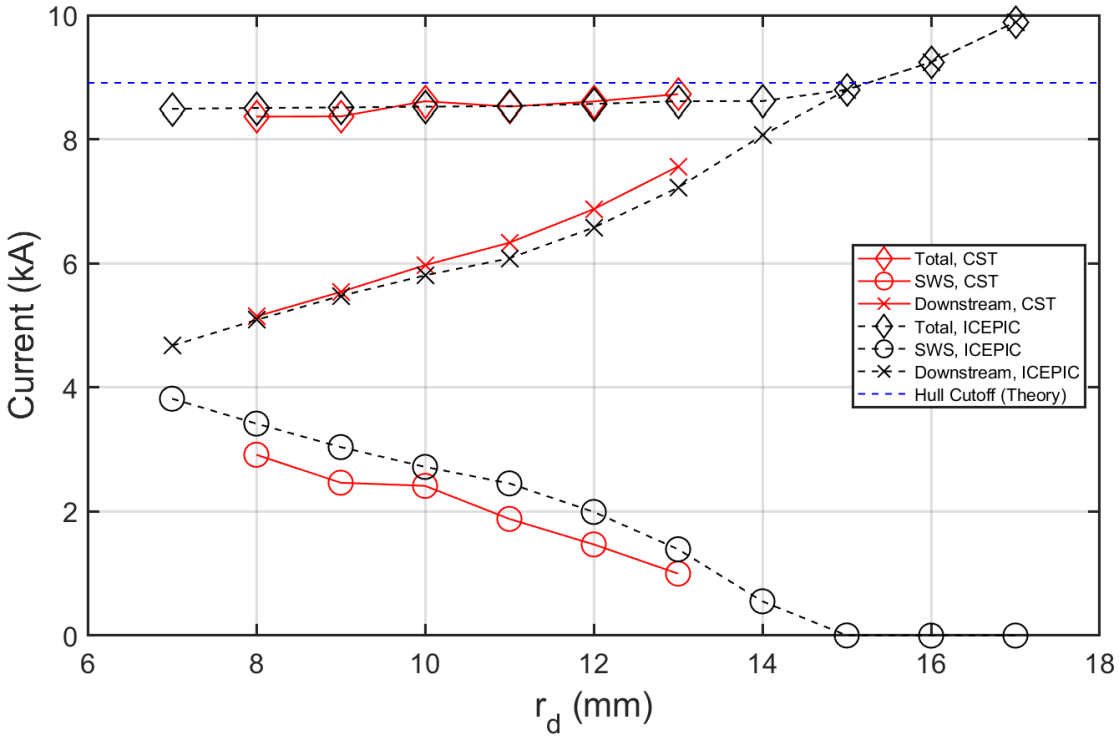

Figure 3.17: Current as a function of r_d. The total current is measured at the input, and the downstream current is measured between the SWS and the downstream diode. The SWS current accounts for the electrons that strike the anode vanes.

All of this suggests that the device must operate at an input (total) current lower than the Hull cutoff condition; discussions in Chapter 6.3 (Figure 6.14-Figure 6.17) will illuminate this is indeed the case, unexpectedly. Specifically, the theory outlined in Chapter 2 revealed that the input current required to achieve the Hull cutoff condition is greater than the input current to achieve slightly higher degrees of magnetic insulation for a given voltage. There is a v-shaped minimum

in the total current where the degree of magnetic insulation, A_a/A_a^{min}, is slightly higher than unity (~1.1), and where the total current is less than the Hull cutoff ($A_a/A_a^{min} = 1$) value (see Figure 6.14a). At 230 kV, this minimum is at 8.02 kA, $A_a/A_a^{min} = 1.05$, whereas the total current is 8.91 kA at Hull cutoff, $A_a/A_a^{min} = 1$. These simulations operate within the v-shaped minimum, where the degree of insulation is greater than unity. However, it is clear that simulations of the device oscillate near the Hull cutoff condition, which is a significant difference from the magnetron, which operates near the BH condition.

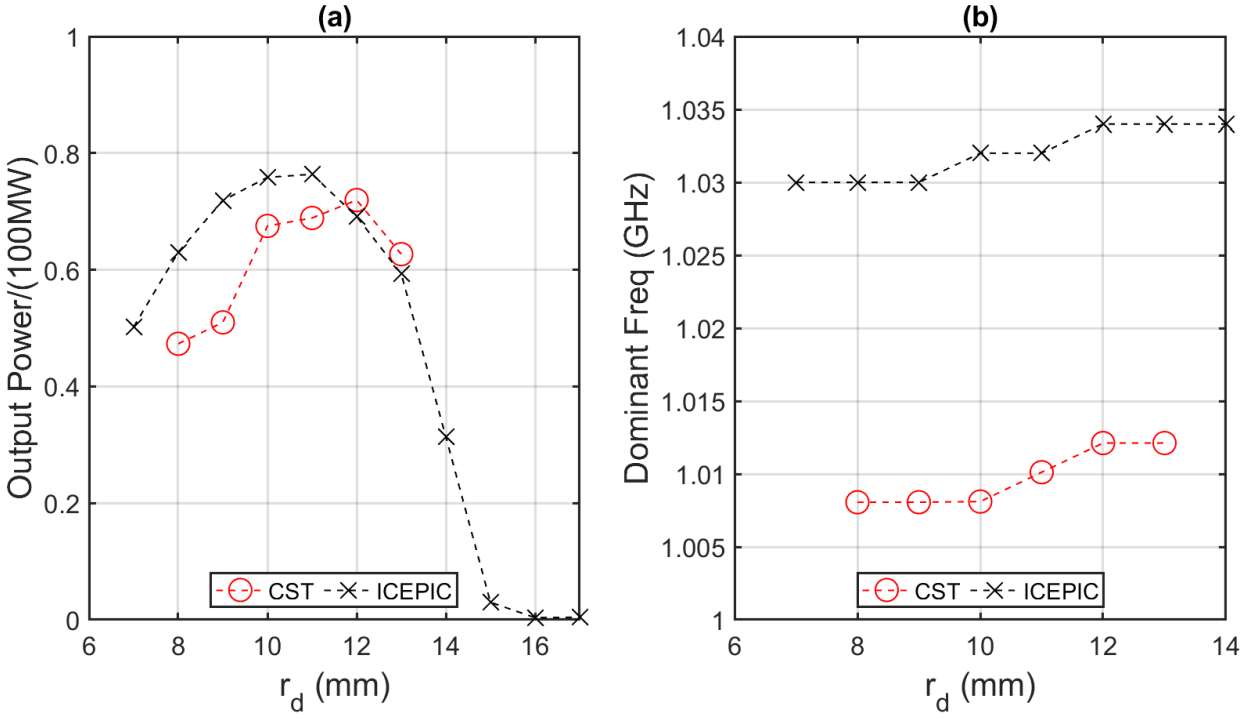

Figure 3.18: (a) Power and (b) frequency as a function of r_d. When properly optimized, the device is simulated to produce 70-80 MW in the π-mode.

The estimated operating frequency of the device, shown in Figure 3.18b, differed by ~20 MHz between the two codes. Using Table 3.1 as a reference and assuming that beam loading results in a frequency shift of approximately 10-30 MHz, these results classify as the π-mode. The ~20 MHz difference between the CST-PS and ICEPIC estimates is likely because the latter was performed with a fixed-cell resolution of 1 mm. The ICEPIC model was composed of a uniform grid with cubic cells of 1 mm in length, making it impossible to resolve the features of the SWS that require 0.5 mm or 0.25 mm resolution. The CST-PS models were performed with a variable mesh grid that snaps to physical characteristics, better resolving these minor differences. For this reason, the CST frequency estimates are considered more accurate.

Figure 3.19 illustrates the voltage and impedance at which these models were performed. For the same reasons discussed in Section 3.2, the CST-PS flattop voltage was fixed at 230 kV, whereas the ICEPIC models experienced a minor droop. Because the total current was constant over these ranges of r_d, the impedance was also steady, near 28 Ω for ICEPIC and 27 Ω for CST.

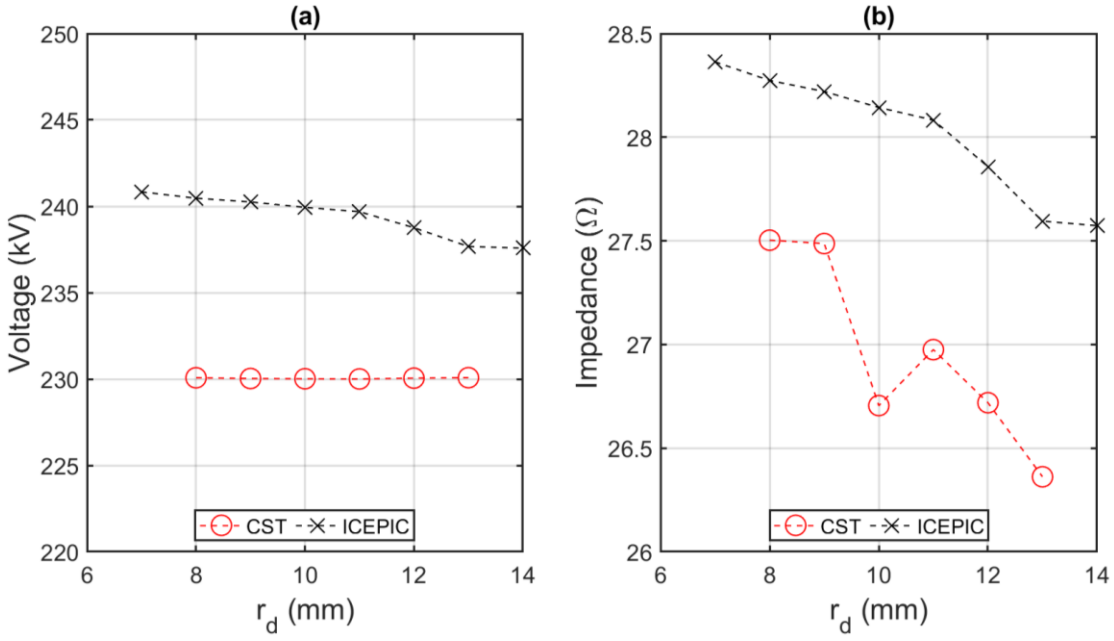

Figure 3.19: (a) Voltage and (b) impedance over r_d. Because the total current was constant for simulated MILO operation and the simulations were performed at fixed voltage, the impedance remained steady over the range that was modeled.

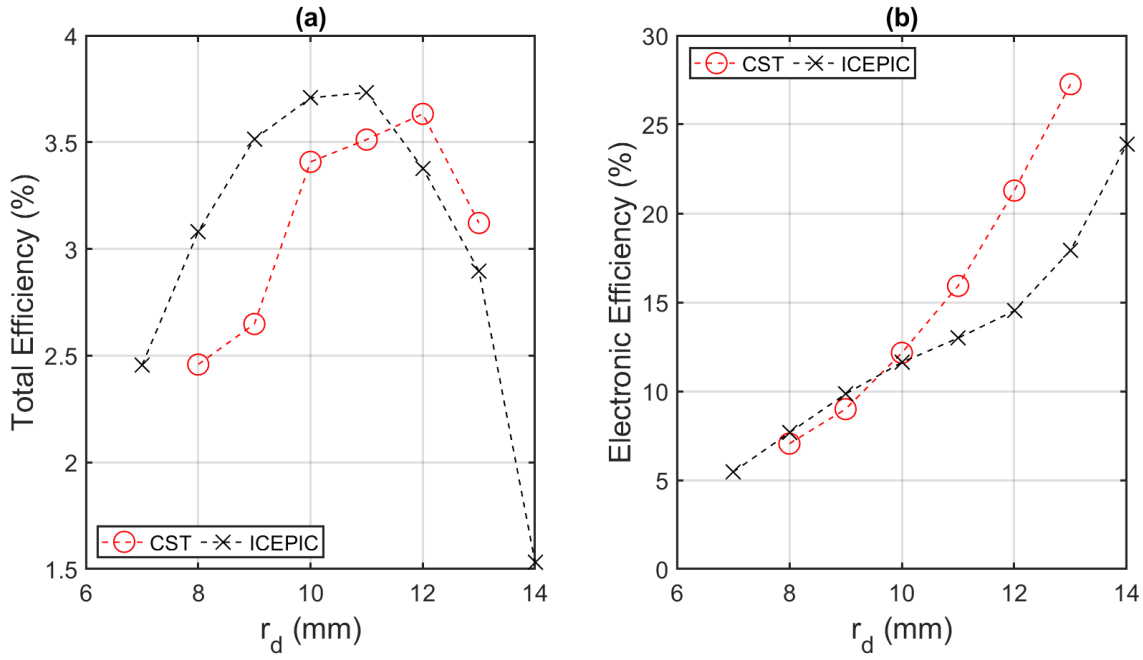

Figure 3.20: (a) Total and (b) electronic (SWS current) efficiency over r_d. Total efficiency in MILO is commonly near 4-6% (Table 1.1), while electronic efficiency is typically quoted near 32% [118], [119].

Finally, Figure 3.20 states the estimated total (total current as drive) and electronic efficiency (SWS current as drive) of the MILO. In these simulations, the total efficiency is the ratio of output power to input power. In contrast, the electronic efficiency is defined here by the electron potential energy transferred to the electromagnetic wave as the electrons are collected on the anode vanes [118], [119]. The estimate for MILO electronic efficiency in [118], [119] is 32%, and is comparable to what was observed in the simulations. The total efficiency in these simulations reached 3.7% when optimized, which is on par with many other MILOs whose efficiency is in the single digits of percent.

Chapter 4 Experimental Configurations

This chapter intends to describe the experimental processes and configurations implemented to measure essential quantities and successfully carry out each experiment. The pulsed power used to deliver voltage to the experimental loads, and the individual experimental assemblies are discussed in detail. Methods of measurement of output power, raw waveforms and spectral quantities, voltage, and current are examined, as well as the hardware necessary to perform these measurements.

4.1 Pulsed Power and Magnetic Field Coils

The Michigan Electron Long Beam Accelerator with Ceramic insulator (MELBA-C) [120] drove both the MILO and magnetron experiments. Shown Figure 4.1, MELBA is a Marx bank consisting of eight pairs of 1-μF capacitors (16 total), and may be charged to ±100 kV; however, in these experiments, they were set to ±30 kV to produce pulses of -300 kV, reducing the physical toll of the collection of hundreds of shots. With the capacitors charged to their peak capabilities, MELBA can produce -1 MV at greater than 10 kA for up to 1 μs (flat-top with crowbar); without crowbar the voltage pulse can extend ~ 4 microseconds limited by diode shorting. MELBA is comprised of a main stage (14 capacitors) and a reverse-charged, Abramyan stage (2 capacitors). The discharged voltage and current from the multiple capacitors in the main stage superimpose to produce the foundation of the output waveform, predominantly characterized by RC decay. The reverse-charged stage is tuned to subtract from the main stage voltage early in the pulse and add to the main stage voltage later in the pulse to provide a flat-top in the voltage output. Typical voltage rise times are between 150 ns to 250 ns, depending on the load. MELBA produced longer and more consistent output waveforms when matched at its characteristic impedance of 100 Ω to 150 Ω. MELBA is not a repetitively pulsed machine; the maximum shot collection rate was roughly one shot per two minutes.

Some dozen copper-sulfate ($CuSO_4$) filled-resistors, encapsulated in Tygon tubing of 1-inch diameter and various lengths, complete the charging circuit between capacitors. The capacitors are charged in parallel, and when MELBA is fired, relays disconnect the charging

circuit, and the Marx bank discharges into the load in series through a cascading breakdown of spark-gap switches. The triggering sequence begins with a +5 V output from the BNC 575 pulse generator, amplified to +300 V to break down a PT-55 generator, which sends a +40 kV pulse to a PT-70 generator. The PT-70 output of -85 kV finally triggers breakdown in the main- Marx stage and Abramyan stage through 1 inch diameter copper sulfate resistors, thus discharging MELBA into the load. In a separate transmission line, the same triggering sequence is applied to the crowbar switch (a low inductance spark-gap switch) parallel to the experimental load designed to absorb the remaining MELBA discharge in ~ 3 Ω, carbon, series resistors after some preordained delay. This delay is typically between 300 ns to 500 ns after the discharge of MELBA, and is intended to avoid total impedance collapse and diode shorting in the experiment. If the characteristic impedance of the experimental load is greater than MELBA's (~100 Ω design) impedance, the crowbar switch will break down easily, but if the load is lower impedance, voltage droop makes it unlikely for the experiment to achieve crowbar. As a result, the magnetron experiments easily crowbarred, which limited damage to experimental hardware; conversely, the MILO experiment rarely achieved crowbar and typically shorted the diode.

Measurements of voltage and current were performed with a parallel, copper-sulfate resistive divider [121] and Rogowski coil [122]. The voltage monitor was embedded in the oil tank where MELBA resides; for the calibration, voltages between 30-80 kV were applied to the cathode with two Febetron-modules and measured with a Northstar HV probe. Over the tested voltage range, a linear trend was observed and scaled up to the voltages at which the experiment was performed. Meanwhile, the Rogowski coil was fixed in a groove within the large-output flange of MELBA. Fundamentally, a Rogowski coil is a series of solenoidal loops wrapped around and insulated from a central wire in the shape of a torus, with the ends of the coil bridged over an output transmission line. By Ampere's Law, a magnetic field within the coil is generated by an enclosed current. Through Faraday's Law, the time-varying magnetic field induces a voltage in the solenoidal turns of the Rogowski coil, which can be measured on an oscilloscope and calibrated to a known standard. With 259 cm of RG-58 coaxial cable, the outer conductor was replaced by a helix of 20 AWG stranded wire at one turn per inch; the two were soldered together at the end of the inner conductor, and the entire coil was shrink-wrapped in plastic. The Rogowski coil was then calibrated in situ by pulsing MELBA into a rod cathode [54] and measuring the returned current

with a Pearson current transformer [123], which is a commonly accepted calibration standard in the pulsed power community.

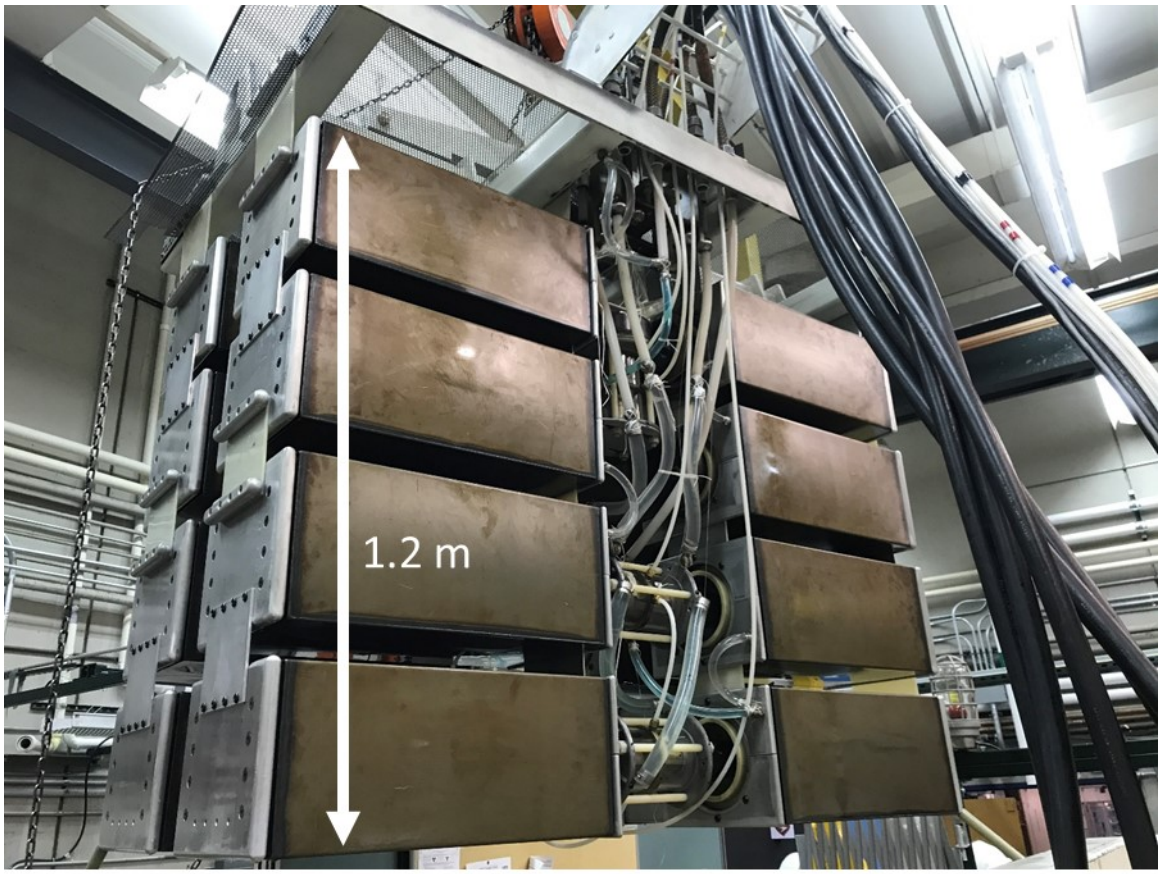

Figure 4.1: MELBA-C suspended above its oil tank. MELBA consists of eight pairs of 1-μF capacitors, of which 14 are charged in parallel and discharged in series into the experimental load. The remaining 2 capacitors are reverse-charged in an Abramyan configuration.

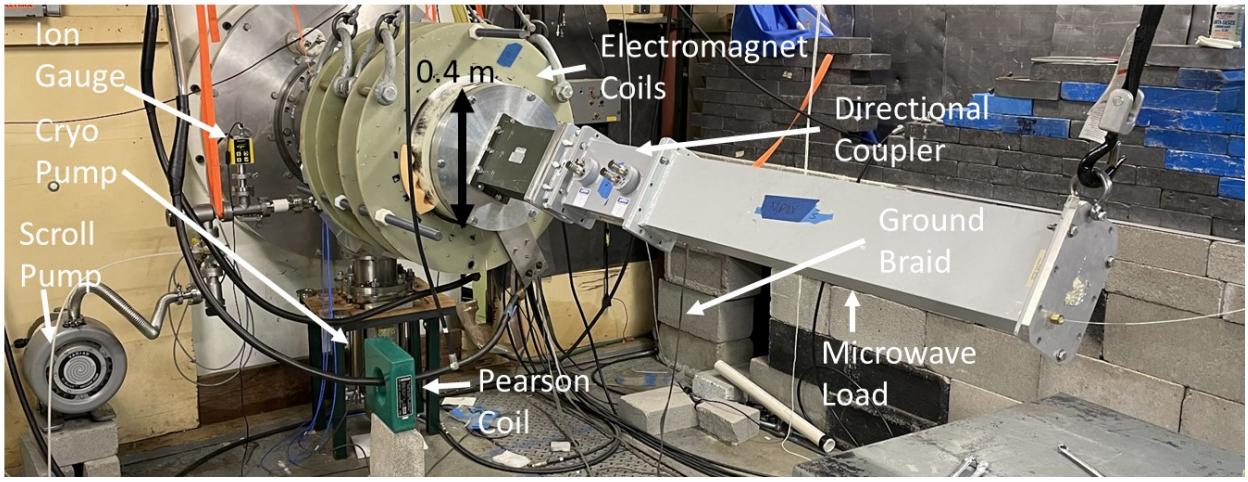

Figure 4.2: Complete MILO assembly with microwave load.

Figure 4.2 shows the completed assembly of the MILO experiment, mostly contained within the experimental chamber. Although the MILO experiment did not utilize the electromagnet coils, they remained a part of the experimental assembly because it was unnecessary to remove them. A Pearson coil was used in the magnetron experiments to measure the current delivered to the Helmholtz coils. Vacuum pressures of approximately 1 μTorr were achieved using a scroll pump first to achieve pressures on the order of 100 mTorr, then switching to a cryopump. The pressure was measured with a dual thermocouple and ion gauge Instrutech Hornet IGM402YCD, isolated from MELBA with a ceramic insulated break. In bringing the chamber back up to atmospheric pressure, the pumps were gated off, and the chamber was backfilled with dry nitrogen to prevent contaminants such as water in the air from becoming embedded in MELBA's ceramic insulator.

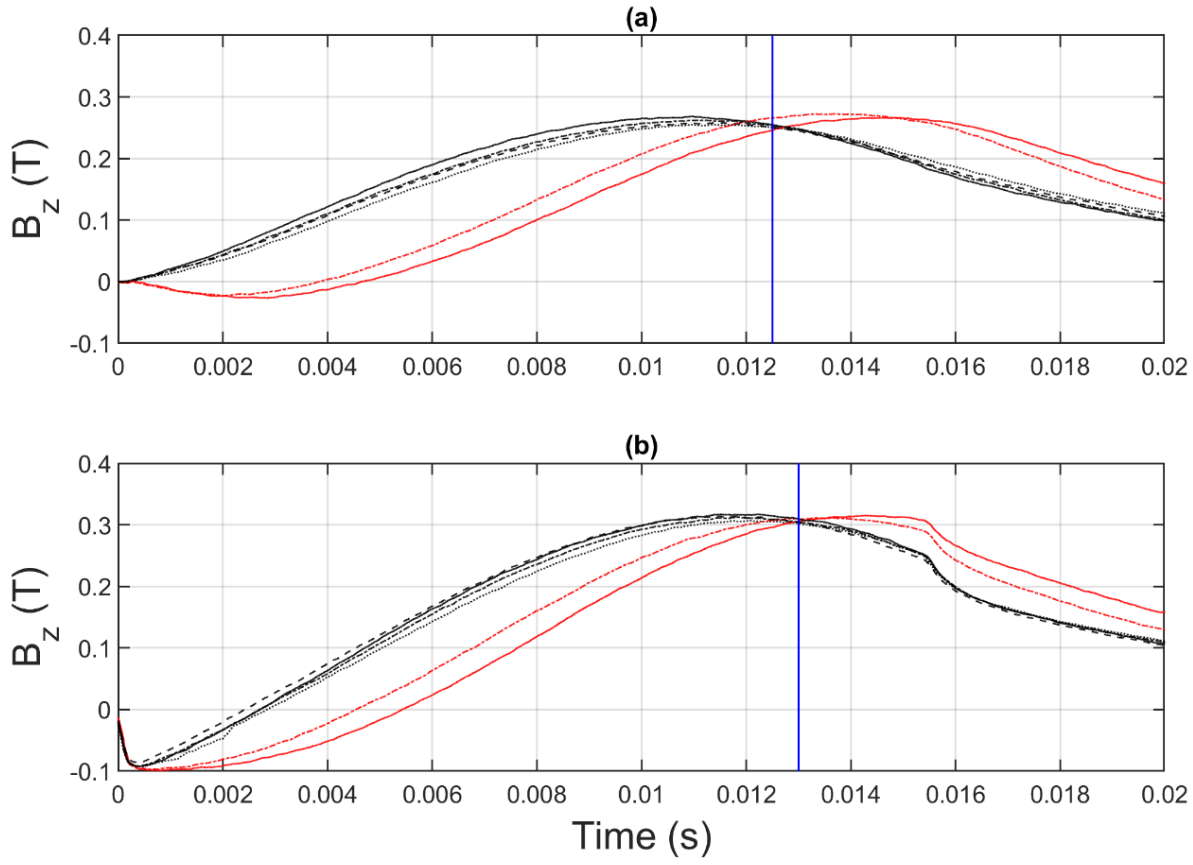

Figure 4.3: Magnetic field calibration for the (a) ISBO and (b) HRPM with the capacitors charged to 5 kV. The magnetic field was measured at six different positions, three of which were in the planar region between the cathode and oscillators (black), two of which were in the cylindrical bends (red), and one between the cathode and planar drift region opposite of the oscillators (black). The magnetic field delay used in each experiment is indicated by the blue line, where field uniformity is maximized.

The magnetic field was established by a pair of solenoids in a near-Helmholtz configuration [124]. The coil radius was 22 cm, and the separation was 27 cm, held consistent with prior RPM experiments on MELBA. After discharging the magnet capacitors to activate the solenoids, MELBA was triggered to discharge into the experiment after a specified delay in time to allow the magnetic field to diffuse into the chamber. This time delay established a near-uniform magnetic field throughout the racetrack-shaped interaction space of the HRPM. The magnetic field was calibrated by measuring the axial field with a Lakeshore 475 Gaussmeter with a HMNA-1908-VR Hall Probe and correlating it to the electromagnet peak current measured from the Pearson coil. The data from the calibration at maximum capacitor charge are shown in Figure 4.3, where the black lines represent the field measured in the planar regions, while the red lines are the field in the cylindrical bends. After performing the calibration, it became apparent that the introduction of the LBO and tuner altered the magnetic field profile within the HRPM so that higher fields could be achieved than in the ISBO; additionally, the magnetic field in the cylindrical bends was maximized later in time than in the planar region. In maximizing uniformity, the selected delay between the initiation of the solenoid discharge and MELBA discharge for the HRPM and ISBO experiments was 13 ms and 12.5 ms, illustrated by the blue lines in Figure 4.3. Respective magnetic fields of up to 0.31 T and 0.26 T were achievable in the HRPM and ISBO experiments, with less than 5% and 10% variation in magnetic field magnitude depending on the physical location of the magnetic field measurement.

4.2 Magnetron Hardware

A concerted effort was made to implement a symmetric, cost-effective, all cavity extraction scheme [125], [126] for calibrated power measurements on the HRPM. This was accomplished by applying the coaxial-all-cavity-extraction (CACE) method [53], [108]. Much of the transmission line was designed by Franzi [108], built, and assembled for a previous experiment at UM. The complete geometry, illustrated in Figure 4.4 and Figure 4.5, extracts power from pairs of SBO cavities into individual coaxial transmission lines. Coupling apertures, one located at the back of each of the six cavities, enable the excitation of a TEM wave in the coaxial lines. The length of the coupling apertures, h, was varied from experiment-to-experiment to change the SBO quality factor. To operate within the physical constraints of the experimental test chamber, the coaxial lines that extract directly from the oscillating cavities are of smaller radius than the Franzi design.

Once the coaxial lines extended to the end of the vacuum flange and exited the chamber, they were flared and tapered to meet the larger radius, which then adapts to waveguide through the implementation of a distributed field adaptor (DFA) in each transmission line. Power measurements were made in the waveguide portion of the transmission lines using directional couplers. The LBO resonant frequency was varied shot-by-shot via translation of cylindrical tuners along the axis of the chamber into each of the three LBO cavities. The distance that the rods were inserted into the LBO, L, was identical in each of the three cavities for any individual shot.

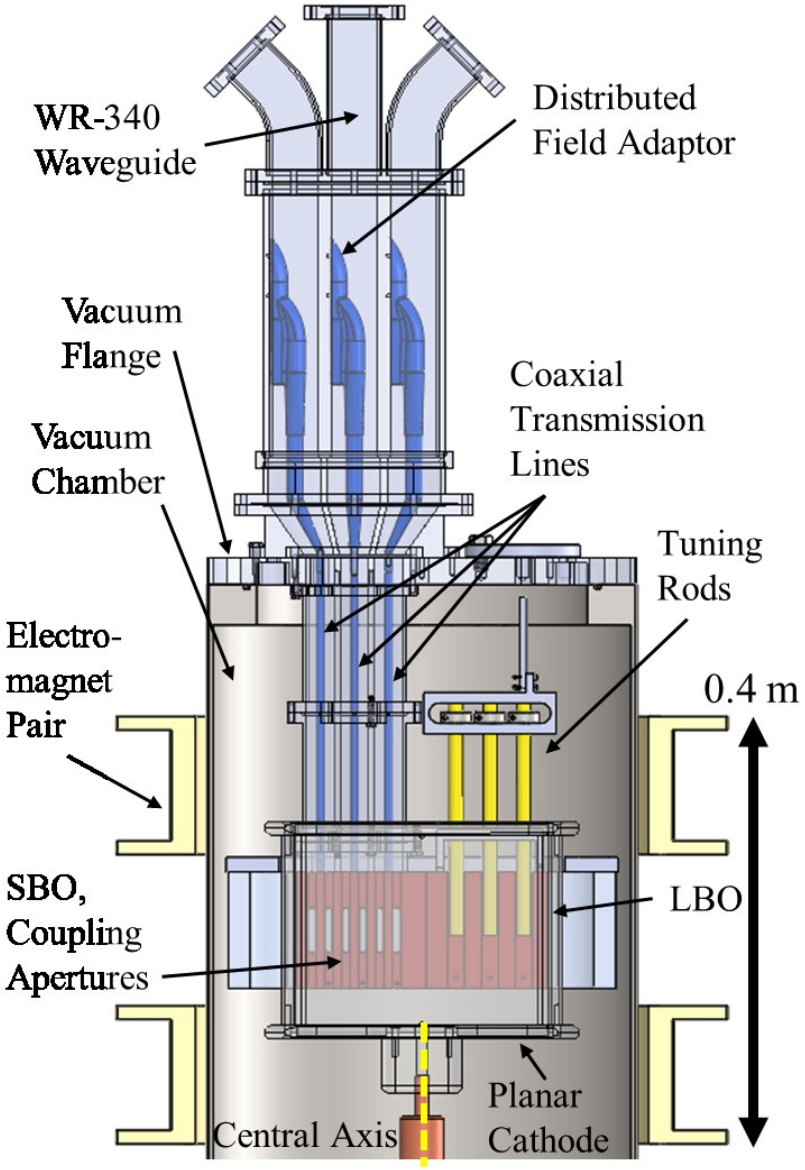

Figure 4.4: CAD rendering of HRPM experimental assembly loaded into vacuum chamber with CACE.

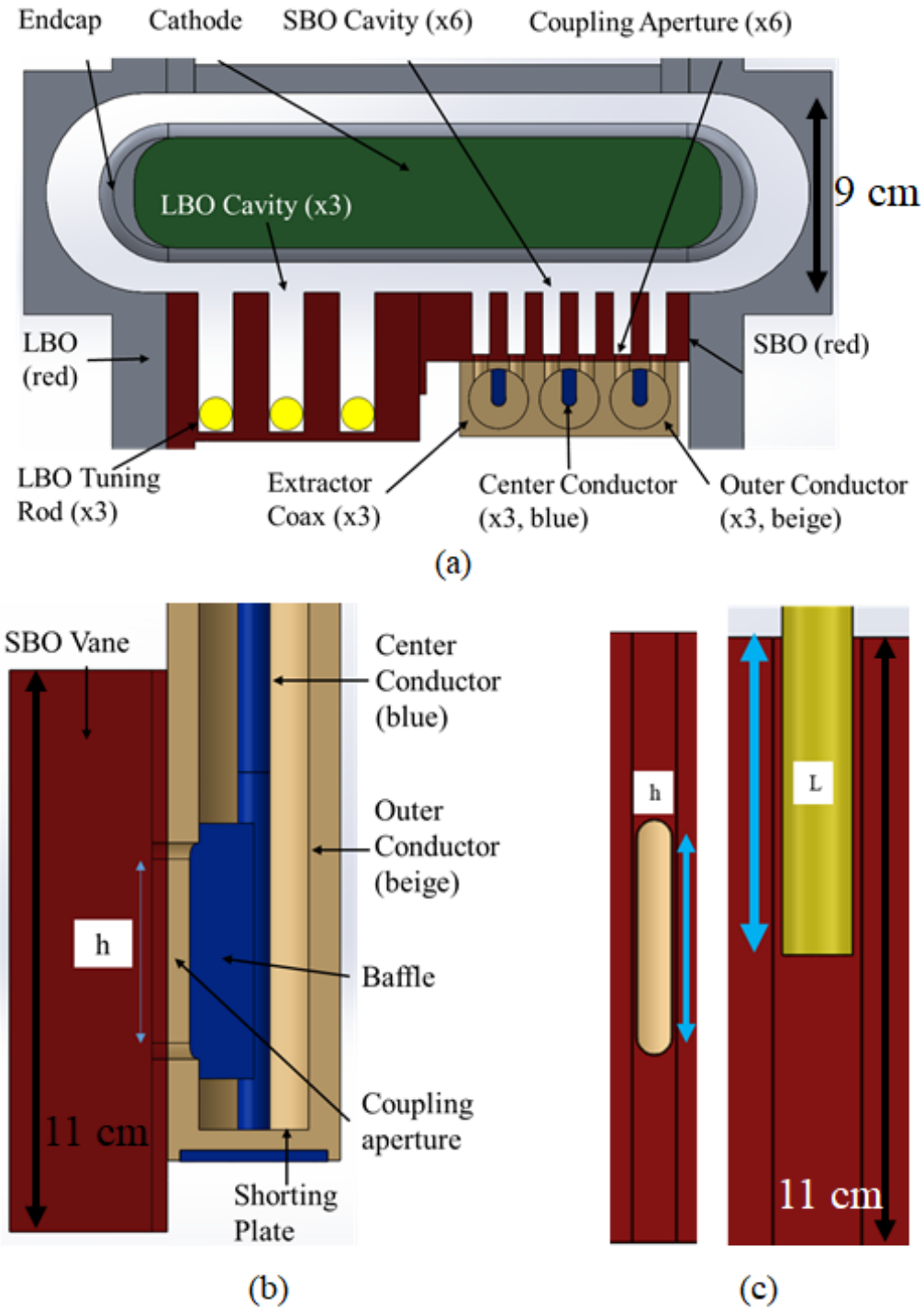

Figure 4.5: (a) Top-down cross-section of the HRPM. (b) Cross-section within a coaxial line of the SBO. (c) Unit cells of the SBO (left) and LBO (right), pictured from the view of the cathode. The two independent variables are illustrated, which are the aperture length h and tuning rod length L.

The slow-wave structures of the HRPM, the extractor, and the tuner were all designed as modular components composed of aluminum-6061 for greater ease of fabrication. The fully

assembled anode, pictured resting on a table and in the chamber, is shown in Figure 4.6. Focusing on Figure 4.6a, the 3-cavity LBO and 6-cavity SBO are readily visible. The extractor, extending upward from the SBO, is mounted directly to the back of the cavities. The cylindrical tuning rods are shown plunging halfway into the LBO cavities. The blue cables are connected to B-dot probes, which mount to recessions in the back of the oscillating cavities. A smoothbore, planar drift region opposes the cavity structures. Figure 4.6b pictures the entire anode loaded into the experimental chamber. Coupling apertures are visible on the back wall of the SBO cavities. The top of the extractor from Figure 4.6a connects to the vacuum plate, forming a seal with the end of the chamber. The B-dot signals propagate down their cables and through the SMA ports shown at the bottom of the image, where easy access to the oscilloscope is achievable. Inside the chamber, the tuner is connected to a translatable shaft adjusted from the outside. This shaft enables the translation of tuning rods along the chamber axis shot-by-shot during experiments without breaking the vacuum.

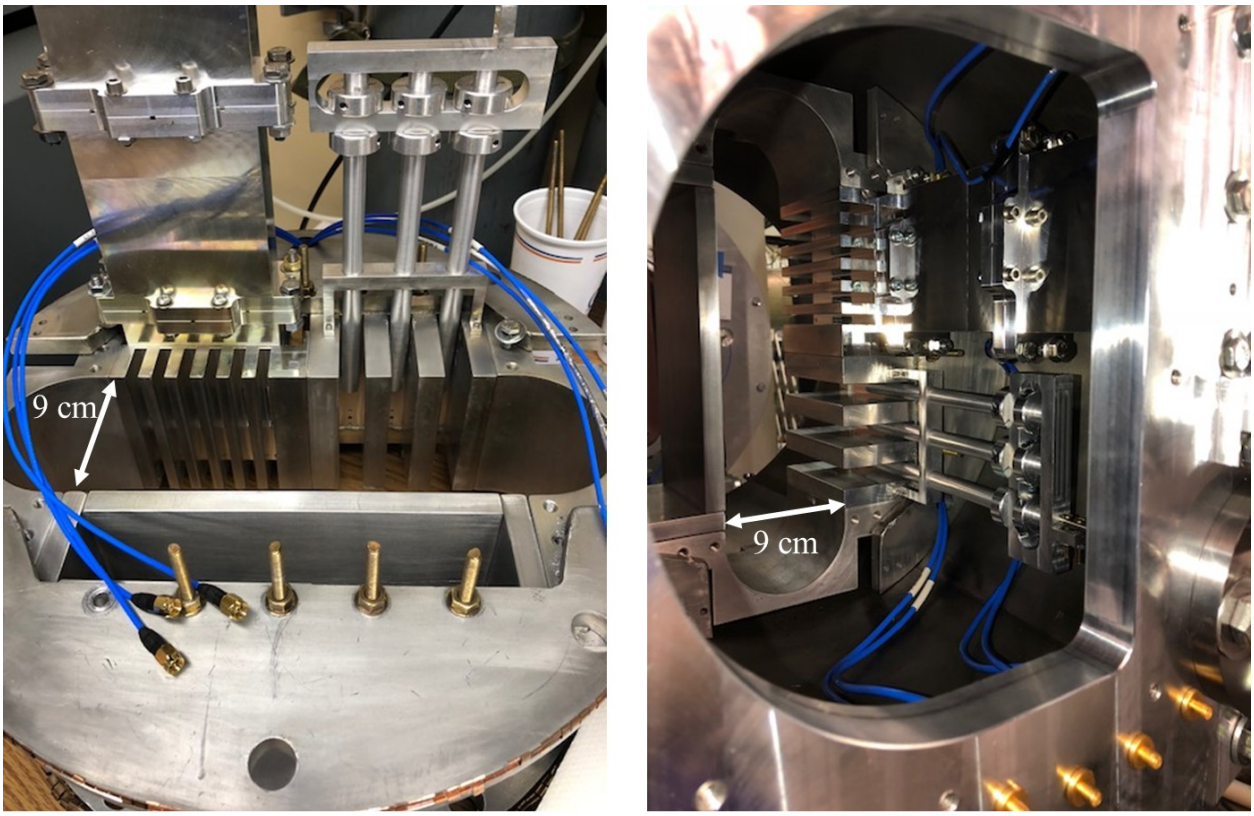

Figure 4.6: HRPM anode. (a) Six SBO cavities (bottom left), three LBO cavities (bottom right). Coaxial extractor (top left) is connected into the back of the SBO. Tuning rods (top right) plunge downward into the anode. (b) HRPM anode loaded into the test chamber with cathode removed. Coupling apertures visible at the deep end of the SBO cavities.

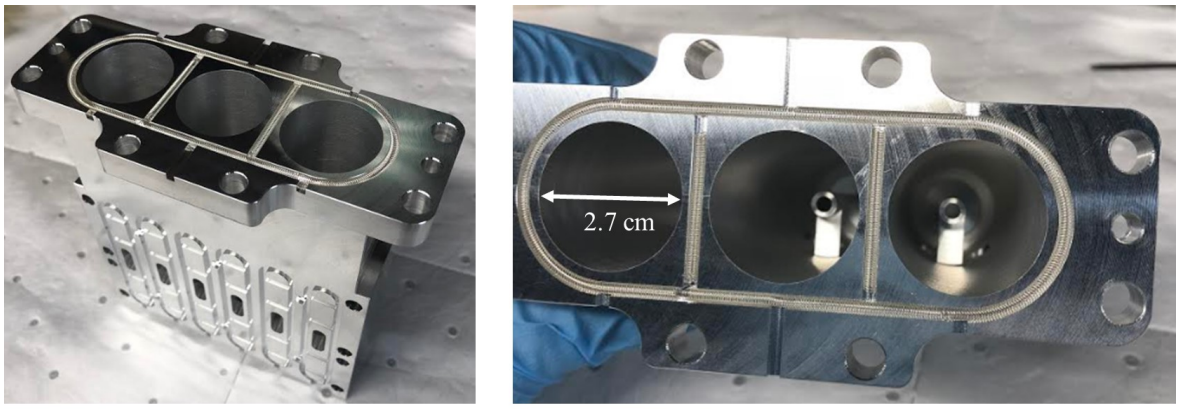

(a) SBO to coax adaptor, with coupling apertures

(b) Interior of adaptor, where the coaxial lines begin

Figure 4.7: SBO adaptor to coaxial transmission lines. The adaptor is the first component of the extractor, which connects directly to the SWS. All six cavities couple into the coaxial lines through the slots shown in (a). The formation of the coaxial line is shown in (b), which extends along the axis of each cylindrical bore.

The first component of the SBO extractor, which connects directly to the posterior side of the resonating cavities, is shown in Figure 4.7. Grooves were machined at every interface between modular components for placement of Bal Seal, which is a spring-like RF-gasket that improves electrical contact at these junctions. These grooves surround each of the coupling apertures shown in Figure 4.7a and the coaxial lines in Figure 4.7b. The interior of the coaxial lines is visible in Figure 4.7b, where the coaxial lines are shorted at the bottom end.

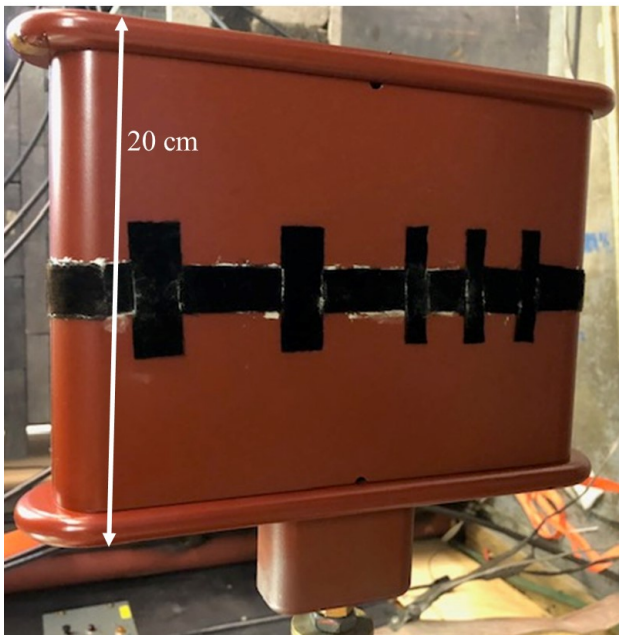

Figure 4.8: HRPM cathode. A central velvet emitter wraps around the entire cathode, and additional velvet strips are placed across every other cavity to promote π-mode growth. The strips for the LBO are on the left, and the strips for the SBO are on the right.

Visualized in Figure 4.8 is the HRPM cathode, equipped with end-hats placed at the top and bottom of the planar structures to mitigate axial endloss [127]. Explosive emission is promoted at the black velvet emitters. One long, emitting strip wraps around the entire solid cathode, while multiple vertical strips oriented parallel to the oscillating cavities are placed for promotion of growth in the π-mode via cathode priming [43]. The central strip is 2 cm in height (along the chamber axis), while the vertical strips are each 4 cm in height. The emitters adhered to the cathode surface with the application of a conductive epoxy. The remainder of the surfaces are coated in five layers of Glyptal, an emission reducing enamel.

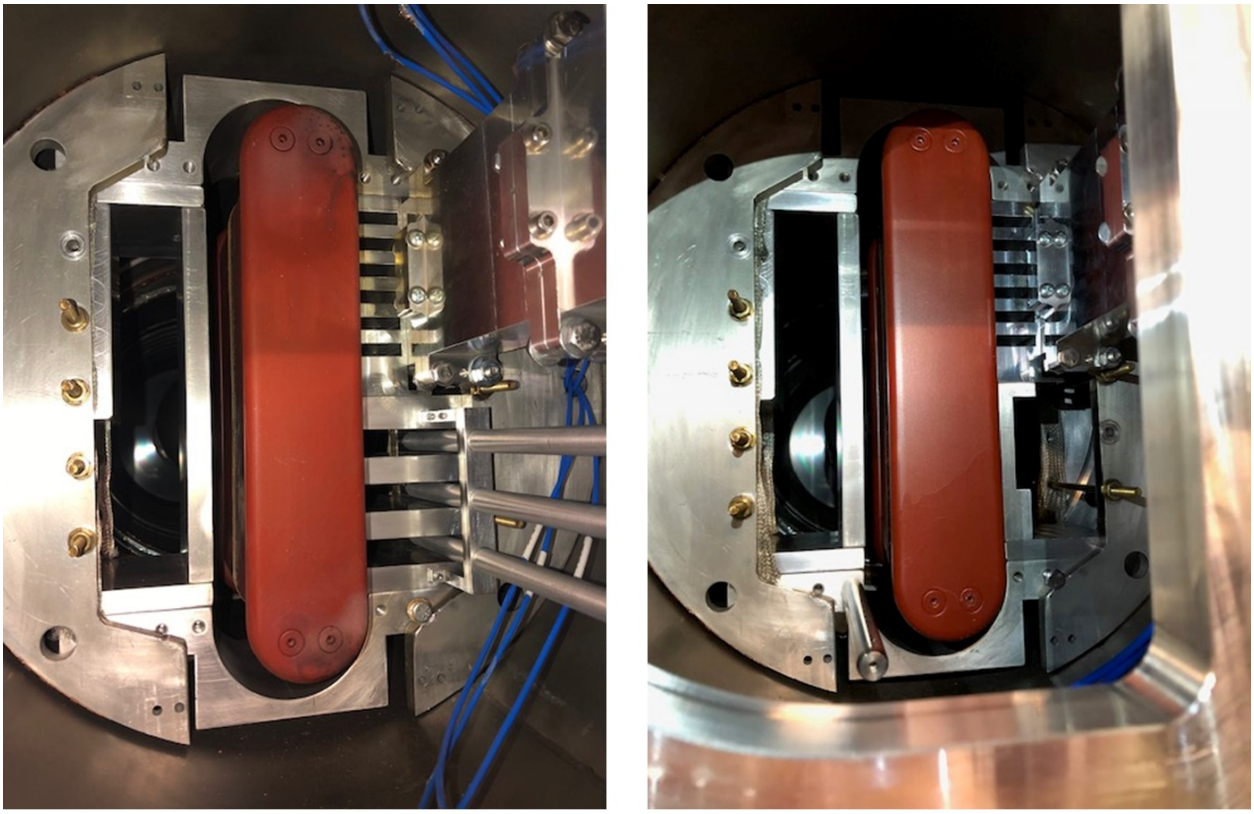

(a) HRPM (b) ISBO

Figure 4.9: (a) HRPM loaded into the chamber, with 3-cavity LBO and 6-cavity SBO both visible, with their tuner and extractor, respectively. (b) ISBO loaded into the chamber. The SBO and its extractor remains, but the LBO and tuner have been replaced by a smoothbore drift region. For length scale, reference Figure 4.6.

The entire experimental assemblies are illustrated in Figure 4.9a and Figure 4.9b, which show the HRPM and ISBO configurations. Obviously, the difference between the two is that the LBO was removed from the ISBO and replaced by a planar drift region. Figure 4.9b was taken before the experiment after a fresh application of Glyptal, whereas Figure 4.9a was taken after an experiment took place. Visible damage appeared on the top of the end-hats, possibly because of

electric field enhancement due to the presence of the blue cables along the same magnetic field lines that increased the local plasma density.

The components that make the transition from coaxial transmission line to waveguide are shown in Figure 4.10. First, Figure 4.10a shows the center conductors of the output coax protruding from the tapered and flared adaptor. These components are slip-fit with the coaxial end of the DFA-340e, the waveguide (WR-340) end of which is shown in Figure 4.10b. In the range of SBO frequencies extracted, DFA-340e demonstrated adequate transmission with S_{21} bound between -1 dB and -0.2 dB [53]. Once the transition from coaxial line to waveguide is made, each transmission line was terminated with an absorbing load with return loss in the range of 15 dB to 20 dB. All measurements of microwave transmission or reflection were performed with a Hewlett-Packard 8772D vector network analyzer.

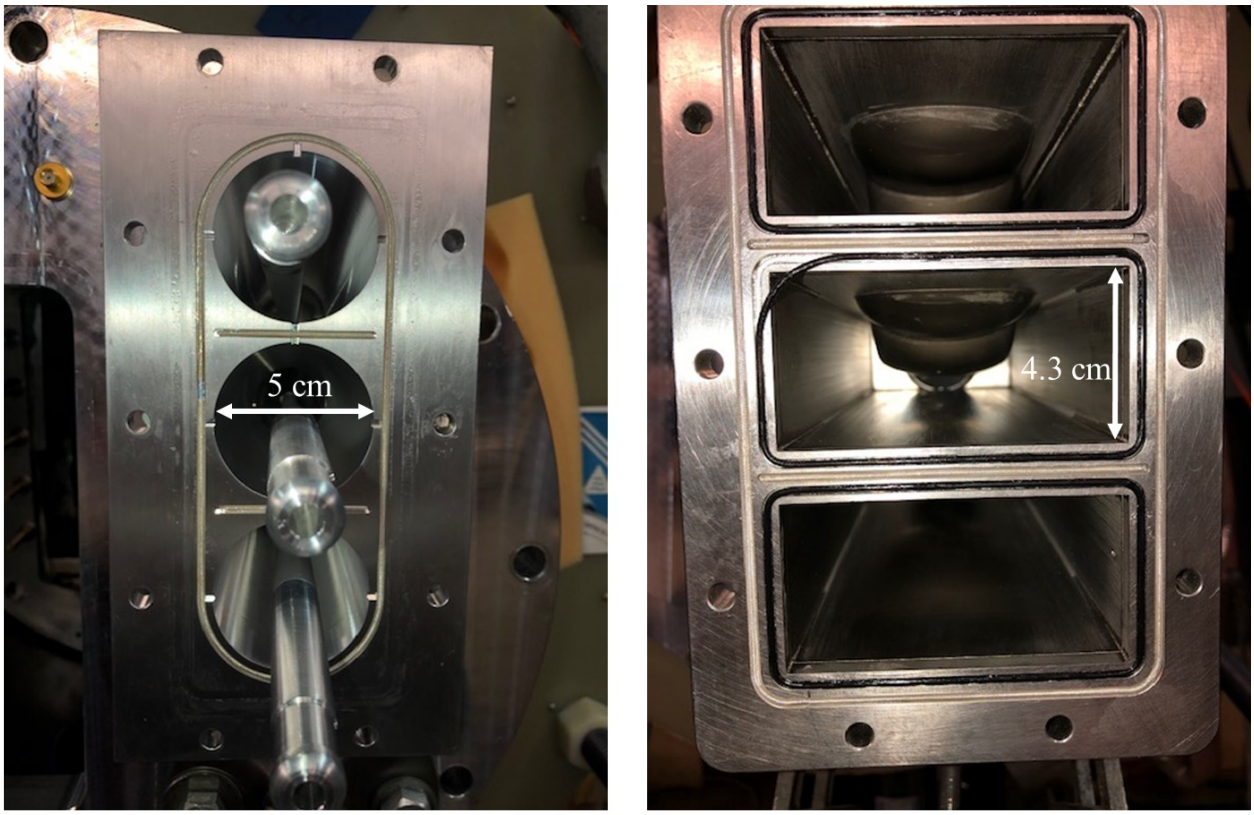

Figure 4.10: Components of the output extractor where the transition from coaxial line to waveguide is made. (a) Center conductor of output extractor protruding from tapered and flared coaxial adaptor. These plug into the DFA. (b) The waveguide end of the DFA. The center conductors pictured in (a) plug into the opposite side of the DFA.

A directional coupler sampled the forward power propagating toward the load between the adaptation from coax-to-waveguide and the microwave terminators of each output. The directional

coupler outputs, each sampled at -53 dB, were delivered to the screen room through individual type-N cables for power measurement and time-resolved signal information. This signal was further attenuated in the screen room with additional in-line power attenuators and split equally into two paths, one sent through a calibrated Low-Barrier Schottky Diode (LBSD) and the other delivered directly to a fast Agilent 54855A oscilloscope. The HP 8472B LBSD detectors can measure up to 12.4 GHz at ±0.3 dB precision. The output voltage of each detector was calibrated using a continuous-wave (CW) microwave source, with a known fraction of its power diverted to an Agilent E4418B EPM Series Power Meter [54]. By measuring the LBSD voltage output on an oscilloscope and accounting for all microwave losses in the transmission line, including the directional coupler loss, cable attenuation, in-line power attenuation, and splitter loss, the power within the waveguide was accurately measured. Fast-waveform and spectral measurements were made possible by the Agilent 54855A oscilloscope, capable of resolving up to 6 GHz. With the application of a fast-Fourier transform (FFT), time-integrated Fourier transforms were obtained to reveal dominant and competing frequency for each output on every shot.

Finally, the microwave B-dot loop used to probe the LBO cavity oscillations is shown in Figure 4.11. These diagnostics were used to capture the RF magnetic field along the direction of the cavity length (along the chamber axis). These measurements were used to ascertain the frequency and phase information of the LBO cavities with respect to each other. The loop was 1.6 mm in diameter, and each signal was carried out of the chamber through an SMA cable. The spectral information from these signals was obtained in the same manner as the SBO frequency from the waveguide outputs.

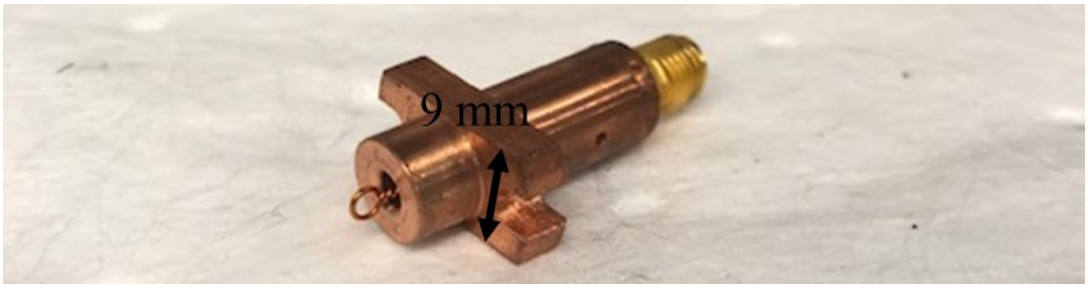

Figure 4.11: B-dot for probing the LBO microwave frequency. The B-dots were inserted into the back of each LBO cavity, where the loop was excited by the cavity magnetic field.

4.3 MILO Hardware

Similar to the HRM, the MILO is comprised of three primary components, which include the cavities, cathode, and extractor. As shown in Figure 4.12, the MILO is azimuthally symmetric

about the axis of the test chamber. Two of the cavities are designed as a microwave choke, while the remainder are resonant cavities designed for electron interaction. The cathode is equipped with velvet to emit in the cavity region and the beam collector. The output coaxial transmission line is formed between the outer radius of the beam collector and the outer coaxial wall, co-radial with the outer radius of the resonant cavities. When the desired π-mode is excited, a TEM wave is launched in the coaxial output line, then linearly tapered with minimal reflections to a smaller cross-section. Like the HRPM, the coaxial output is transformed into waveguide (WR-650) through implementation of DFA-650c. This DFA has adequate transmission from 0.94 GHz to 1.02 GHz with S_{21} between -0.2 dB and -0.02 dB [53].

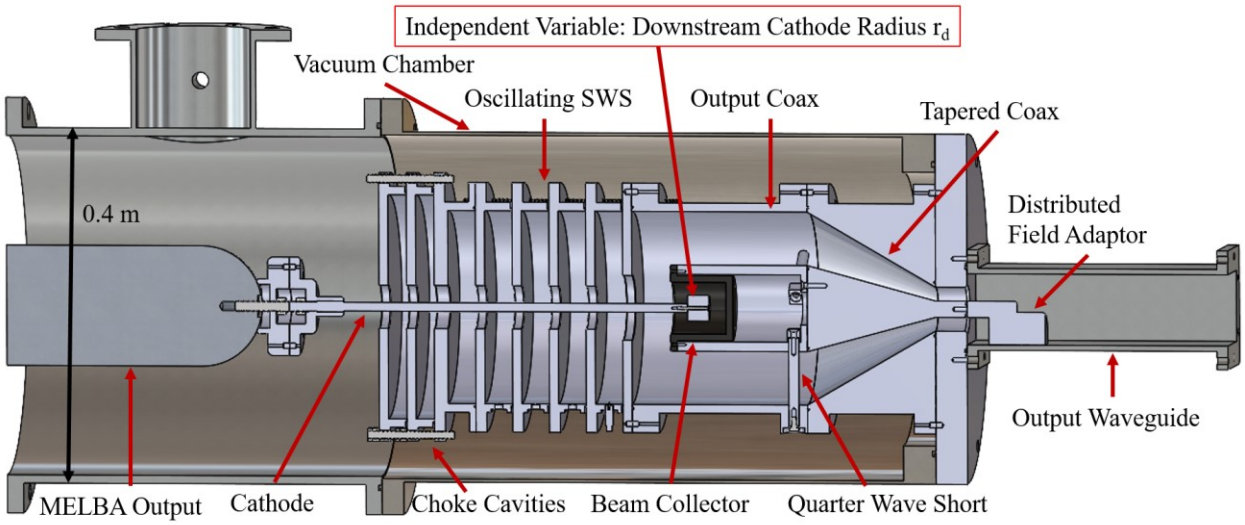

Figure 4.12: Full design of the MILO, labeled by component.

The MILO components are visualized in Figure 4.13. The cavity disc comprises the SWS when multiple of these parts are stacked upon themselves. Each disc consists of the SWS vane and cavity back wall. Bal Seal is placed at the junction between cavities to form a good electrical contact. The resonant cavities were machined out of #303 stainless steel, whereas the choke cavities were fabricated out of #6061 aluminum. The piece that adapts the choke cavities to the resonant cavities is slightly different with two flanges, and the final vane is merely a disc without the outer cavity wall, each feature demonstrated in Figure 4.12. Precision dowel pins were placed at every junction to ensure that satisfactory alignment was established between components, with a tolerance of ± 0.001".

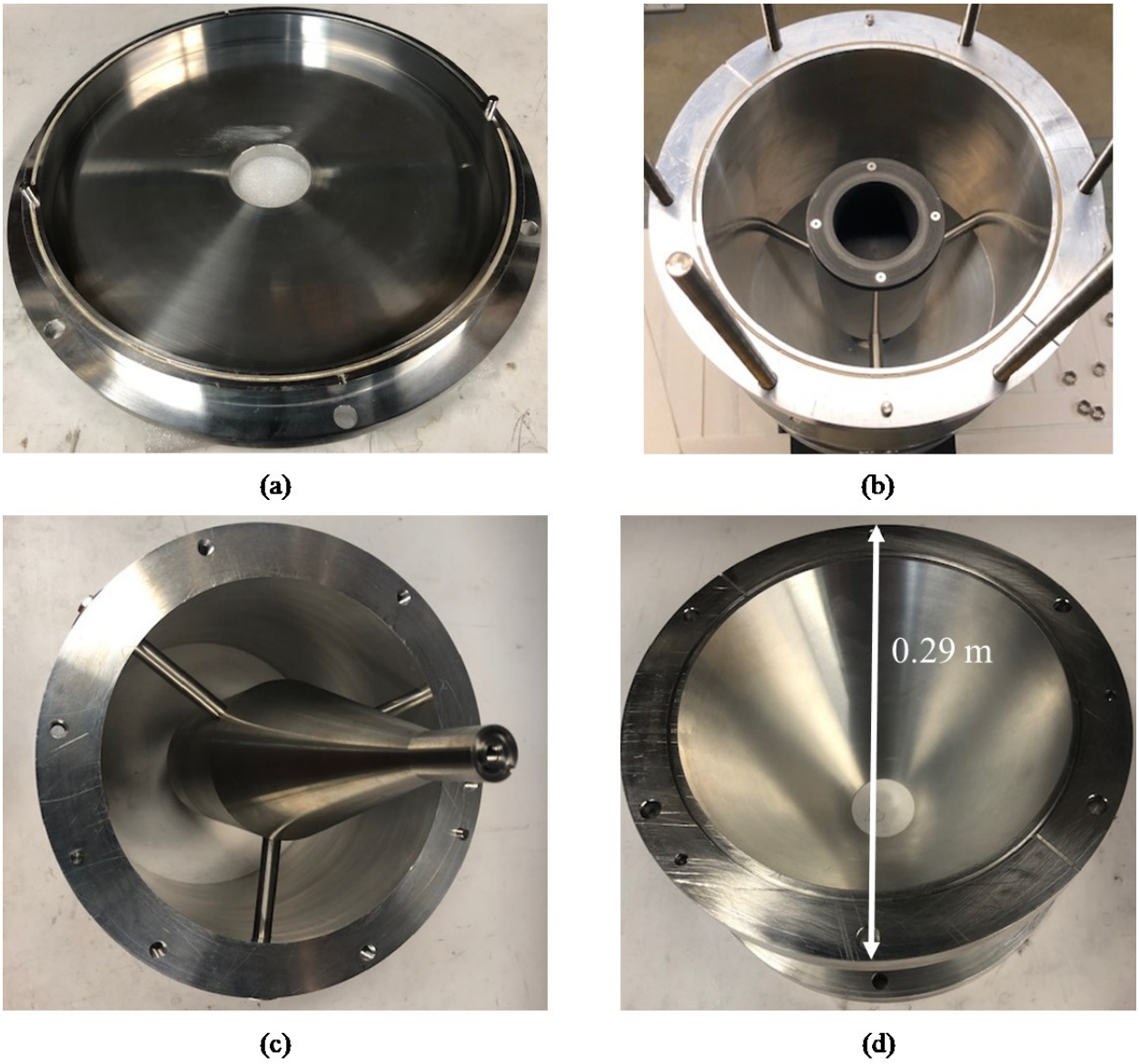

Figure 4.13: MILO components. (a) Modular cavity disc, which forms the SWS when stacked upon itself. (b) Assembled coaxial extractor, showing the quarter-wave shorting stubs, graphite beam collector, and tapered outer diameter. Components from (c) and (d) are mated to produce this assembly. (c) Output coax assembled with the beam collector, tuned support rods, and inner conductor. (d) Tapered outer conductor.

Figure 4.13b illustrates the extractor assembly produced by combining the coax and beam collector with the tapered outer conductor, shown in Figure 4.13c and Figure 4.13d, respectively. The beam collector is where the downstream current is collected from the cathode, establishing magnetic insulation for MILO operation. The material used was vacuum grade POCO graphite, which forms dust when it is impacted/sublimated by high-velocity electrons and shorted-discharges, rather than sputtering and depositing the cathode like a metal anode. The inner conductor of the coaxial transmission line is formed by the outer radius of the beam collector and

the tapered segment of the transmission line, both fabricated out of #303 stainless steel. The quarter-wave shorting stubs, which are transparent to the RF wave, provide physical support for the beam collector and inner conductor and a means to conduct collector current to ground. The rods establish a physical and electrical connection to the outer radius of the coax, which is #6061 aluminum. The linearly tapered outer conductor mates with the flange shown in Figure 4.13c. Cavity structures are then stacked on top of the alignment rods shown in Figure 4.13b, beginning with the final vane, then the resonant cavities, and finally the choke cavities.

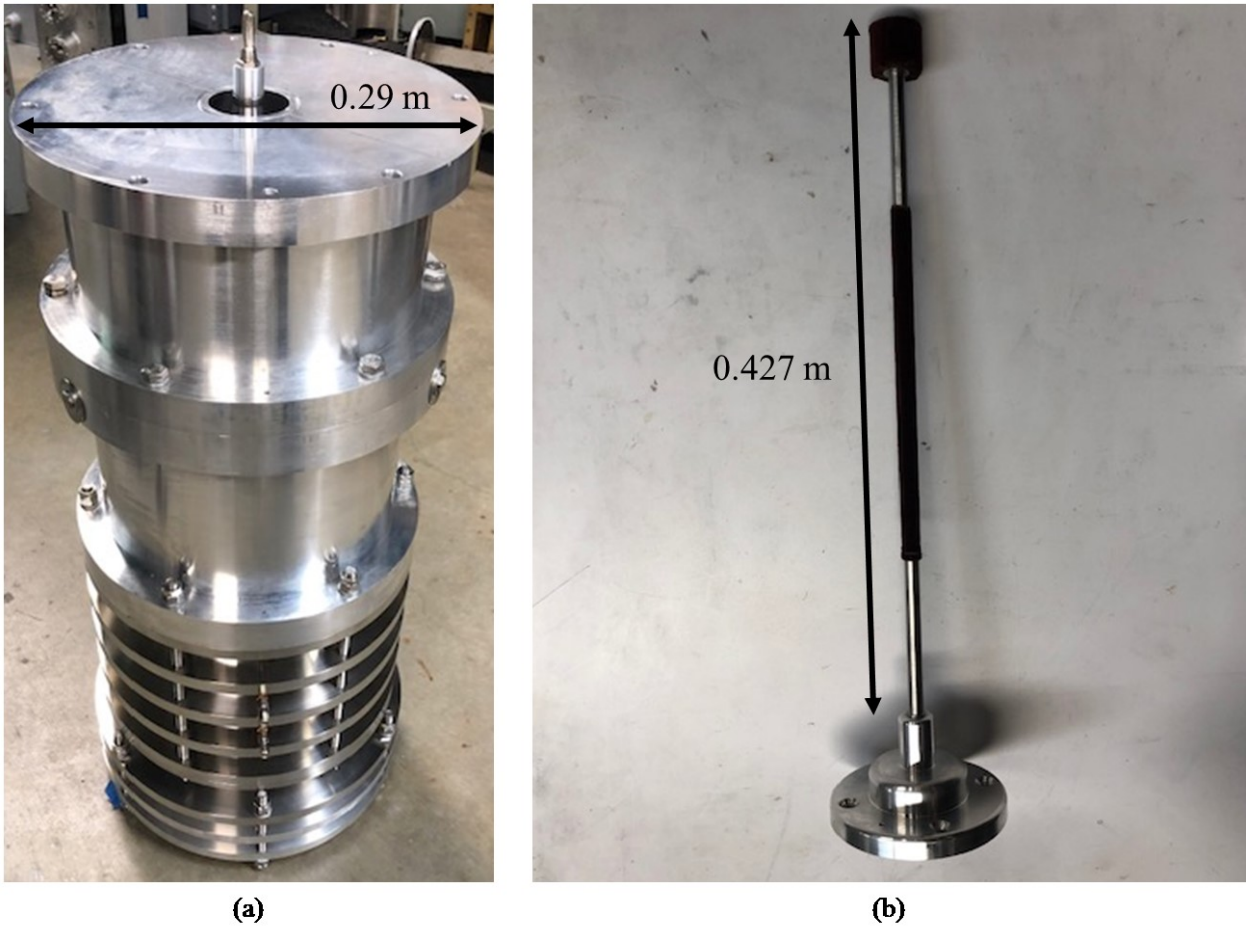

Figure 4.14: (a) Assembled MILO anode. The cavities are the disc-shaped structures at the bottom, while the aluminum extractor sits atop them. (b) MILO cathode. Emission is allowed in the cavity region and in the downstream diode. The emitter in the cavity region covers the full SWS, including choke and resonant cavities.

The complete anode assembly is shown in Figure 4.14a. The visible segments are the choke cavities, resonant cavities, coaxial output, and tapered transmission line from bottom to top. The center conductor extends outward such that its banana plug can mate with DFA-650c. The total length of this assembly is 65 cm, almost exactly the length of the test chamber. The cathode, shown

in Figure 4.14b, allows emission in the cavity region and the downstream diode. The emitter used was red cotton velvet, which was sewn around the #303 stainless steel pieces that form the cathode. Unlike the magnetron experiments, no conductive epoxy was used to hold the velvet on the metal surfaces, and Glyptal was not used. The velvet emitter was 31.5 cm long, which encompassed the entire length of the SWS (including the choke and resonant regions) with 2 cm of additional length preceding the first vane of the choke section. The independent variable in this experiment was the downstream cathode radius, r_d, which was varied between 0.8 cm and 1 cm. The cathode radius in the SWS region was 0.7 cm.

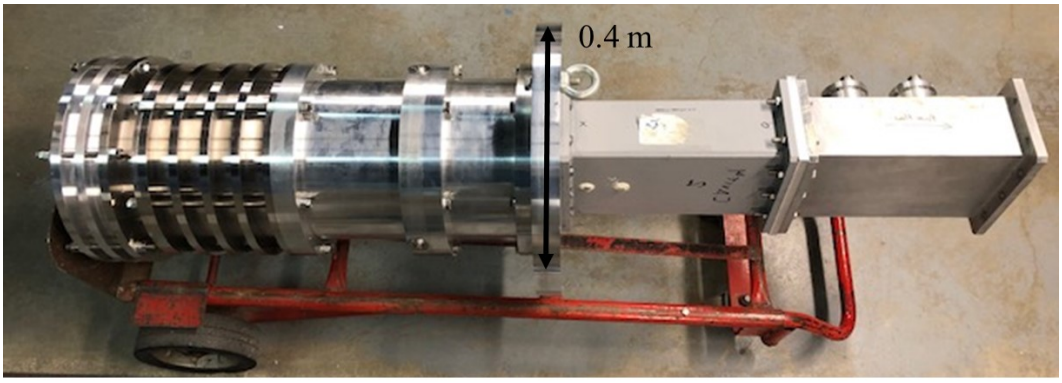

(a)

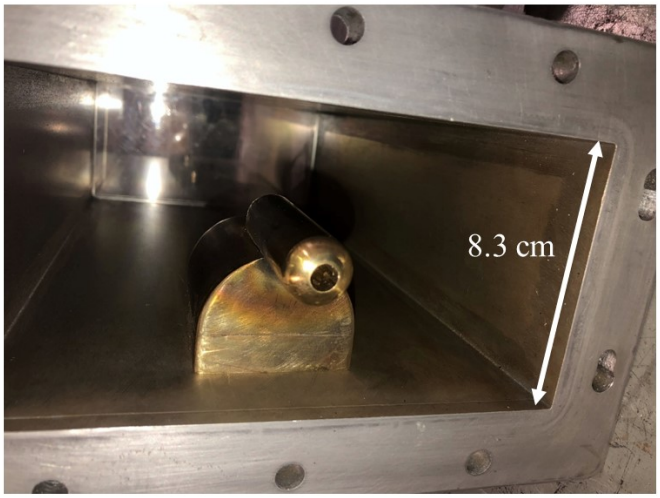

(b)

Figure 4.15: (a) MILO anode with output waveguide mounted. (b) DFA-650c within the output waveguide.

The complete experimental assembly, with vacuum flange, output waveguide, and directional coupler, is shown in Figure 4.15a, along with DFA-650c in Figure 4.15b. The DFA is located within the first piece of waveguide that connects to the vacuum flange, where the inner conductor of the MILO output coax makes an electrical connection. A Lexan window between the

directional coupler and output waveguide establishes the vacuum interface. The outer radius of all MILO components was carefully designed so the device could be loaded directly into the open end of the vacuum chamber and secured at the vacuum flange. After mounting the cathode to the output voltage stalk of MELBA, the experimental chamber loaded with the MILO could be guided onto the output flange of MELBA.

Finally, the complete assembly of the MILO into the MELBA experimental test facility is illustrated in Figure 4.2, shown toward the beginning of this chapter. Although the electromagnets were not used in this experiment, they remained mounted to the chamber. The signal coupled out of the directional coupler was carried to the screen room by high-voltage Type-N cables to measure frequency and power. Although it is not easily visualized in this picture, an insulating Lexan break between the output waveguide and directional coupler was implemented to prevent high voltage swings from being carried into the screen room during operation. The directional coupler was then grounded with a braid strap, which can be seen in this image hanging on the right of the directional coupler. The output waveguide was terminated with a 4-foot Eccosorb load with a return loss of 9 dB or more, depending on the frequency; return loss was minimized at 9 dB and 993 MHz. At the end of the terminator, a fiber optical cable was fed into the waveguide to measure the presence of visible light during the operation of the MILO.

Chapter 5 Harmonic Recirculating Planar Magnetron Experiments

This chapter presents and analyzes the results obtained in the Harmonic Recirculating Planar Magnetron experiment. First, to gain a baseline understanding of the operation of the device, the results from the Isolated S-Band Oscillator (SBO) experiment will be discussed. This control is necessary to ascertain the importance of introducing the L-Band Oscillator (LBO) into the experiment when the HRPM is analyzed in the second section. In the third section, the quality factor study will be discussed, and its important conclusions regarding harmonic frequency locking. In total, these experiments investigated three different quality factors, which will generally be referred to as the high Q, moderate Q, and low Q experiments throughout each section. The relative phase difference between output signals from the LBO and SBO, in both the HRPM and the isolated-SBO (ISBO), are analyzed in the fourth section. Finally, in section five, the reversed magnetic field experiment results will be presented, where the direction of the electron spokes was reversed to flow from the SBO toward the LBO.

5.1 Isolated S-Band Oscillator Operation

Experiments were performed wherein the LBO was removed entirely from the HRPM and replaced with a smoothbore drift region, a configuration referred to as isolated-SBO (ISBO). ISBO experiments were performed to isolate the effect the LBO has on SBO operation, an interaction that makes the HRPM unique. Figure 5.1 illustrates MELBA shot 17593 from the ISBO experiment, where the voltage and current are overlaid by the individual waveguide output power and the instantaneous sum of the generated microwave power. At the instant of peak microwave generation, the voltage and current were 950 A and 230 kV, extracting 39 MW to result in a peak total efficiency of 18%. The full width at half max (FWHM) of the power pulse was 21.2 ns, and the total microwave energy produced was 0.96 J. The applied magnetic field was 0.26 T.

The raw signals from the output waveguides were sampled by a 6-GHz, 20-GSa/s Agilent 58455A oscilloscope. Spectral analysis of these signals from MELBA shot 17593 is demonstrated in Figure 5.2. The dominant frequencies in each waveguide differ by at most 5.6 MHz, and there is little to no evidence of mode competition. Stable operation in a single mode is corroborated by

the absence of beating on the output power in Figure 5.1. The output frequency from a single shot is defined as the arithmetic mean of the three waveguide outputs, which is 2.0713 GHz in this shot; this will be referred to as the "composite frequency" henceforth. Particle-in-cell (PIC) simulations of the ISBO using CST-Particle Studio (PS) demonstrate operation of the 5π/6 mode at 2.070 GHz, which is in excellent agreement with the experimental output for this specific shot. It is therefore concluded that MELBA shot 17593 oscillation is dominant in the 5π/6 mode. Clear dominance of a single mode is typically desired for oscillators such as the magnetron; competition between modes often leads to reductions in output power and efficiency. A small harmonic component near 4 GHz is observed ~20 dB below the fundamental frequency on two waveguides.

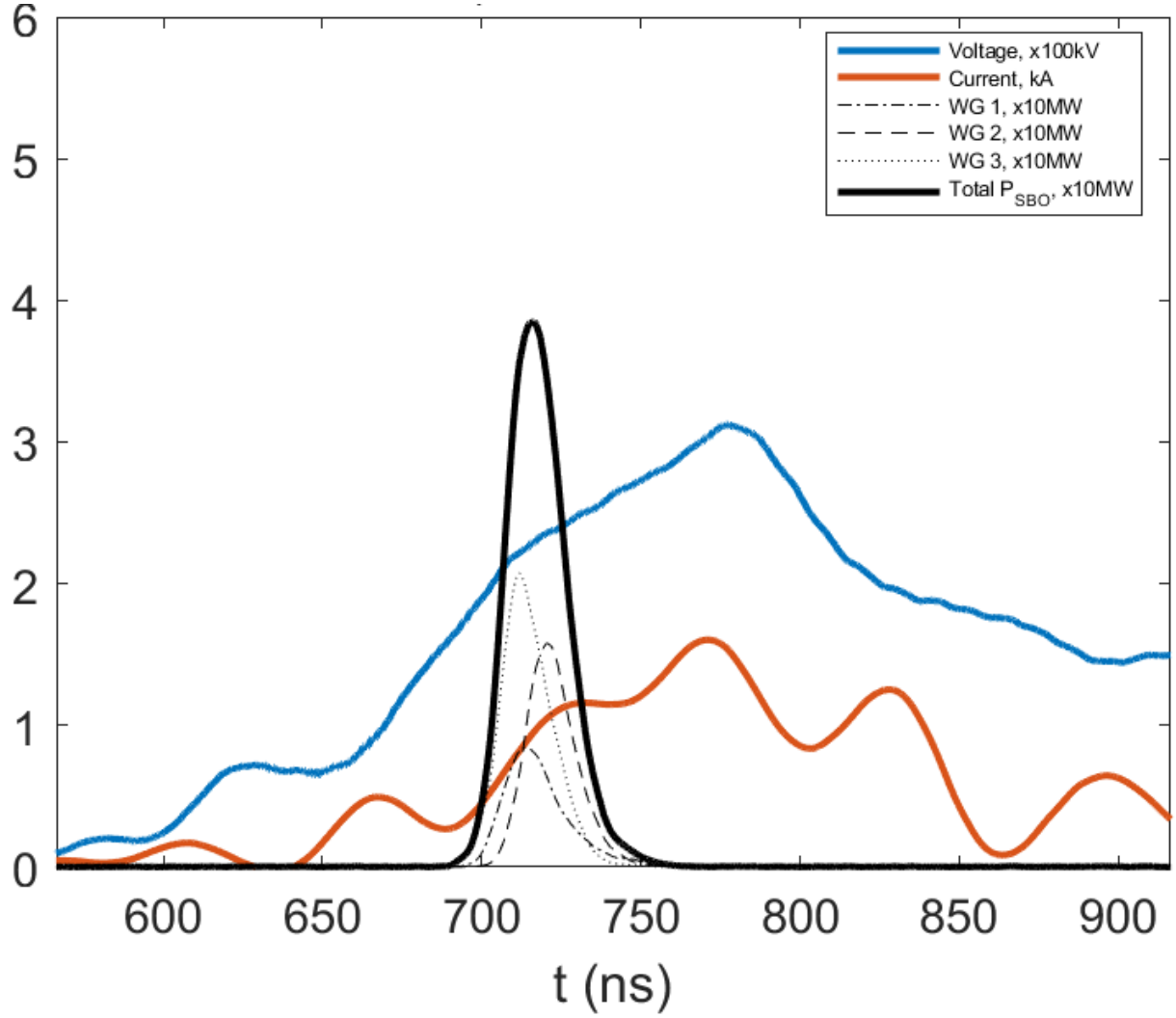

Figure 5.1: MELBA shot 17593, testing the isolated S-Band Oscillator in the low Q configuration. The instantaneous peak power of the SBO is nearly 40 MW on this shot, where the current and voltage are 950 A and 230 kV, respectively.

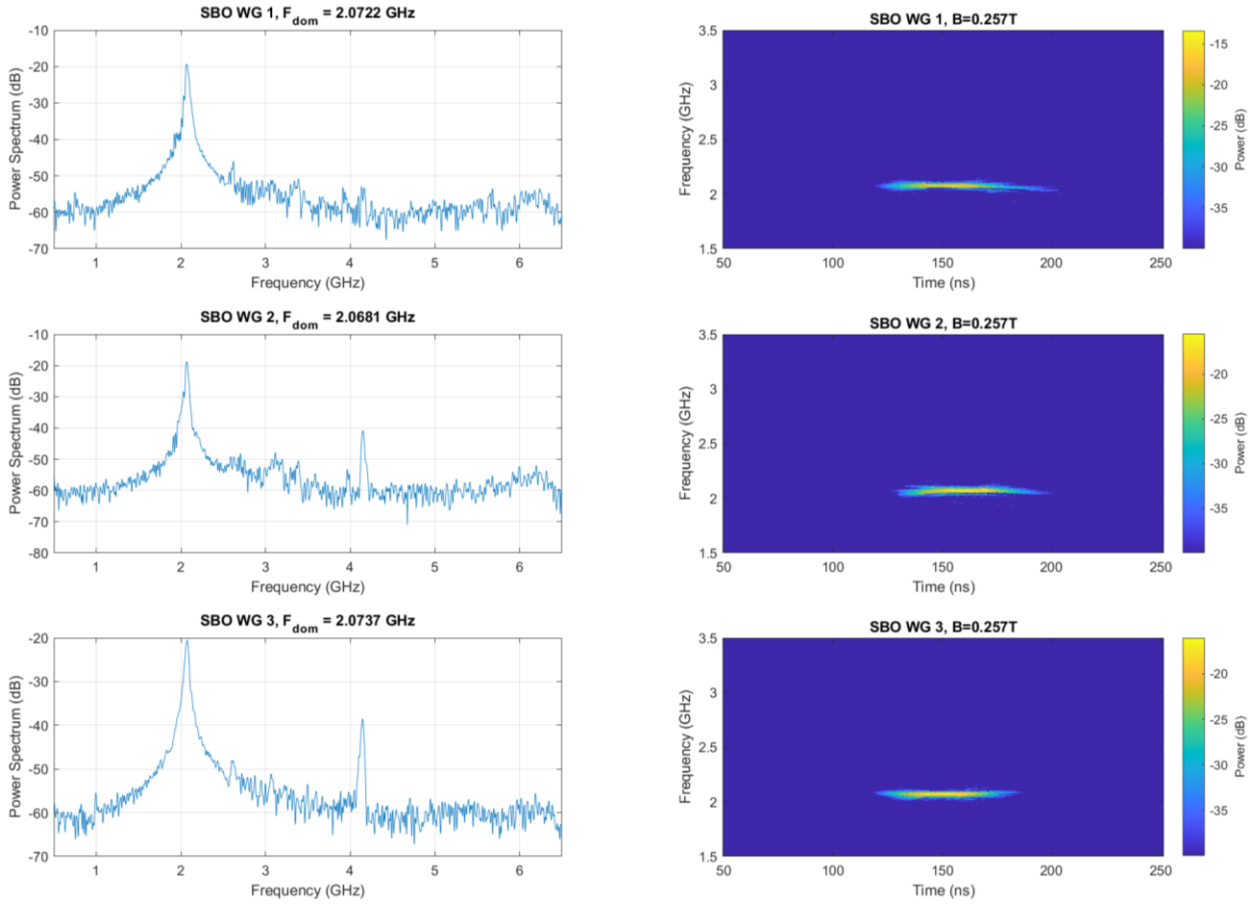

Figure 5.2: Spectral analysis of the signals from shot 17593. On the left is the Fourier transform, and on the right is the time-frequency analysis. One clear dominant mode is observed, which is identified as the 5π/6 mode.

In MELBA shot 17612, represented in Figure 5.3, there was significant competition between the 5π/6 mode and the 4π/6 mode. In this figure, the digital Fourier transform (DFT) reveals the dominant output frequency to be 1.9423 GHz. However, the presence of the 5π/6-mode as a nearly equally prevalent, simultaneous operating state is clear from the time-frequency analysis (TFA). As a result, a significant beating of the signal envelope, misshaping the output power pulse from the near-Gaussian waveform, was observed in Figure 5.1. Again, low level (-20 dB) harmonic signals are observed at ~4 GHz. With an applied field of 0.21 T, the peak instantaneous output power was 20 MW, collected at 740 A and 220 kV, resulting in a peak efficiency of 12% and producing a total of 0.59 J. These are well below the average that was observed at this specific magnetic field.

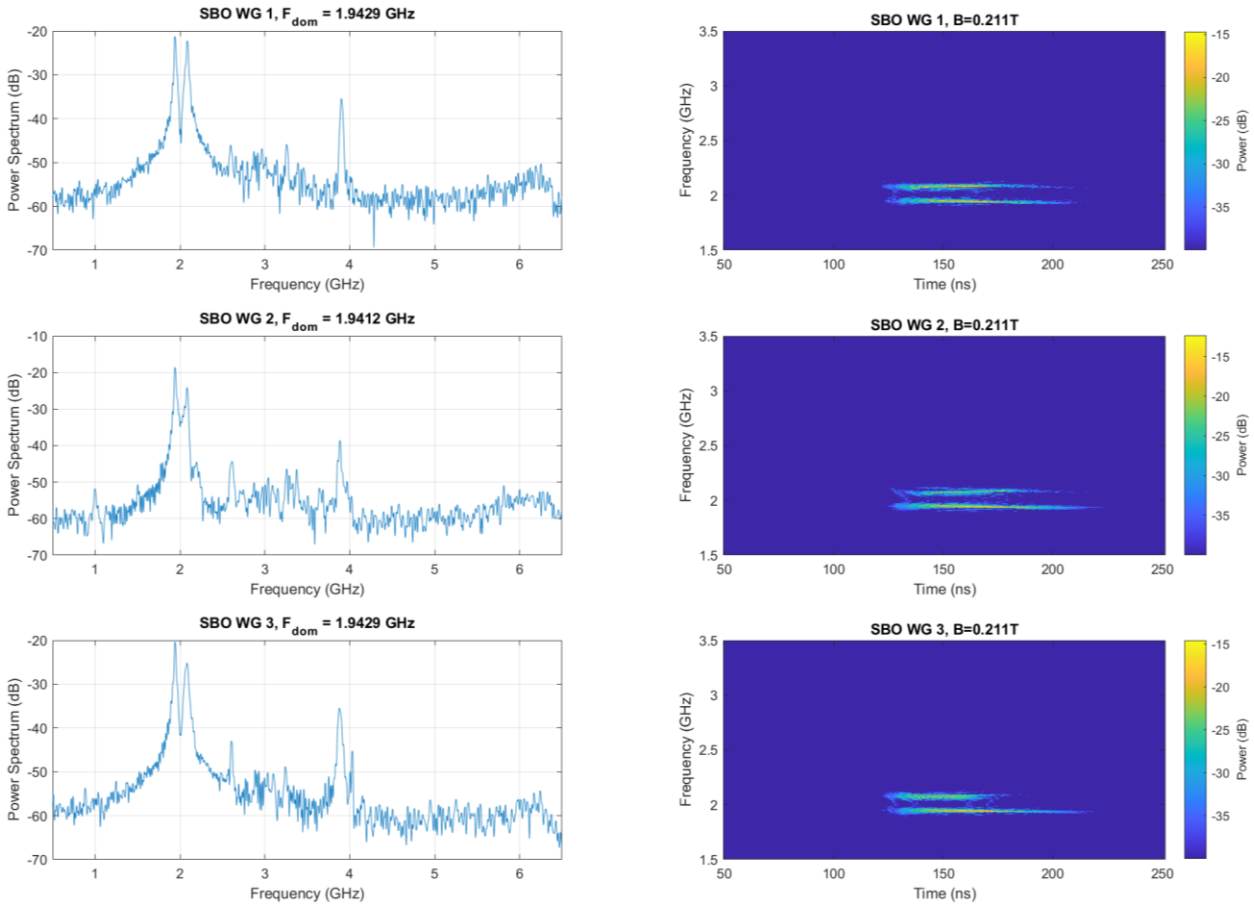

Figure 5.3: Spectral analysis of the signals from shot 17612. On the left is the Fourier transform, and on the right is the time-frequency analysis. There is substantial mode competition between the 5π/6 mode and the 4π/6 mode, with the latter considered dominant.

The frequency and power information from the ISBO experiment are displayed in Figure 5.4 and Figure 5.5. In Figure 5.4, the ellipses represent clusters of shots all taken at an individual magnetic field, where the width and height represent one standard deviation in the composite frequency and magnetic field measurements. Conversely, the crosses toward the bottom of the graph represent individual shots; not enough of them were dominant in the lower frequency 4π/6 mode to obtain adequate statistics to be expressed through ellipses. Three different configurations were tested, where the length of the coupling aperture (of length h, described in Chapter 3) that enables microwave power to transfer from the SBO cavities to its extractor was varied between 28 mm (h_1), 32 mm (h_2), and 36 mm (h_3). These will be referred to as the high Q_t, moderate Q_t, and low Q_t experiments, respectively. In the ISBO experiment, 50, 77, and 64 total shots were taken for $h=h_1, h_2, h_3$, respectively, evenly distributed among the magnetic fields tested. The cold test total quality factors (Q_t) and resonant frequencies of relevant modes are summarized in Table 5.1.

Table 5.1: Cold test quality factor and frequency of the relevant modes observed in hot test, listed as a function of the aperture length h. The π-mode quality factor is inversely proportional to h, whereas the 5π/6 mode was relatively unaffected.

h_n (mm)	5π/6-mode		π-mode	
	f (GHz)	Q_t	f (GHz)	Q_t
$h_1 = 28$	2.158	270	2.196	440
$h_2 = 32$	2.121	260	2.155	240
$h_3 = 36$	2.084	290	2.107	140

Experiments in Figure 5.4 showed that the SBO 5π/6 mode was consistently the dominant operating state. The extracted frequency from each of the three experiments is much closer to the expected 5π/6 frequency, obtained from cold test and PIC simulations, than the π-mode estimates. Notably, the π-mode was utterly absent from these experiments.

Two bounds limited the magnetic field range in this experiment. The lower bound is the minimum possible field while maintaining repeatable crowbar, and the upper bound was the maximum field limited by the largest bank charge to drive the solenoids.

At h_1, the 5π/6 mode was dominant every shot, while for h_2 and h_3 it was dominant on 74% and 75% of the shots, respectively. At h_2 and h_3, the 4π/6 mode was dominant on 20% and 15% of shots. The remaining shots (6% at h_2, 10% at h_3) demonstrated mode competition to the degree that one mode was dominant in one output, while another mode dominated in the other two outputs. For these shots, the composite frequency was bounded between the 4π/6 and 5π/6 modes. These shots are excluded from Figure 5.4 because it is not apparent they agree with the estimates from cold tests and PIC simulations, but it is only because there was significant competition between the 4π/6 and 5π/6 modes.

The output power characteristics are illustrated in Figure 5.5 and overlaid with the estimates from CST-PS simulations operating in the 5π/6-mode. The center of each circular data point is located at the arithmetic mean of the magnetic field and output power for that cluster of shots, while the vertical and horizontal error bars represent one standard deviation in the collection of these measurements. At h_1, h_2, and h_3, the highest average output powers achieved were 9.9 ± 1.7 MW, 18 ± 5.2 MW, and 37 ± 12 MW, at magnetic fields of 0.22 T, 0.21 T, and 0.21 T, respectively. The CST-PS power prediction is an overestimate because the simulations were performed at 300 kV, whereas the experiment would often fire in the range of 200 to 275 kV.

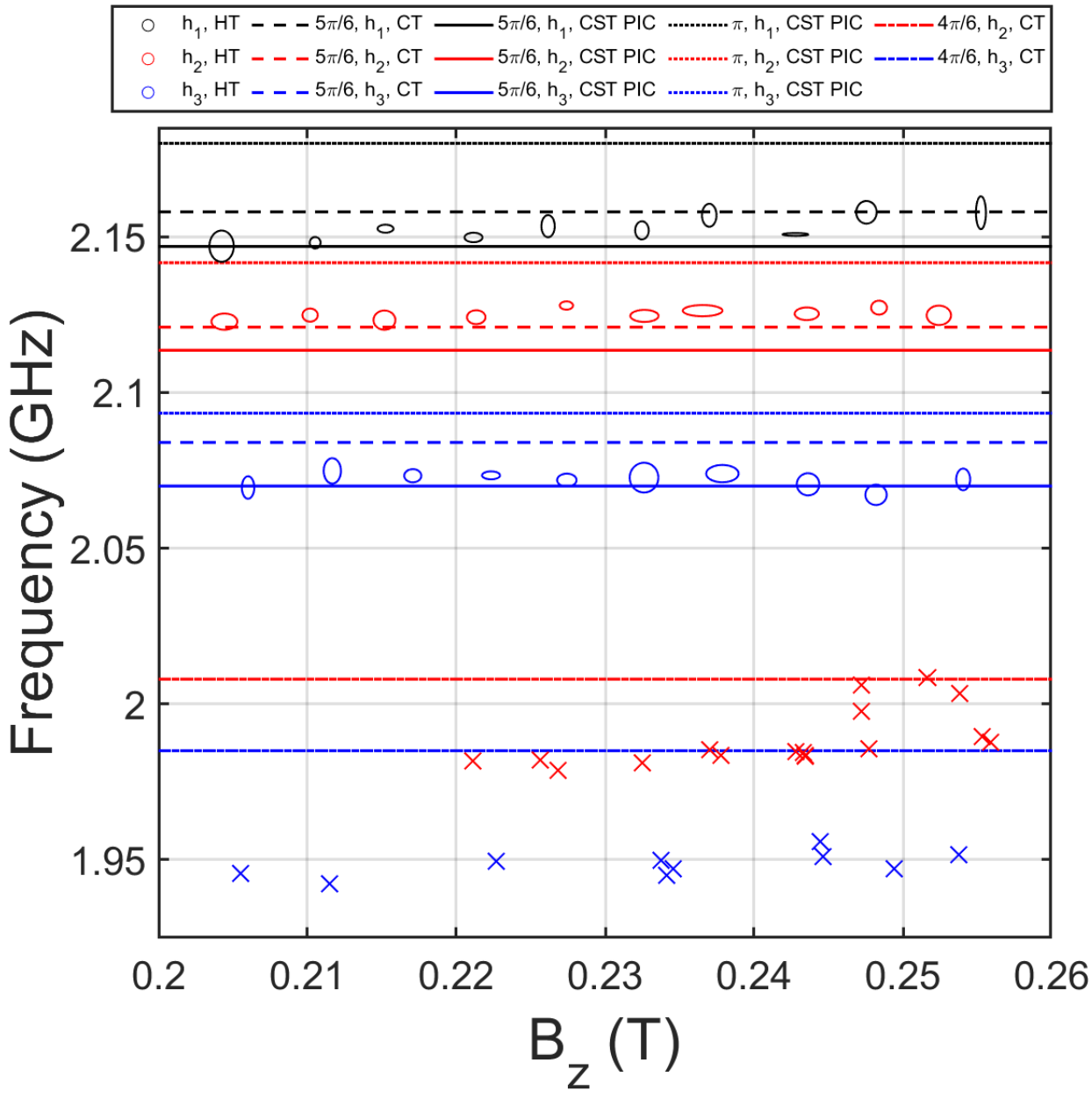

Figure 5.4: Output frequency of the ISBO as a function of magnetic field and h. Each ellipse is centered at the arithmetic mean of the magnetic field and composite frequency for a cluster of shots demonstrating dominance in the 5π/6 mode, while each X represents an individual shot that was dominant in the 4π/6 mode. The width and height of each ellipse represent the standard deviation in the magnetic field and output frequency.

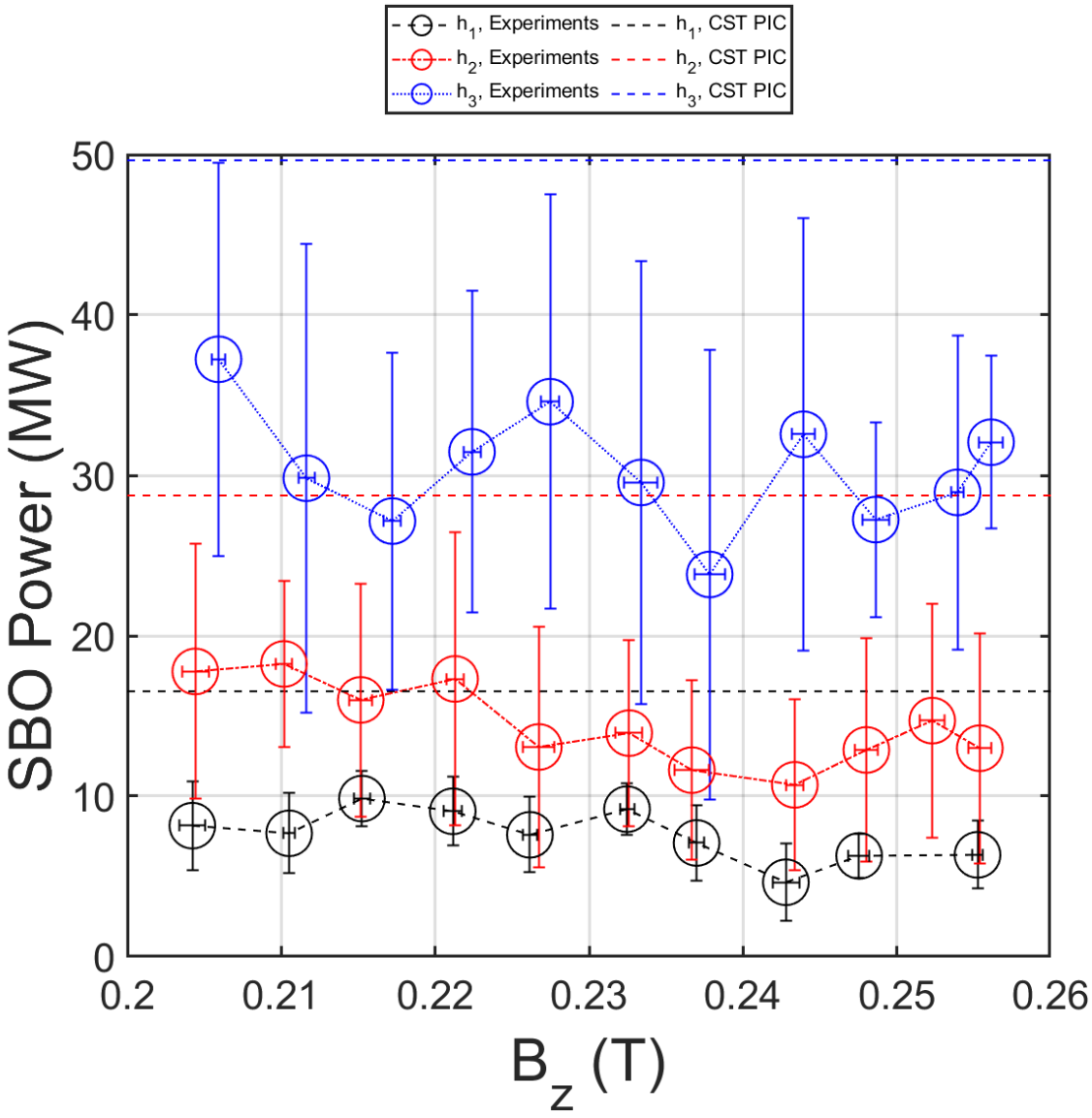

Figure 5.5: Output power as a function of the magnetic field and aperture length (h). Across all magnetic fields, the ISBO output power was proportional to the aperture length (h). CST consistently overestimated the power because the simulations took place at higher voltages.

As expected from intuition and simulation, the output power across all magnetic fields increased as h was increased from experiment to experiment. However, the 5π/6 total quality factor Q_t was relatively unchanged in these three experiments: 270 at h_1, 260 at h_2, and 290 at h_3. It is typically assumed that for magnetrons, the total quality factor is equal to the parallel sum of the extraction quality factor Q_e and the unloaded quality factor Q_u, the latter of which should be unaffected by changes made to the extractor [112]. This result is somewhat of a paradox; the increase in power extraction implies that Q_t would be inversely proportional to h. The data seems to suggest that this is the case for Q_e, but for Q_t to remain the same, this would mean that Q_u must

be linearly proportional to *h*. It is unclear why this would be the case. Perhaps how the cold test was acquired proved problematic for the 5π/6-mode (excitation of the SWS through the two boundary waveguides). The use of B-dots may be preferred to cold test the structure in individual cavities. The waveguide excitation of two cavities simultaneously may be problematic due to the mode structure of the 5π/6 mode, which has a null advancement in one of the center cavities.

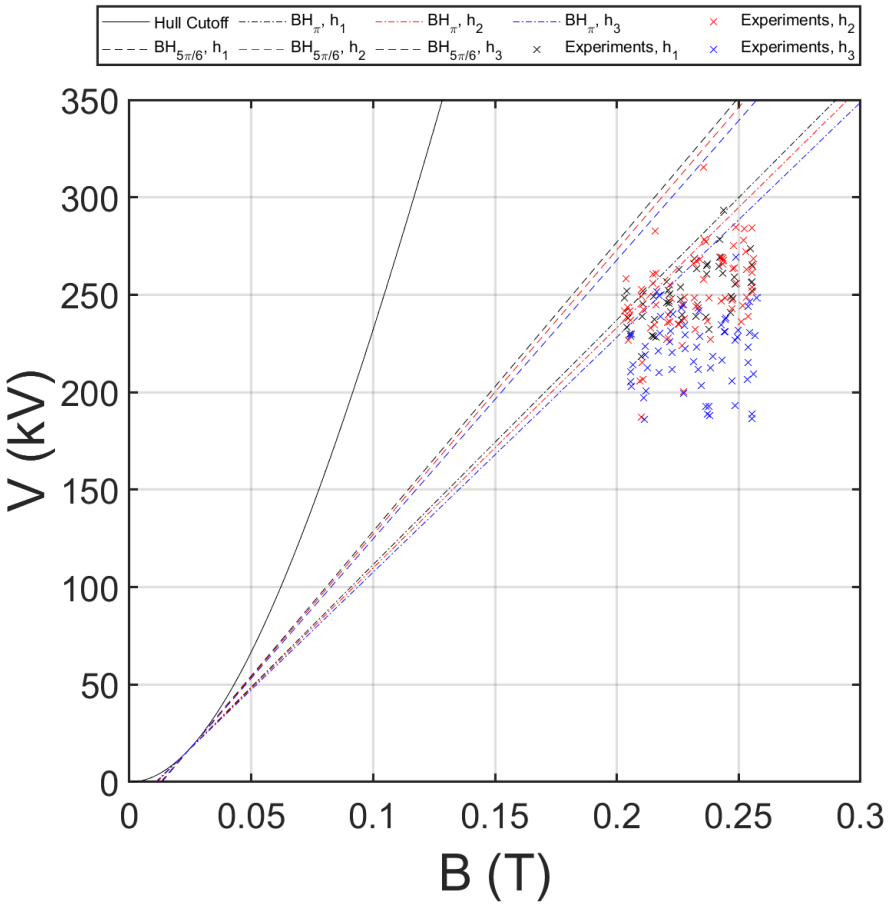

Figure 5.6: Hull cutoff and Buneman-Hartree conditions overlaid with experimental data when peak microwave generation was observed for the ISBO. Nearly every shot operated beneath the π-mode BH condition, likely because of gap closure due to plasma expansion.

The Hull Cutoff (HC) and Buneman-Hartree (BH) conditions were calculated for the HRPM geometry and overlaid with the experimental data in Figure 5.6. For the experimental data points, the value along the y-axis represents the voltage at which peak power was generated. For the vast majority of shots, peak power generation occurred at voltages well beneath the BH condition. The most likely explanation for this is gap closure due to anode and cathode plasma expansion, which effectively reduces the AK gap distance [128]. The slope of the BH condition for a planar magnetron is proportional to the AK gap distance. As cathode plasma expands toward

the anode, by the time that synchronism is achieved after more than 100 ns into the voltage pulse, the gap is likely significantly smaller than the simple distance between the anode and cathode surfaces. Meanwhile, it is worth noting that the 5π/6 mode was observed to become dominant in CST-PS simulations at -300 kV, 0.17 T, and the π-mode demonstrated optimized power generation at -300 kV, 0.24 T (Chapter 3), which both agree well with the BH conditions for these modes.

5.2 HRPM Operation

With a fundamental understanding of the ISBO characteristics, it is now appropriate to compare the HRPM geometry where the LBO modulates the electron hub into spokes as they flow in the direction towards the SBO. Figure 5.7 illustrates MELBA shot 17744 from the low Q experiment, where voltage, current, SBO output power, and uncalibrated LBO pulse envelope are overlaid. With an external magnetic field of 0.28 T, the peak output power from the SBO is 38 MW, at which instant the voltage and current are 260 kV and 1.3 kA, resulting in a peak efficiency of 11%. The LBO and SBO FWHM for this shot were 23 ns and 44 ns, respectively, and the total energy extracted was 1.2 J. Power extraction was not implemented on the LBO. In this shot, the LBO and SBO begin to oscillate and peak at nearly identical instants.

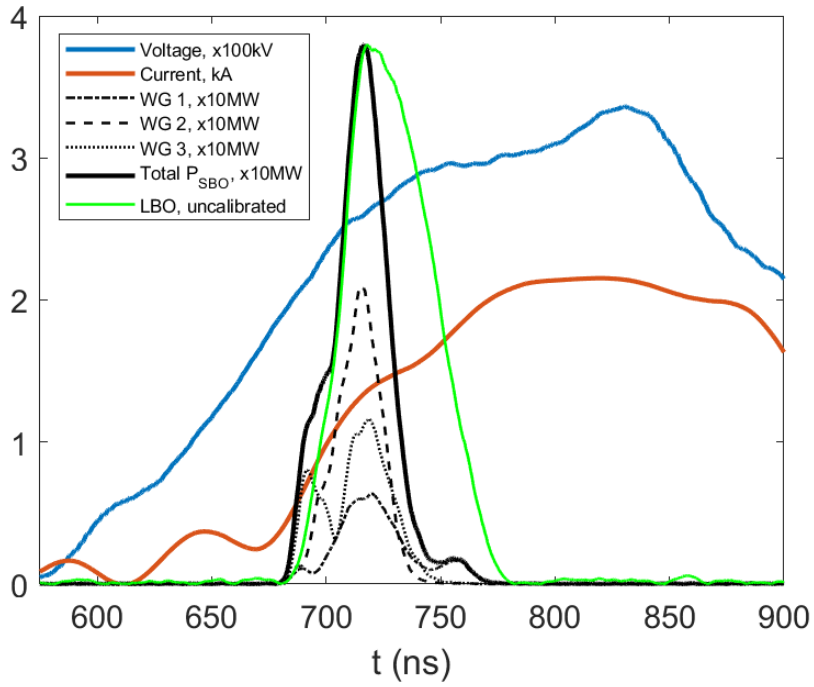

Figure 5.7: MELBA shot 17744 overlaying voltage, current, SBO output power, and LBO pulse envelope. This shot utilized the low Q experiment ($h=h_3$) with the tuner length set to 4.75 cm (L=4.75 cm). The peak output power was 38 MW, at which time the voltage and current were 260 kV and 1.3 kA.

Each of the three LBO cavities were probed by individual B-dot probes, which were sampled directly by a 6-GHz, 20-GSa/s Agilent 58455A oscilloscope in the same manner as the SBO. Time-frequency analysis of these signals reveals the spectral components in time and the dominant frequency, as shown in Figure 5.8. The LBO signal frequencies from the various cavities were in excellent agreement, separated by less than 1.5 MHz at most on shot 17744, and this was true in general. The LBO rarely demonstrated mode competition. As it was tuned from shot to shot, it reliably produced a single tone in agreement with the simulation and cold test results (Chapter 3), where the frequency was a linear function of the tuner length (*L)*. Shot 17744 is an example that demonstrated harmonic frequency locking, where the SBO resonated at a dominant frequency very close to the second harmonic of the LBO. The arithmetic mean frequency, or composite frequency, of the LBO signals was 1.0529 GHz, and thus its harmonic was 2.1057 GHz.

Meanwhile, the SBO composite frequency was 2.1047 GHz, which is within 1 MHz of the composite LBO harmonic frequency, and is in good agreement with the expected output frequency of the π-mode in the low Q experiment. As discussed in 5.1 and illustrated in Figure 5.4, the ISBO did not produce any shots where the dominant frequency was near 2.1 GHz, which suggests the conclusion that the introduction of the LBO is enforcing this locked state. The primary caveat given here is the ISBO could not be tested at a magnetic field any higher than 0.26 T. In contrast, shot 17744 had an applied magnetic field of 0.28 T. The introduction of the LBO and its tuner altered the magnetic field profile within the magnetron such that higher fields could be achieved. Nonetheless, the π-mode was not even observed as a competing mode in the ISBO experiments; after introducing the LBO and increasing the magnetic field by 10%, the SBO is suddenly capable of resonating at a frequency much closer to its π-mode. This phenomenon justifies the investigation of the role the LBO plays in determining the SBO dominant frequency, which will be discussed in subsequent sections of this chapter.

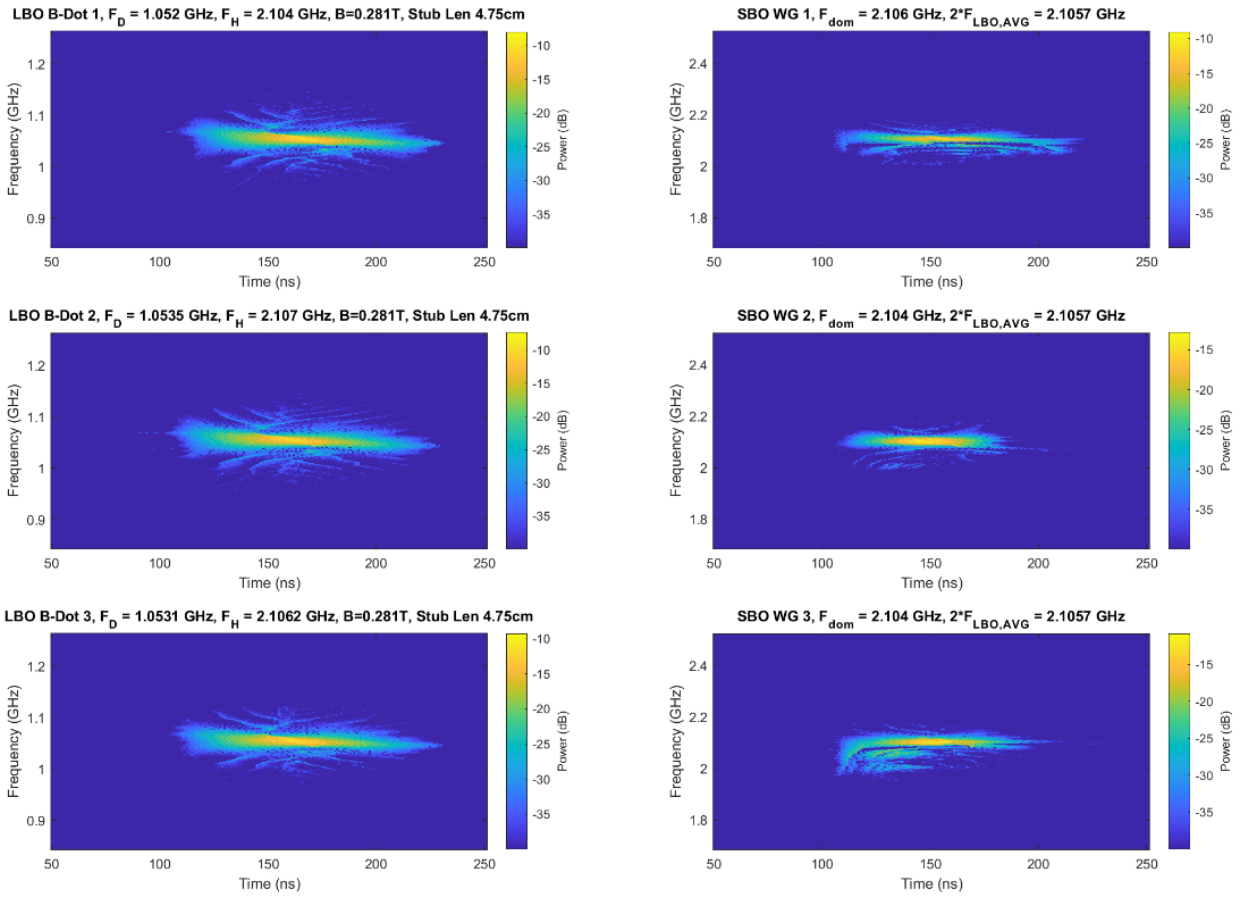

Figure 5.8: Time-frequency analysis of the LBO and SBO signals from MELBA shot 17744, demonstrating spectral purity, minimal mode competition, and harmonic frequency locking, where the SBO dominant frequency was equal to the second harmonic of the LBO dominant frequency.

Current and voltage characteristics are compared between the ISBO and HRPM low-Q experiments in Figure 5.9. In general, the HRPM operated at higher voltage and current; several reasons contribute to this. First, the HRPM typically reached peak power generation later in time than the ISBO. The voltage rise time t_{vr} is defined as the time between the instances where 10% of maximum voltage and 90% of maximum voltage are reached, whereas the time to peak power t_{pk} is defined as the time between the instances of 10% voltage rise and peak power generation. In each experiment, the average behavior of the SBO was to reach peak microwave generation while the voltage was still ramping upwards, whether in the HRPM or isolation. However, since peak microwave power for the HRPM was observed later in time compared with the ISBO, it was firing even later on the voltage rise, resulting in additional gains in voltage and current. All of this information is summarized in Table 5.2, along with the magnetic field for each experiment. Another reason the current at peak microwave extraction is elevated in the HRPM experiment

would be the presence of the LBO, which would draw current itself and was very often oscillating at this instant.

Why would the HRPM take longer to reach peak power generation than the ISBO? The simplest explanation is that the magnetic field in the HRPM experiments was higher than in the ISBO experiments. A high magnetic field was also observed to delay startup time in CST-PS simulations of the device and observed in prior experiments [54]. At the same time, the introduction of the LBO often substantially increased the SBO pulse length, effectively increasing the time between startup and the generation of peak power, which will be discussed shortly.

Table 5.2: The voltage rise time t_{vr}, time to peak power t_{pk}, and magnetic field B_z for each of the high Q_t (h_1), moderate Q_t (h_2), and low Q_t (h_3) experiments of the ISBO and HRPM. In general, the magnetron began oscillations and reached peak microwave generation before the voltage flat top had been reached.

h_n (mm)	Quality Factor	t_{vr} (ns)		t_{pk} (ns)		B_z (T)	
		ISBO	HRPM	ISBO	HRPM	ISBO	HRPM
$h_1 = 28$	High	158 ± 17	163 ± 29	130 ± 18	155 ± 31	0.205-0.255	0.308
$h_2 = 32$	Moderate	146 ± 18	148 ± 21	111 ± 21	129 ± 19	0.205-0.255	0.284
$h_3 = 36$	Low	156 ± 23	163 ± 27	106 ± 22	127 ± 20	0.205-0.255	0.283

The HRPM and ISBO output power and efficiency in the low Q_t experiment (where the best device performance was observed) are both displayed in Figure 5.10. Across all shots in the low Q_t experiment, the HRPM generated an average power of 22 ± 7 MW at 7.3 ± 2.4% efficiency, whereas the ISBO produced 30 ± 11 MW at 15 ± 6% efficiency on average. Not only did the ISBO operate at higher power on average, but it also was capable of reaching much higher peak powers (some shots exceeded 50 MW). In comparison, the HRPM did not surpass 40 MW operation. It is conjectured that this is an artifact of the beam kinetics impinging upon the SBO. In the HRPM, the SBO receives a heavily modulated hub of electrons, possibly making it more difficult to modulate at its base frequency to reach the same peak power as when the electron hub was unmodulated. Because the average output power of the ISBO was higher and its input cathode power was lower when compared with the HRPM, it reached higher total efficiencies.

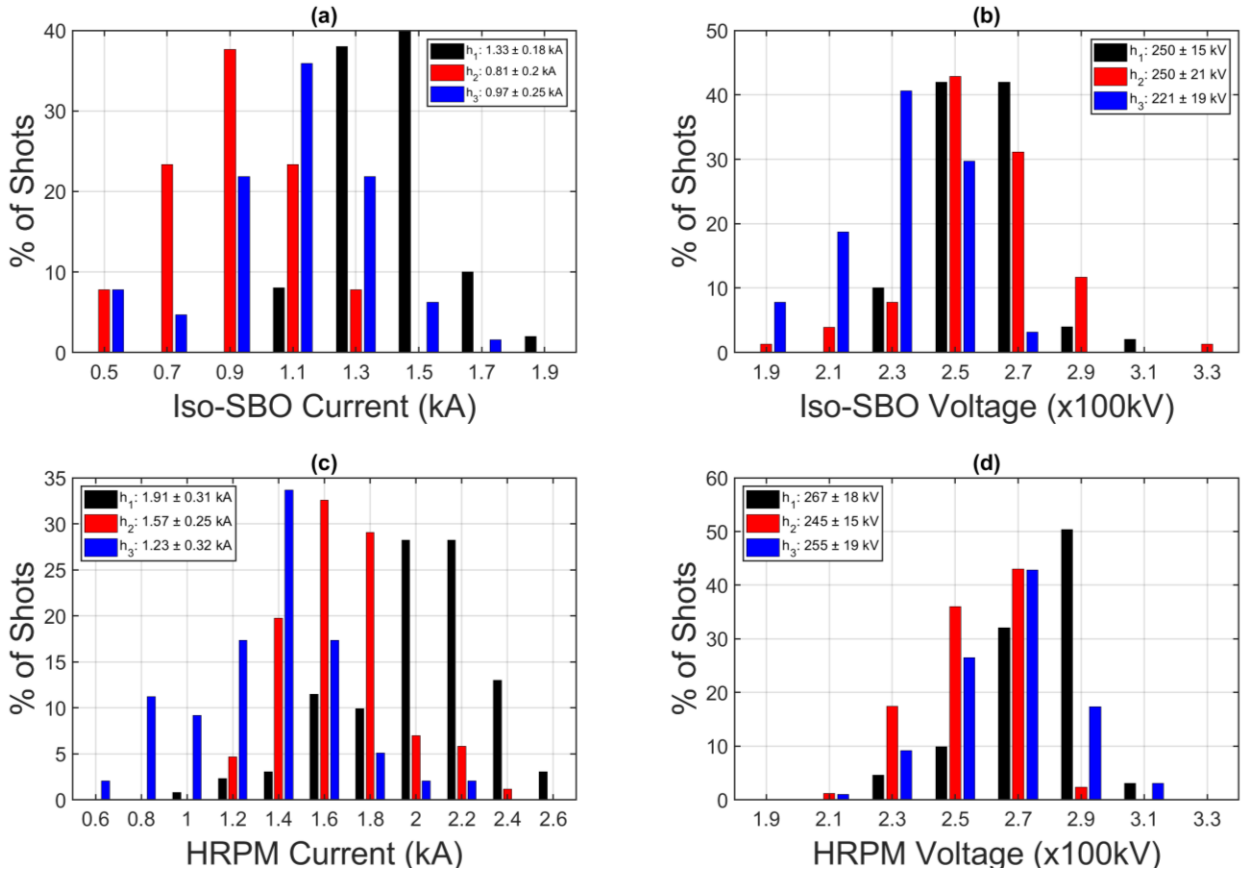

Figure 5.9: Current in the ISBO (a) and HRPM (c) as a function of the quality factor; bin width is 0.2 kA. Voltage in the ISBO (b) and HRPM (d) as a function of the quality factor; bin width is 20 kV. The axis label indicates the high point in the bin range. While both the ISBO and HRPM would reach peak power generation on the voltage rise, the HRPM generally arrived at this point later in time, thereby operating at higher currents and voltages on average.

Another factor that reduces the HRPM efficiency is the LBO itself would draw current, but none of its microwave energy was extracted. Overall, the efficiency is low compared to other relativistic magnetrons [13] and lower than those expected from ICEPIC simulations at these magnetic field ranges. It is suspected that a large portion of the current exits the interaction space as endloss, which was observed to damage or destroy components in the chamber such as cables. The PIC models of the ISBO do not demonstrate endloss currents, and as a result, the current drawn by the SBO is less than 500 A. If this prediction is accurate, it may be assumed that roughly half of the current in the experiments is endloss, indicating that electronic efficiency, which only considers confined electrons, may be twice as high as the total efficiency.

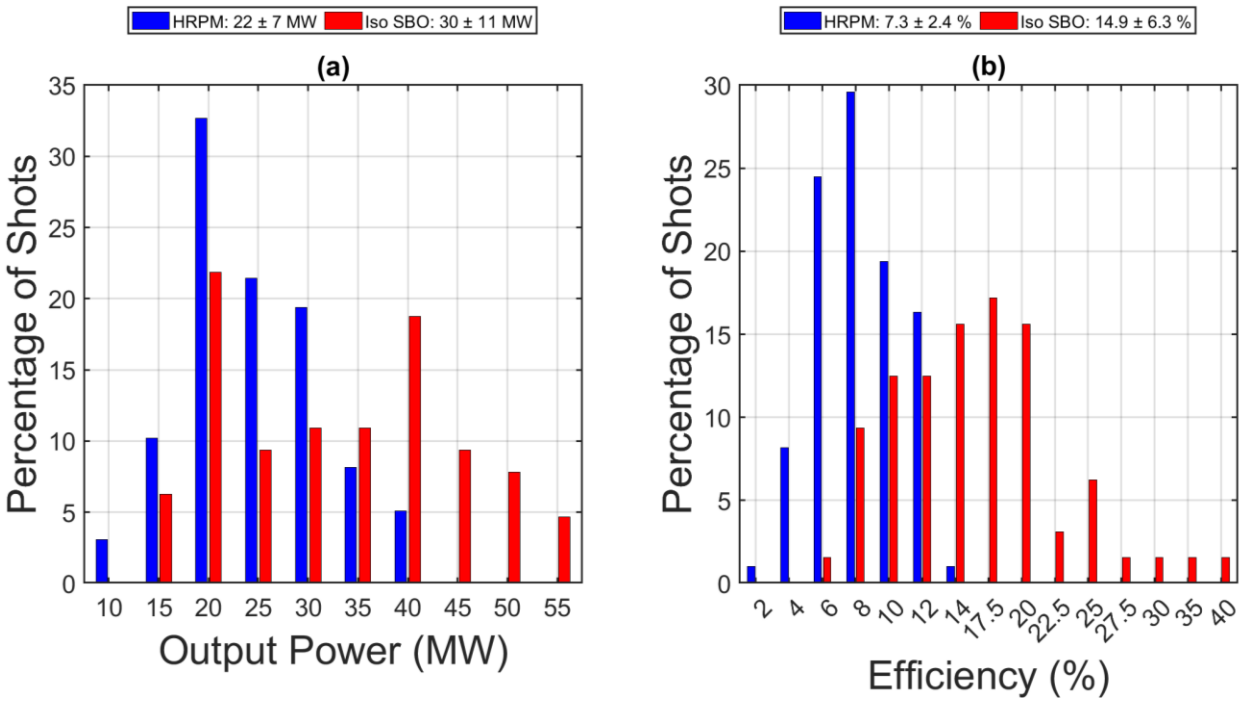

Figure 5.10: (a) Histogram of output power comparing operation between the ISBO and HRPM in the low Q experiment. The ISBO operated at higher power on average. Bin width is 5 MW, and the axis label indicates the upper end of the range (e.g., first bin is 5 to 10 MW). (b) Histogram of efficiency comparing operation between the ISBO and HRPM in the low Q experiment, where the axis label indicates the upper end of the range (e.g., first bin is between 0% and 2%). Because the HRPM was observed to operate at higher voltage and current and produced less output power, the efficiency is substantially lower than the ISBO.

Table 5.3: Startup time t_s for the ISBO and HRPM and startup time t_s and pulse length τ for the LBO. The overlap percentage describes the average fraction of the SBO pulse where the LBO is also under operation; if the LBO starts and ceases operation before and after the SBO, respectively, then this quantity becomes 100%.

h_n (mm)	Quality Factor	t_s (ns), ISBO	SBO t_s (ns), HRPM	LBO t_s (ns)	LBO τ (ns)	Overlap Pct. (%)
$h_1 = 28$	High	114 ± 17	122 ± 31	129 ± 28	83 ± 17	94 ± 10
$h_2 = 32$	Moderate	93 ± 21	106 ± 19	106 ± 19	120 ± 25	97 ± 6
$h_3 = 36$	Low	88 ± 21	100 ± 17	106 ± 18	89 ± 17	91 ± 7

Table 5.3 summarizes the various startup times for the ISBO and HRPM experiments as a function of the aperture length *h or Q*. The SBO demonstrated slightly longer startup times in the HRPM than in isolation, and on average, the LBO started less than 10 ns after the SBO. The LBO pulse length was roughly the same for the high Q_t (h_1) and low Q_t (h_3) experiments but was substantially larger in the moderate Q_t experiment (h_2). In this same experiment, the HRPM exhibited nearly identical startup times from the LBO and SBO, and the largest fraction of simultaneous operation was observed between LBO and SBO. It is possible that this specific

quality factor causes these effects or that the particular tuning range for the moderate Q_t experiment was beneficial to LBO operation. Most importantly, for the vast majority of HRPM shots, the LBO and SBO demonstrated startup at nearly the same time, and the LBO continued to operate for over 90% of the SBO power pulse.

As mentioned previously, the HRPM often demonstrated significantly larger SBO pulse lengths than the ISBO. Figure 5.11 illustrates the microwave pulse lengths, peak power, and energy produced of the ISBO and HRPM for the three different SBO quality factors to elucidate the effect of pulse shortening across the experiments. It is not uncommon for relativistic magnetrons that are pulse-shortened by AK gap closure to experience shorter pulses if they are designed for higher frequencies, nor is it unusual for output power to decrease as pulse length increases [129], [130]. As described by Price et al., the microwave power P and pulse energy E are expected to scale with the pulse length τ as $P \alpha \tau^{-(n+1)/n}$ and $E \alpha \tau^{-1/n}$, where n is assumed 1.5 for a Child-Langmuir diode. Counterintuitively, to reach higher power and energy per pulse, shorter pulses are desired.

The HRPM, however, demonstrated some exciting behavior that does not obey these scaling laws. In Figure 5.11, the Price scaling laws for energy and power are fit to the results from the ISBO. In the high Q_t and low Q_t experiments, the HRPM-SBO pulse lengths were an average of 72 ± 15 ns and 77 ± 17 ns, which corresponds to a significant increase of 61% and 52% from the average ISBO measurements, respectively. If it is assumed that $P \alpha \tau^{-5/3}$, then it is expected that the average output power would drop from 7.6 MW → 3.5 MW (high Q) and 30.4 MW → 15 MW (low Q), corresponding to a decrease in output power of 54% (high Q_t) and 50% (low Q_t), respectively. The HRPM demonstrated performance above these expectations, with average measurements of 5.2 ± 2.6 MW (32% decrease) and 22 ± 7 MW (28% decrease) in the high and low Q_t experiments, respectively.

The gains made in terms of the output energy were more significant. Under the assumption that $E \alpha \tau^{-2/3}$, the increase in pulse length in the HRPM compared with the ISBO would result in an expected decrease of energy by 27% and 24% for the high and low Q_t experiments, respectively. The measurements show that increasing the HRPM pulse length had little effect on the output energy in the high and low Q_t experiments, where the percent change was -7.5% and 1.3%, respectively.

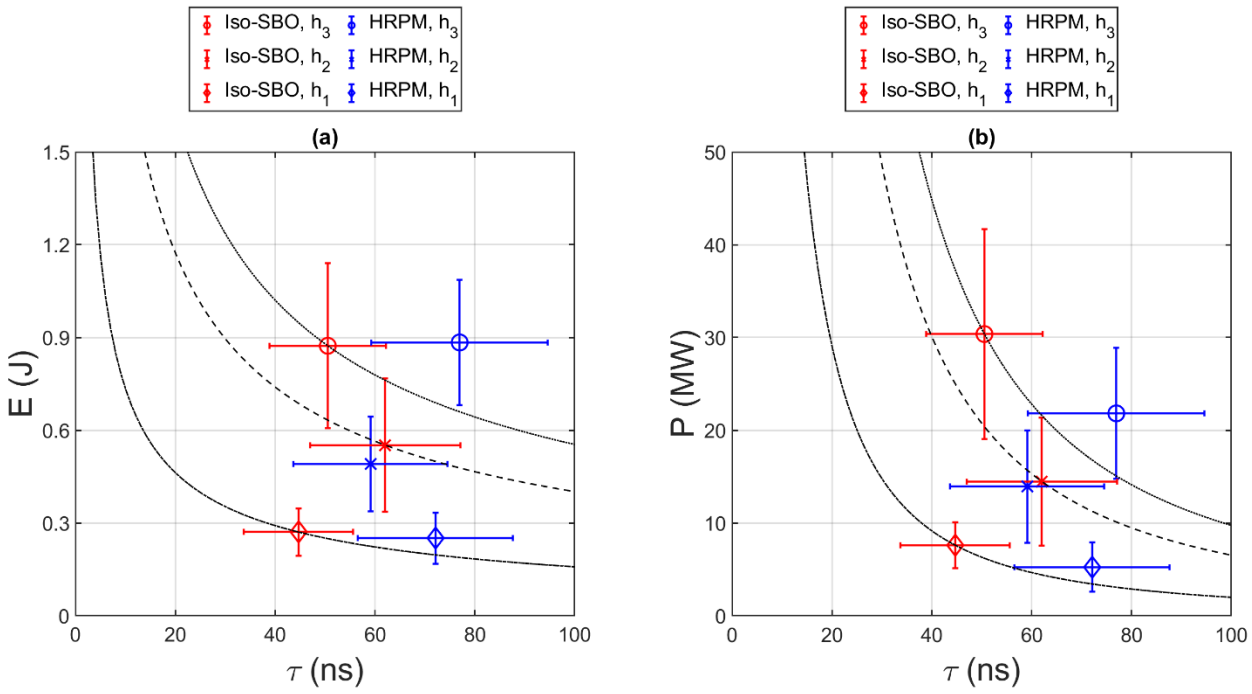

Figure 5.11: (a) Output energy from the SBO as a function of the pulse length τ and the aperture length h for the ISBO and HRPM. (b) Output power from the SBO as a function of the pulse length τ and the aperture length h for the ISBO and HRPM. In each figure, the scaling laws are applied from Price et al. [129], [130] and are fit to the ISBO measurements.

The moderate Q_t experiment was quite different from the other two. Shorter pulses were observed, decreasing from 62 ± 15 ns to 59 ns ± 15 ns in the ISBO and HRPM, respectively. The expectation is that this would result in an increase in power and energy in the HRPM, but the opposite was observed in both cases; the output power and energy were statistically nearly equal with 15 ± 7 MW (ISBO) to 14 ± 6 MW (HRPM), and 0.55 ± 0.22 J (ISBO) to 0.49 ± 0.15 J (HRPM). It is difficult to understand why the HRPM would demonstrate very similar changes in performance for the high and low Q_t experiments compared with the ISBO, but remain relatively unchanged in the moderate Q_t experiment. The large LBO pulse lengths in the moderate Q experiment raise suspicion the LBO may not operate at the same power level across all three experiments, which may affect the results seen in Figure 5.11. Extraction from the LBO and examination of its operation in isolation in a subsequent investigation would be necessary for identifying the root cause of these variations.

The following conclusion in regards to pulse shortening can be made. Suppose the device is indeed space charge limited. In that case, it appears the introduction of the LBO has the potential to increase SBO pulse lengths at no expense to the output energy production and a reduced cost of the output power compared to other relativistic magnetrons. For worst-case parameters in the

moderate Q_t experiment, the introduction of the LBO forms a multi-frequency magnetron at limited expense of SBO pulse lengths, output power, and energy. However, the critical point is that the addition of the LBO can lock the SBO into the pi-mode, the most desired mode for applications (shown in Section 5.3).

5.3 HRPM Quality Factor Study

One of the reasons the HRPM [65] was originally designed was to investigate the harmonic frequency locking phenomena (and mode-locking) observed in prior experiments of the Multi-Frequency Recirculating Planar Magnetron (MFRPM) [131]. The MFRPM also had an LBO and SBO intended to operate near 1 GHz and 2 GHz, respectively. In MFRPM experiments, the SBO frequency locked to the second harmonic of the LBO, generating a tone not observed in isolated-SBO experiments. On the other hand, the LBO was observed to operate in the same mode in the MFRPM as it did in isolation.

It was hypothesized that the system behaved as a damped, driven harmonic oscillator, where the locking mechanism was the harmonic content of the electron spoke modulation as the LBO-modulated beam propagated toward the SBO, thereby seeding operation at the LBO harmonic frequency. In an Adler-like master-slave locked state [132], the driving oscillator is the LBO, the driven oscillator is the SBO, and the excitation frequency is the second harmonic of the LBO frequency. When operating independently, the driven oscillator will operate at a mode-dependent, free-running frequency. If the SBO is driven at its desired π-mode frequency, it is expected to deliver a local maximum in output power. If the SBO is driven slightly off the resonant peak, it is expected to oscillate at the excitation frequency but with reduced power generation. The quality factor Q_t of the SBO is inversely proportional to the bandwidth of an individual mode. Therefore the harmonic locked bandwidth is predicted to increase as the quality factor is decreased. Thus, in this dissertation, the HRPM was designed with a frequency-adjustable LBO, and tested at several values of SBO π-mode quality factor. These figures of merit are listed in Table 5.1.

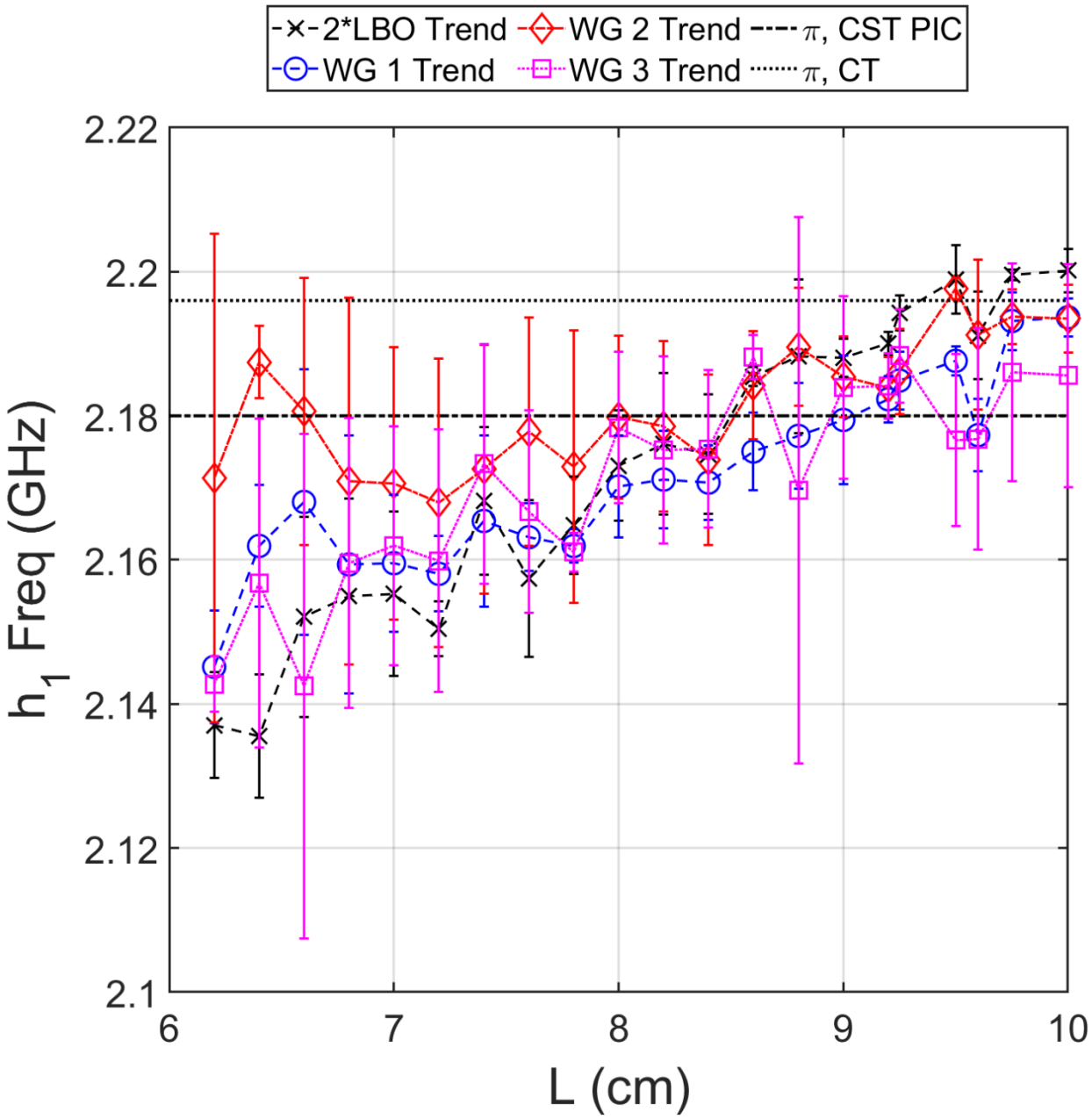

Figure 5.12: LBO harmonic frequency and SBO output frequency from the three different waveguides in the high Q_t experiment, overlaid with the π-mode frequency from experimental cold test as well as PIC simulations in CST. Maximum SBO output power is observed at L = 8.4 cm (SBO composite frequency of 2.173 GHz ± 7.1 MHz), which is within 10 MHz agreement of the CST-PS π-mode free-running frequency (2.180 GHz).

The frequency results of the high, moderate, and low Q_t experiments are displayed in Figure 5.12, Figure 5.13, and Figure 5.14, respectively. In each case, a series of shots were taken across multiple values of the tuner length L. The displayed data points for each output waveguide are centered at their averages for that tuner position. The LBO harmonic frequency was sampled directly using microwave B-dots, and the dominant frequency from an individual shot was

obtained through Fourier analysis. A single, composite LBO frequency was determined for each shot as the arithmetic mean of the dominant frequency retrieved from all available B-dot signals. This distinction is made because across the three quality factors tested, different amounts of B-dot signals were sampled. In the high Q_t experiment, only the middle cavity was probed. In the moderate Q_t experiment, all three cavities were sampled, but the two outer cavities' B-dot probe signals failed midway through the experiment because stray electrons destroyed the cables connecting them to the scope. In the low Q_t experiment, all three cavities were probed successfully on every shot. Thus, for a specific value of L, the displayed data point is the average harmonic of the composite frequencies retrieved from the LBO.

The frequency results of the high Q_t experiment are displayed in Figure 5.12, for which 131 shots were collected. As expected from the microwave cold test, the LBO harmonic frequency was increased as L was increased, which was observed across all experiments. Figure 5.12 demonstrates the most erratic results from the three experiments, where the locked range is the least clear and shot-to-shot variance was the greatest. It appears that SBO waveguide (WG) 1 and 3, the two outer waveguides, tracked the closest to the LBO harmonic frequency, while the central WG 2 had a greater tendency to operate at a higher frequency. The SBO error bars in the range of L from 6.2cm to 7.6 cm were particularly large, and the averages typically don't agree with any mode observed in cold test, because each waveguide would often demonstrate dominance at either the LBO harmonic or near the π-mode cold test frequency. This behavior was inconsistent, resulting in large error bars with the average frequency bounded between the LBO harmonic and the π-mode cold test frequency. Based on the overall agreement between each waveguide average and the LBO harmonic frequency, the locked range is determined to be from L = 7.8 cm → 8.6 cm (2.165 → 2.182 GHz). Still, even within this range, numerous shots are not locked, which results in significant variance. Within this locked range, maximum power generation is observed at L = 8.4 cm (see Figure 5.15), which agrees within 10 MHz of the π-mode free-running frequency observed in PIC simulations of the device. Thus, it is concluded that maximum power output was observed when the π-mode was driven on resonance in the high Q_t experiment.

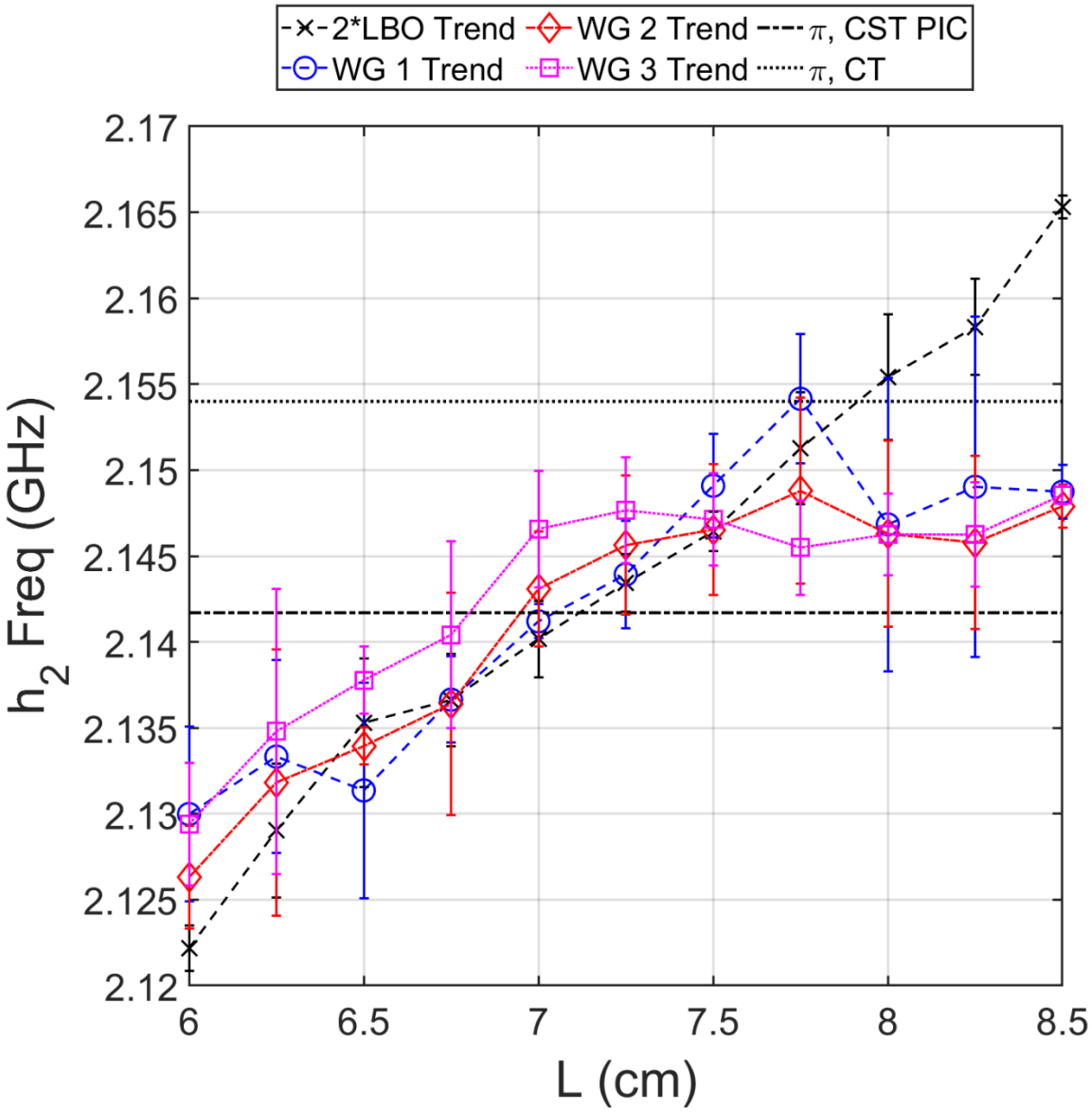

Figure 5.13: LBO harmonic frequency overlaid with SBO output frequency for the three separate waveguides in the moderate Q_t experiment, overlaid with the π-mode frequency from the experimental cold test and PIC simulations in CST. Maximum SBO output power observed at L = 7.5 cm (SBO composite frequency of 2.148 GHz ± 2.8 MHz), where the SBO frequency is between the CST-PS π-mode free-running frequency (2.1417 GHz) and the π-mode cold test value (2.154 GHz).

A total of 88 shots were taken in the moderate Q_t experiment, and the dominant LBO and SBO frequencies are displayed in Figure 5.13. Improved consistency was observed from shot to shot, resulting in significantly shorter error bars. The LBO frequency demonstrated a linear correlation with *L,* and the average SBO frequency of each waveguide was bound to the LBO harmonic much more consistently. This trend improved from the high Q_t experiment, where apparently the WG 2 oscillated independently from WG 1 and WG 2. The improved overall coherence of the SBO in this experiment indicates the lower quality factor enabled stronger

coupling between the LBO and SBO. In this case, the locked range is L = 6.5 cm → 7.75 cm (2.134 GHz → 2.149 GHz). Maximum power output was observed at L = 7.5 cm (see Figure 5.15), where the SBO frequency was directly between its π-mode cold test frequency and the free-running π-mode frequency that was observed in PIC simulations. Thus, just as in the high Q_t experiment, it is concluded that maximum power output was observed when the SBO was driven at its free-running π-mode frequency. The transition out of the locked range, observed from L = 8 cm → 8.5 cm, is also worth noting. From L = 8 cm → 8.5, the average frequency from each waveguide remains close to the measured frequency when maximum power output was observed (L = 7.5 cm). At the specific values of L = 8 cm and 8.25 cm, the error bars for WG 1 and 2 are relatively large, indicating that some shots were still locking to the LBO harmonic. Finally, once L = 8.5 cm, the structures are entirely unlocked, where the SBO continues to operate in the π-mode, but the LBO harmonic frequency is over 15 MHz larger. Given that π-mode operation was not observed in the ISBO experiments (albeit at lower magnetic fields), this implies the LBO can influence the mode of operation in pi-mode even in the absence of harmonic frequency locking. It is also interesting that locked operation ceases if L is tuned slightly higher than the point of maximum power generation L_{max}, but the LBO harmonic influences the SBO for a more extensive range if $L < L_{max}$. It is hypothesized that the SBO makes a transition into the neighboring 5π/6 mode, whose free-running frequency was observed to be 2.126 ± 0.002 GHz, and its $\underline{Q_t}$ is nearly identical to that of the π-mode (Table 5.1) in this experiment. For $L > L_{max}$, there is no neighboring mode to be excited because the π-mode is the highest frequency mode on the fundamental bandpass.

Frequency results from the low Q_t experiment are given in Figure 5.14, where the most stable and consistent adherence of the SBO frequency to the LBO harmonic frequency was observed. This data set consists of a total of 93 shots, where nearly every shot demonstrated harmonic locking. Seven outlier shots are shown in Figure 5.14, which exhibit dominance in the 4π/6-mode in the rightmost waveguide (WG 3). Out of these seven shots, two of them also displayed 4π-6 mode dominance in the central waveguide (WG 2). The locked range is from L = 2 cm → 4.75 cm (2.072 – 2.105 GHz), the largest of the three experiments. Unlocked operation occurs at L = 5 cm, where the SBO seems to enter a similar transition into unlocked operation in the π-mode that was observed in the moderate Q_t experiment. Unfortunately, L was not extended to higher values, so it is impossible to say if this complete transition was made. Maximum power extraction in the low Q_t experiment is observed for L = 4.5 cm, where the SBO experimental

frequency falls between the π-mode cold test frequency and the free-running π-mode frequency obtained in PIC simulations. Similar to the moderate Q_t experiment, locked operation falls away quickly when $L > L_{max}$.

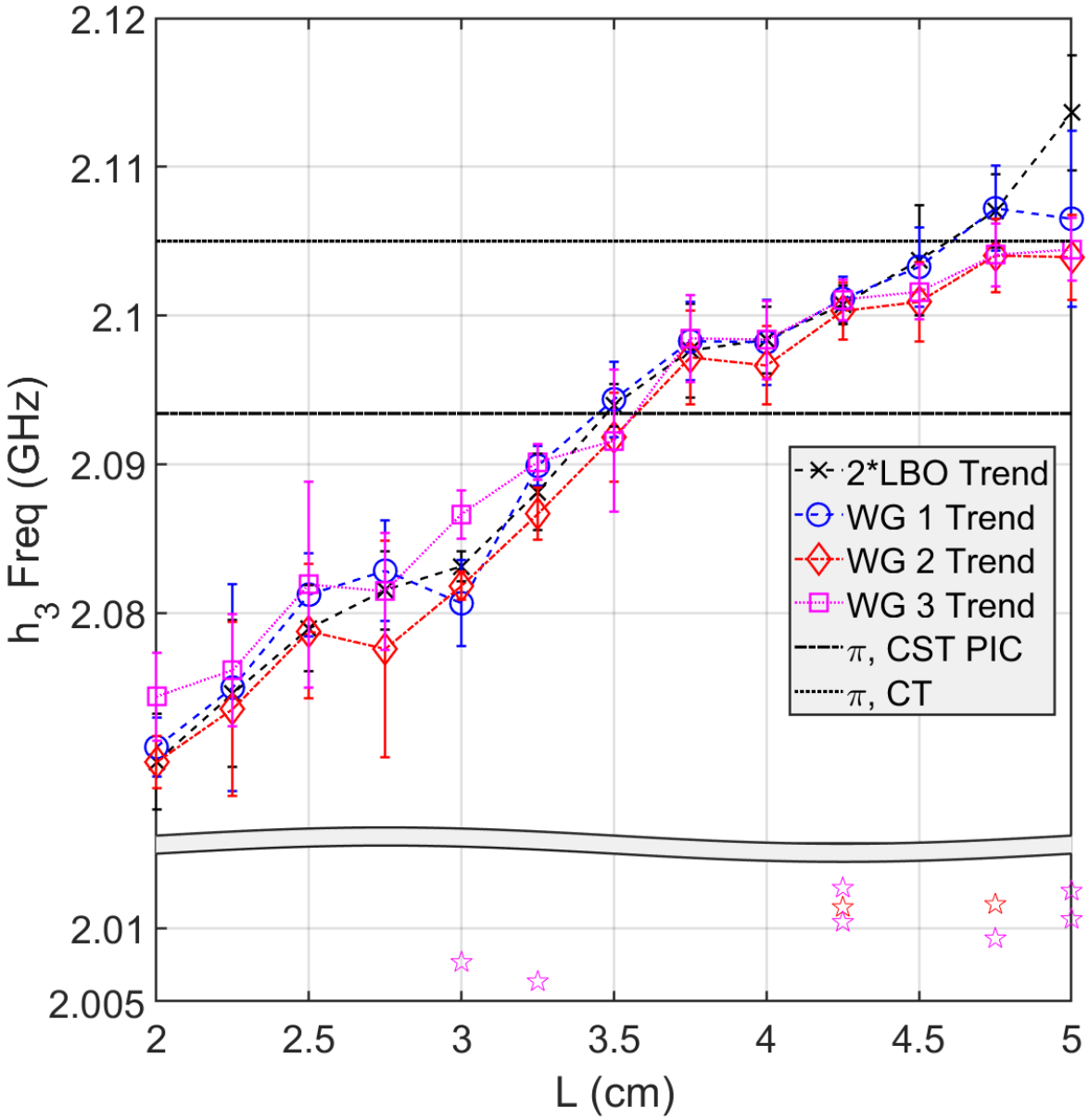

Figure 5.14: LBO harmonic frequency overlaid with the three SBO waveguide outputs in the low Q_t experiment, overlaid with the π-mode frequency from experimental cold test and PIC simulations in CST. Maximum output power is observed at L = 4.5 cm (SBO composite frequency of 2.102 GHz ± 1.5 MHz), where the SBO frequency is between the π-mode cold test value (2.105 GHz) and the π-mode free-running frequency from CST-PS simulations (2.0934 GHz). Seven outlier shots were 4π/6-mode dominant in WG 3, and two of these shots were 4π/6-mode dominant in WG 2.

Finally, the high, moderate, and low Q_t output power measurements are given in Figure 5.15. As expected from the cold test quality factors of the π-mode and the ISBO experiments,

output power increased as *h* increased in the HRPM experiments. Simulations in CST-PS corroborate a first-order prediction of the output power in each experiment. These simulations were performed at -300 kV cathode voltage. Because magnetron microwave power scales with a power of the voltage [133], these estimates would likely be more accurate if they were completed at a voltage where the magnetron would operate in the experiment. Optimized performance metrics of the HRPM are listed in Table 5.4.

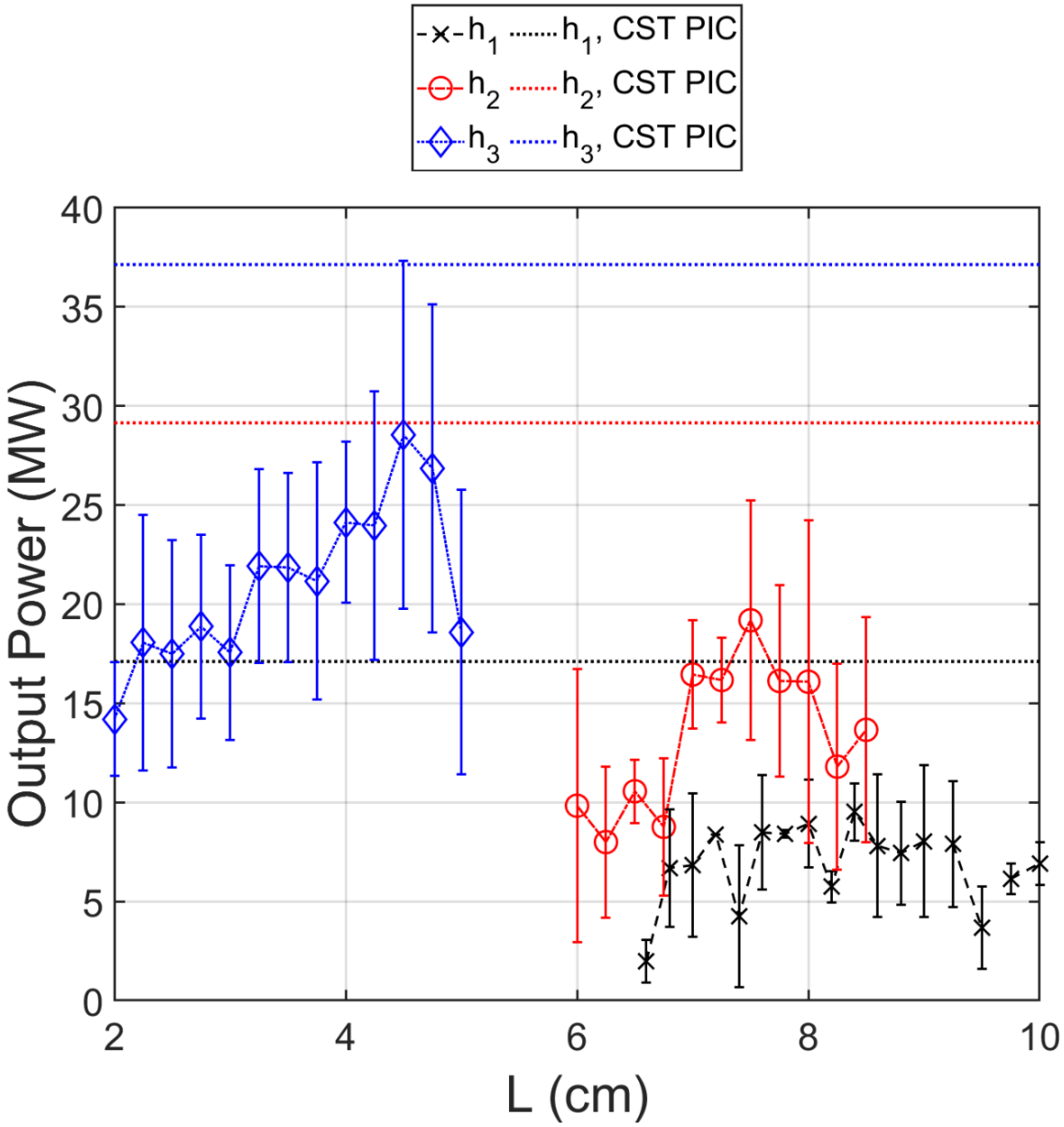

Figure 5.15: SBO output power for high Q (h_1), moderate Q (h_2), and low Q (h_3). CST-PS predictions are from the ISBO, performed at a voltage of -300 kV. Output power increases as h increases.

Table 5.4: Summary of metrics from HRPM experiment for the high (h_1), moderate (h_2), and low (h_3) Q_t experiments. The optimal tuner position, maximum power, experimental frequency, expected frequency, and locked range are listed as a function of h.

h_n (mm)	Quality Factor	L_{max} (cm)	P(L=L_{max}) (MW)	f(L=L_{max}) (GHz)	CST-PS f_π (GHz)	Locked Range (MHz)
$h_1 = 28$	High	8.4	9.5 ± 1.4	2.173 ± 0.0071	2.180	17
$h_2 = 32$	Moderate	7.5	19 ± 6	2.148 ± 0.0028	2.154	15
$h_3 = 36$	Low	4.5	28 ± 9	2.102 ± 0.0015	2.0934	33

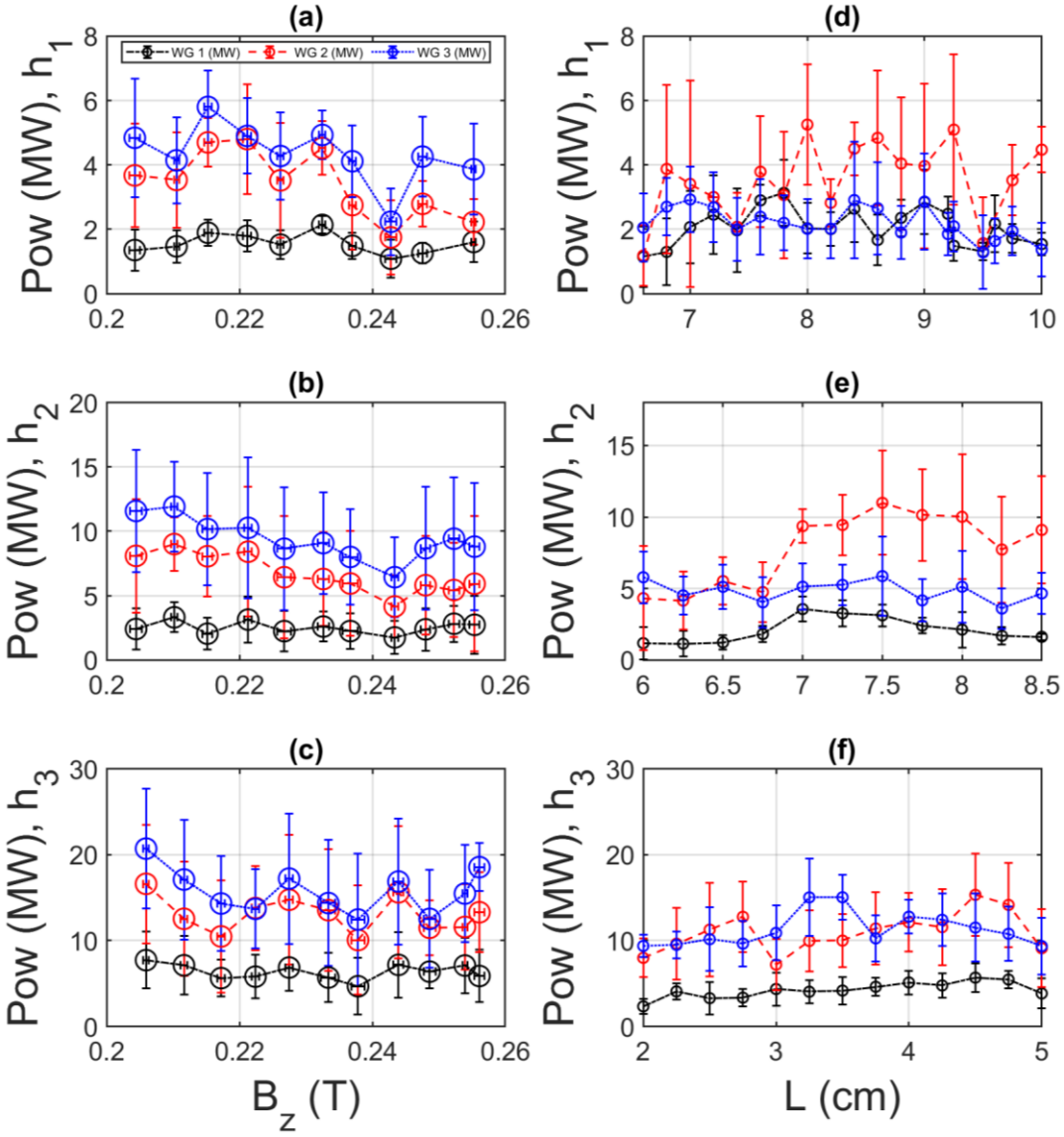

Figure 5.16: Peak output power in each waveguide from the ISBO experiment for high Q_t (h_1), moderate Q_t (h_2), and low Q_t (h_3) as functions of the applied magnetic field B_z. (a, b, c) Peak output power in each waveguide from the HRPM experiment for high Q_t (h_1), moderate Q_t (h_2), and low Q_t (h_3) as a function of the tuner length L (d, e, f). These are all measured at different times, because each waveguide reaches its peak power generation at different instants. The legend in (a) also applies to (b-f).

To this point, the stated power metrics have been the instantaneous maximum of the sum of all three waveguide outputs. The maximum value of the individual peak from each waveguide is plotted in Figure 5.16 for the ISBO and HRPM experiments, which occur at different instants in time, which can characterize the modes of operation that were observed in the experiment. In each of the ISBO experiments, the rightmost WG 3 demonstrated the highest power, followed by WG 2, and then WG 1. This result suggests that, as the beam propagates from left to right, the modulation of the spokes becomes greater and enforces a more robust response from the later cavities. Expectations from PIC simulations of the 5π/6-mode are contradicted by this evidence. In the simulations, WG 3 is expected to produce the most power, but WG 2 is expected to produce the least power due to the null phase advancement in a central cavity. In the HRPM, when the SBO was driven on π-mode resonance to generate maximum power, the central WG 2 produced the most power, followed by WG 3 and then WG 1; this is the expected behavior from CST-PIC simulations for the π-mode. As L is decreased in the HRPM and the excitation frequency moves closer to the 5π/6-mode free-running frequency, the power profile from the ISBO experiment is recovered, and WG 3 produces just as much power as WG 2, if not more. Again, it is also worth noting that the HRPM operated in the π-mode, but the ISBO did not at all. While the ISBO experiments took place at slightly lower magnetic fields than HRPM experiments, the difference in mode selection of the SBO between the ISBO and HRPM experiments is significant.

To summarize the results of the HRPM experiments on the effects of the quality factor, it is best to reference Table 5.4. At several different values of the SBO π-mode quality factor, the LBO harmonic frequency was swept across a broad range of frequencies to excite the SBO. In each experiment, harmonic frequency locking was observed. As the quality factor decreased, the locked state improved the shot-to-shot consistency of the SBO frequency, and the locked range increased from high Q_t to low Q_t. When the π-mode was driven near its free-running frequency, maximum power generation from the SBO was observed. These qualities are consistent with the driven oscillator hypothesis, strongly suggesting that the electron beam modulation locks and drives the connection between the two oscillators. The role of the magnetic field will be further considered in section 5.5, where the results from a reversal in the magnetic field will be examined.

5.4 Phase Analysis

It remains important to characterize the phase stability of the locked state. For oscillators implemented in microwave systems such as phased arrays, phase differences between components must be repeatable to achieve constructive interference [134]. Phase locking is a condition wherein the variance of the phase difference between two signals is minimal on a shot-to-shot basis, specifically $< \pm 10°$ [54], [66], [135]. Thus, an analytic routine was developed to ascertain the phase difference between oscillators on a per-shot basis, outlined in [54]. First, the output signals were splined, smoothed, and filtered. After that, the Hilbert transform was applied to the processed signals to obtain the phase information. A specific window Δt was chosen where phase comparison was performed, defined as the interval wherein the SBO was operating at > 80% of its peak power generation. This decision was preferred over an interval such as the full width at half max (FWHM) because, at this broad of a window, there was a high probability that one of the waveguides would produce very low powers. The signal-to-noise ratio was so poor in these shots that phase information could not adequately be retrieved. The 80% interval remained large enough for adequate phase analysis and guaranteed phase retrieval for the vast majority of shots from the LBO and SBO. As outlined in Table 5.3, the LBO consistently demonstrated operation over the same time interval as the SBO. Results in this section draw from the low Q_t experiment because this was the only test in which every signal was collected from each of the three LBO B-dots and all three SBO waveguides, enabling a complete treatment of all signals. Of the 93 shots taken for the low Q_t HRPM experiment, eight of them were removed because there was either inadequate overlap of LBO and SBO oscillation in time, or weak oscillations resulted in poor signal-to-noise ratio that rendered extraction of phase subpar. Six of the 64 shots were removed from the ISBO experiment under the same rationale.

Figure 5.17 illustrates the average window over which phase analysis was performed for the ISBO and HRPM experiments as a function of the magnetic field and tuner length, respectively. Because SBO pulse lengths were longer in the HRPM experiment (Figure 5.11), the resulting window sizes are larger. The smallest average window size is just below 10 ns; at 1 GHz and 2 GHz, this corresponds to roughly 10 cycles and 20 cycles, respectively. When the SBO π-mode was driven on resonance in the HRPM and the highest powers were observed, the window size increased to 18 ns on average. Regardless of the magnetic field, the ISBO did not exceed an average of 15 ns for Δt.

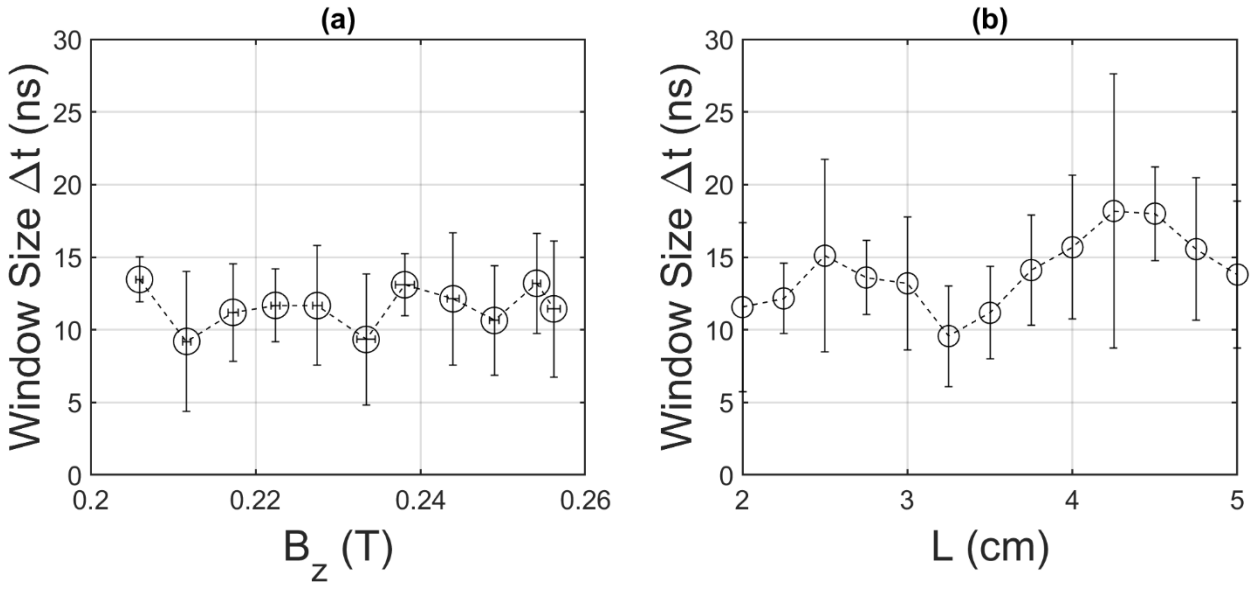

Figure 5.17: Window size over which the phase analysis was conducted for (a) the ISBO experiment and (b) the HRPM experiment, both performed at low Q_t.

One signal's phase was subtracted from another in every shot, its mean value calculated over the interval Δt, and wrapped to the domain [0°, 360°]. If the phase difference between two vectors was more than 180°, it was mirrored about 180° ($\Delta\phi \rightarrow 360° - \Delta\phi$ for $\Delta\phi > 180$) to obtain the smallest angle between two complex vectors, so that it does not matter which leads the other. The phase difference between two signals may then be broken into a histogram with bins between 0° and 180°, and plotted over an independent variable.

Because there are three outputs from the SBO, it is impossible to characterize a single phase for the overall oscillator. Instead, the phase difference between each signal must be considered. The phase difference between the leftmost, central, and rightmost WG 1, 2, and 3, respectively, must be represented in three different quantities. Defined here is the phase difference between WG 2 and 1 ($\Delta\phi_{S21}$), WG 3 and 1 ($\Delta\phi_{S31}$), and WG 3 and 2 ($\Delta\phi_{S32}$). Each of these is displayed for the ISBO experiment in Figure 5.18. Overall, the phase difference is biased towards larger values, with very few instances occurring between 0° and 30°. The phase difference $\Delta\phi_{S21}$ demonstrates some capacity for operation near 160°, but $\Delta\phi_{S31}$ and $\Delta\phi_{S32}$ do not show consistent bias. Error bars are quite large, often more than 30°. Only one of these may be considered phase-locked, which is $\Delta\phi_{S21}$ at the second-highest magnetic field examined near 0.254 T. As discussed in Section 5.1, the ISBO operated primarily in the 5π/6-mode. These results suggest that this mode is highly undesirable for applications where each of the three waveguide outputs must be combined. It

would be impossible to introduce the appropriate phase difference between each leg of the output with repeatability.

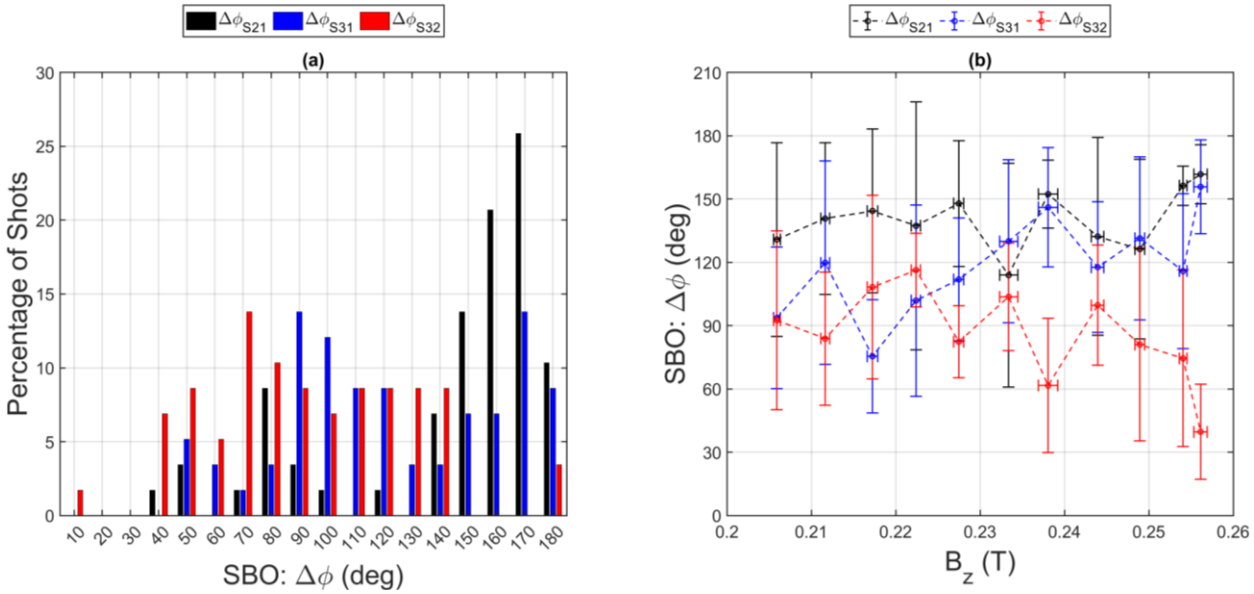

Figure 5.18: Phase difference between each SBO waveguide in the ISBO experiment. In (a), the histogram bins from left to right span across [0°, 10°], [10°, 20°], and so on, such that the axis labels mark the top end of the bin. The phase difference between each signal does not exhibit bias toward any specific value across all magnetic fields, with exception of $\Delta\phi_{S21}$, which demonstrates reduced variability at higher magnetic fields.

In a similar technique to the SBO, the phase of the LBO must be characterized through three different quantities, namely the phase difference between cavity 2 and 1 ($\Delta\phi_{L21}$), cavity 3 and 1 ($\Delta\phi_{L31}$), and cavity 3 and 2 ($\Delta\phi_{L32}$). The results are displayed in Figure 5.19, which reveals interesting and unexpected behavior. The phase difference between the two outer cavities, $\Delta\phi_{L31}$, is phase-locked across the full range of L, clustered toward slight differences of less than 20°. Because these are two individual cavities of the same oscillator, this is relatively unsurprising. The central cavity 2, on the other hand, appears to operate at a phase difference respective to the outer cavities that is entirely random. Remarkably, $\Delta\phi_{L21}$ and $\Delta\phi_{L32}$ fall almost uniformly into every bin of the histogram in Figure 5.19a. The identified mode of operation is the expected π-mode, so the expectation is that there would be some consistent phase difference between each LBO cavity, but apparently is not the case. The two outer cavities are strongly linked to each other, while the central cavity resonates at a phase difference irrespective of the other two. Unfortunately, there was no isolated-LBO experiment to which these measurements may be compared, so the possibility that the SBO is influencing this behavior cannot be ruled out. However, the LBO demonstrated a nearly identical operation in the reversed magnetic field experiment, which will be discussed in the next section.

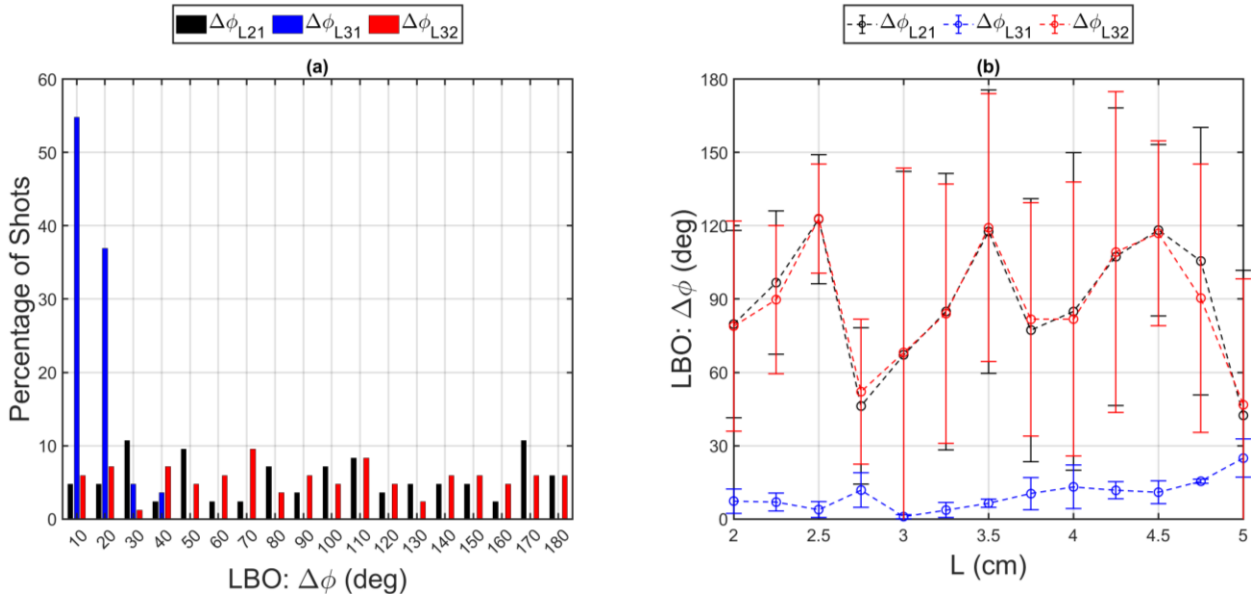

Figure 5.19: Phase difference between each LBO cavity in the HRPM experiment. In (a), the histogram bins from left to right span across [0°, 10°], [10°, 20°], and so on, such that the axis labels mark the top end of the bin. Phase locking is observed between LBO cavity 1 and 3 across the entire range of L that was measured. The phase of the central cavity 2 appears to vary randomly on a shot-to-shot basis with respect to either of the other cavities.

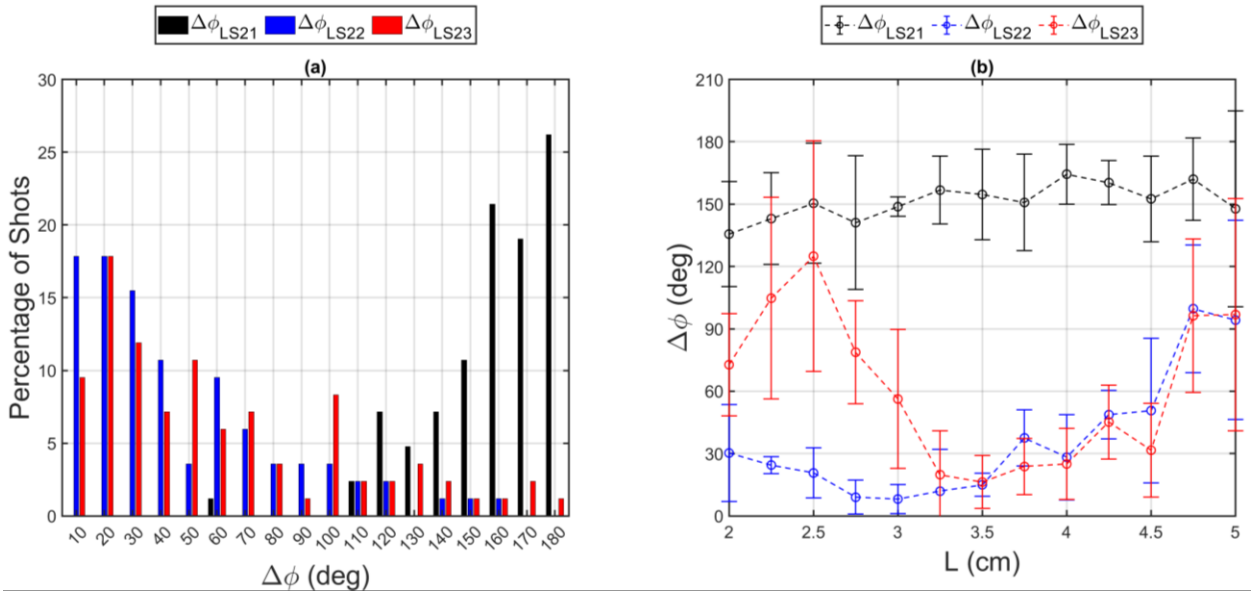

Figure 5.20: Phase difference between LBO cavity 2 and each SBO waveguide. In (a), the histogram bins from left to right span across [0°, 10°], [10°, 20°], and so on, such that the axis labels mark the top end of the bin. There is an apparent preferential selection in the phase difference in each of these measurements, with lower variance across several ranges of L. Harmonic phase locking is observed between LBO cavity 2 and SBO waveguide 2 in multiple instances from L = 2.25 cm → 3.5 cm, as well as $\Delta\phi_{LS21}$(L=3cm).

In characterizing the phase difference between the LBO and SBO, an extra step was applied to the LBO signals in multiplying the phase by two and rewrapping within the domain of [-π, π] radians to obtain the phase of the harmonic. Because there are three LBO signals and three SBO

signals, there are nine phase differences to diagnose. The phase difference between LBO cavity 2 and each SBO waveguide is represented in Figure 5.20 as $\Delta\phi_{LS21}$, $\Delta\phi_{LS22}$, and $\Delta\phi_{LS23}$, which demonstrates radically different results from the ISBO experiment of Figure 5.18. Significantly, the phase difference has substantially improved repeatability. In particular, $\Delta\phi_{LS22}$ shows small phase angle differences with minimal variance over much of the tuning range. Phase locking, or more specifically harmonic phase locking, is observed for $\Delta\phi_{LS22}$ at several data points over L = 2.25 cm → 3.5 cm. The phase difference between cavity two and the leftmost waveguide $\Delta\phi_{LS21}$ was consistently near 150° across the full range of L. This suggests LBO cavity 2 enforced a phase difference determined by the electron drift velocity and the drift space length between the LBO cavity and SBO WG 1. From Figure 5.14, it is reasonable to hypothesize the SBO is driven in the π-mode from L = 3.5 cm → 4.5 cm, and it is in this range where all of $\Delta\phi_{LS21}$, $\Delta\phi_{LS22}$, and $\Delta\phi_{LS23}$ demonstrate the most repeatable phase differences collectively. For L beneath this range, $\Delta\phi_{LS23}$ breaks phase synchronism with $\Delta\phi_{LS22}$ and becomes significantly less repeatable.

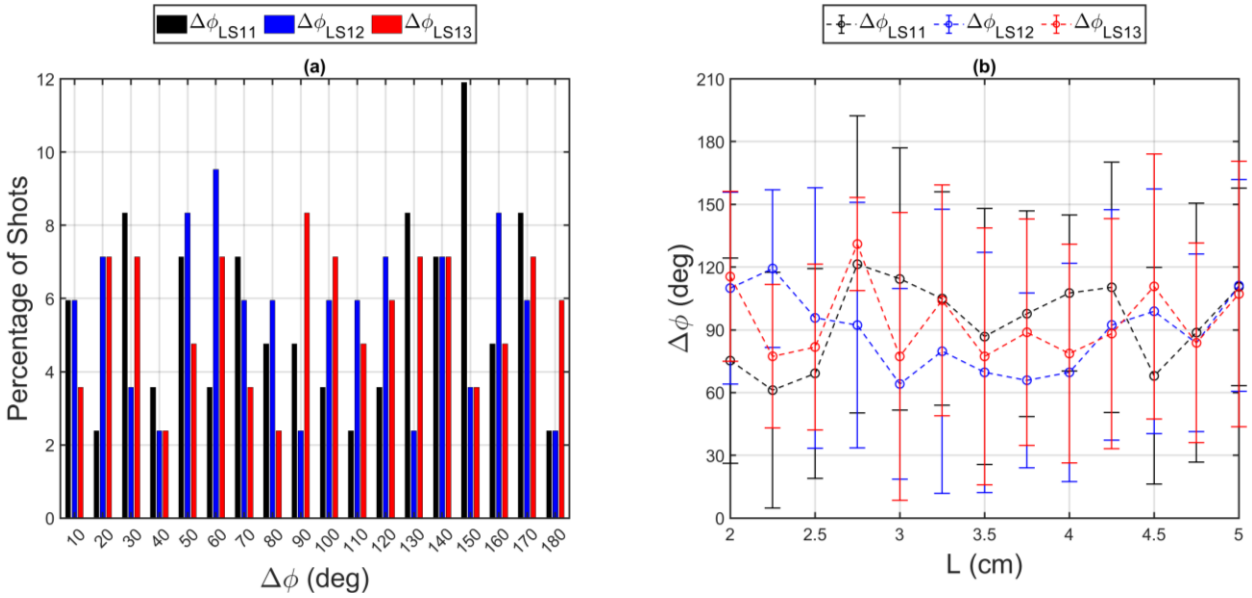

Figure 5.21: Phase difference between LBO cavity 1 and each SBO waveguide. In (a), the histogram bins from left to right span across [0°, 10°], [10°, 20°], and so on, such that the axis labels mark the top end of the bin. No repeatable phase difference between any of these signals is observed.

Unsurprisingly, there was no repeatable phase relationship between LBO cavity 1 and any of the SBO waveguides, because the phase difference between LBO cavity 2 and the other cavities was random. Figure 5.21 illustrates $\Delta\phi_{LS11}$, $\Delta\phi_{LS12}$, and $\Delta\phi_{LS13}$ are evenly distributed across phase, with no control of the phase difference. Because LBO cavity 1 was phase-locked to LBO cavity 3, very similar results were obtained for $\Delta\phi_{LS31}$, $\Delta\phi_{LS32}$, and $\Delta\phi_{LS33}$. This lack of influence between

the outer LBO cavities on the SBO phase suggests that LBO cavity 2 drives the repeatable phase differences observed in Figure 5.20.

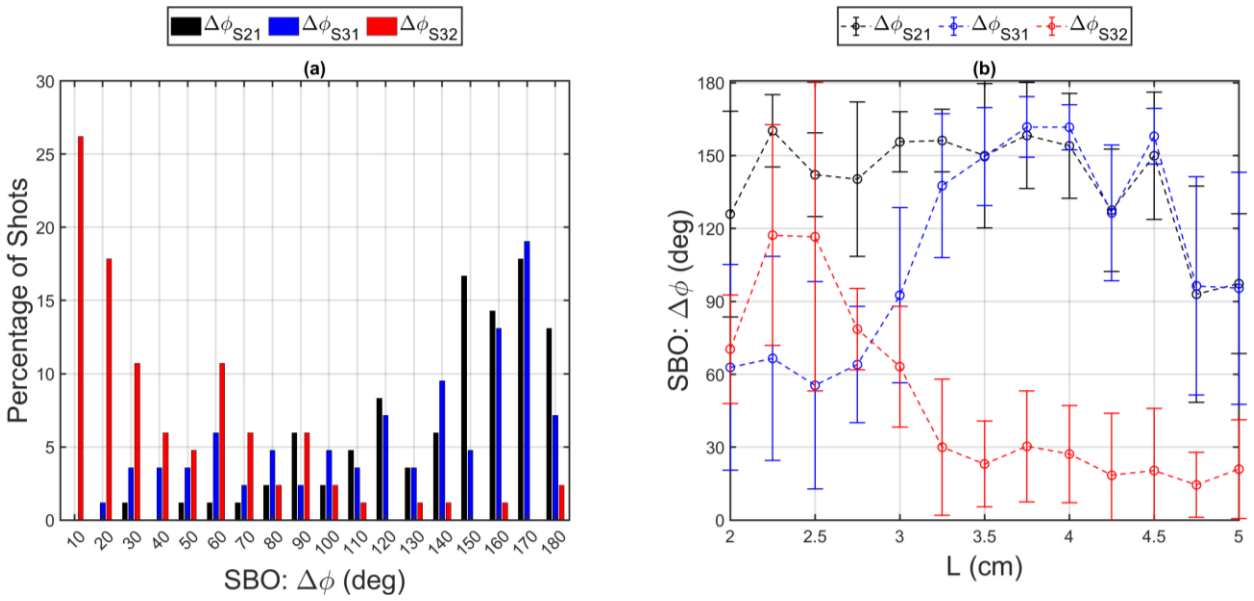

Figure 5.22: Phase difference between each SBO waveguide in the HRPM. In (a), the histogram bins from left to right span across [0°, 10°], [10°, 20°], and so on, such that the axis labels mark the top end of the bin. Compared with the ISBO in Figure 5.18, the repeatability in the phase difference between each waveguide is improved in the range where π-mode is excited from L = 3.5 cm → 4.5 cm.

The phase difference between each SBO waveguide was less consistent in comparison with $\Delta\phi_{LS21}$, $\Delta\phi_{LS22}$, and $\Delta\phi_{LS23}$, but was still improved from the ISBO experiment. It is clear from Figure 5.22 that a phase selection was imprinted upon the SBO in the same region of L = 3.5 cm → 4.5 cm, where the π-mode was excited, and the most repeatable measurements of $\Delta\phi_{LS21}$, $\Delta\phi_{LS22}$, and $\Delta\phi_{LS23}$ were obtained. While the waveguides were not phase-locked to each other, this result is significant if an attempt were to be made to combine the three waveguide outputs into one channel or used to drive a phased array. In both applications, the phase difference must be repeatable to achieve constructive interference.

The repeatability of the phase difference between every signal in the low Q_t HRPM experiment is finally demonstrated in Figure 5.23. The plotted values include the length of the vertical error bars from Figure 5.18-Figure 5.22 (each from part b). Figure 5.23a succinctly shows no repeatable phase difference between LBO cavity 1 or 3 with the central LBO cavity 2 or any of the SBO waveguides, while also presenting the phase locking of these cavities to each other. Repeatable phases are observed between cavity 2 and each waveguide signal, particularly waveguide 2, which demonstrated harmonic phase locking in multiple instances. In the range of L = 3.5 → 4.5 cm, where the π-mode was excited by the LBO harmonic, the SBO demonstrated the

most consistent phase differences when considering all three signals. The ISBO, shown in Figure 5.23b, broadly did not demonstrate the same repeatability compared to the HRPM, especially when the HRPM operated in the π-mode. If the ISBO had oscillated in π-mode, similar phase differences might have been retrieved. Still, this mode was not observed, so a direct comparison of π-mode operation cannot be made between the two configurations.

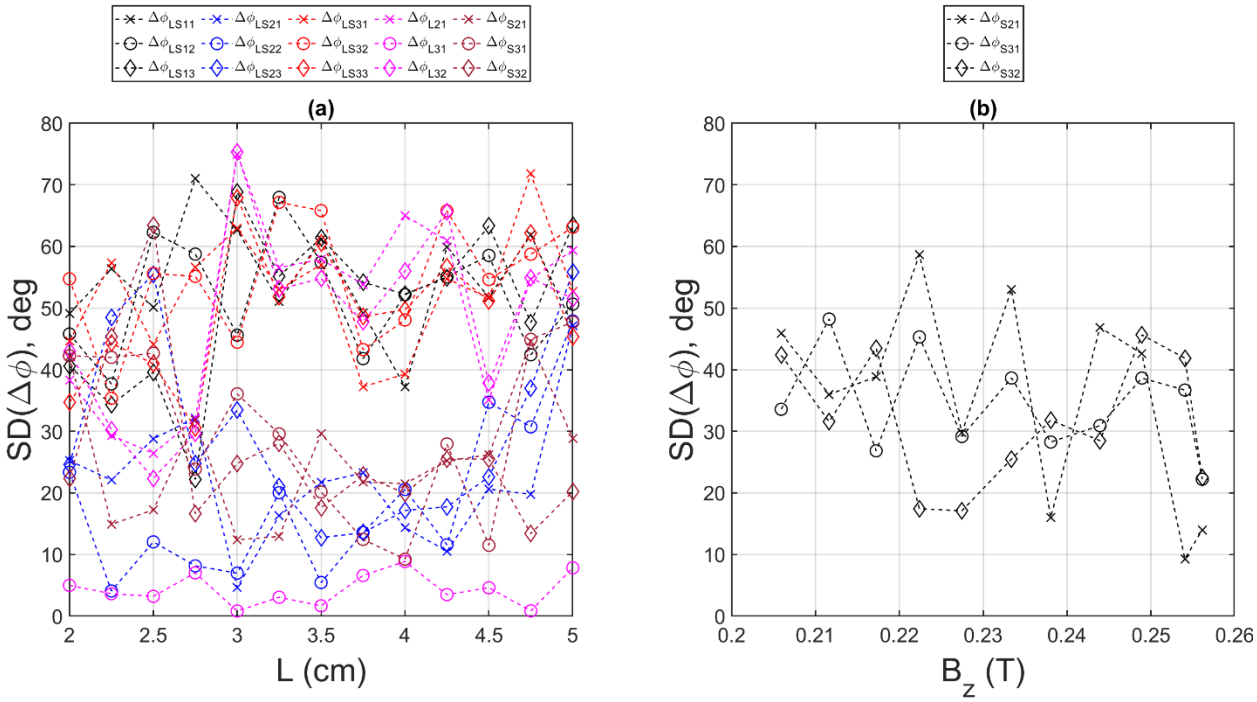

Figure 5.23: (a) Standard deviation of the mean phase difference between every signal in the HRPM experiment. (b) The standard deviation of the mean phase difference between every signal in the ISBO experiment. Two signals are considered phase-locked if the standard deviation is less than 10°. The repeatability of phase difference $\Delta\phi_{S21}$, $\Delta\phi_{S31}$, and $\Delta\phi_{S32}$ are improved in the HRPM experiment when compared with the ISBO experiment.

5.5 Reversed Magnetic Field Experiment

Up to this point, all experiments have utilized an applied magnetic field in the "forward" direction, which directs flow of the electron hub from the LBO directly into the SBO. In the low Q_t HRPM experiment, an additional test was performed where the magnetic field was reversed so the electron hub would drift from SBO to LBO. If this magnetic field orientation were to produce the same results presented in Figure 5.14, it would contradict the hypothesis that the oscillators are locked to each other through the LBO harmonic content in the beam spokes. In the reversed magnetic field experiment, this harmonic content would need to be substantially preserved after traveling around the entire planar smoothbore drift region on the opposite side of the cathode and both cylindrical bends.

An equivalent version of Figure 5.14 is plotted for the reversed magnetic field in Figure 5.25, where the examined tuning range was $L = 3.75$ cm → 5 cm. It becomes immediately apparent that the LBO, with the reversed magnetic field, consistently produced nearly the same harmonic excitation observed in the forward magnetic field experiment. On the other hand, each SBO waveguide behaved much differently than with the forward magnetic field. Operation in the 4π/6-mode and 5π/6-mode was more frequent, which were both excited in the ISBO experiment. Some shots were dominant near the LBO harmonic frequency, but it's inconclusive whether they were locked or operating in the π-mode in an unlocked state. As a result, the average SBO WG frequency shifted between 2 GHz and the LBO harmonic frequency with large error bars. The only exception to this is at $L = 4$ cm where WG 2 and WG 3 demonstrated operation near the π-mode resonant frequency.

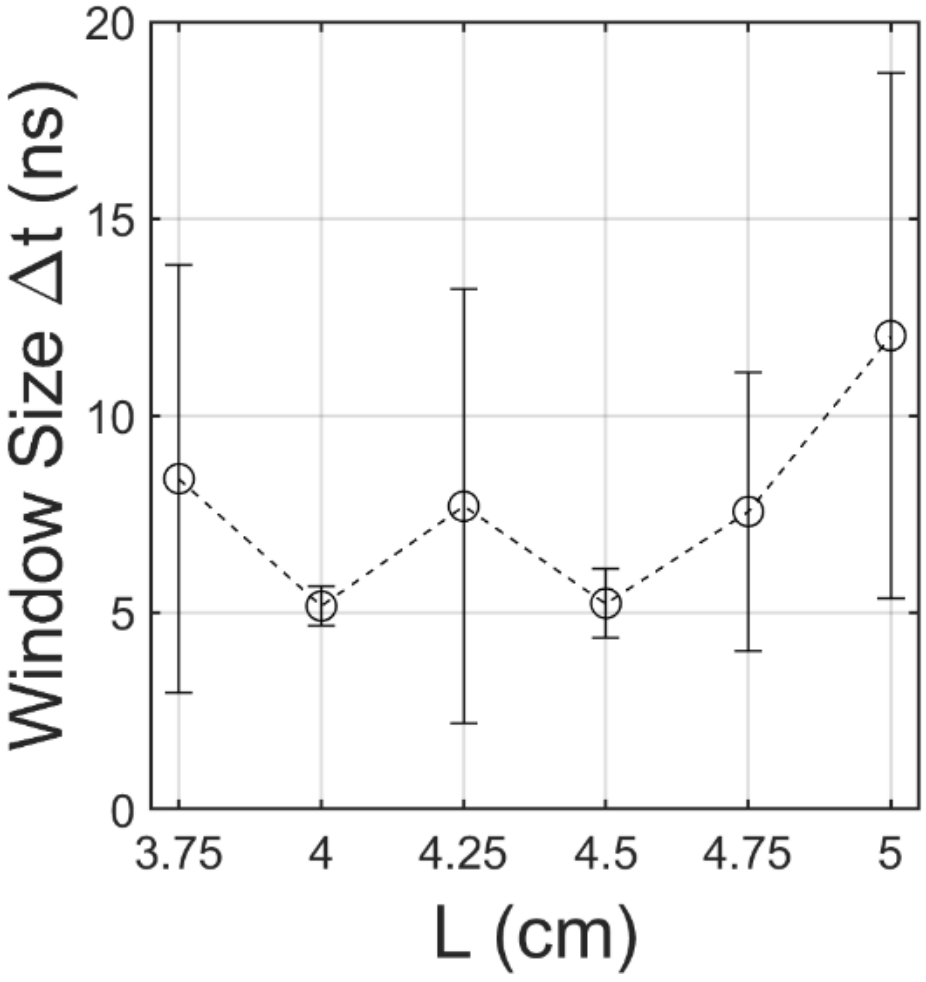

Figure 5.24: Window size in the reversed magnetic field experiment. They are significantly smaller than those observed for the ISBO and HRPM experiments with the forward magnetic field (Figure 5.17).

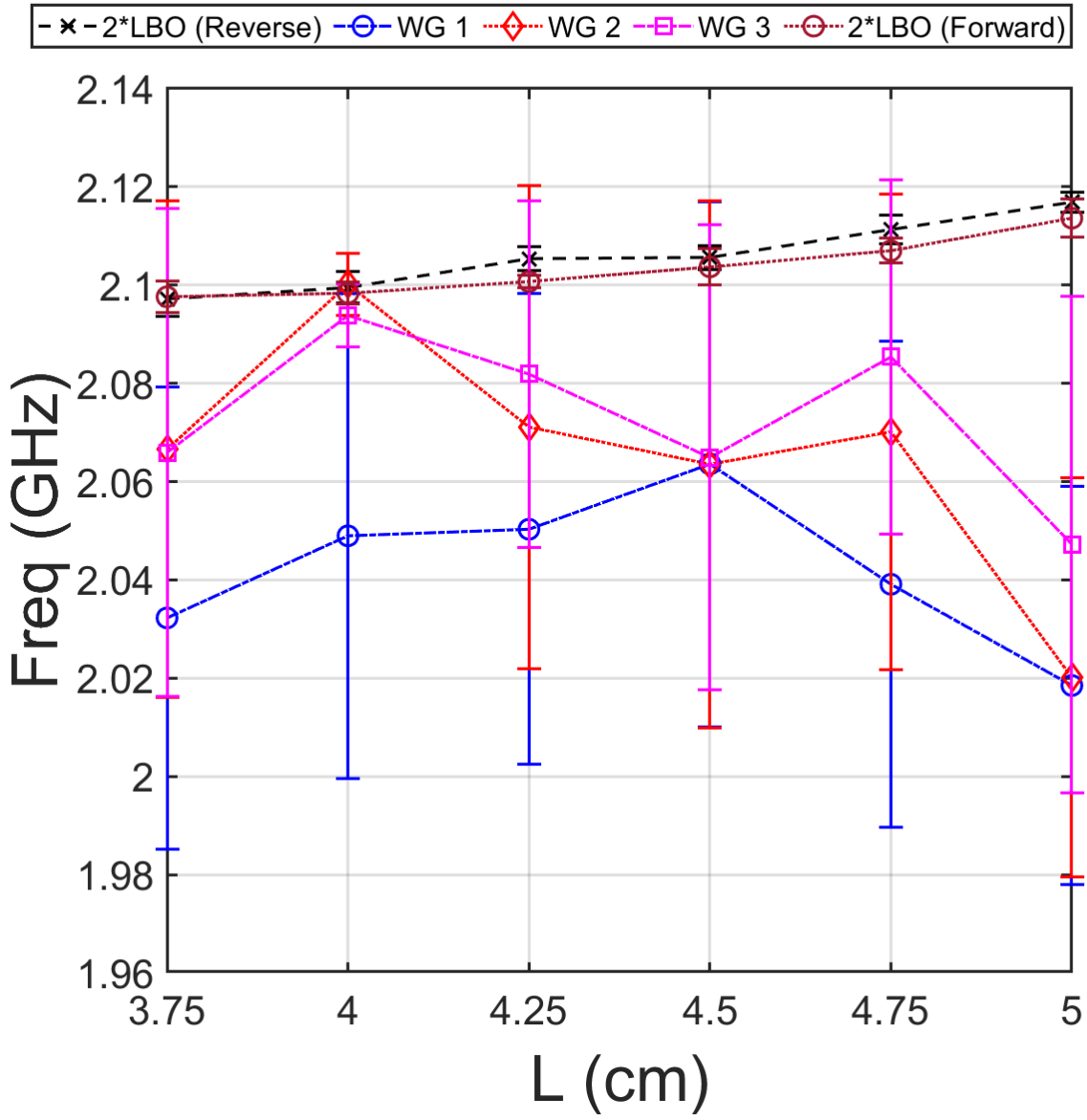

Figure 5.25: Dominant frequency for the reversed magnetic field experiment of the HRPM, taken at low Q_t. Harmonic frequency locking is significantly diminished, as operation in nearby competing modes became much more prevalent than in the forward magnetic field experiment (Figure 5.14).

The same selection algorithm for phase analysis outlined in Section 5.4 was reapplied to the data obtained in the reversed magnetic field experiment. Figure 5.24 plots the time windows of the phase analysis, which are substantially smaller than the ISBO or HRPM experiments with the forward magnetic field. These reduced temporal windows are likely caused by the large degree of mode competition throughout the experiment, which resulted in frequent beating of the power envelope rather than the typical Gaussian-shaped pulses observed with the forward magnetic field.

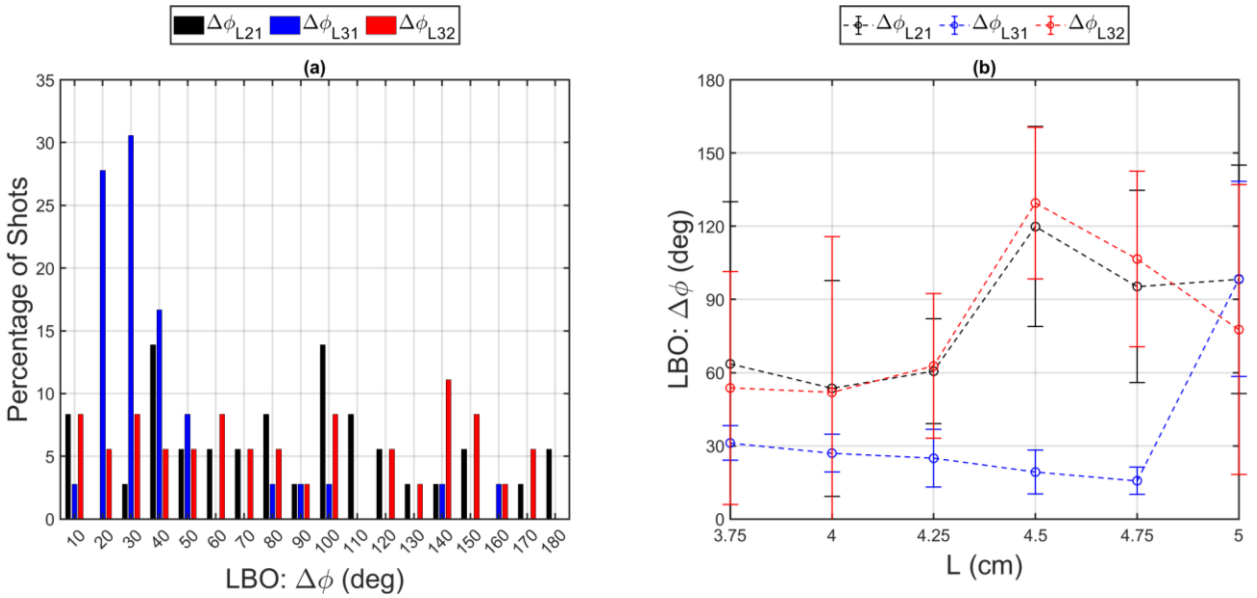

Figure 5.26: Phase difference between LBO cavities in the reversed magnetic field experiment of the HRPM at low Q_t. In (a), the histogram bins from left to right span across [0°, 10°], [10°, 20°], and so on, such that the axis labels mark the top end of the bin. The phase differences and their associated variance are very similar to what was observed in the forward magnetic field experiment (Figure 5.19).

Figure 5.26 displays the phase difference between each LBO signal analyzed in the reversed magnetic field test. The results are very similar to the forward magnetic field experiment, given in Figure 5.19. For the most part, the two outer cavities remain phase-locked to each other, while the central cavity does not demonstrate preferential phase selection compared to the outer cavities. It is also worth noting the LBO operated virtually the same with the forward and reverse field, whereas the SBO demonstrated significantly degraded and less consistent operation. This asymmetry lends credence to the notion that the LBO is the driving oscillator in this system, validating the forward propagating beam.

Figure 5.27 and Figure 5.28 show the phase difference between LBO cavity 2 and the SBO waveguides and the phase difference between the SBO waveguides relative to each other, respectively. The consistent phase differences obtained with the forward field in Figure 5.20 and Figure 5.22 are entirely diminished. These results strongly suggest the LBO can be used to enforce a repeatable phase difference at the SBO through the modulation of the electron hub in the forward beam direction.

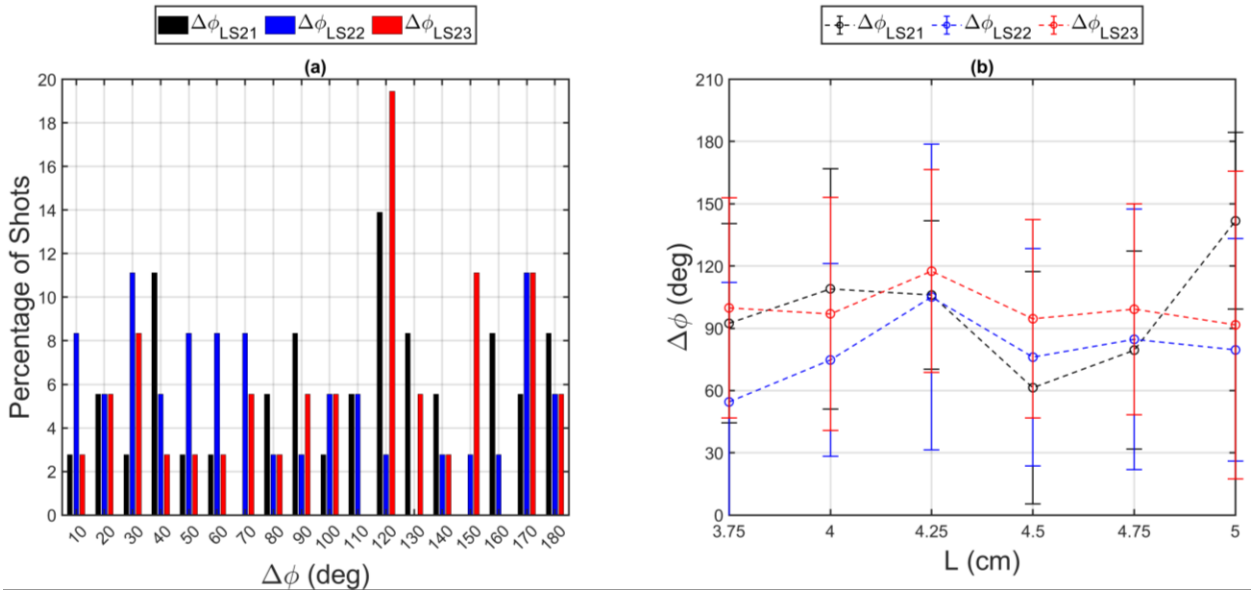

Figure 5.27: Phase difference between LBO cavity 2 and each of the SBO waveguides in the reversed magnetic field experiment of the HRPM at low Q_t. In (a), the histogram bins from left to right span across [0°, 10°], [10°, 20°], and so on, such that the axis labels mark the top end of the bin. The consistent phase difference exhibited in the forward magnetic field experiment (Figure 5.20) is no longer observed.

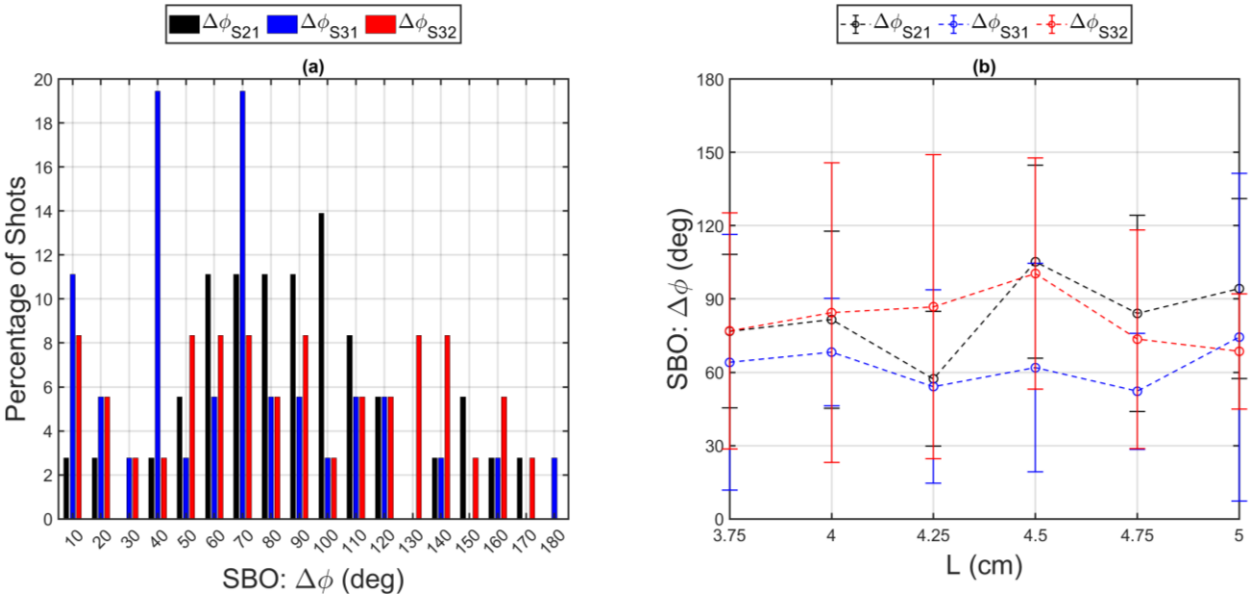

Figure 5.28: Phase difference between each SBO waveguide in the reversed magnetic field experiment of the HRPM at low Q_t. In (a), the histogram bins from left to right span across [0°, 10°], [10°, 20°], and so on, such that the axis labels mark the top end of the bin. The consistent phase difference exhibited in the forward magnetic field experiment (Figure 5.22) is no longer observed.

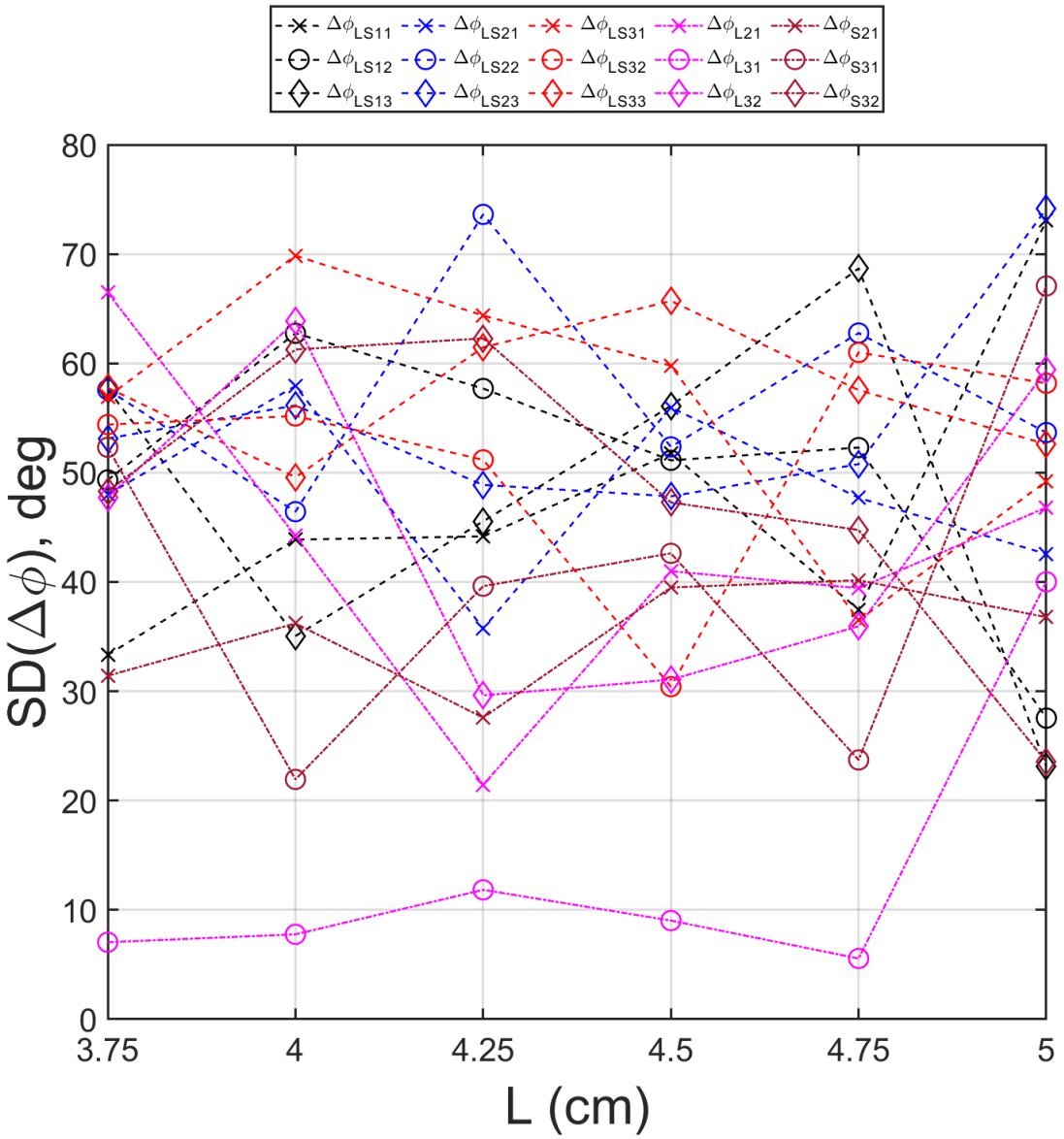

Figure 5.29: Standard deviation of the phase difference between each signal in the reversed magnetic field of the low Q_t HRPM. The repeatability is generally lower in these measurements than in the HRPM experiments with forward propagating beam (Figure 5.23a).

Finally, the standard deviations of all measured phase differences between all signals for the full range of L in the reversed magnetic field experiment are presented in Figure 5.29. The two outer LBO cavities remained phase-locked to each other, but there was no repeatable phase relation between any two different signals. The contrast in SBO operation between the forward magnetic field experiment and reversed magnetic field is stark. In the former, the SBO may be tuned using the LBO harmonic frequency to minimize the phase difference between each SBO waveguide.

With the magnetic field reversed, the selection of SBO operating frequency is no longer observed, and all consistency in phase difference is removed. This experiment further corroborates the assertion that the HRPM oscillates in a master-slave locked state, coupled through harmonic content in the modulated beam, propagating in the forward direction.

Chapter 6 Magnetically Insulated Line Oscillator Experiments

The experimental results for the MILO are presented in this chapter. This is the first MILO operated with a total input current of less than 10 kA, to the author's knowledge. This result is significant because the MILO is a self-insulating device that typically operates with 50-60 kA. In Section 6.1, the general experimental behavior of the device is detailed in terms of common characteristics such as output power, frequency, and impedance, among others. Section 6.2 illustrates the physical changes to the hardware observed after the experiment and discusses how these may reveal operational characteristics. Finally, Section 6.3 compares the experimental data to the theory derived in Chapter 2. It is argued that the device operated close to Hull cutoff, which is thus in a Brillouin flow state unique to MILO operation.

6.1 MILO Characteristics

The MILO experiments discussed in this chapter encompass MELBA shots 18084-18208. In these experiments, the cathode radius within the cavity region r_c was set to 7 mm, best illustrated in Figure 4.12. The downstream cathode was centered within the beam collector, and the downstream cathode radius r_d was iterated between 8 mm and 10 mm in two experiments as the independent variable. This adjustment of r_d was the only difference between the two experiments; the anode was left undisturbed in its vacuum chamber, and the cathode rod was not removed. Of the 125 total shots, 21 were taken with r_d set to 8 mm, and 104 with r_d set to 10 mm. Two of these shots (with r_d = 10 mm) were removed entirely from the data set because the voltage and current measurements were corrupted. Zero external magnetic field was applied to the experiment; the magnetic field for synchronous interaction was established entirely by driven currents within the MILO. The intent of altering r_d was to inject a varying amount of current into the downstream diode. In turn, the downstream current would establish a proportional magnetic field within the cavity interaction space. Like the magnetron, the MILO also requires a synchronous layer within the electron hub to interact, the axial velocity of which is dictated by the local ExB drift velocity (scaling as E/B). Oscillation can occur by synchronizing this axial electron hub flow with the phase velocity of the desired MILO operating mode. Thus, the objective of altering r_d is similar to

adjusting the magnetic field in a magnetron. The experimental issue with this MILO configuration is that the chamber must be opened and the downstream cathode must be replaced or otherwise altered to vary r_d.

The primary measurements for these experiments were the total input current, applied voltage, and microwave output signal. These are all overlaid in the sample MELBA shot 18180 shown in Figure 6.1. The peak microwave power achieved on this shot was 22 MW, the instant at which the voltage, current, impedance, and total efficiency were 250 kV, 9.3 kA, 27 Ω, and 1%, respectively. The MILO fired near the peak of the voltage pulse, and there is a notable inflection point in the current trace during the voltage rise and before the MILO commences oscillation. This inflection suggests magnetic insulation in the interaction space may have been established before MILO operation, enabling synchronism later in time. Shot 18180 is one example shot that failed to crowbar. Total impedance collapse was characteristic of nearly every shot in the MILO experiments because of the rapidly increasing current due to AK-gap plasma diode closure.

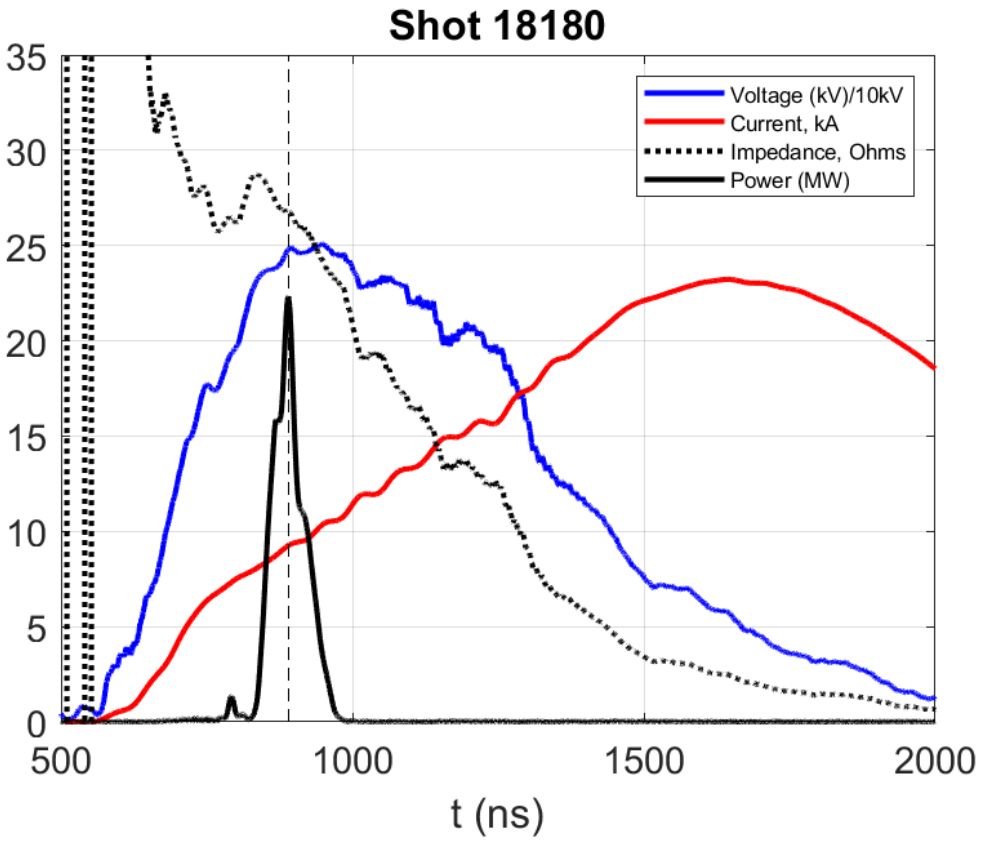

Figure 6.1: MELBA shot 18180 overlaying voltage, current, impedance, and power. A peak microwave power of 22 MW was generated, the instant at which the voltage, current, and impedance were 250 kV, 9.3 kA, and 27 Ω, respectively.

Spectral analysis of the raw output signal from shot 18180 is shown in Figure 6.2, including a time-integrated Fast Fourier Transform (FFT) and a time-frequency analysis (TFA) diagram. One clear, dominant frequency is observed, with a peak at 994 MHz. Harmonic content in this signal is more than 20 dB below the dominant peak. The TFA consistently reveals operation at a single frequency near 1 GHz, without cessations in resonance.

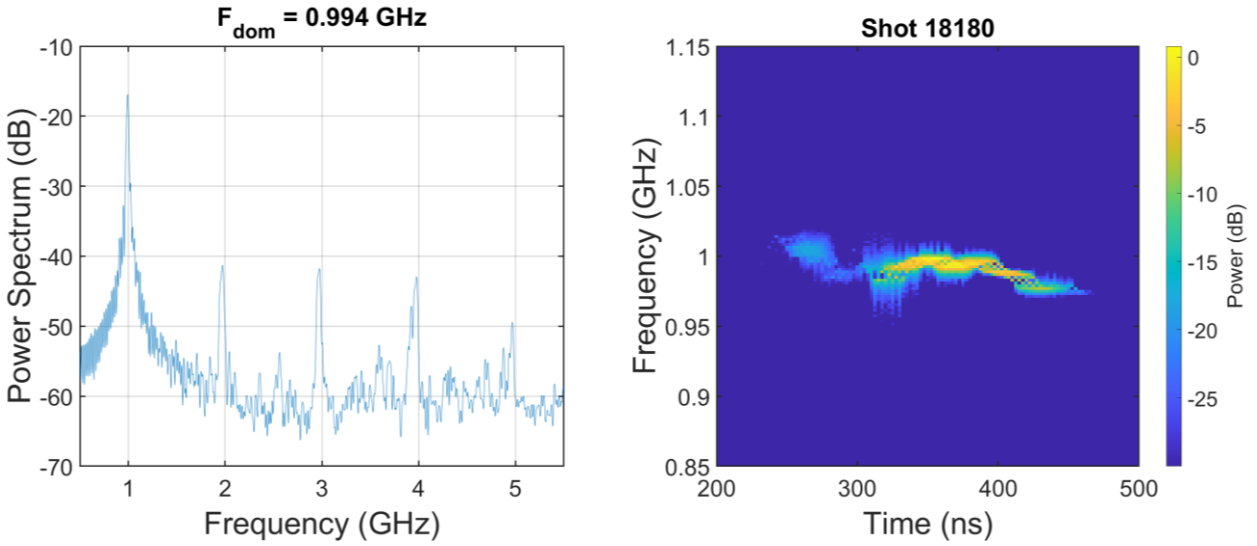

Figure 6.2: FFT (left) and TFA (right) of the output waveguide signal for shot 18180. The dominant frequency was 994 MHz, with very little mode competition.

The output power from every shot across both experiments is displayed in Figure 6.3. All shots with r_d set to 8 mm are to the left of the vertical dashed line, while r_d = 10 mm shots are to the right. Overlaid upon the individual data points are the average and standard deviation using a 10-shot moving window average. The experiment with r_d = 8 mm was performed first, and it was terminated after 21 shots because the generated output power was not satisfactory and did not appear to be improving. Within the first 20 shots for r_d = 10 mm, it was immediately apparent that the conditions for high power generation had become more suitable. The average output power consistently increased over the first 40 shots, implying that a substantial number of shots are required to condition the cathode. From shot 18140 to 18160, the rolling-average power remained stable near 13 MW before dropping down to 7 MW between shots 18160-18180. Toward the end of the experiment, the rolling-average power eclipsed 15 MW. Peak, extracted microwave power was in the range of 15-25 MW for some 30 shots (~ 43%) between shots 18130 and 18200. The average output power from these two experiments was 1.4 ± 1.4 MW and 10 ± 7 MW, respectively.

In the final seven shots, the voltage pulse delivered to the cathode deteriorated significantly, indicating the cathode had reached a critical failure (partial shorting), which will be shown in Section 6.2. The peak voltage for these shots was significantly lower than the typical MILO operating voltage (roughly 250 kV, shown in Figure 6.7), and the power consequently diminished. Thus, the voltage pulse was required to reach 200 kV at peak voltage to be considered to calculate the rolling and cumulative averages. This criterion eliminated seven shots from the $\underline{r_d}$ = 10 mm data set (including 6 of the final 7, and shot 18177), in addition to the two that were eliminated for reasons discussed earlier. As a result, the r_d = 10 mm data set effectively consists of 95 shots (out of the 104 total).

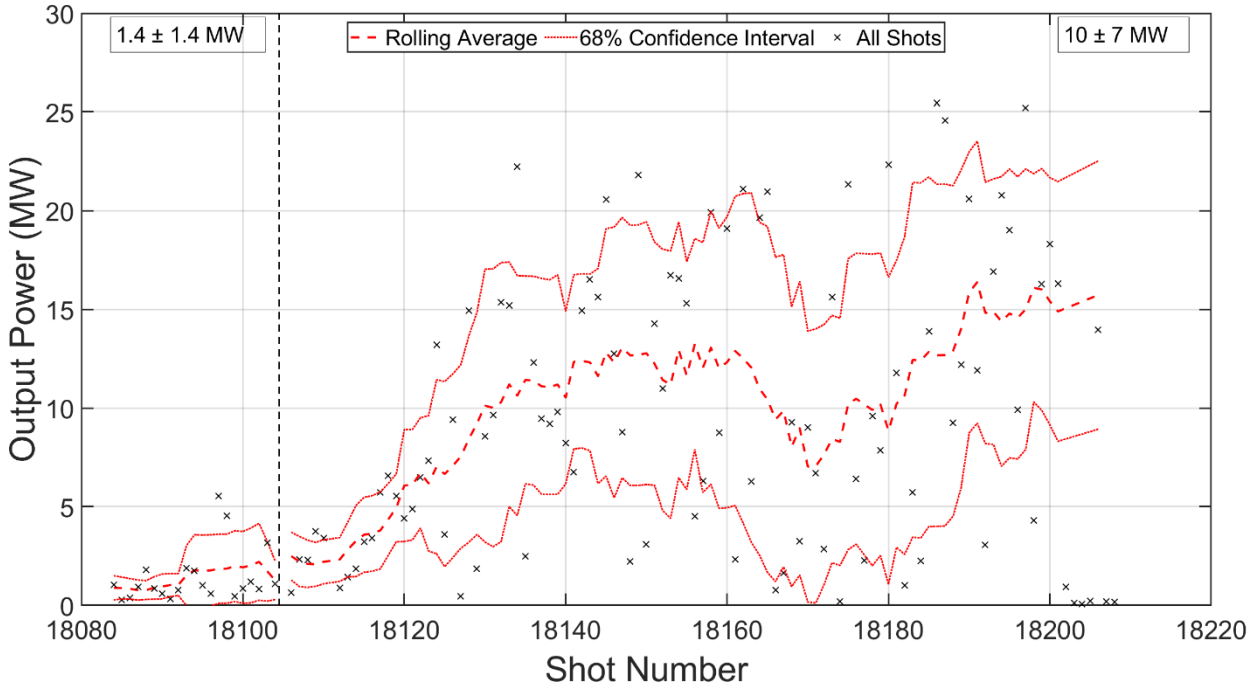

Figure 6.3: MILO microwave output power over shot number, with rolling average overlaid. The experiments with r_d = 8 mm and 10 mm are to the left and right of the vertical black dashed line, respectively. Estimated output power from PIC simulations for this experiment was approximately 70 MW.

The power generated by the MILO on a per-shot basis was extremely irreproducible. From shots 18160-18167, the MILO produced over 19 MW four separate shots and less than 3 MW on three others. It is speculated that this is due to triple points and plasma jets on the emitters within the downstream diode and in the SWS region, which can result in the inconsistent formation of a Brillouin hub in the SWS region. There is also large variability in the output power in magnetron experiments on MELBA, but not to this degree. The primary difference between the two experiments is that the magnetron's magnetic field exists before forming the electron hub, which

can help stabilize cathode plasma formation and electron flow. In the MILO, the insulation and synchronism of the electron hub rely heavily on the quality and consistency of the dynamic emission in the downstream diode. The simulation results in Figure 3.17 imply that varying r_d causes a tradeoff between downstream current and spoke current. Implementation of an experimental diagnostic to measure the current draw in the downstream diode could shed light on this issue, which could be achieved by placing a Rogowski coil between the extractor and the final vane of the SWS.

The projected output power was approximately 60-75 MW in simulations of the MILO at 230 kV in CST-PS and ICEPIC, a factor of 2-3 greater than the best shots achieved in the experiment. This discrepancy is another instance where knowledge of the current drawn in the downstream diode would be beneficial. By measuring the total input current and the downstream diode current, it can be assumed that the difference between the two is the current collection on the SWS (possibly spoke current). The simulations may have overestimated the current available within the electron hub, resulting in outsized expectations for power output. At the same time, it remains possible that the entire physical parameter space of the downstream diode has not been adequately explored as of yet. Given the dramatic difference between operating at $r_d = 8$ mm and 10 mm, additional experimentation with $r_d = 9$ mm, 11 mm, or even higher values may yield more improvement. The PIC simulations predicted comparable operation across the range $r_d = 8$ mm → 13 mm, so it would be sensible to investigate the remainder of this parameter space. It would also be instructive to vary the cathode radius inside the SWS.

Output frequency data from the two experiments are displayed in Figure 6.4 and overlaid with the expected mode frequencies obtained in HFSS and CST-PS. The operating frequency can also vary substantially, by 20 MHz or more from shot-to-shot. Identification of the operating mode is not straightforward. A viable case can be made that dominant operation was observed in either the 4π/5 mode or the π-mode of the structure's fundamental band-pass, each of which couple into the output waveguide via the extractor with greater than 10 dB return loss.

The 4π/5-mode frequency was not excited under the investigated conditions in particle-in-cell simulations, so there is no expectation for its oscillation in the MELBA experiments. One can assume that the drop in frequency (due to beam loading) incurred by the π-mode between the HFSS model and the CST-PS model (1.041 GHz – 1.008 GHz = 33 MHz) would be the same for the 4π/5-mode, in which case its estimated hot-test frequency would be 0.976 GHz. If this were the

case, nearly all data points in both experiments would fall within the range of the 4π/5 cold-test and hot-test estimates, which would satisfy the criteria that were generally applied in identifying the dominant mode in the magnetron experiments (even though the phase velocities of the two modes differ by 20%).

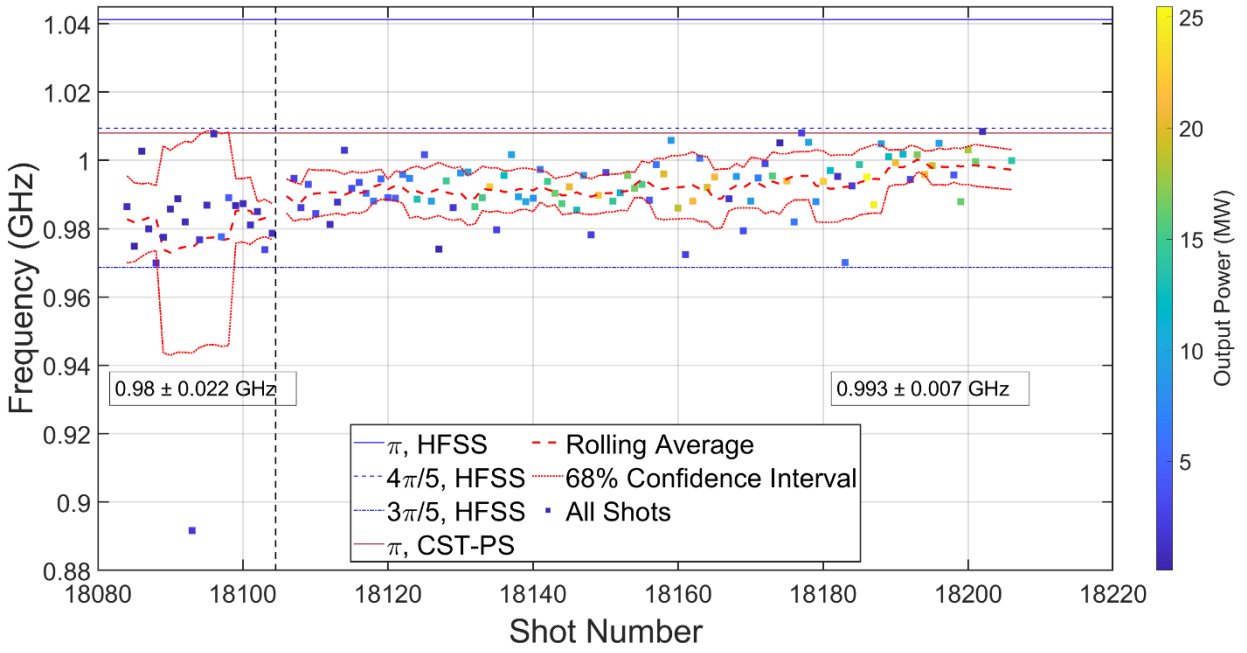

Figure 6.4: MILO microwave frequency over shot number with rolling average and expected frequency overlaid. The experiments with r_d = 8 mm and 10 mm are to the left and right of the vertical black dashed line, operating at 0.98 GHz ± 0.022 GHz and 0.993 GHz ± 7 MHz, respectively.

Alternatively, it could be argued that the bulk of the shots in the r_d = 10 mm experiment were dominant in the π-mode, except seven shots operating near 0.976 MHz, which are likely the 4π/5 mode. The average frequency in the r_d = 10 mm experiment was 993 ± 7 MHz, and the expected CST-PS hot estimate was 1.008 GHz. This 15 MHz difference is larger than expected, but acceptable. Over the final 20 shots of the experiment where the MILO demonstrated its best performance, the rolling average shifted upward within 10 MHz of the CST-PS π-mode hot-test estimate, which is satisfactory agreement. It is also not surprising that the simulations may underestimate the effect of beam loading in the experiments, where the device operated near Hull cutoff (to be expanded upon in Section 6.3) with a large fill factor. Finally, it must be considered that both CST-PS and ICEPIC predicted π-mode operation for these experiments, and the 4π/5-mode did not appear in these simulations. For these reasons, it is concluded the dominant operating mode for the r_d = 10 mm experiment was the π-mode.

It is less convincing to make this same operating mode argument for the r_d = 8 mm experiment, given that its average frequency is even lower. Figure 6.5 illustrates that the shots operating near 0.976 GHz have roughly the same output power in both experiments; thus, they are likely the same mode, which was previously designated as the 4π/5 mode. In this case, the two outliers (f > 1 GHz), appear to be π-mode dominant.

Ultimately, as it will be shown in Section 6.3 (Figure 6.16b and Figure 6.17b), the phase velocities of the π-mode (0.3c) and 4π/5-mode (0.36c) are generally significantly less than the edge velocity of the Brillouin hub when the MILO was operating, according to the theory derived in Chapter 2. It is possible that either of the modes could have strongly interacted with the beam, and it is difficult to tell them apart with only the frequency information at the output.

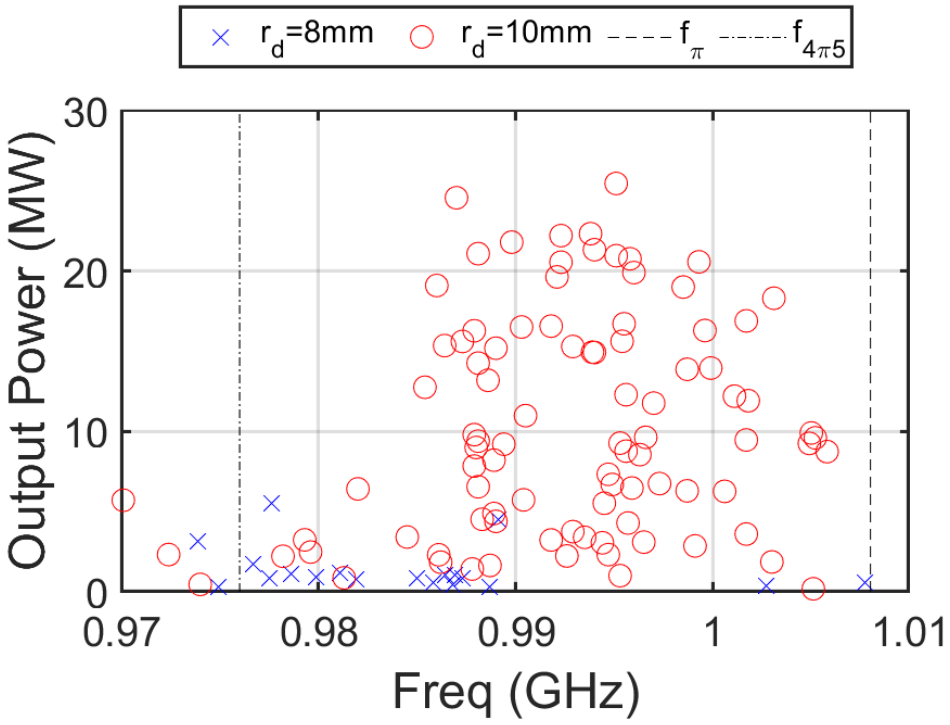

Figure 6.5: Power over frequency for both experiments, compared with hot mode frequency simulation predictions. The majority of r_d = 8 mm shots skew toward the expected 4π/5 frequency, while the r_d = 10 mm experiment agrees more with the π-mode frequency.

The high variance in output power may also be due to mode competition with trapped modes that do not couple into the extractor. The cutoff frequency for WR-650 waveguide is 908 MHz, below which power decays exponentially into the output waveguide. On shot 18147, two peaks were observed at 8 MW and 8.8 MW, separated by 100 ns with the power dropping below 1 MW in-between. Time-frequency analysis of this shot, shown in Figure 6.6, revealed mode-competition near 890 MHz, which is below the waveguide cutoff frequency. This mode appeared

in numerous other shots where the output power was low, particularly in the relatively unsuccessful r_d = 8 mm experiment. The culprit is most likely the π-mode of the choke section, located at 912 MHz. The choke is only two cavities, and the mode did not appear in hot simulations of the device, so this result is surprising. However, the velvet emitter did extend into the choke section, which is not common in other devices. Typically, the cathode is tapered in the choke section [80], [136]–[138], but this technique was not applied to the cathode rod because its radius was relatively small. Nonetheless, this cathode technique should be attempted in future experiments. Another candidate would be the 2π/5-mode, which is unlikely because its expected frequency (844 MHz) is lower than the measurements, and its phase velocity is very high. It is unclear to what degree this mode was present in the r_d = 10 mm experiment; the mode competition induced by the choke might have been more harmful than the positive benefits it provided. Additional experiments with the choke removed or with emission disabled in this portion of the device should be performed to see if the mode remains or if the output power improves.

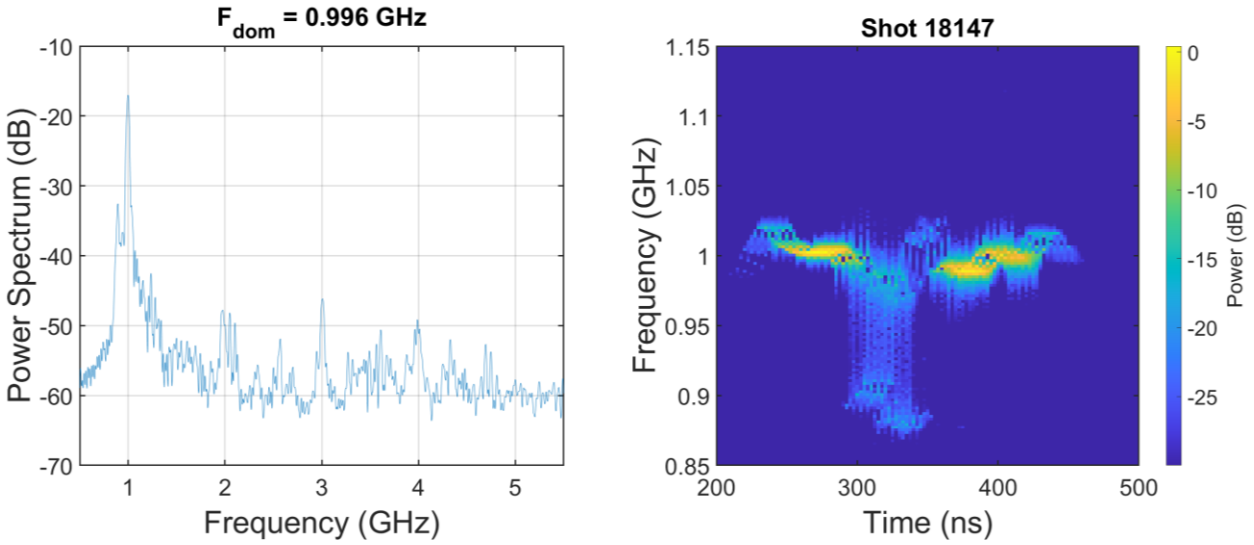

Figure 6.6: FFT (left) and TFA (right) of the output waveguide microwave signal for shot 18147. This shot demonstrated multiple peaks in the output power, one at 8 MW and the other at 8.8 MW. There was mode competition with a mode at 890 MHz, beneath the waveguide cutoff frequency, which is likely the π-mode of the choke section.

Successful implementation of additional diagnostics such as cavity B-dots to measure oscillations independent of the extractor would also be desirable. These were attempted on multiple oscillating cavities but failed to produce a useful output signal. It is conjectured that this occurred because the MILO was not well-grounded directly to the chamber in proximity to the cavities. Prior experiments without extraction successfully probed cavity oscillations, where the anode was mounted within the chamber on a pair of support wheels. Such supports were not

implemented in these experiments because the extractor supported the device in the chamber through its mounting to the end-flange. Implementation of a support wheel in proximity to the cavities may alleviate this issue and improve the ease of loading and unloading the MILO from the experimental chamber.

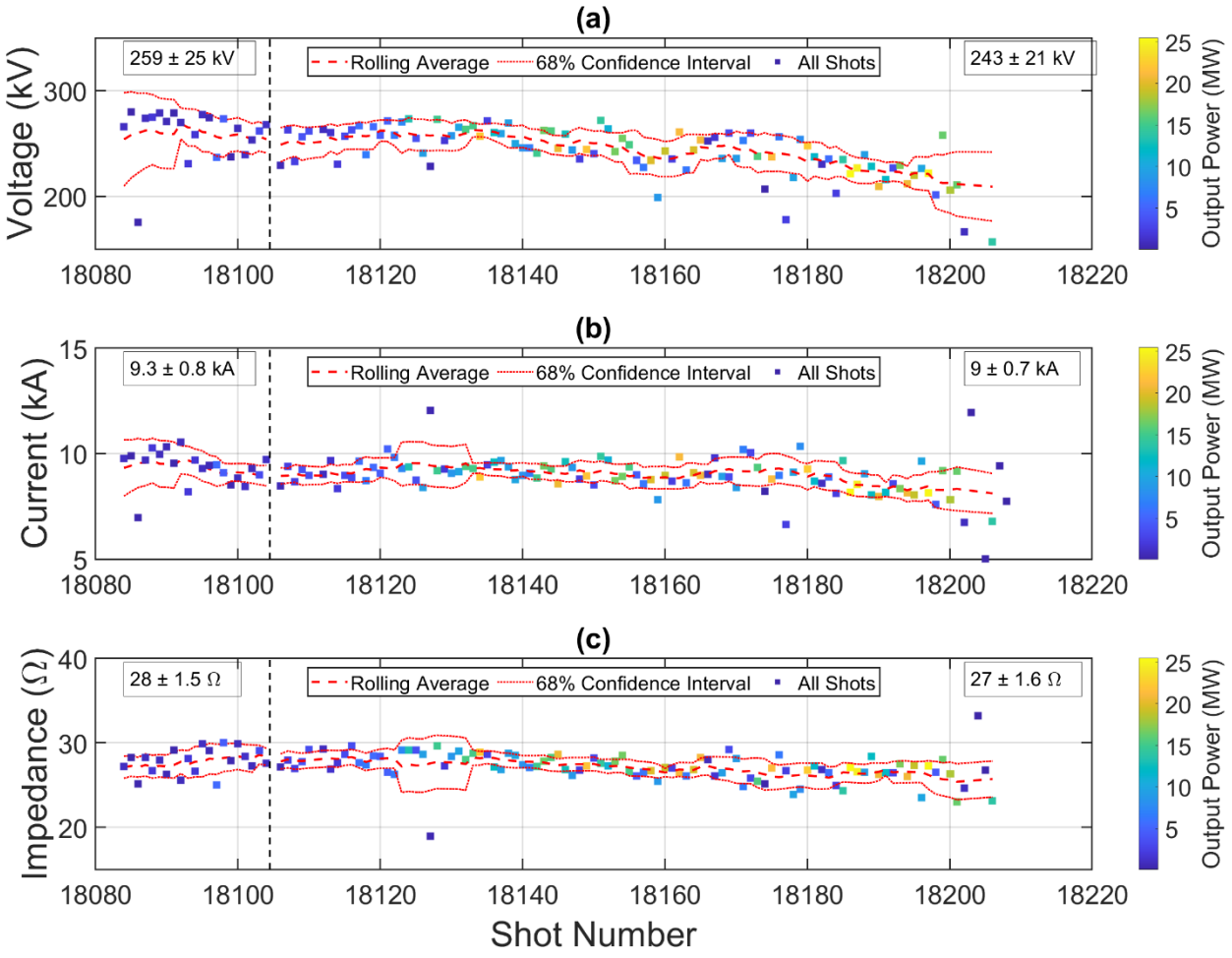

Figure 6.7: Voltage (a), current (b), and impedance (c) over shot number, with rolling average overlaid. These values are taken at the instant of peak microwave generation. Notably, the current at operation is less than 10 kA. The impedance was the most consistent indicator of when the MILO would oscillate, and it agrees well with the PIC estimates that were near 28 Ω. The experiments with r_d = 8 mm and 10 mm are to the left and right of the vertical black dashed line, respectively.

Pulsed power characteristics at the instant of peak power generation are given in Figure 6.7. The voltage, current, and impedance were all relatively consistent across both experiments. As opposed to the RF output power, where the standard deviation was nearly as large as the average, the standard deviation for these parameters was less than 10% of the average value. Regardless of the voltage or current, the MILO tended toward excitation at roughly the same impedance, which is proportional to the beam velocity (V/I α E/B). The experimental

measurements agree very well with the fixed-impedance operation observed in the PIC estimates, which were in the range of 27-28 Ω. In a broader investigation of r_d, it would be interesting to see if the operational impedance varies or remains the same as in these two experiments; however, improved operation likely relies heavily on the consistent formation of an electron beam near the cavities. As more shots were taken, the startup time decreased (Figure 6.9), resulting in operation at reduced voltage and current; counterintuitively, this resulted in higher power generation. Significantly, operation at less than 10 kA was achieved (in agreement with simulations and Lau's theory [93]) and at a relatively high impedance for MILO devices.

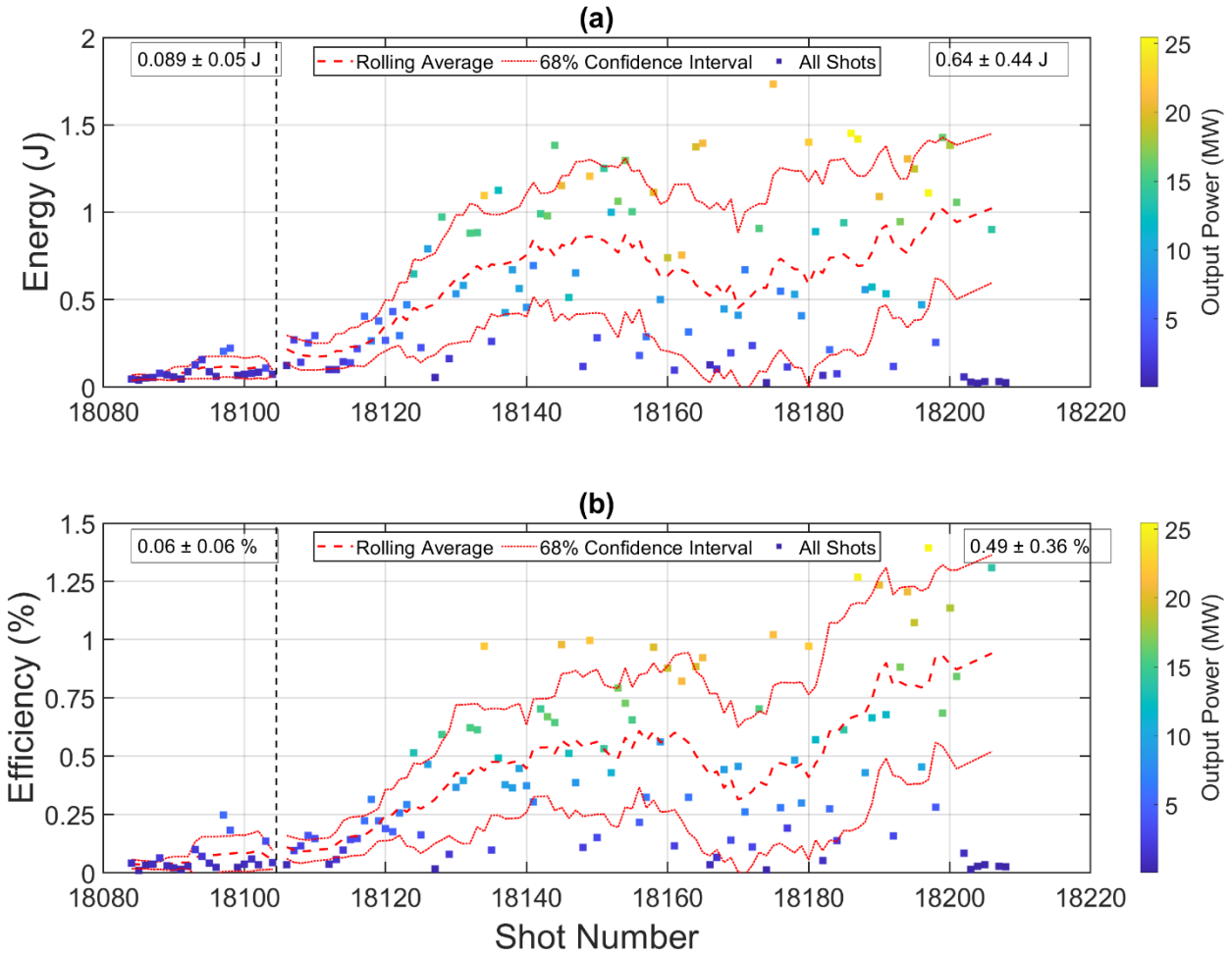

Figure 6.8: Total microwave pulse energy (a) and total efficiency at the instant of peak microwave generation (b), over shot number with rolling average overlaid. The experiments with r_d = 8 mm and 10 mm are to the left and right of the vertical black dashed line, respectively.

The total pulse energy and efficiency are shown in Figure 6.8. Because both of these parameters are proportional to the output power, they were maximized on shots where the power was high. The highest power shots achieved efficiencies between 1% and 1.5% and total energy

between 1 J and 1.5 J. The overall efficiency in the r_d = 10 mm experiment was 0.49% ± 0.36%, but the rolling average approached 1% over the last 20 shots. MILO efficiencies are commonly in the single digits of percent. The efficiency may be improved by adding a cavity to form a 6-cavity structure, which was shown to enhance the output power in simulations without significantly increasing the input current.

Finally, microwave pulse length and startup time are shown in Figure 6.9. Pulse lengths of the r_d = 8 mm experiment had a large degree of variance because the output peak was relatively small compared to the noise floor. Shots where several megawatts were measured enabled reliable estimates of the pulse length, which was on the order of 100 ns. In the r_d = 10 mm experiment, the MILO oscillated near the peak of the voltage. The oscillation startup time was 251 ± 53 ns, while the voltage rise time was very similar at 253 ± 23 ns.

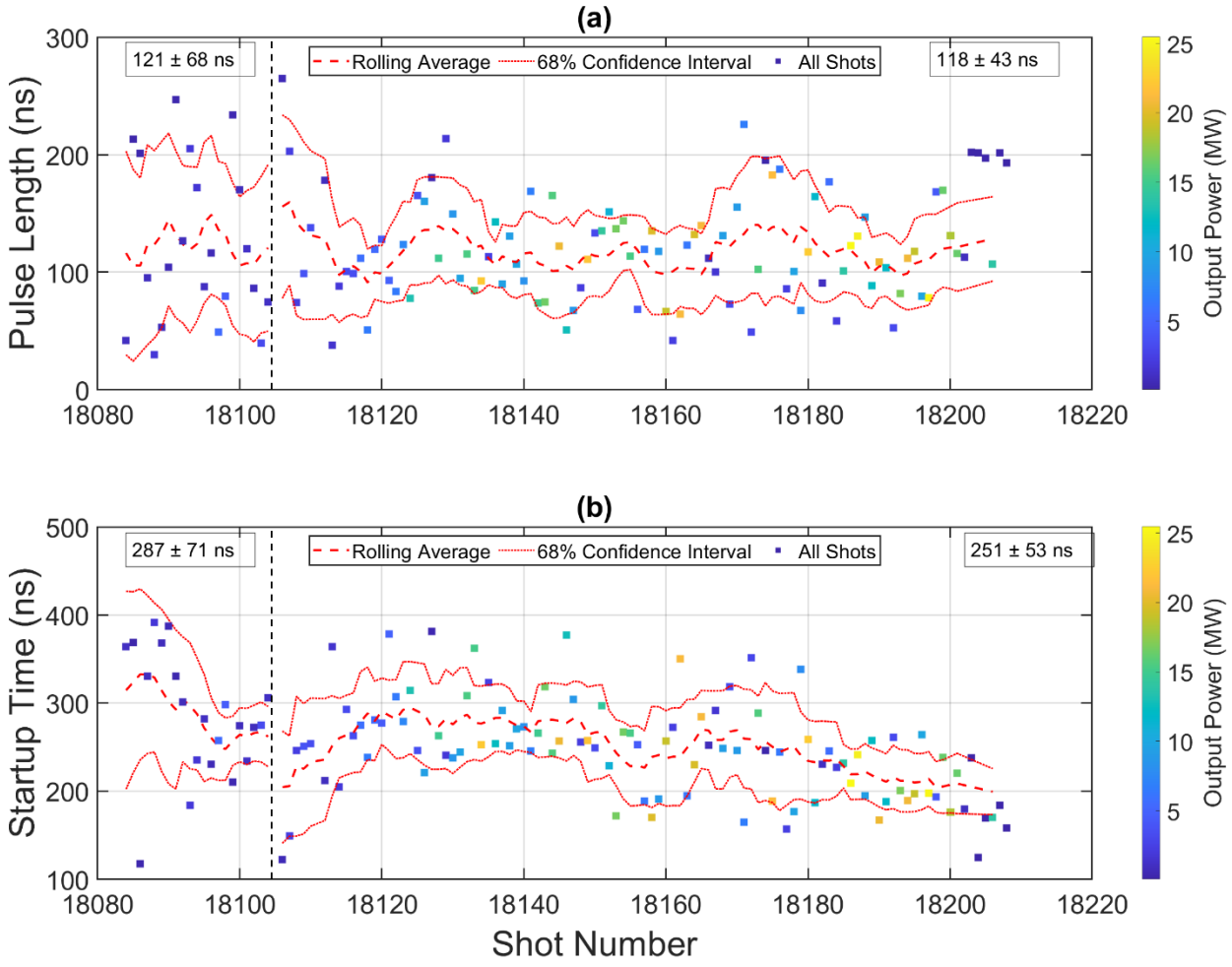

Figure 6.9: Microwave pulse length (a) and startup time (b) over shot number with rolling average overlaid. The experiments with r_d = 8 mm and 10 mm are to the left and right of the vertical black dashed line, respectively.

6.2 Hardware Disassembly and Inspection

Upon completion of the experiments reviewed in the prior section, the MILO was disassembled for inspection of damage. The SWS components are shown in Figure 6.10. These discs are stacked upon each other in the labeled order to compose a modular circuit. The final and penultimate vanes were covered in ablated graphite dust from the repetitive pulsing of the MILO into the downstream diode graphite anode. The vanes closer to the extractor, which experienced the largest electric fields in simulation, have more pronounced burn marks on the face where the spokes made impact. The burn-marks grew darker at larger radii, indicating the electrons were pulled deeply into the cavities. This pattern indicates operation in a microwave mode rather than the pre-insulation phase where electrons stream directly across the gap, which would be expected to produce comparable damage on each vane.

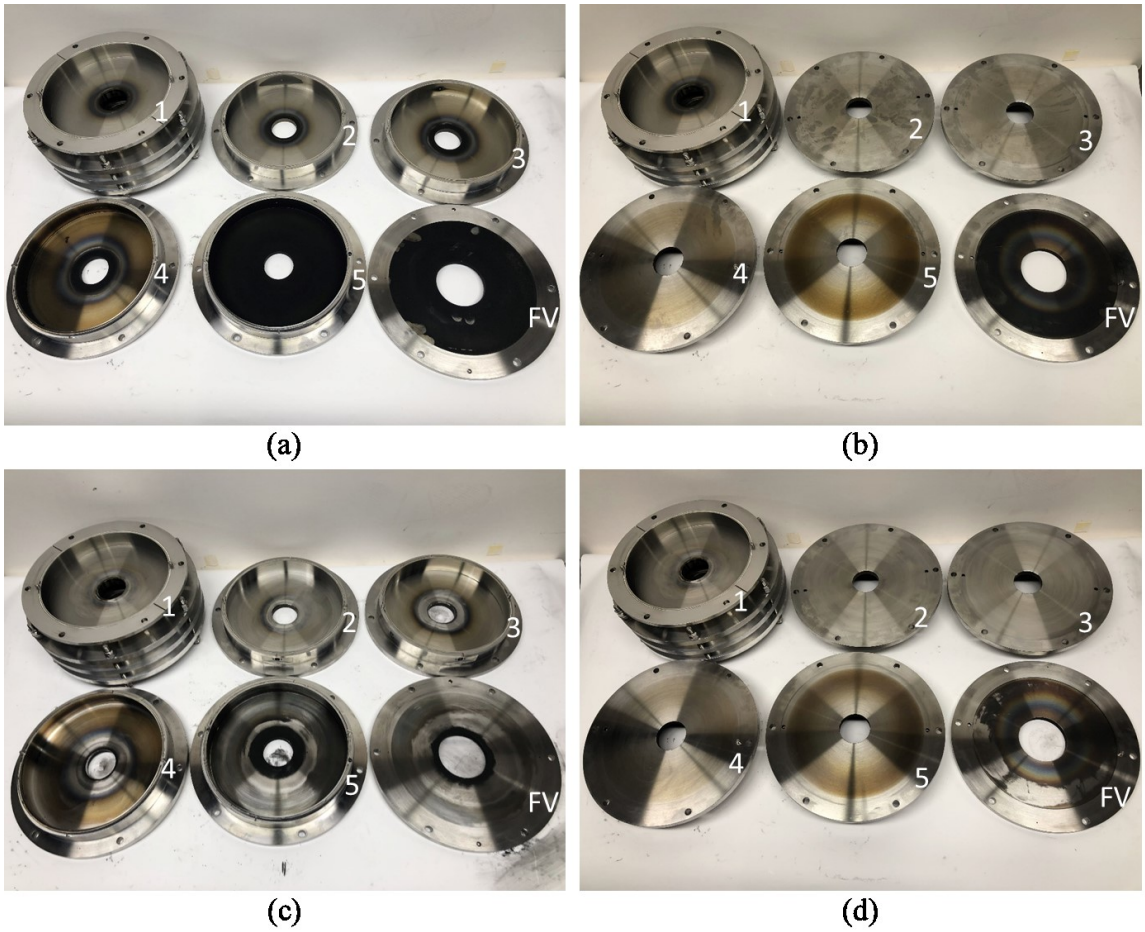

Figure 6.10: MILO SWS disassembled. Cavities one through five are pictured from left to right and top to bottom, with the final vane in the lower right. (a) The back of each vane, which is not exposed to the electron spokes, are shown face up. (b) The front of each vane is shown face up. This is where the electron spokes make direct impact with the SWS. (c,d) These are identical to (a,b), respectively, but pictured after cleaning off the ablated graphite dust with acetone.

The downstream cathode is considered the component that limited the MILO experiment to 104 shots in the r_d = 10 mm experiment. Velvet has previously been used on other MILO devices to extract 10^5 shots [9] without replacing the cathode, so the velvet itself is unlikely to be the problem. Instead, its fabrication method proved problematic. The downstream cathode consisted of a stainless steel cylinder encapsulated in a sleeve of velvet composed of two pieces, one of which was circular that covered the top of the cathode and a rectangular piece that wrapped around the lateral surface area. These two velvet pieces were sewn together and pulled over the metal cylinder such that the seams were at the corner of the top circular surface. As shown in Figure 6.11, these seams were destroyed over the course of the successful r_d = 10 mm experiment. Counterintuitively, the destruction of the downstream cathode emitter may explain the improved MILO performance later on in the experiment. As the top circular portion of the velvet was damaged and lost electrical contact with the metal cylinder, it likely emitted less current altogether, thus enabling more current to be drawn on the velvet cathode rod in the cavity interaction space. When the velvet made physical contact with the graphite anode in the final shots of the experiment, it shorted and became impossible to achieve the voltages necessary for operation. Future iterations of this cathode may benefit from brazed carbon fiber, only placing the emitter on the lateral cylindrical surface, switching to a graphite cathode, or gluing the velvet onto the metal with a conductive epoxy rather than relying on the sewn threads to hold up over hundreds of shots.

Conversely, the velvet on the cathode rod near the cavities was constructed by wrapping a rectangular piece around the lateral surface of the rod and sewing it to make snug contact with the metal surface. It remained structurally intact despite being sewn, probably because a much larger fraction of the current was emitted on the downstream cathode. This velvet emitter was also coated in graphite despite being relatively distant from the graphite anode. Pulse lengths did not suffer as more shots were taken, despite the improvements in output power, indicating that the graphite coating had little effect on gap closure.

(a) (b)

Figure 6.11: Disassembled cathode. (a) The disassembled cathode is shown to the right, pictured next to a clean and unused cathode on the left. The velvet on the rod maintained structural integrity, but was coated in graphite dust. (b) The velvet on the downstream cathode was originally sewn to encapsulate a metal cylinder, which was connected to the cathode stalk with a bolt. After 104 shots, the velvet deteriorated at the sewn seams and almost completely detached from the top circular face of the cathode.

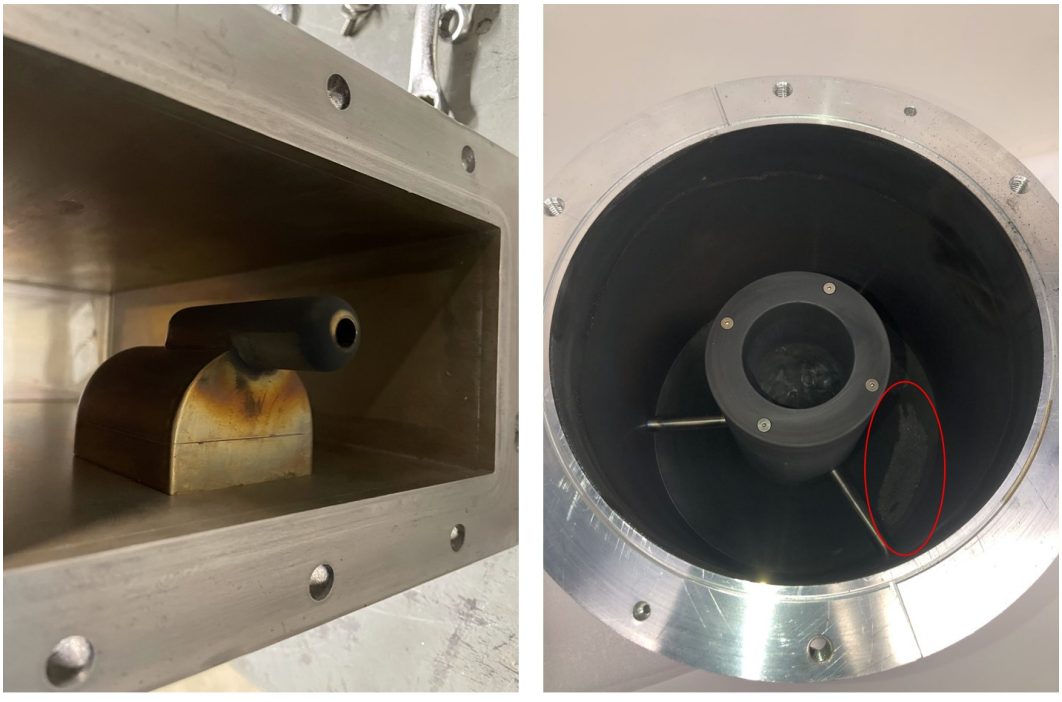

(a) (b)

Figure 6.12: Components of the disassembled extractor. (a) The DFA was covered in graphite dust, which may have contributed to breakdown in the output waveguide. (b) The tapered coaxial extractor was also covered in graphite dust. A large arc is circled on the tapered portion of the output coaxial line.

A layer of graphite dust coated the entirety of the coaxial output extractor and the distributed field adaptor (DFA), which transitioned the coaxial output wave into the TE_{10} waveguide mode, illustrated in Figure 6.12. A large arc is also visible on the outer conductor of the tapered portion of the coaxial line, as well as burn marks on the DFA. These features raised questions about whether the microwaves were cut off or reflected by breakdown and generation of plasma within the extractor. Under consideration of optical fiber measurements of light exposure in the output waveguide made in conjunction with a photo-multiplier tube (PMT), this seems unlikely (shown below).

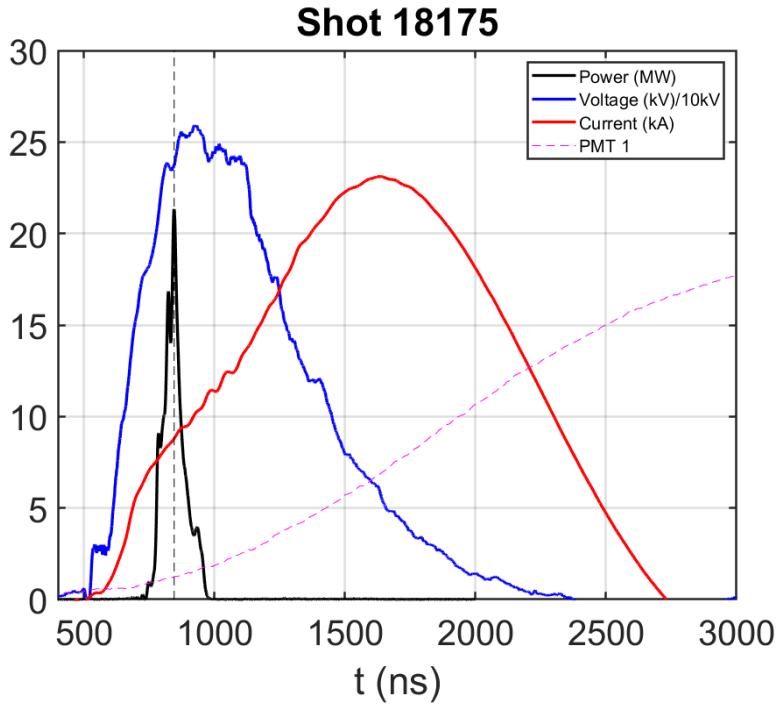

Figure 6.13: Shot 18175 is overlaid with a fiber optic measurement of visible light within the output waveguide. Light was present in the waveguide on every shot, but its peak was measured much later in time than when microwaves were observed. The light exposure over the duration of microwave generation was minimal in comparison to the peak.

An optical fiber was placed on the atmospheric side of the microwave window to measure visible light within the extractor. A sample of these measurements, shown in Figure 6.13, demonstrates significant presence of visible radiation in the output waveguide, thus indicating the presence of a plasma likely due to diode plasma shorting. This light was measured on every shot, regardless of the peak microwave generation. The peak of these light measurements was nearly always an order of magnitude larger than it was at the instant in which microwave generation ceased. Critically, this peak occurred much later in time. The plasma was likely generated later on as the input current reached maximum and traveled to ground through the DFA. Ultimately, this

suggests that microwaves were limited by ordinary gap closure in the cavity region. The presence of this plasma and the resultant wear and tear on the hardware could be mitigated by making larger gaps in the coaxial-to-waveguide transition. Still, it is unlikely this would significantly increase microwave power or pulse length.

6.3 Comparison with Theory

In Chapter 2, a comprehensive theory of Brillouin flow was derived for the geometry of interest in these MILO experiments. In this theoretical treatment, the full electric and magnetic fields and Brillouin flow profile become defined after specifying the geometry with boundary conditions, namely the anode voltage V_a and total magnetic flux A_a. The magnetic flux at Hull cutoff, A_a^{min}, is the minimum flux required to insulate the coaxial diode, and it is uniquely determined by the anode voltage through Eq. 2.46. In defining the voltage and total flux as boundary conditions, the degree of magnetic insulation immediately follows. The degree of magnetic insulation is otherwise referred to as the *flux ratio,* A_a/A_a^{min}. Because the primary interest is the characterization of the Brillouin flow in an insulated state, where the hub height is less than the AK gap distance, the flux ratio is by definition greater than one.

The approach in Chapter 2 is inherently ambiguous to the method of magnetic field generation. In the case of the MILO, the magnetic flux is established by a combination of cathode wall currents I_c and the space charge current carried in the Brillouin hub I_e (see Eqs. 2.74-2.75). These currents add together to compose the total input current to the device, $I_c + I_e = I_a$. With the theory, the magnetic field at the anode and cathode may be obtained. Ampère's Law can then be used to ascertain I_a, I_c, and I_e, each as a function of the voltage and flux ratio. Plots for these quantities are shown in Figure 6.14 and Figure 6.15, tailored to the voltages and dimensions (~250 kV, r_c = 7 mm, r_a = 25 mm) applicable to the experiments described in Section 6.1.

Intuitively, it is expected that to raise the flux ratio beyond Hull cutoff in a MILO, the total injected current must be increased monotonically. The theory reveals that the operation of a magnetically insulated transmission line near Hull cutoff is more nuanced. Depicted in Figure 6.14a and Figure 6.15a is the total current required to achieve varying degrees of magnetic insulation over a range of voltages. *At constant voltage as the flux ratio decreases towards unity, there exists a v-shaped curve wherein the flux ratio becomes a double-valued function of the total current*. *Within this v-shaped curve, the total current required to insulate the diode is less than the*

current at Hull cutoff. The upper bound of this double-valued region is designated I_a^{dbl}, and it is equal to the total current at Hull cutoff. The flux ratio over which the v-shaped curve spans is thus $1 < A_a/A_a^{min} < A_a(I_a = I_a^{dbl})/A_a^{min}$, beyond which the total current increases monotonically with the flux ratio. The lower bound of the double-valued region is I_a^{min}, and its associated flux ratio is $A_a(I_a = I_a^{min})/A_a^{min}$.

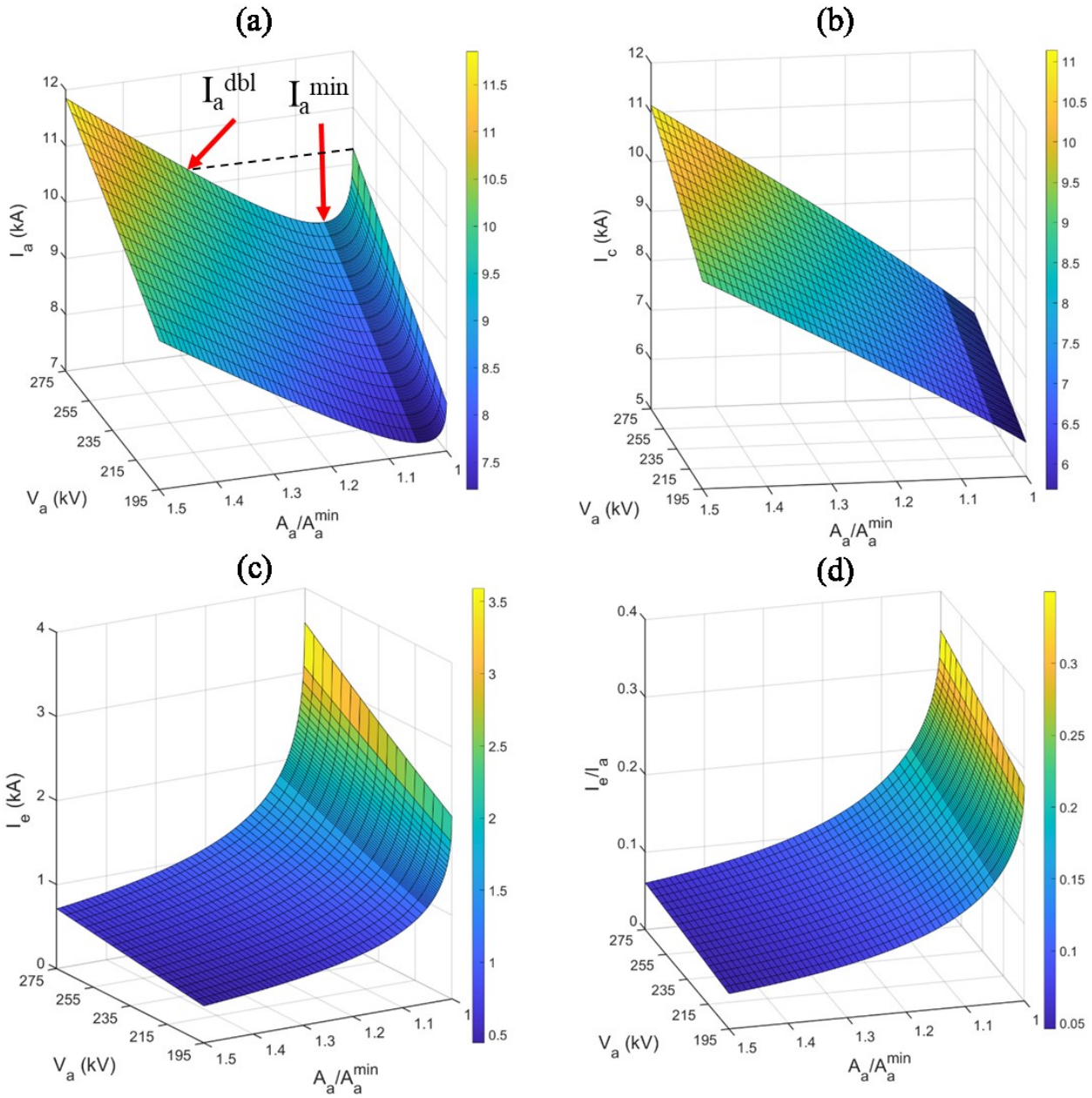

Figure 6.14: Total current I_a (a), cathode current I_c (b), electron hub current I_e (c), and I_e/I_a (d) as a function of voltage V and flux ratio A_a/A_a^{min}, as determined from Eqs. 2.74-2.75. A v-shape in I_a appears as the flux ratio approaches unity, due to the large increase in I_e in this parameter space. The lower and upper bounds of the anode current in the v-shaped region are I_a^{min} and I_a^{dbl}, which at constant voltage are the minimum current and the current at Hull cutoff, respectively. (a-c) are specific to the geometry applied in the experiment, while (d) is general. The same information is presented in Figure 6.15, in two-dimensional form.

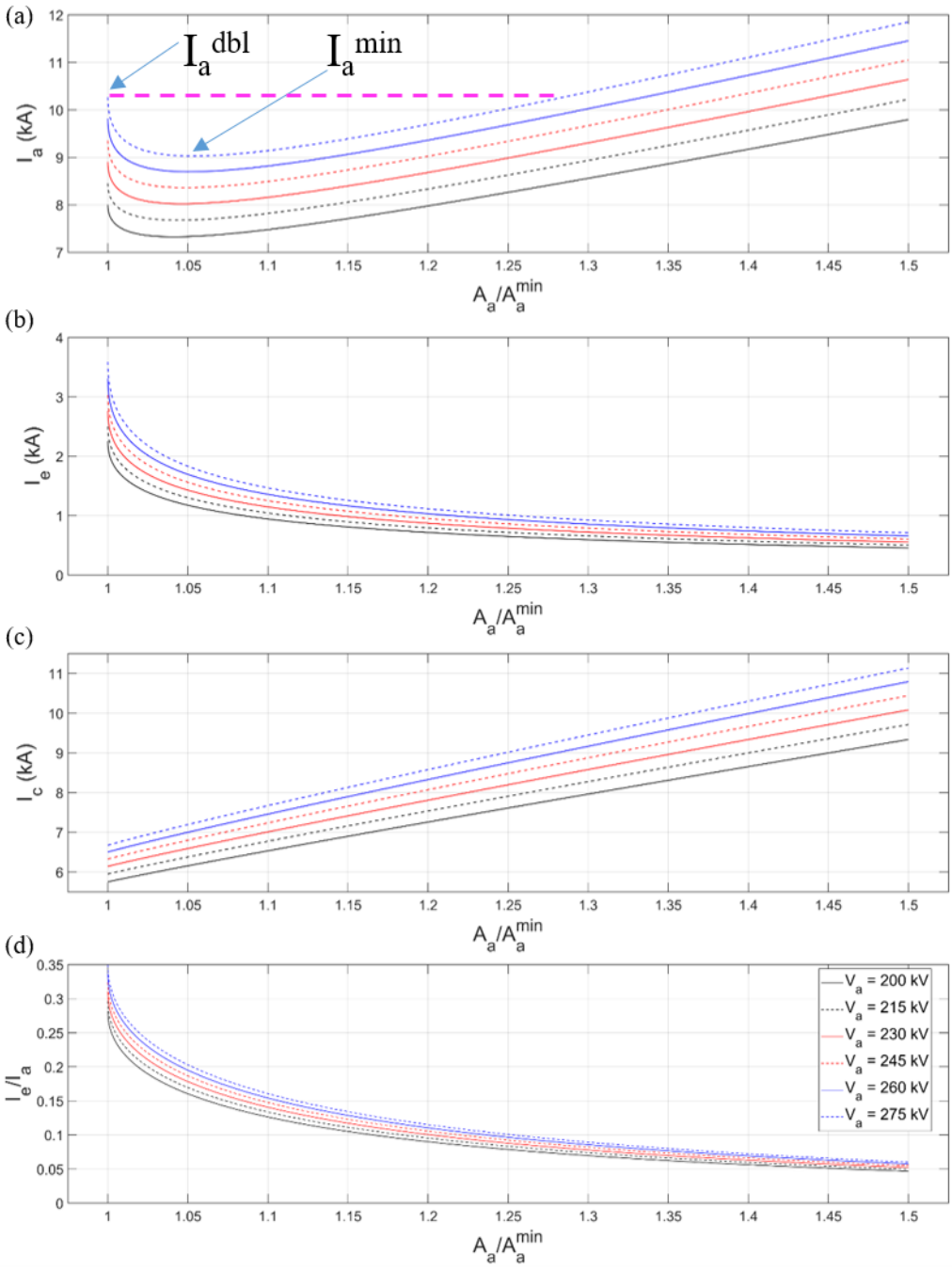

Figure 6.15: Parameterized, two-dimensional plot of the same information given in Figure 6.14, with the flux ratio as the abscissa. The legend in (d) applies to all other plots in this figure. In (a), the v-shaped curve is detailed for V_a = 275 kV. I_a^{min} is called out directly at the bottom of the v-shaped curve, while I_a^{dbl} is the current required at A_a/A_a^{min} = 1. The v-shaped region exists across the domain where $I_a^{min} < I_a < I_a^{dbl}$, marked by the dashed pink line.

As magnetic insulation is being lost (i.e., as the flux ratio decreases towards unity), the current carried within the electron hub increases sharply while the cathode wall current remains steady. This is captured in both Figure 6.14 and Figure 6.15 (b and c). This is where the v-shaped

nature of the total current originates. The extent to which I_c or I_e contribute to the total magnetic flux depends on the flux ratio. In Chapter 2, the hub current was shown to contribute little to the total flux in a well-insulated diode. This result is reaffirmed in Figure 6.14d and Figure 6.15d, which demonstrates that if the flux ratio is greater than 1.3, the electron hub current comprises less than 10% of the total current. However, as the flux ratio decreases towards unity, the hub current plays an increasingly important role in maintaining insulation (alternatively, the gradual lack of insulation makes the hub current larger). The vast majority of experimental shots were within 195 kV < V_a < 275 kV, and 1 < A_a/A_a^{min} < 1.3; in this parameter space, the electron current could be anywhere between 10% or 33% of the total current. By Ampère's Law, the hub therefore contributes these same proportions to the magnetic field in the vacuum region. These proportions are increased at higher voltages, which is relevant to the vast majority of other MILOs in the literature. Thus, to maximize the current available within the electron hub, it is preferred to operate the MILO near Hull cutoff. However, it is salient to wonder how this condition changes during oscillation where spokes are generated.

Although the total current is unintuitive near Hull cutoff, Figure 6.16 and Figure 6.17 (a and b) demonstrate the hub radius is indeed a monotonically decreasing function of the flux ratio, along with the edge velocity of the Brillouin hub. Both of these parameters become strong functions of the flux ratio as Hull cutoff is approached. The phase velocity of the π-mode, at 0.3c, is significantly lower than the edge velocity in this parameter space, indicating the mode becomes synchronous with a Brillouin layer deep within the hub. The theoretical maximum efficiency for a MILO, which assumes all hub electrons participate in converting their potential energy to RF, and which ignores the fact that the resonant layer is somewhere inside the Brillouin hub, instead of at the top of the Brillouin hub, is defined $\eta = I_e(V_a - \phi_b)/(I_a V_a) = (1 - \gamma_b^{-1})(1 - \phi_b/V_a)$. This trend is shown in Figure 6.16c and Figure 6.17c. The numerator represents the potential energy drop from hub edge to the anode, which vanishes to zero at Hull cutoff. Conversely, there is an excess of cathode current applied toward establishing magnetic insulation in the limit of large flux ratio, which reduces efficiency. There is a maximum efficiency point at fixed flux ratio (A_a/A_a^{min} = 1.06) very commonly within the v-shaped curve. At this maximum efficiency point, the gradient is in the direction of increased voltage, suggesting the maximum efficiency improves at higher voltages. At 230 kV, the maximum theoretical efficiency is 9.3%. When properly

optimized, PIC estimates at 230 kV projected 3.7% total efficiency, and total efficiency in the experiments was maximized at 1.4%.

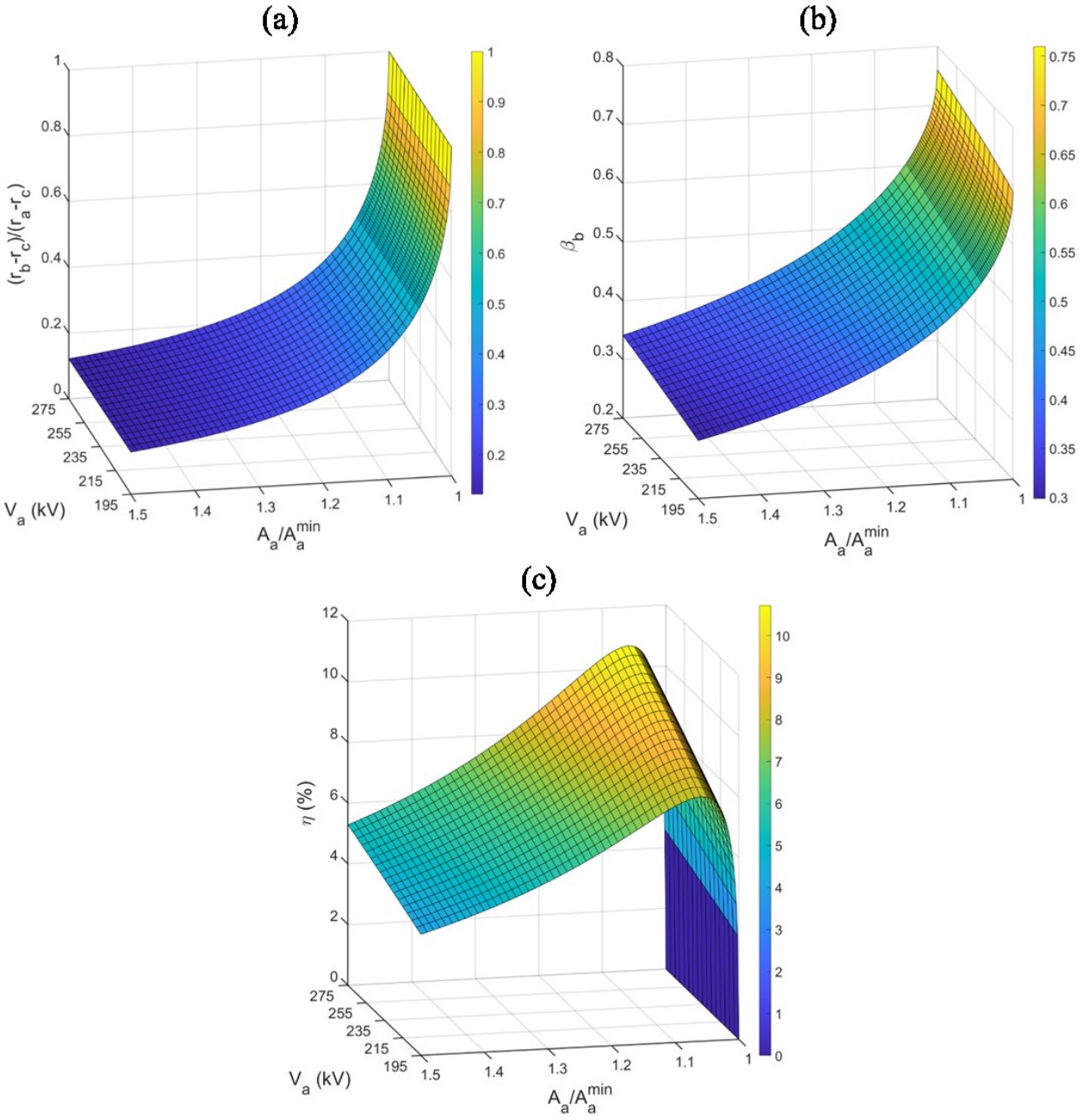

Figure 6.16: Normalized hub radius (a), Brillouin hub edge velocity (b), and maximum total efficiency (c) as a function of voltage and flux ratio. Despite the double-valued nature of I_a, the diode is in fact insulated for $A_a/A_a^{min} > 1$. The maximum total efficiency is very commonly in the double-valued range of I_a, located at a saddle point at $A_a/A_a^{min} = 1.06$, independent of the voltage.

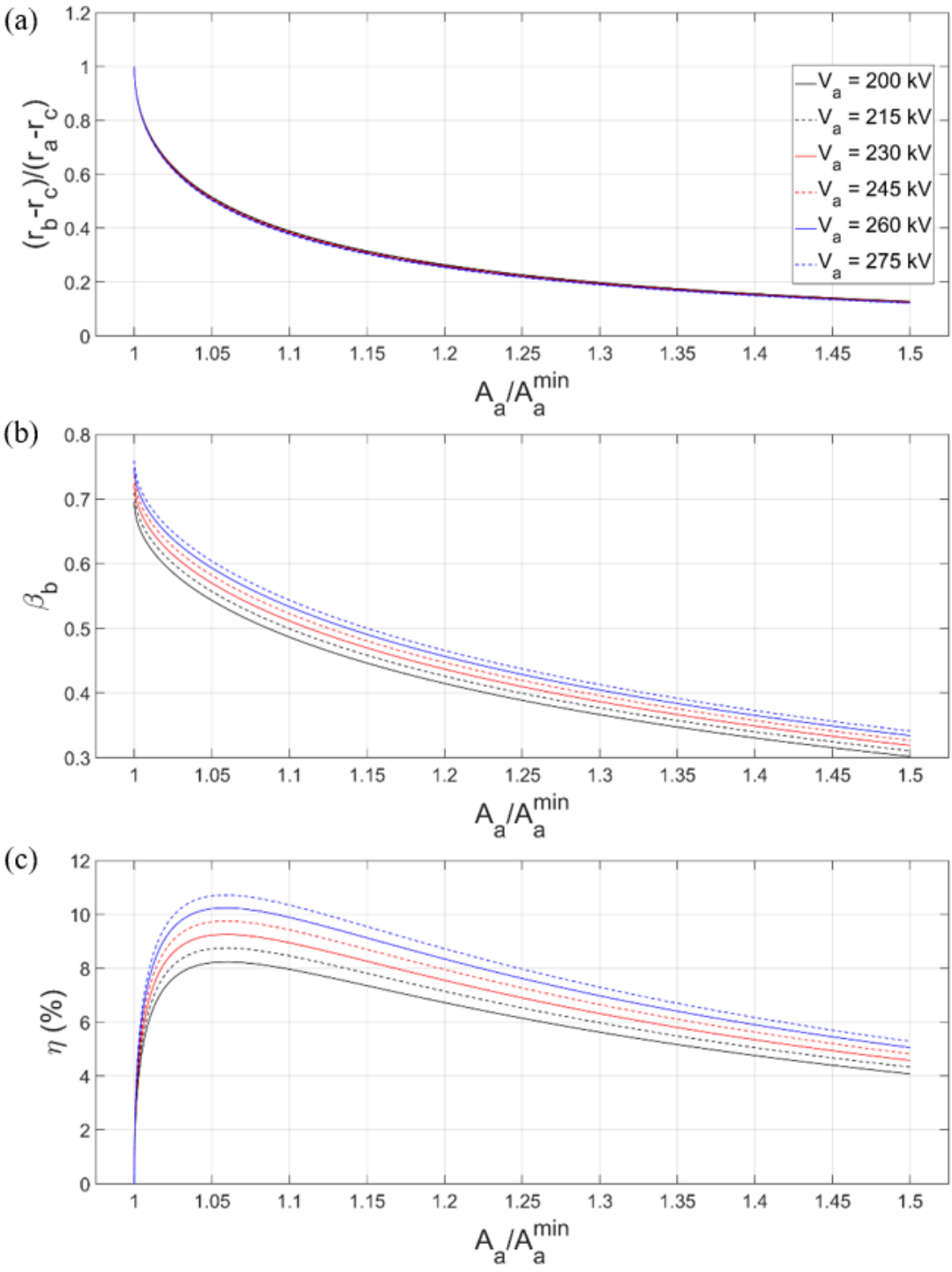

Figure 6.17: Parameterized, two-dimensional plot of the same information given in Figure 6.16, with the flux ratio as the abscissa. The legend in (a) applies to all other plots in this figure. The traces overlap in (a) because the normalized hub height is a weak function of the voltage.

The measured voltage and total current from the experiments are compared directly with the traces for Hull cutoff (I_a^{dbl}), Buneman-Hartree (I_a^{BH}), minimum current (I_a^{min}), and other curves

of constant flux ratio in Figure 6.18. The v-shaped, double-valued region is thus bounded between the solid black line (I_a^{min}) and dashed black line (I_a^{dbl}). In the r_d = 8 and 10 mm experiments, 81% (17/21) and 82% (77/94) of shots achieved maximum microwave power within the double-valued current range, respectively. At the instant of peak power generation, no shots were observed to resonate when the total current was less than I_a^{min}. Except for one shot, all others took place between I_a^{min} and I_a^{BH}. The PIC simulations of the device predicted operation at 8.5 kA and 230 kV (27 Ω), which is squarely in the double-valued region along with the majority of shots.

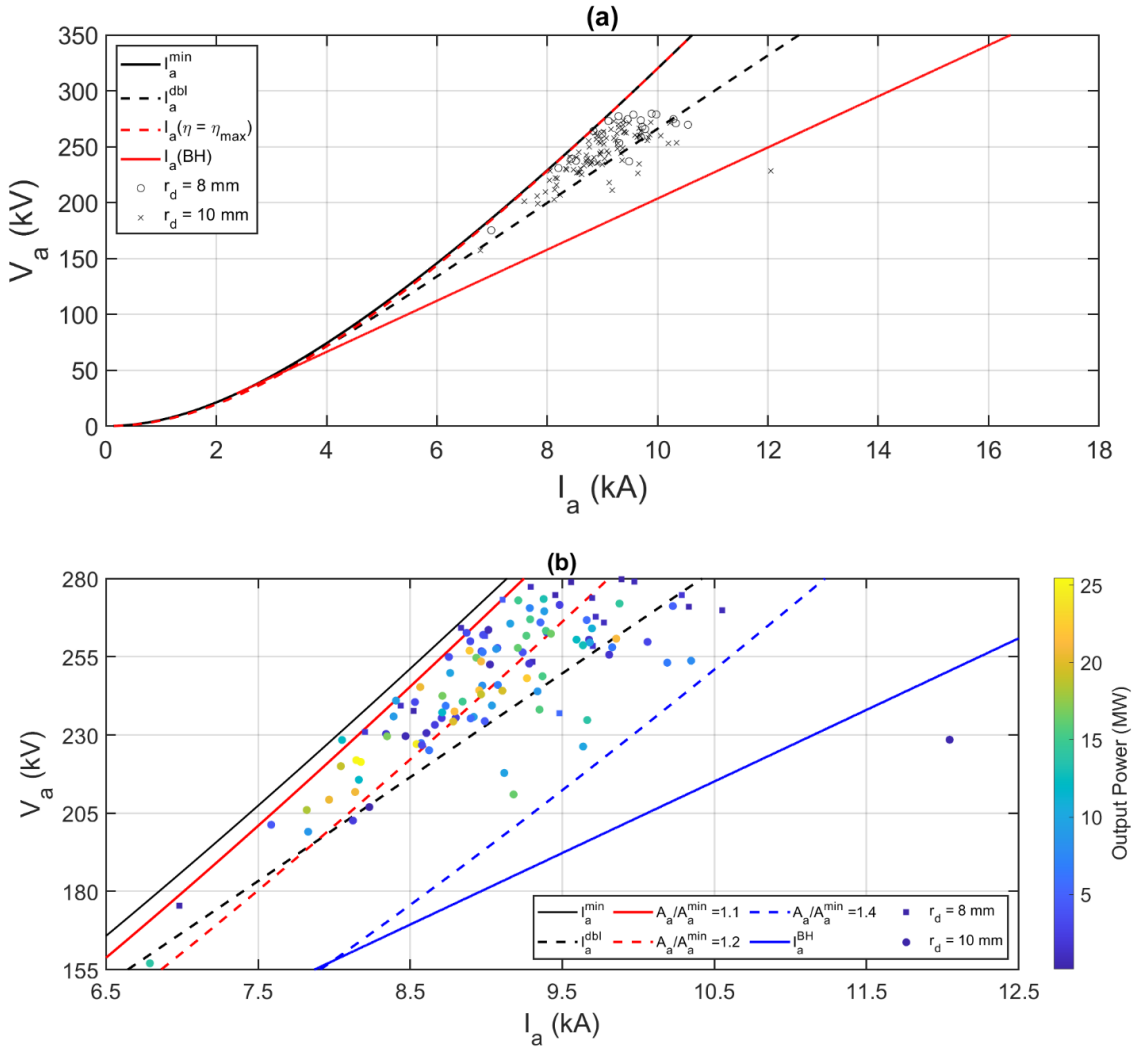

Figure 6.18: (a) Voltage and current from each shot overlaid with theory. (b) Voltage and current from each shot overlaid with theory, with bounds narrowed and color bar to represent output power. I_a^{min} and I_a^{dbl} are the minimum and maximum current in the double-valued range, the latter of which is the current at Hull cutoff. The majority of shots fall within the double-valued region. Not a single shot is observed below the I_a^{min} threshold. Simulations at 230 kV estimated a total current of 8.5 kA, which falls within the double-valued region.

The propensity for the device to operate at currents beneath the Hull cutoff value I_a^{dbl}, in the double-valued region, in both experiments and simulation is a highly original result for MILOs.

It must be considered that there is a physical reason for this tendency, although it is unclear at this time what that would be. At the same time, it is also possible that the device was designed with a particular phase velocity that becomes synchronous with the Brillouin flow specifically in this regime. It would be interesting to investigate an alternative design of this MILO, with the SWS designed to interact at a reduced phase velocity. Intuitively, it is expected that this may enable interaction with the Brillouin hub insulated beyond the double-valued region, where the edge velocity is lower. However, this is unlikely because the MILO phase velocity of ~0.3c is relatively low. Such a device, however, would be predisposed for less efficient operation. On the other hand, these experimental results suggest that a SWS with rescaled phase velocity would operate at a different voltage and current, but remain within the v-shaped curve. Given the v-shaped curve and a specific phase velocity, it may be possible to quantify the range of impedance over which the device is likely to operate.

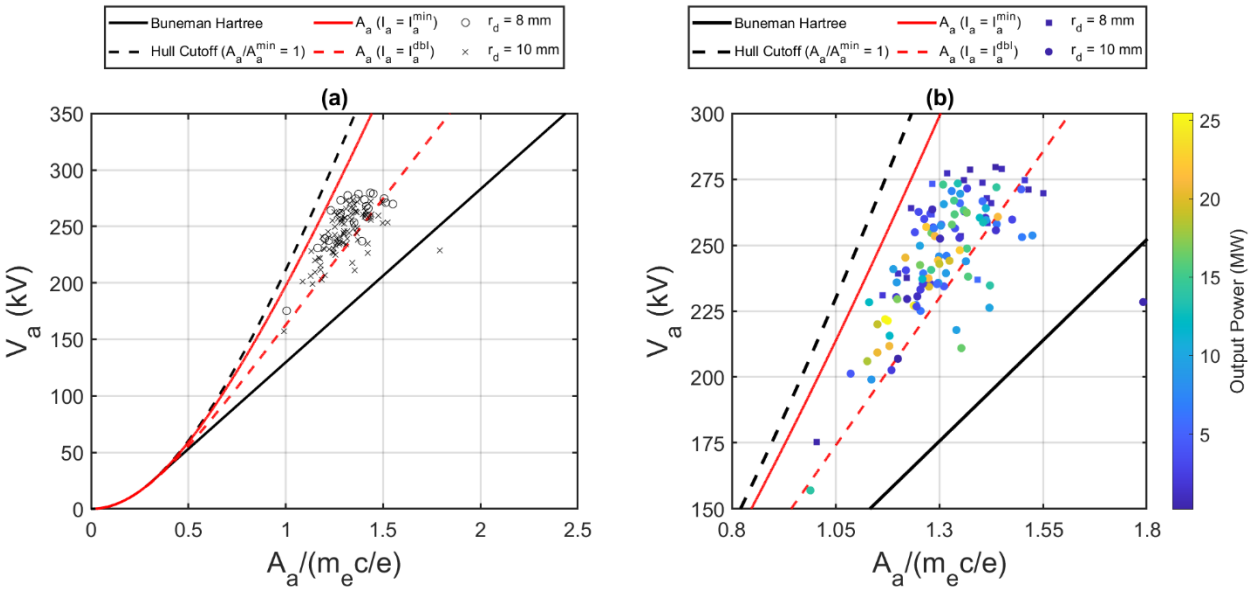

Figure 6.19: (a) Voltage and normalized flux from theoretical conditions and experimental data points. (b) Voltage and normalized flux from theoretical conditions and experimental data points with color bar representing output power. With the exception of one shot, all others fall within the range between the Hull cutoff and Buneman-Hartree conditions.

Using the quantitative values that produced Figure 6.14a and Figure 6.15a as a lookup table, the measured current can be mapped to the flux ratio as a function of the voltage. Thereafter, it is uncomplicated to convert from the flux ratio to the normalized flux using the Hull cutoff condition, Eq. 2.48; this information is displayed in Figure 6.19. It was straightforward to map shots where the current was not in the double-valued portion of the v-shaped curve, because this is where the current is a unique function of the flux ratio. However, if the measured current was

between I_a^{min} and I_a^{dbl} for its specific voltage, there was no unique flux ratio to map the current. For this reason, it was assumed the flux ratio was greater than $A_a(I_a = I_a^{min})/A_a^{min}$ (between the two red lines), expressly ignoring the branch where I_a is inversely proportional to the flux ratio (the left side of the v-shaped curve in Figure 6.15a). This is the reason that no shots appear in the range $1 < A_a/A_a^{min} < A_a(I_a = I_a^{min})/A_a^{min}$ (equivalently, between the black dashed line and solid red line), although there is no concrete rationale for making this assumption.

It is possible that some of the shots that are placed between the two red lines in Figure 6.19 actually fall between the dashed black line and solid red line (i.e., they actually took place on the left-hand side of the v-shaped curve in Figure 6.15a). However, it is impossible to know this without making an approximate measurement of the cathode current I_c. This is another instance where the implementation of a Rogowski coil to measure the current drawn downstream of the SWS would be helpful, because it would provide an estimate of the cathode current. The cathode current monotonically increases with the flux ratio, so there would be no discrepancy in identifying the flux ratio through this method.

Figure 6.19 is directly comparable to Figure 2.2, and is more analogous to the BH diagram typically applied to the magnetron, where the magnetic field is the abscissa. Of course, it does not make much sense to use magnetic field on the abscissa for a MILO in this coaxial geometry, because it is a function of the radius. With one exception, every shot was mapped into the region between Hull cutoff and Buneman-Hartree resonance. Recall that in this region, there exists a resonant layer synchronous with the phase velocity of the electromagnetic mode, and operation is theoretically possible. The experiments operated just above the Hull cutoff condition where insulation is achieved, but never below it.

From Figure 6.19, it is clear that MILO operates far from the Buneman-Hartree condition which was newly discovered, Eq. 2.69. This is in sharp contrast to magnetrons, where operation close to the Buneman-Hartree conditions was usually noted. This is an alternate statement that MILO operates closer to Hull cutoff than the Buneman-Hartree condition.

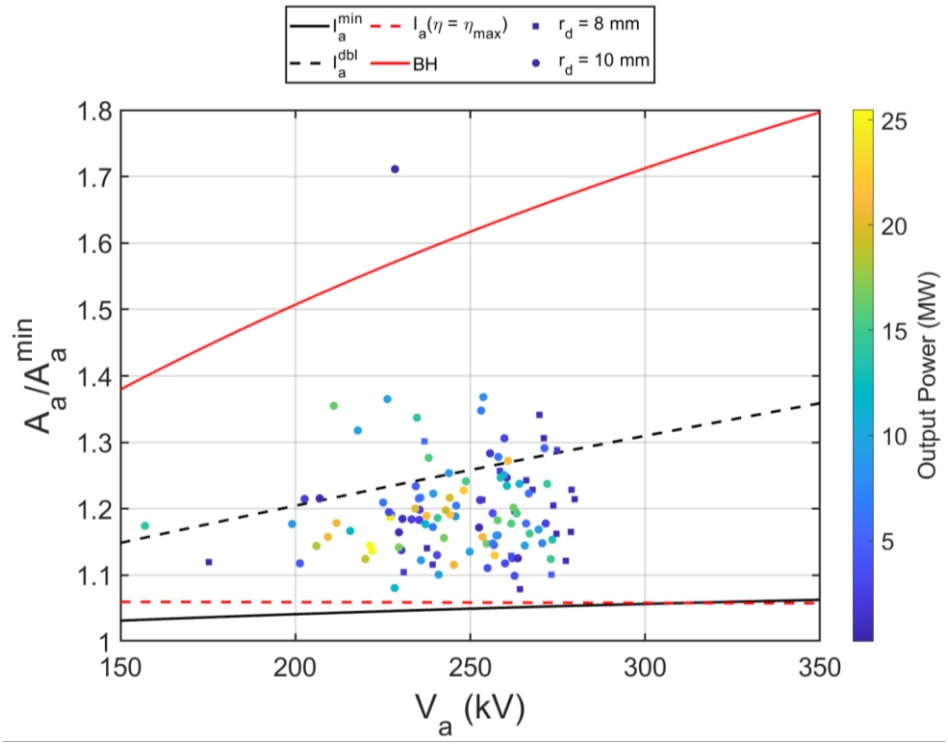

Figure 6.20: Flux ratio for theoretical conditions and experimental data points as a function of voltage. Operation was very commonly observed with the flux ratio in the range $1 < A_a/A_a^{min} < 1.3$.

Finally, the flux ratio mapped to each data point is given along with various conditions from the theory in Figure 6.20. The BH condition would correspond to a flux ratio near 1.5, but over 90% of shots were observed with a flux ratio less than 1.3. Many of these were beneath the flux ratio limit that encapsulates the double-valued region.

Chapter 7 Summary and Conclusions

In this final chapter, a summary is presented of the experiments that were performed and the novel findings that were obtained. Suggestions for future work are also provided.

7.1 Summary

Through a combination of foundational theoretical predictions, rapid prototyping with simulation tools, and experimental investigation, significant contributions were made to the science of multi-frequency magnetrons, and to the operation of high-impedance, moderate current MILOs. A summary of the investigations that took place for these two devices is given here.

7.1.1 HRPM

The development of the HRPM was significantly motivated by the prior work of Greening on the MFRPM [54]. The MFRPM was the first magnetron to demonstrate simultaneous generation of megawatt power levels from two different oscillators in a single device; however, its architecture was limited to the generation of two tones only, and the frequencies could not be controlled by the user. Thus, in the MFRPM, frequency locking resulted in operation in an undesired mode on the SBO. Keeping these limitations in mind, the HRPM was designed such that the RPM geometry could potentially generate four or more frequencies simultaneously. Its two planar oscillators were placed adjacent to each other in the RPM geometry, leaving a smoothbore drift region on the opposite side of the cathode that could feasibly be replaced by a pair of oscillators scaled to different tones.

Harmonic frequency locking is a novel phenomenon first noticed for magnetrons in the MFRPM experiment at UM [66]. It was observed that, over a range of magnetic fields, the SBO would operate at exactly the second harmonic frequency of the LBO. It was hypothesized that the two oscillators behaved as a damped driven harmonic oscillator system, where the LBO and SBO were the driving and driven oscillators, respectively, and were coupled by the harmonic beam content from the LBO-modulated spokes. This content excited the SBO to operate at the exact integer harmonic frequency, shifted from the free running frequency of a normal SBO eigenmode.

The physics of this interaction would thus be controlled by the LBO excitation frequency and the SBO mode quality factor (which dictates the bandwidth of a given eigenmode). Maximum power output is expected from the SBO when driven on resonance.

The HRPM was designed utilizing the HFSS, CST-PS, and ICEPIC simulation codes with the specific intention of investigating this hypothesis. The LBO was mounted with a tuner to shift its frequency from shot-to-shot. The SBO was equipped with an all-cavity extraction scheme to measure its output power, and its quality factor could be changed over the course of three different experiments with ease. The Buneman-Hartree equation was satisfied for both structures to allow microwave generation with the same (E/B) beam velocity.

The HRPM experiments were conducted at high Q, moderate Q, and low Q. In each of these experiments, the SBO was excited with a range of frequencies from the LBO by varying the tuner position. As the quality factor decreased, SBO performance improved. Not only did its output power increase, but also its resonant frequency tracked in a more consistent and linear manner with the LBO harmonic frequency. The range of harmonic frequency locking increased as the quality factor decreased. By correctly tuning the LBO, the SBO desired π-mode was excited. When the SBO π-mode was driven close to its expected free-running frequency, maximum power output was observed. Experiments at the same quality factors were performed with the SBO in isolation by removing the LBO and replacing it with a smoothbore, planar drift region. In these isolated experiments, the SBO operated predominantly in the 5π/6 mode, and the π-mode was not observed. The optimized SBO power in isolation in the undesired 5π/6 mode was 9.8 ± 1.7 MW (high Q), 18 ± 5 MW (high Q), and 37 ± 12 MW (high Q), whereas the optimized HRPM power in the desired π-mode was 9.5 ± 1.4 MW (high Q), 19 ± 6 MW (high Q), and 28 ± 9 MW (high Q).

An additional experiment was performed where the magnetic field direction was reversed, forcing the electrons to travel in the opposite (ExB) direction. Harmonic locking did not occur in this configuration because the harmonic content from the LBO-modulated spokes would significantly demodulate before reaching the SBO. This supports the initial hypothesis that the LBO and SBO couple through harmonics within the electron beam.

A phase analysis of the LBO and SBO outputs was conducted for the low Q and reversed magnetic field experiments. The phase difference between SBO signals was very inconsistent in the isolated SBO experiment as a function of the magnetic field; the standard deviation in the phase difference was often greater than ±30° and rarely less than ±20°. In the HRPM, harmonic phase

locking occurred (standard deviation of phase difference < ±10°) between the center LBO cavity and the center SBO waveguide if the LBO was tuned properly. The standard deviation of the phase difference between SBO outputs was less than ±30° for a large portion of the HRPM tuning range near the π-mode frequency, but did not exhibit phase locking. When the magnetic field direction was reversed, the SBO phase correlation became comparable to the measurements from the isolated SBO experiment.

7.1.2 MILO

MILO devices are commonly operated at currents near 50 kA and impedance of 5-15 Ω, achieving GW power levels at ~5% total efficiency. The primary development goal of the MILO presented in this dissertation was to push the operating requirements of this device, specifically the current required to achieve magnetic insulation, as low as possible. This achievement was made conceptually possible with the contemporary Brillouin flow treatment developed by Y.Y. Lau [93], which used the voltage and coaxial aspect ratio to predict the current required to achieve varying degrees of magnetic insulation in a coaxial diode with axial flow. Simulations performed in ICEPIC and CST-PS at 230 kV estimated power generation of 70-80 MW and 8.5 kA total current. An experimental investigation of the MILO found its power generation was highly irreproducible with large variance at 10 ± 7 MW at 1 GHz, identified as the π-mode. The best shots of the experiment were observed toward the end of the run, right before the cathode failed, where power and efficiency reached 25 MW and 1.5%, respectively. The MILO consistently operated at a voltage, current, and impedance of 243 ± 21 kV, 9 ± 0.7 kA, and 27 ± 1.6 Ω, respectively. A comparison of the Brillouin flow theory with the experiments revealed operation in a novel Brillouin flow state. Most importantly, our MILO experiments (200-300 kV, ~ 10 kA) seem to operate primarily at a magnetic flux barely above that required for magnetic insulation, typically just between 5 to 30 percent above the Hull cutoff value. Within this typical operating state, the current required to achieve magnetic insulation is actually less than the requirement to achieve Hull cutoff. This is quite different from our experiences with relativistic magnetrons where the operating magnetic field is at least 1.5 times the Hull cutoff value typically. We thus conclude that MILO operates close to Hull cutoff whereas magnetrons operate close to the Buneman-Hartree condition.

7.2 Conclusions

Conclusions drawn from the magnetron and MILO investigations are given below.

7.2.1 HRPM

By placing two adjacent planar oscillators on one side of the planar RPM geometry, the HRPM demonstrates the feasibility for a crossed-field oscillator to generate two locked frequencies at 1 GHz and 2 GHz. Note that this type of device could potentially produce four or more tones simultaneously. To benefit from harmonic frequency locking, sequential oscillators must be an integer harmonic of their upstream neighbor. With the implementation of a frequency agile LBO, the SBO frequency was also tunable by leveraging harmonic frequency locking. Varying the SBO quality factor and LBO frequency over several experiments revealed features consistent with the driven oscillator hypothesis, such as increased bandwidth as the quality factor was reduced. Harmonic frequency locking was no longer observed when the magnetic field (direction of electron flow) was reversed, proving the proximity of the harmonic cavities to the electron spokes produced by the fundamental cavities was important. In considering all of the evidence from the HRPM experiments, it is concluded that the harmonic beam content in the spokes was the coupling mechanism between the oscillators, and the LBO drove the SBO in an Adler-like master-slave condition. The locked state enabled SBO operation in the desired π-mode, when it was otherwise unobserved in isolated-SBO experiments. Although states of harmonic phase locking were observed in some instances between the center LBO cavity and SBO waveguide, this was not broadly the case; phase locking was not observed between the LBO and either of the other SBO waveguides. For this reason, the locked state is considered frequency locked, and not phase locked. However, the phase difference between SBO waveguides in the HRPM demonstrated more consistency than what was observed in the isolated SBO experiments. Phase-locking between RPM cavities will be an area of further investigation at UM.

7.2.2 MILO

This MILO demonstrates the viability of MILO operation at drastically lower current than the vast majority of other devices in the literature (~50-60 kA); to the author's knowledge, this is the lowest current at which MILO operation has been achieved (~9 kA). This research makes MILO operation with higher impedance and lower capacitance pulsed power more viable.

Additionally, the physics of MILO operation was substantially advanced by the discovery of a novel operating state through the treatment in [93], where the total current dips below the Hull cutoff current, despite being magnetically insulated. Over 80% of all experimental shots operated within the double-valued parameter space insulated just above Hull cutoff. A significant physics finding was that this MILO demonstrated a clear tendency for operation close to the Hull cutoff condition, instead of the Buneman-Hartree condition where magnetrons commonly operate.

7.3 Future Work

Methods and concepts for improving and expanding the experiments are provided in this section.

7.3.1 HRPM

One of the most important extensions of these experiments would be the achievement of phase-locking between cavities in the RPM. This is the subject of a new AFOSR project just beginning at UM.

While the HRPM demonstrated a proof of concept for potential magnetron operation at more than two frequencies, this work remains to be shown experimentally. When considering future prototypes, an additional pair of oscillators tuned to 1.5 GHz and 3 GHz placed on the opposite side of the cathode is realistic. Going to substantially higher frequencies would likely require reconsideration of the anode height, which dictates the frequency of axial cavity modes. There is already a small separation in frequency between the SBO fundamental circuit mode and the first higher order axial mode.

Multispectral sources are also far more appealing with power extraction from every oscillator. Implementation of a microwave extractor to the LBO would be a worthwhile upgrade to the HRPM. In an identical investigation, this could significantly alter the behavior of the LBO and SBO with beneficial and negative consequences. Extraction from the LBO would very likely improve the total efficiency. However, in the experiments performed in this dissertation, the LBO is a comparatively high Q oscillator with little drift of its resonant frequency. By reducing its quality factor, the repeatability of the LBO and SBO frequencies could potentially be diminished. Furthermore, it is unclear whether extraction would affect harmonic content in the hub and consequently the kinetic interaction between the oscillators. There are also engineering challenges

in maintaining frequency agility while extracting power; it could be challenging to combine these mechanisms with minimal interference between the extractor and tuner.

Additional experiments with further reductions of the SBO quality factor would be of interest. Past experiments have shown that, with RF priming, magnetrons can achieve higher power at otherwise prohibitively low quality factors without RF priming [139]. A reduction of the SBO quality factor below the critical level required for oscillations from noise would disable power generation in the isolated SBO experiment. The introduction of the LBO and the associated harmonic beam content could be considered an alternative to RF priming, which provides the excitation required to get the SBO to start. This would potentially enable SBO microwave generation at otherwise unachievable power levels.

7.3.2 MILO

Time constraints limited the experimentation that could take place with this MILO. Only one successful experiment, with 104 shots, was obtained at the specific downstream cathode geometry r_d = 10 mm; the r_d = 8 mm experiment was terminated after 21 shots because its performance was poor. Additional experiments could be performed with r_d = 9 mm, 11 mm, 12 mm, and 13 mm. The drastic difference between the r_d = 8 mm and r_d = 10 mm experiments instill optimism that additional variations of r_d would yield improved output powers.

Additional experimental diagnostics are necessary. Most importantly, there must be a method to measure the current collection in the downstream load. It is speculated that the experiment began to produce significant levels of power when the downstream cathode began to fail, thus reducing its current draw and enabling more emission into the cavity interaction space. Consistent generation of an electron hub in the cavity interaction space is considered vital in the literature [140], [141]. The rudimentary cathode used in these experiments did not capitalize on these concepts. This suspicion could be confirmed by implementing a Rogowski coil between the SWS and the output coaxial transmission line. Measurements of the load current also provide an estimate of the current collected on the SWS, enabling a more detailed analysis correlating successful shots to the location of current collection.

Successful probing of the anode cavities using B-dot loops would be very helpful in diagnosing the modes of operation in every shot. Preliminary experiments without microwave extraction were successful in probing the cavities. It is speculated that this is because this anode

was grounded directly to the support wheel, providing a less inductive path to the ground than what was available in the experiments with extraction. An additional failure mechanism is mode competition, but this cannot be confirmed by measuring only the output waveguide signal. Furthermore, evidence of oscillations from the microwave choke were observed in the microwave extractor. These cavities should also be probed directly, and experiments should be considered with the choke section removed completely. Detection of trapped modes is also an advantage of B-dot loops.

The HRPM concept could be extended to this MILO. Initial simulations are underway in which a set of S-Band cavities are placed between the LBO and the extractor. Potentially, the two structures could be frequency locked to each other in the same manner as the HRPM. This addition could yield similar benefits, such as frequency and phase control.

The most important consequence of this MILO research is the discovery of the double-valued v-shaped curve as magnetic insulation approaches the Hull cutoff condition. The propensity for the experiments to operate in this regime draws significant interest because it is a more restrictive range than the generally accepted bounds of the Hull cutoff and Buneman-Hartree conditions for crossed-field devices. The physical reason for the appearance of the v-shaped minimum and the validity of the Brillouin flow theory as the flux ratio approaches unity (where insulation is rapidly lost) both warrant investigation. The flux ratio where the double-valued domain of the v-shaped curve ends also increases as a function of voltage. For the typical MILO operating at 500 kV, the v-shaped curve may extend up to $1 < A_a/A_a^{min} < 1.5$. According to the Brillouin flow theory, the upper end of this range is well insulated, yet its total current may still be below the Hull cutoff current. A comprehensive comparison of this theory with the typical MILO found in the literature is necessary.

Appendices

Appendix A HRPM Detail Drawings

This appendix includes drawings of the parts that were used to complete the HRPM experiments. All measurements are in inches. All components were manufactured from aluminum-6061.

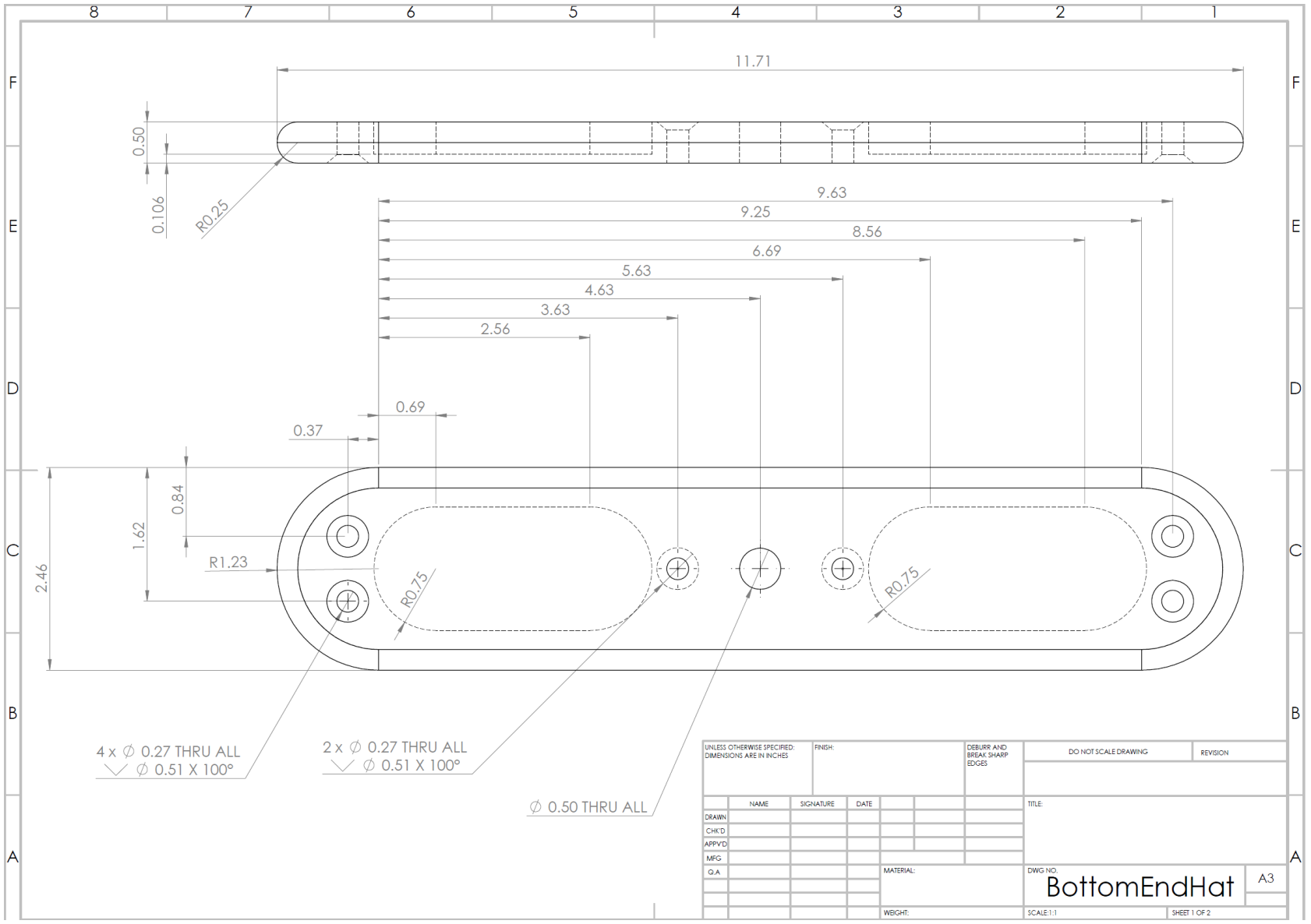

Figure A.1: Bottom endhat of cathode.

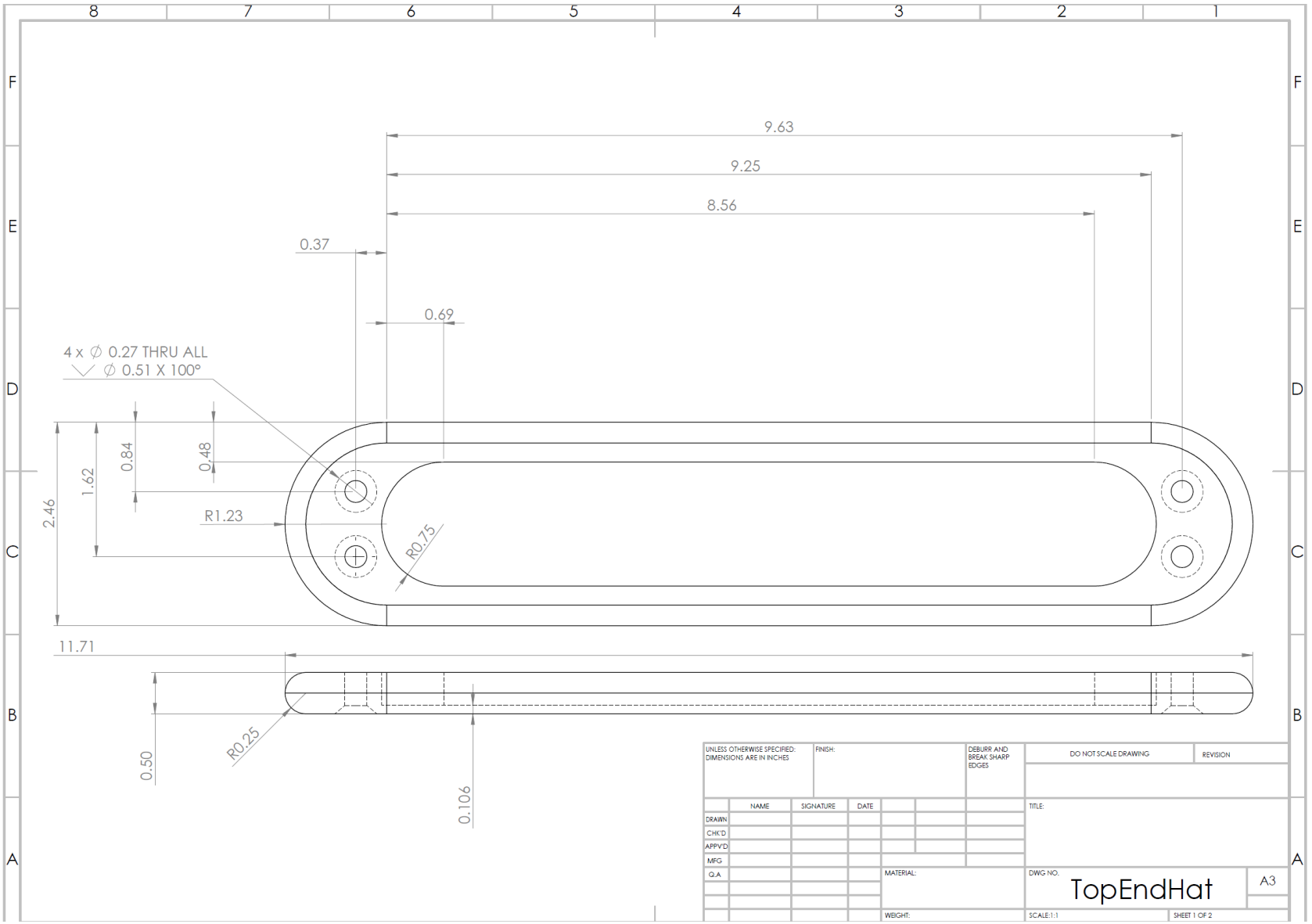

Figure A.2: Top endhat of the cathode.

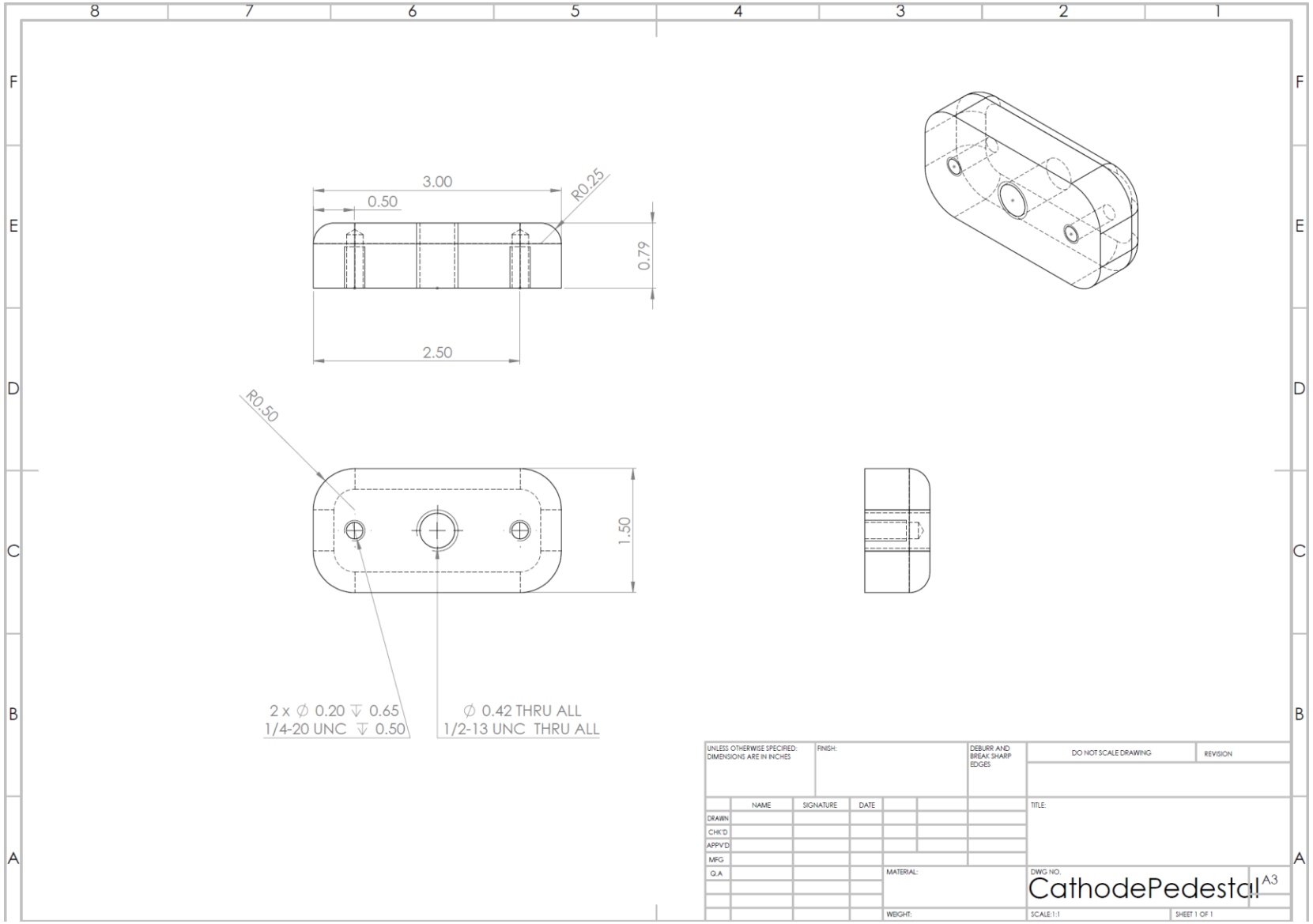

Figure A.3: Piece that adapts from MELBA output stalk to bottom endhat.

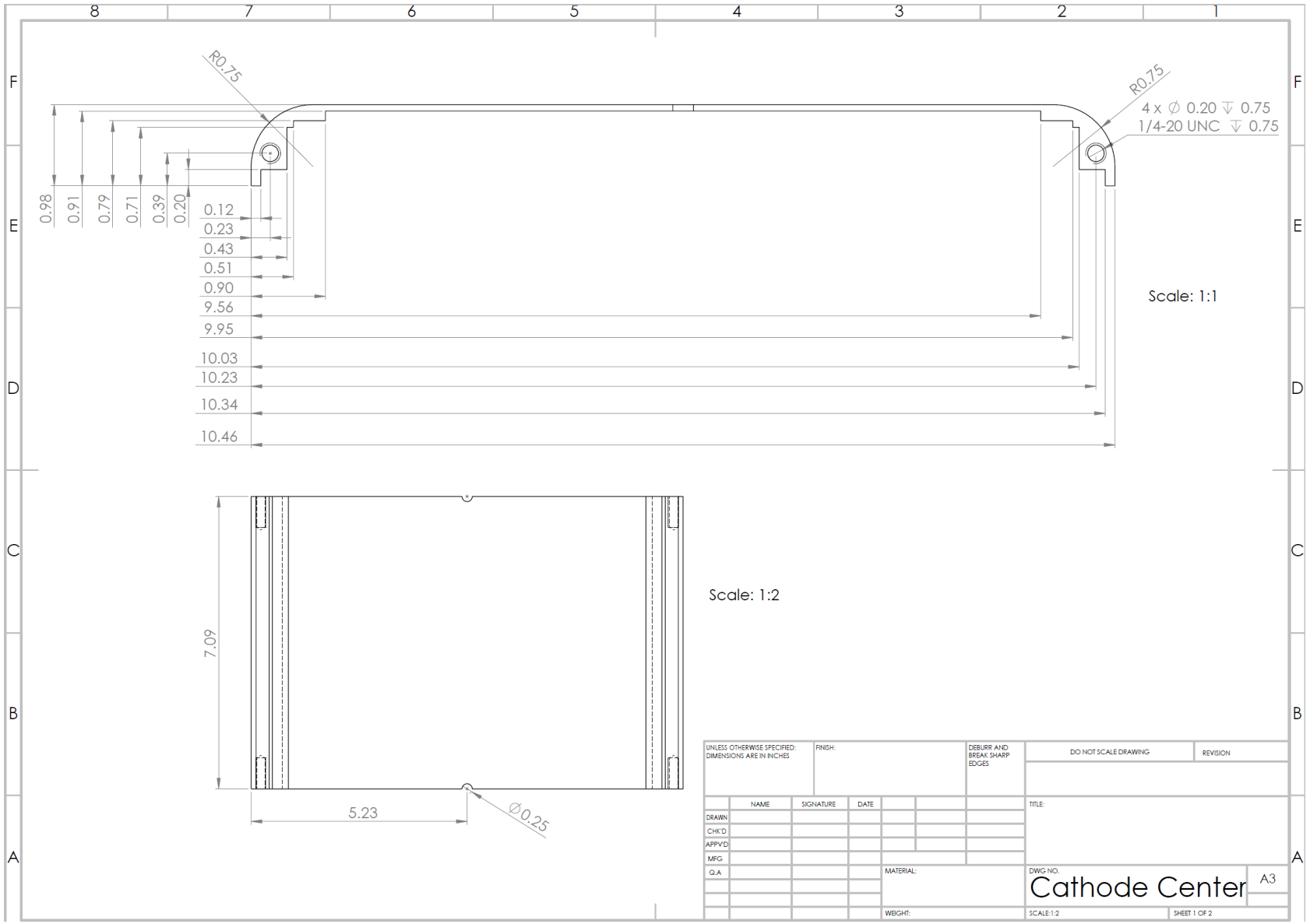

Figure A.4: Planar cathode face that goes between the endhats.

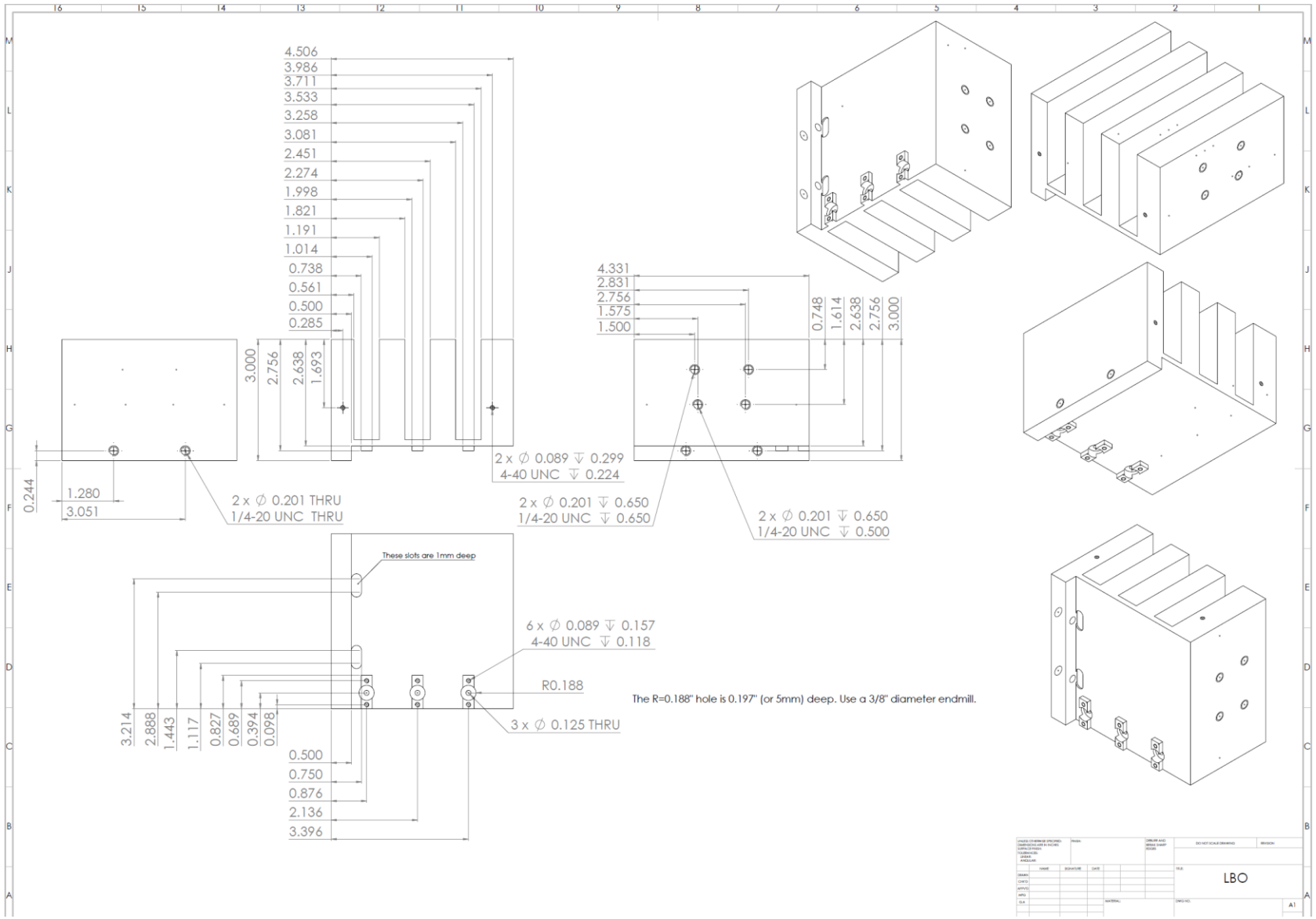

Figure A.5: L-Band Oscillator with three cavities.

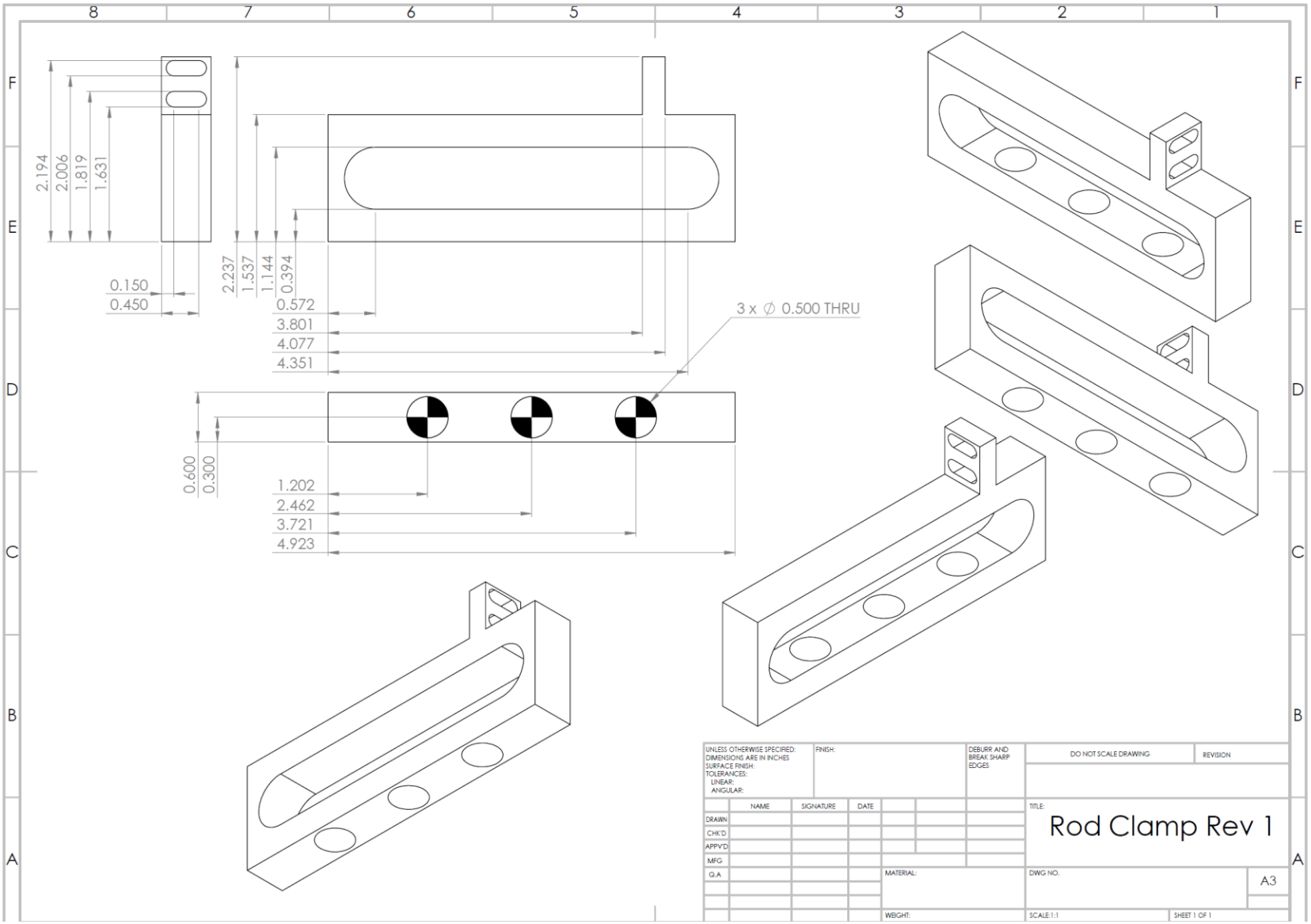

Figure A.6: Alignment piece that translates the tuning rods using the external tuner.

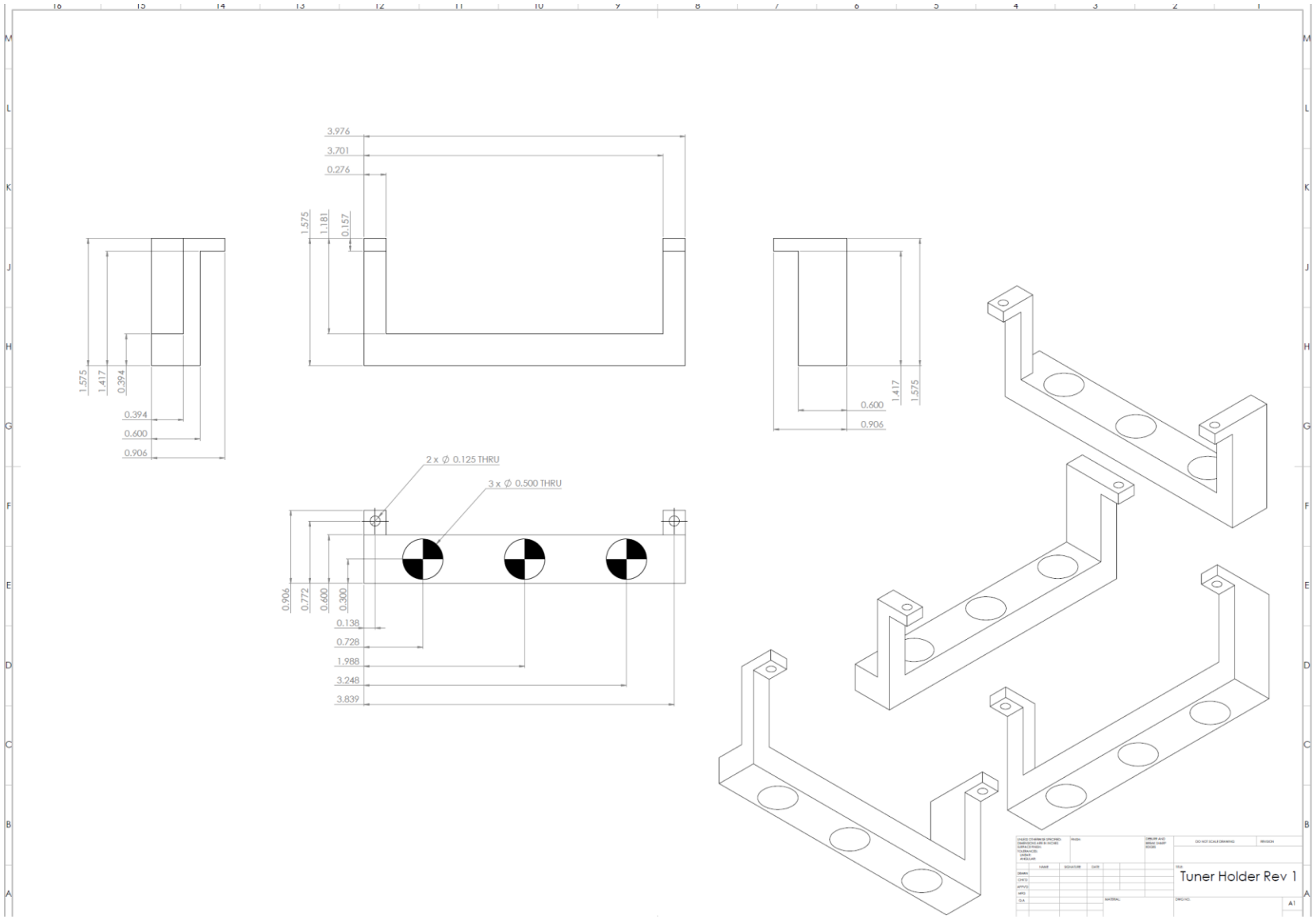

Figure A.7: Alignment piece that guides the tuning rods into the cavities.

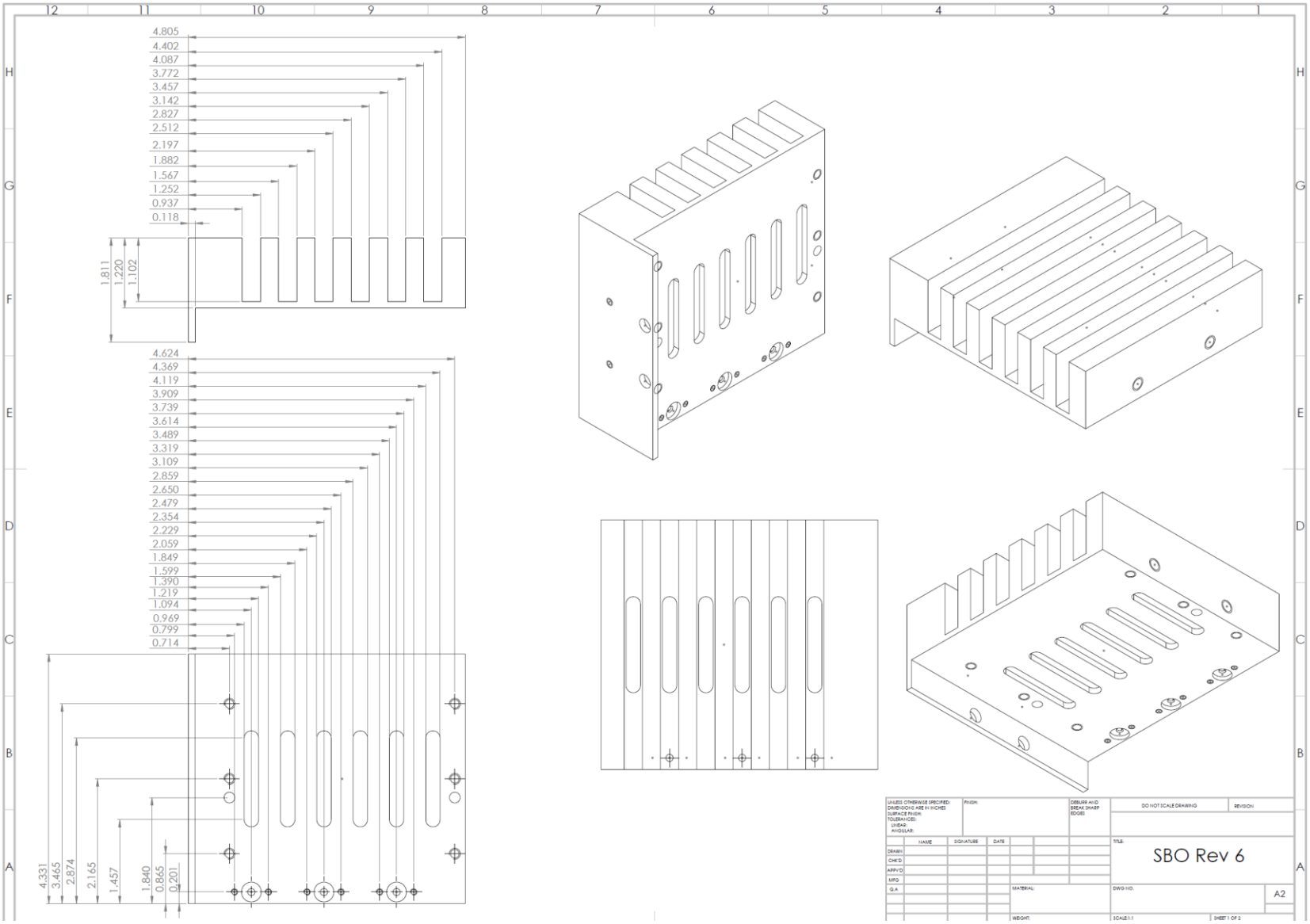

Figure A.8: S-Band Oscillator with six cavities.

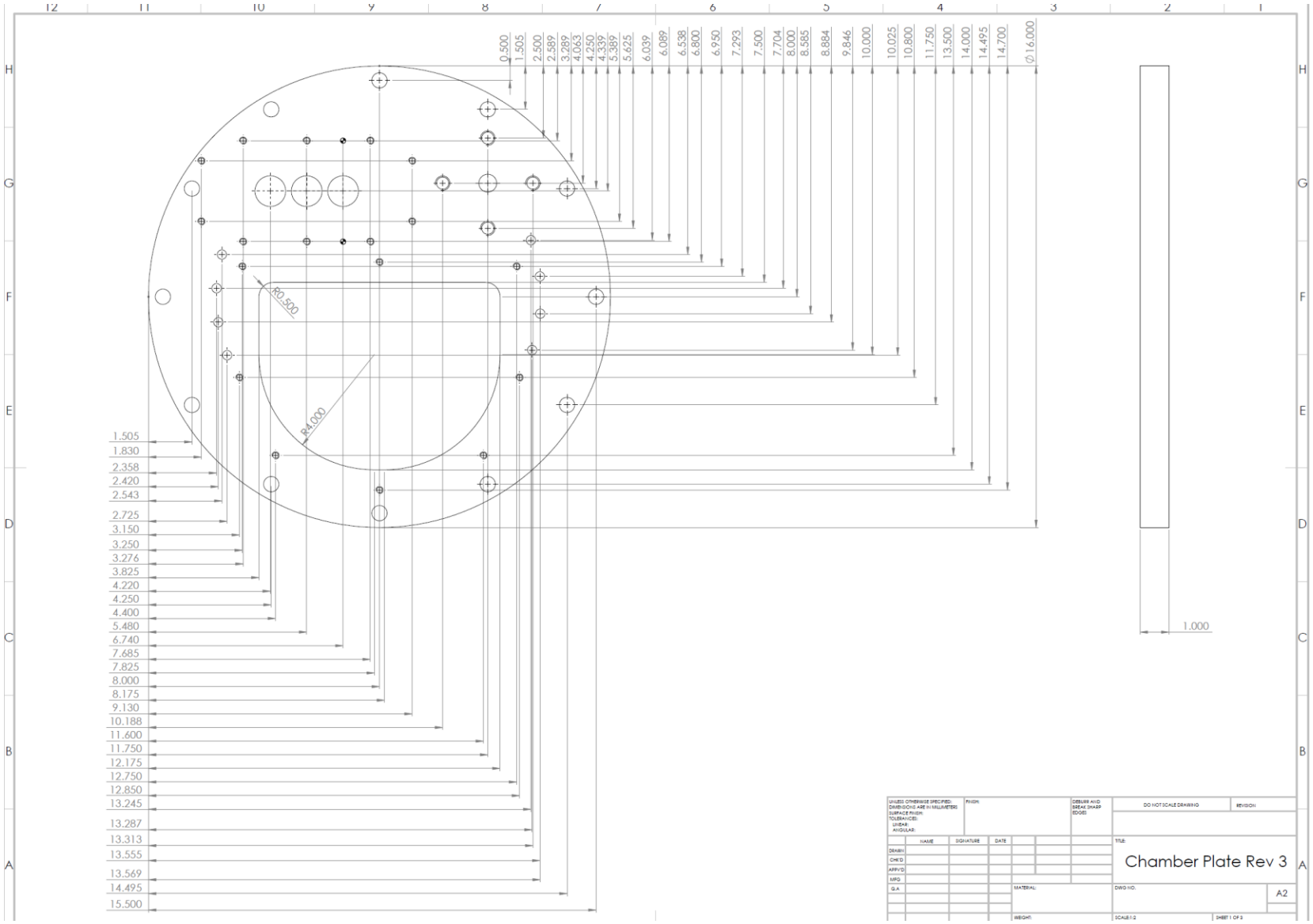

Figure A.9: Vacuum flange that mates to the experimental test chamber.

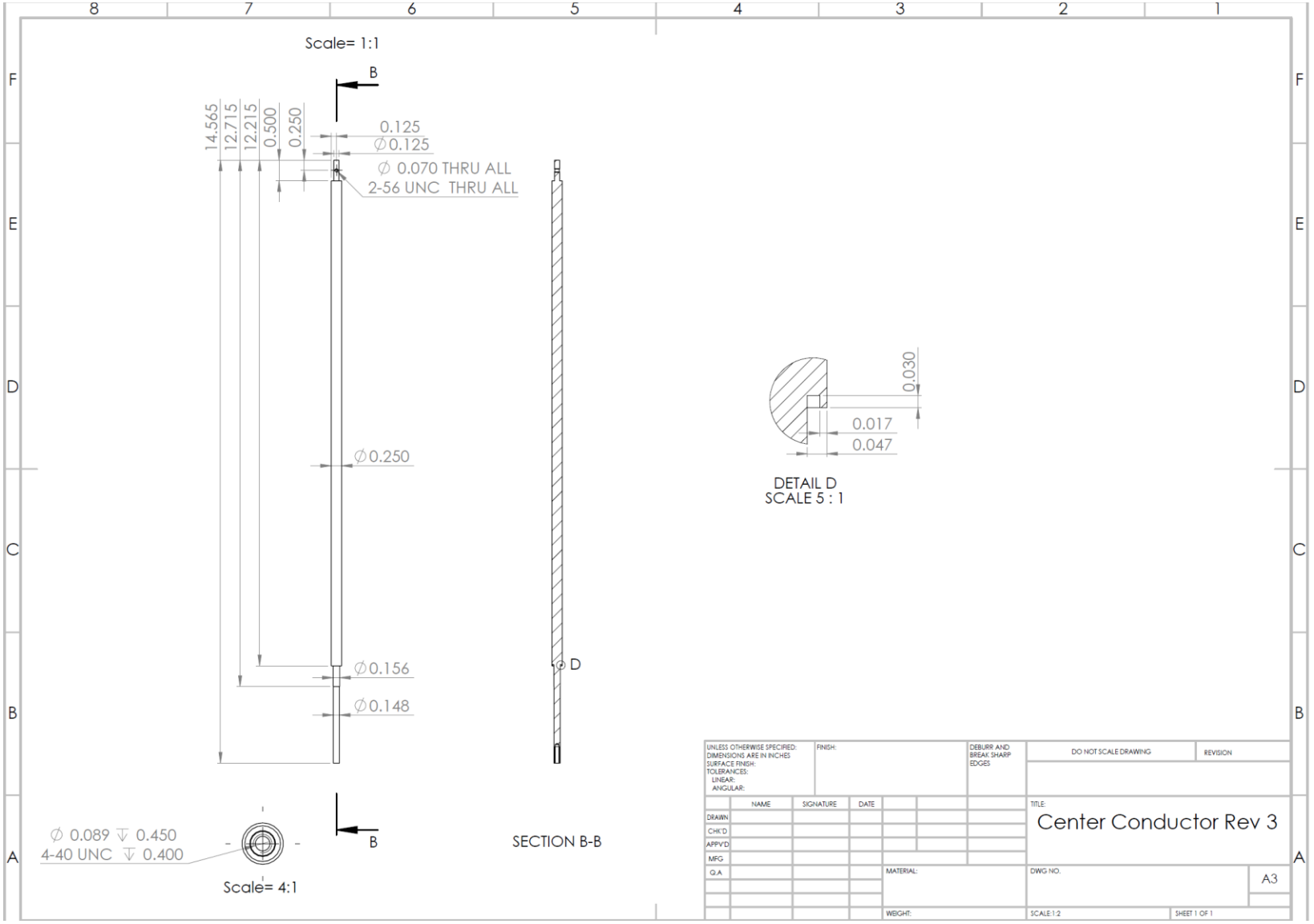

Figure A.10: Center conductor in the small-diameter portion of the coaxial lines.

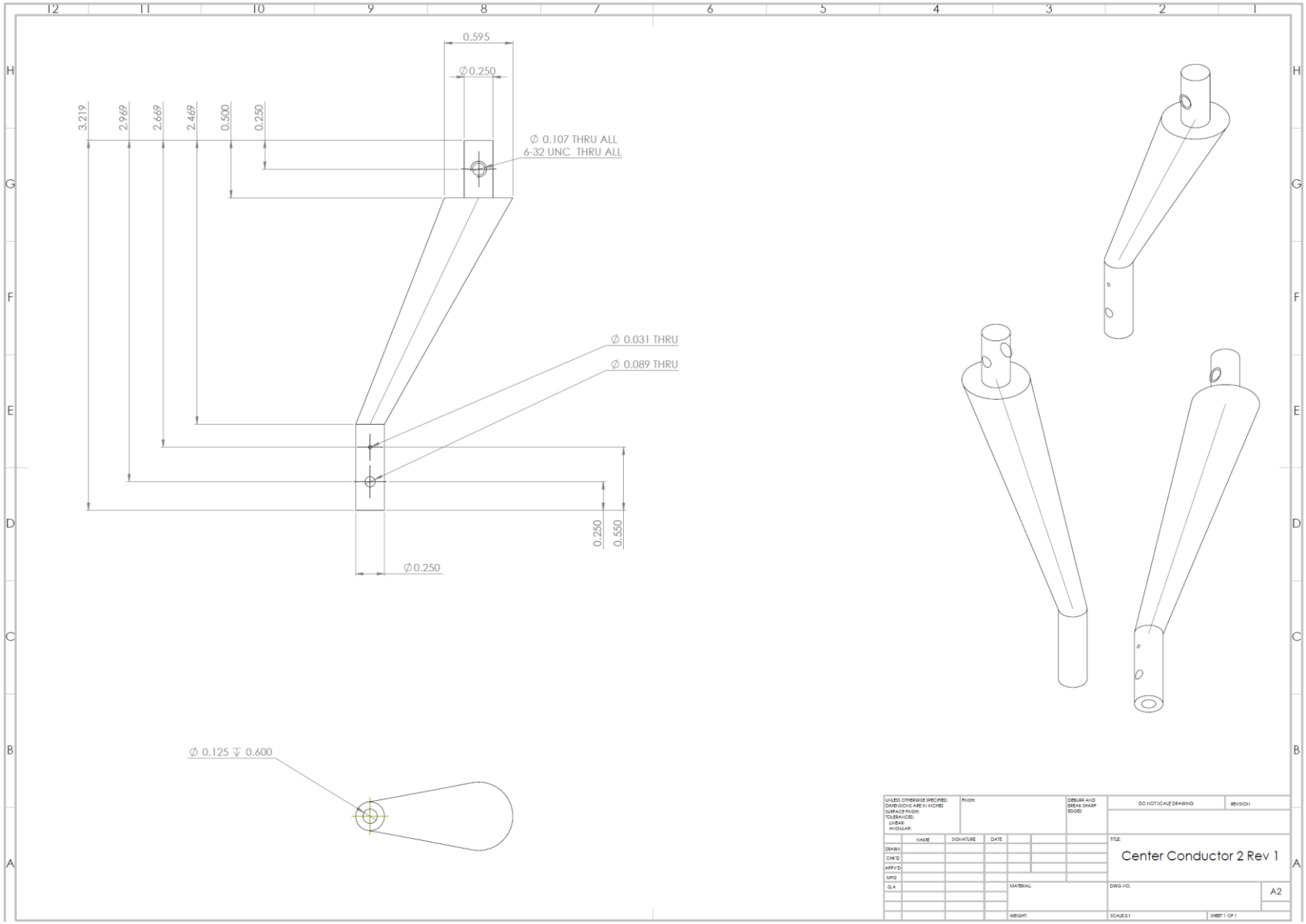

Figure A.11: Center conductor within the tapered and flared coaxial lines.

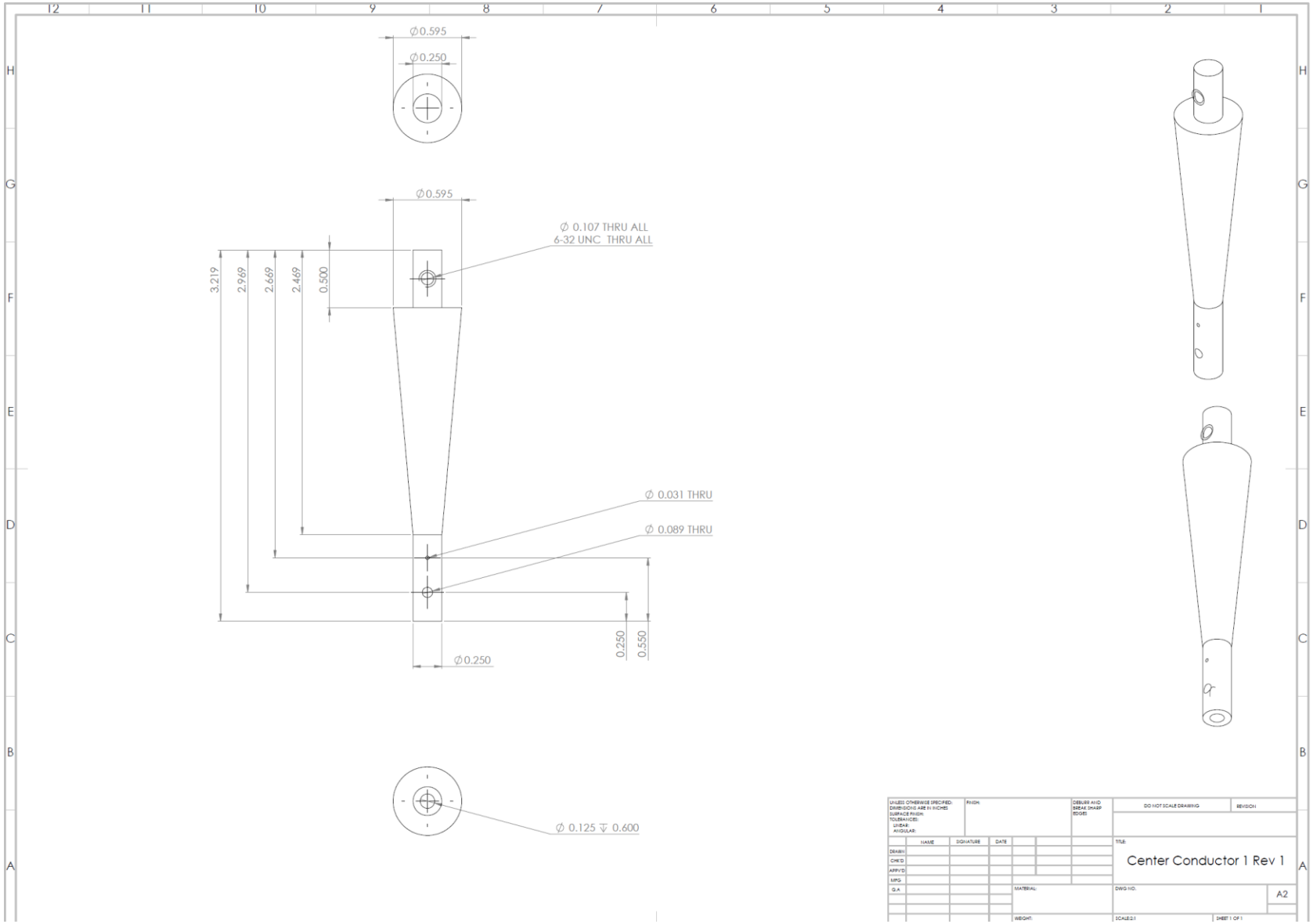

Figure A.12: Center conductor within the tapered coaxial line that is not flared.

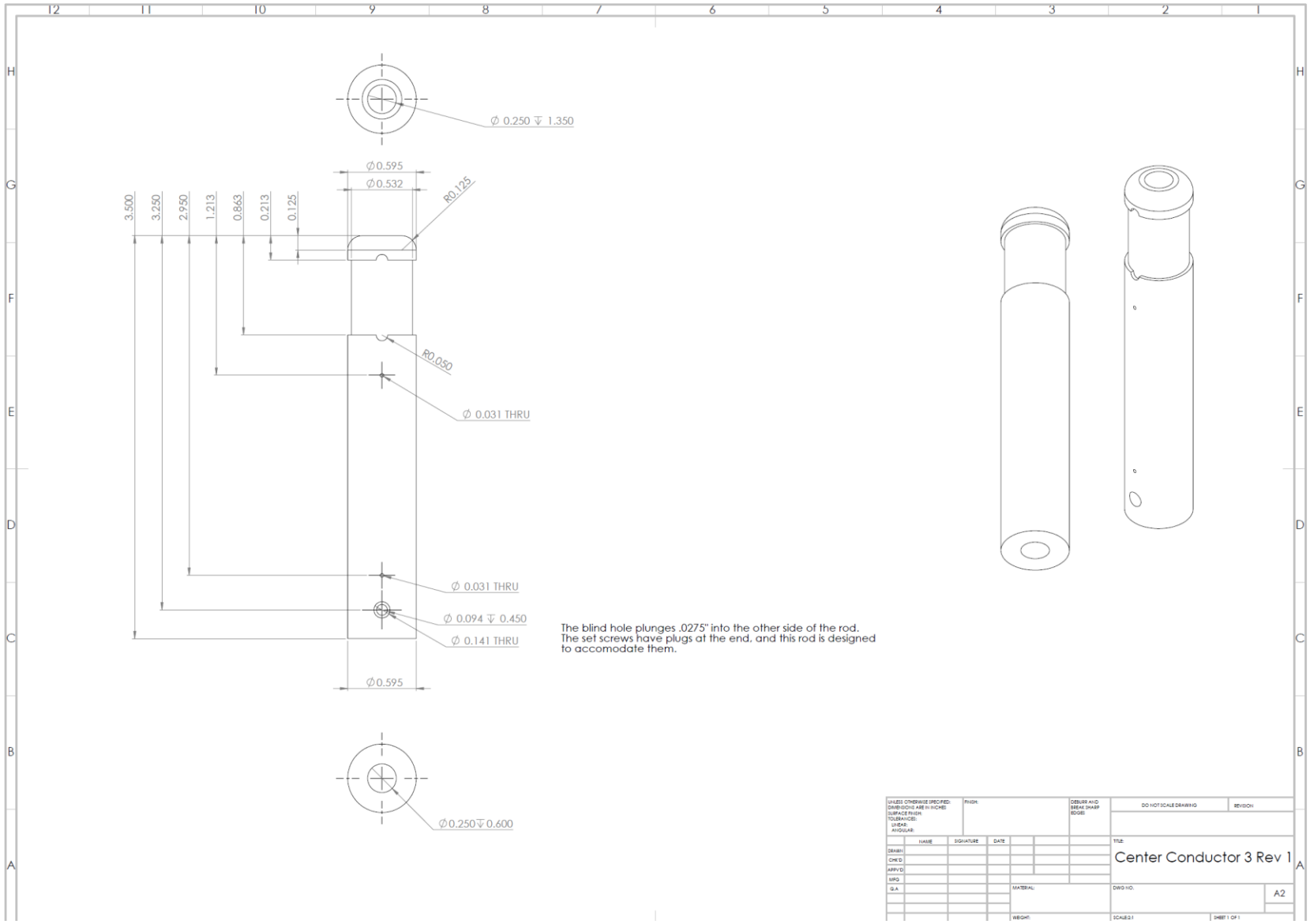

Figure A.13: Center conductor that mates to the output DFA from RPM-CACE.

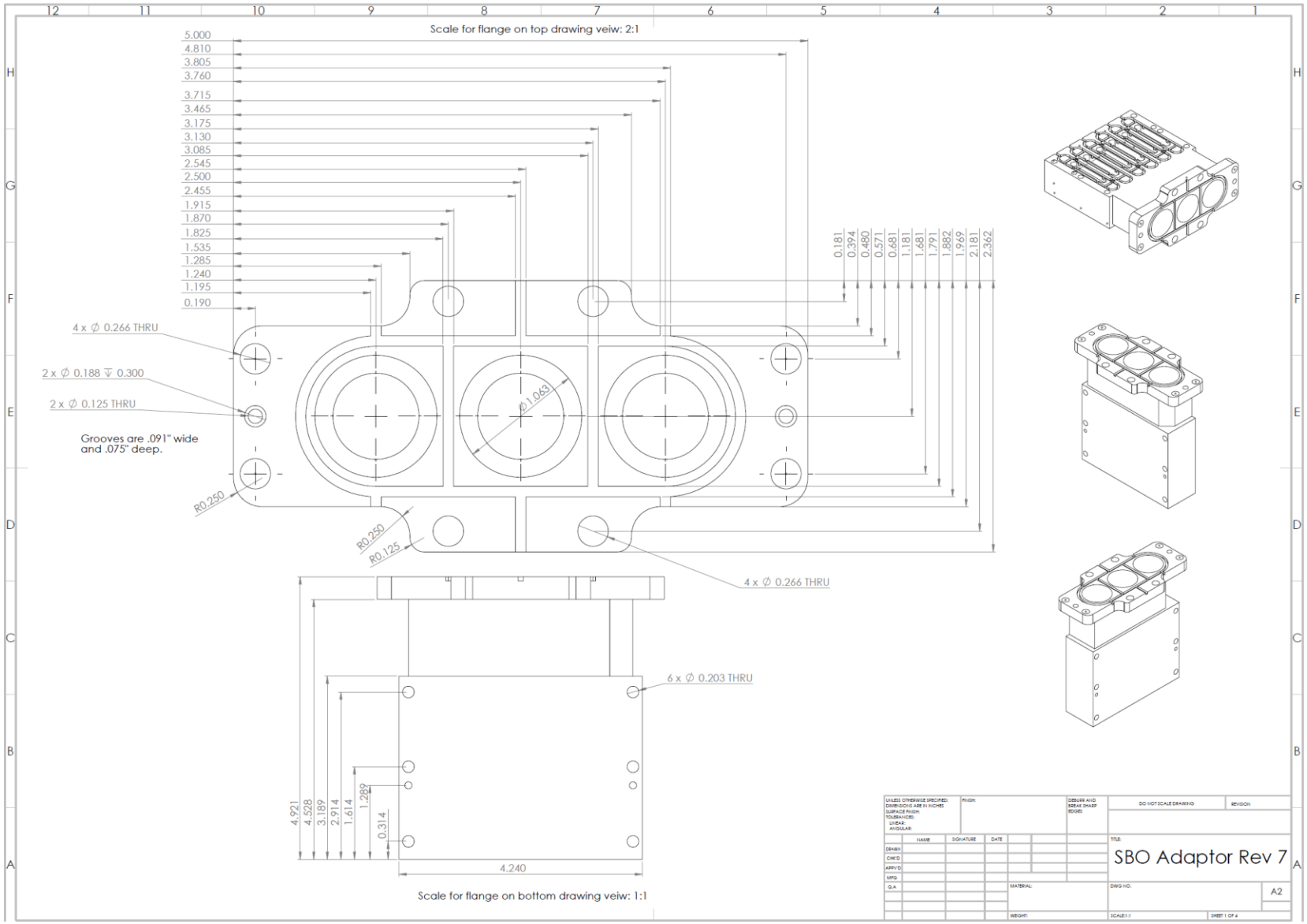

Figure A.14: SBO adaptor, where the coaxial lines mate to the oscillating cavities.

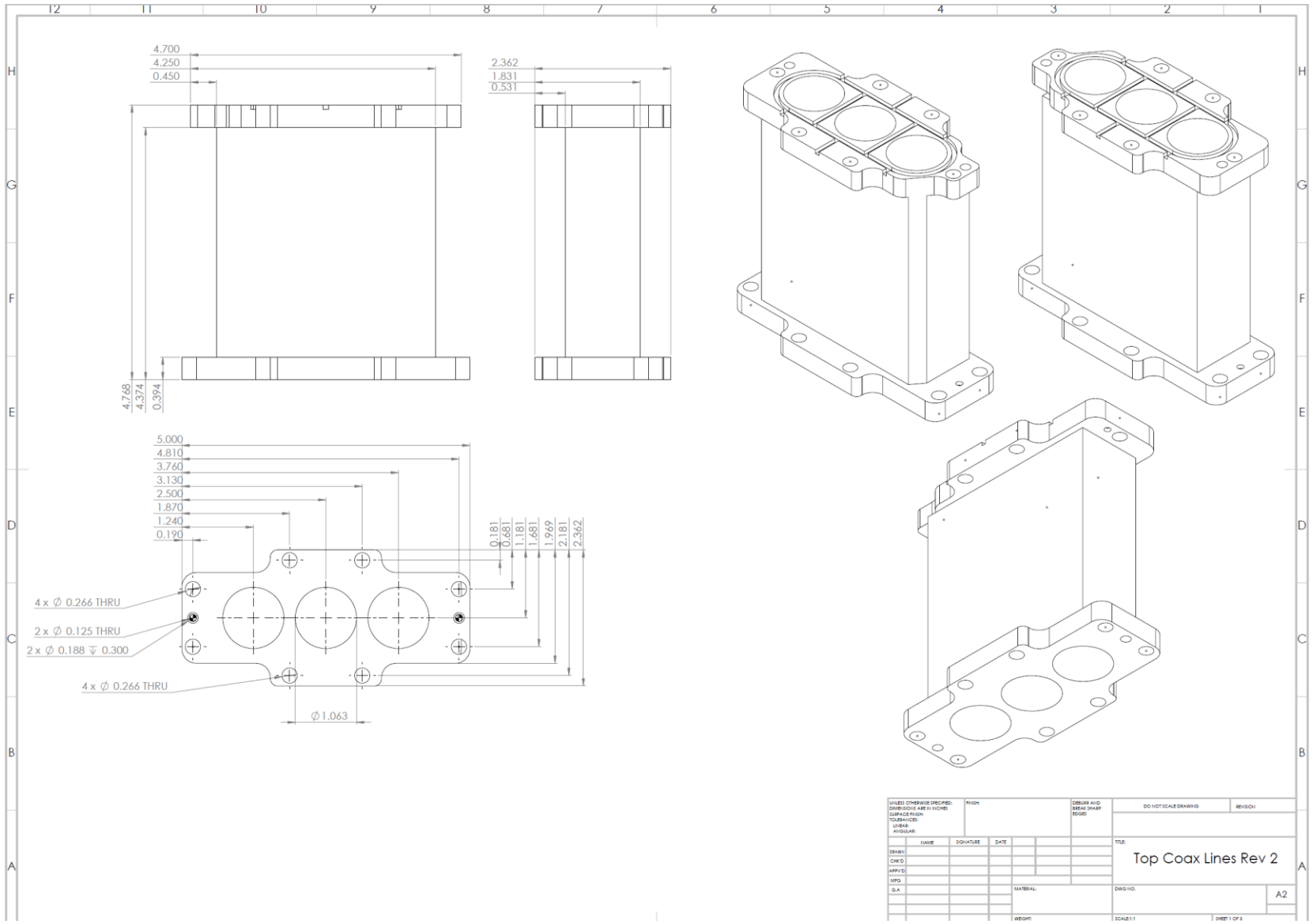

Figure A.15: Coaxial line outer conductor that mates the SBO adaptor to the vacuum flange.

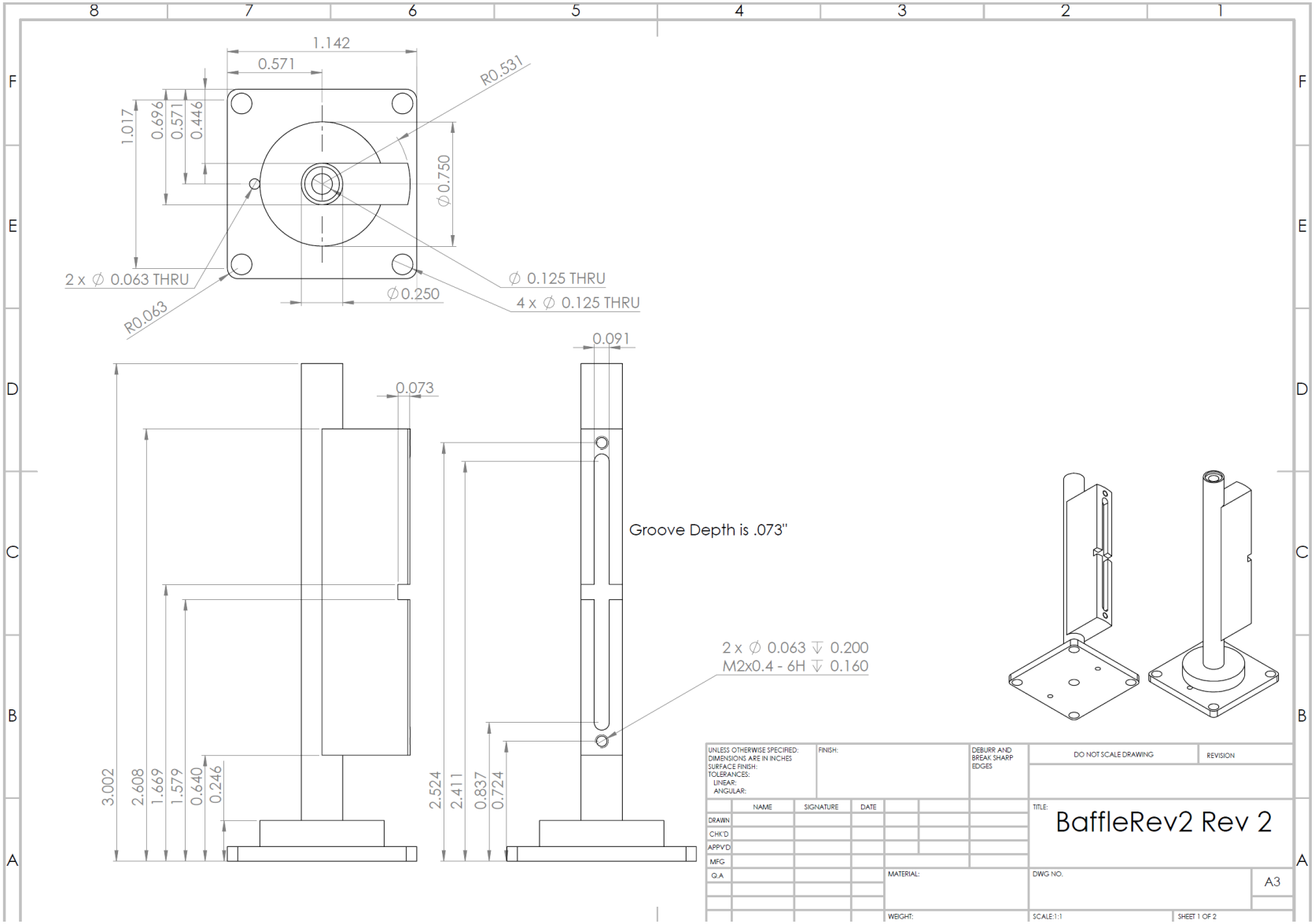

Figure A.16: Coaxial line baffle where the TEM wave is launched.

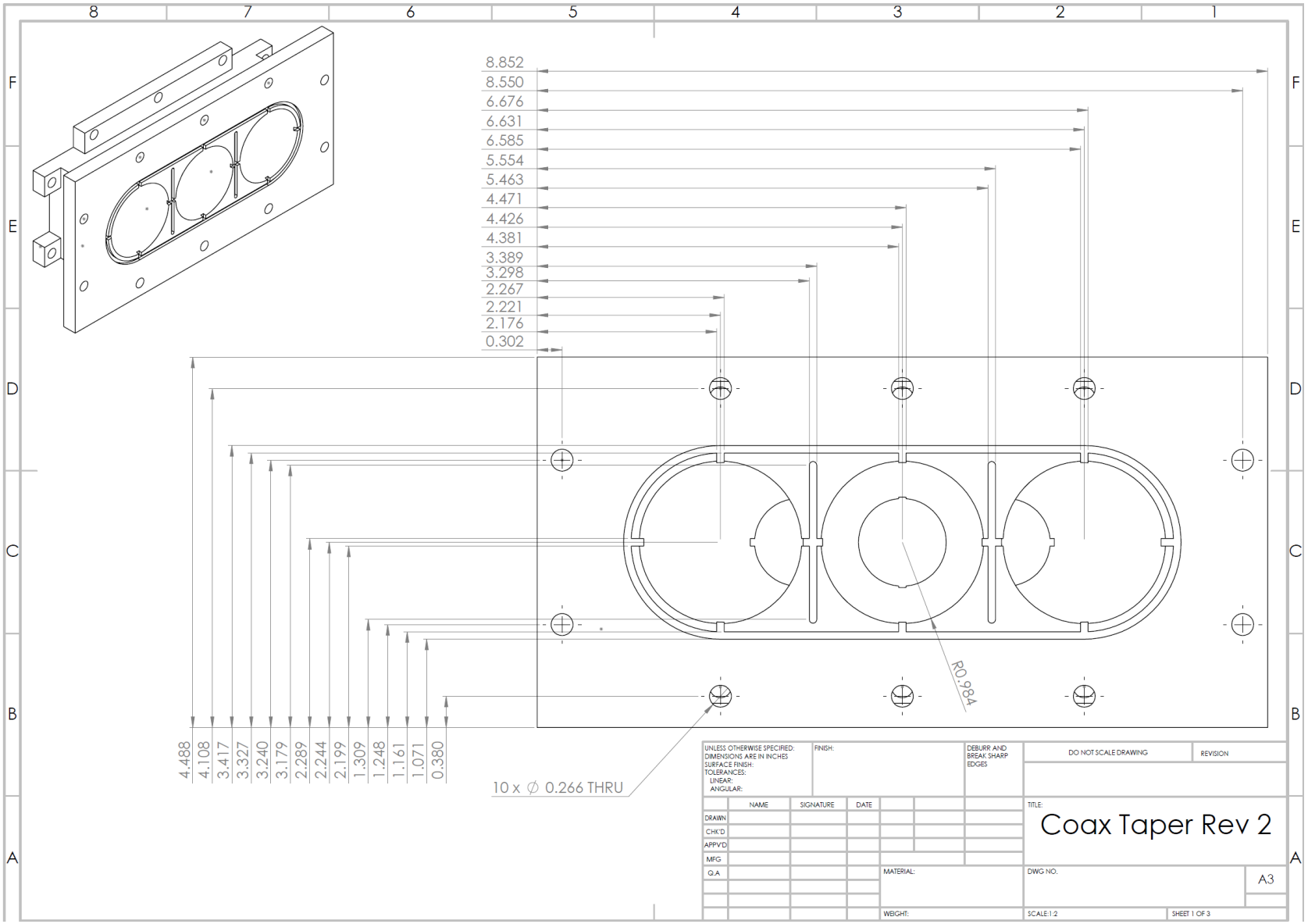

Figure A.17: Coaxial taper that adapts from the small coaxial line within the chamber to the larger coaxial line outside of the chamber.

Appendix B MILO Detail Drawings

This appendix includes drawings of the parts that were used to complete the MILO experiments. Units and materials used are indicated in the lower right of each drawing.

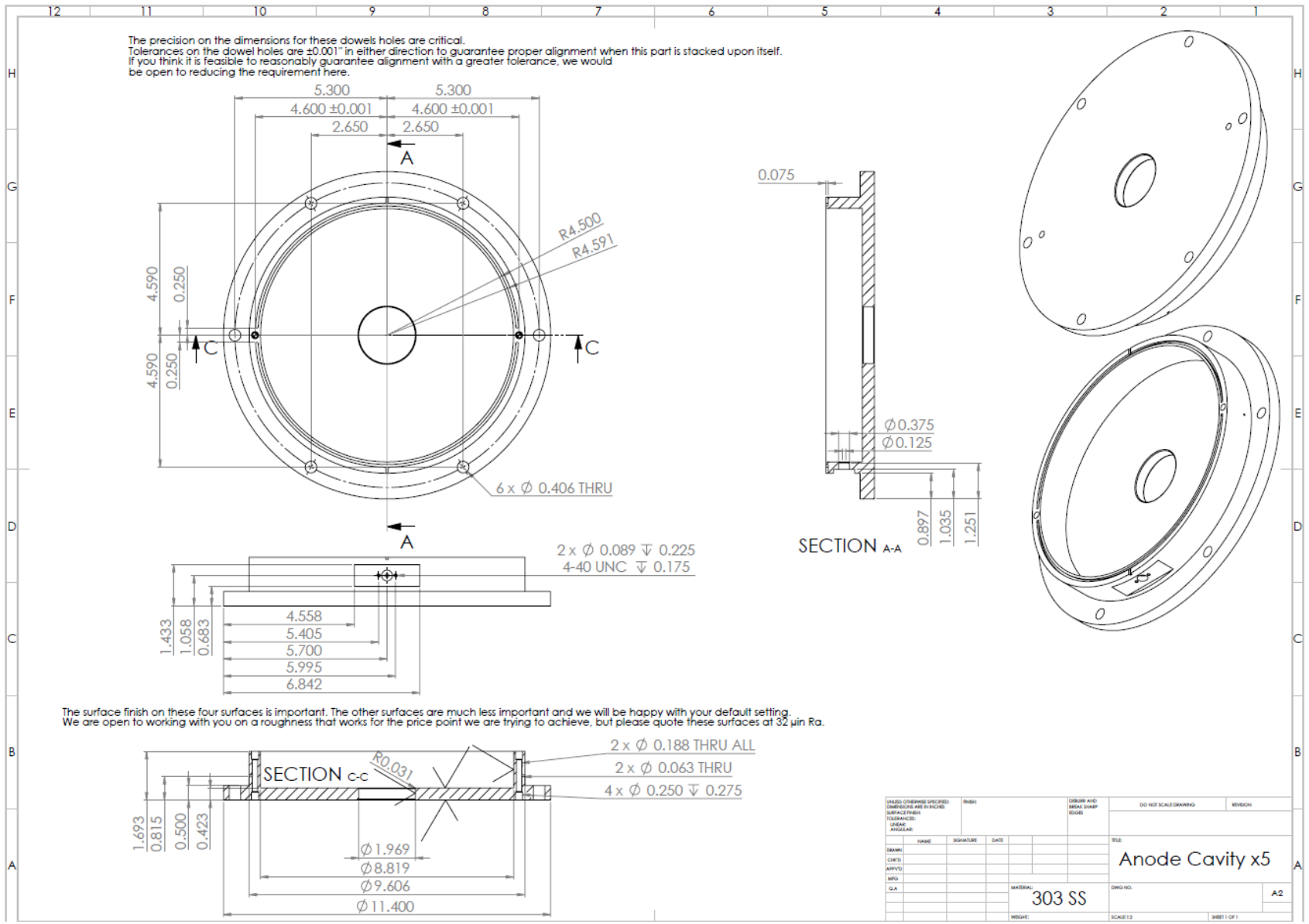

Figure B.1: MILO oscillating cavity disc.

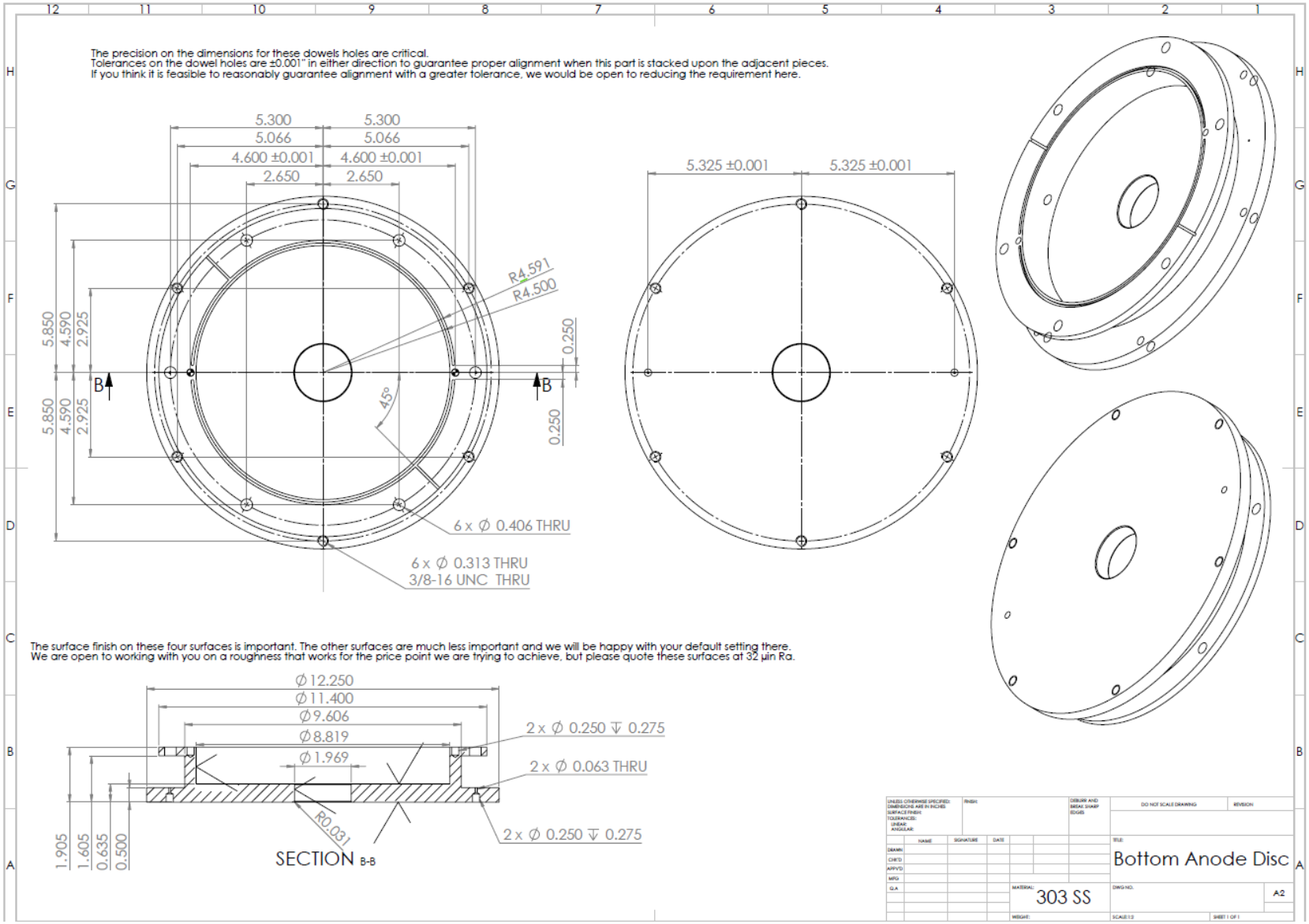

Figure B.2: Anode cavity that adapts from choke section to oscillating cavities.

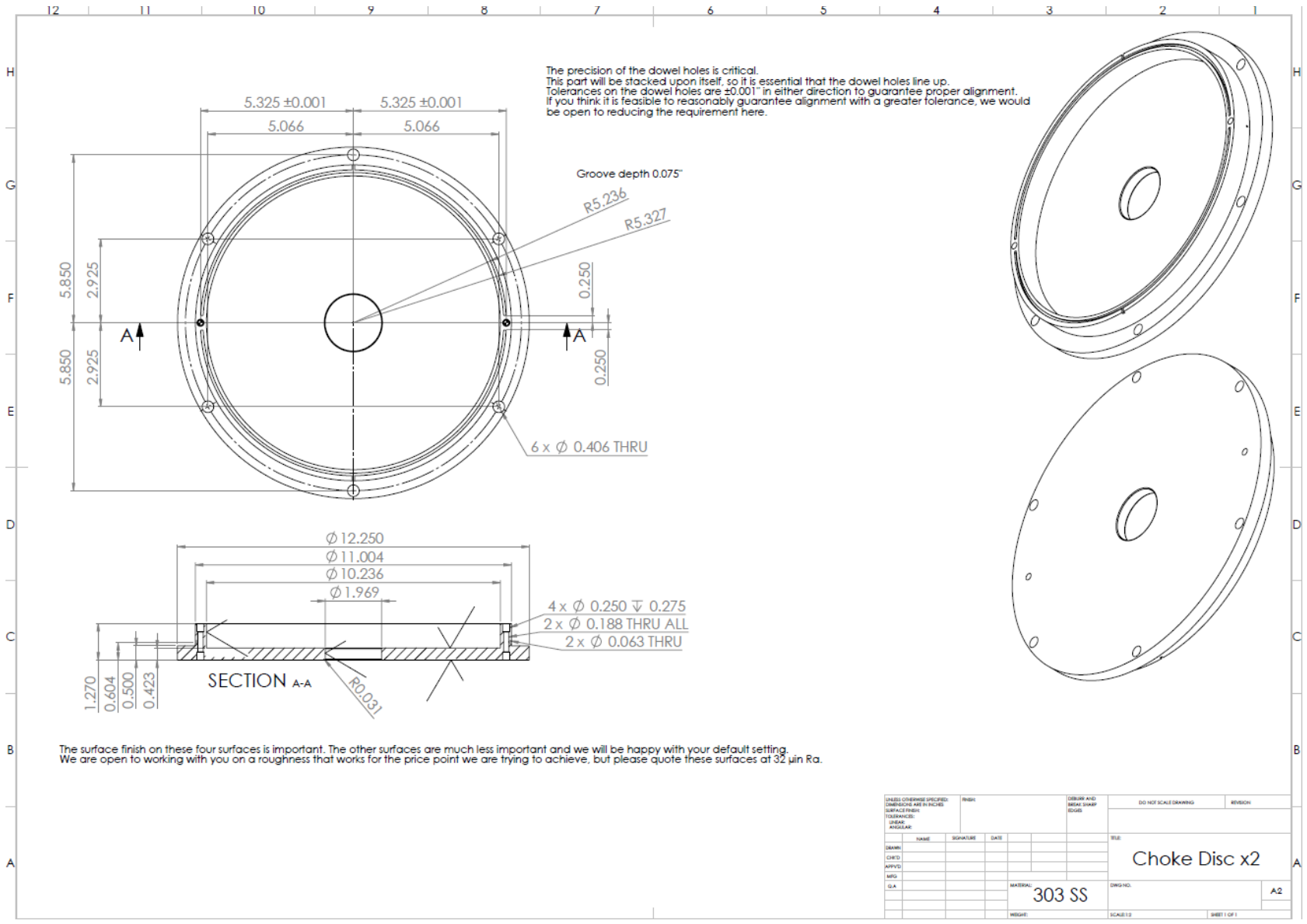

Figure B.3: Choke disc that forms the choke region.

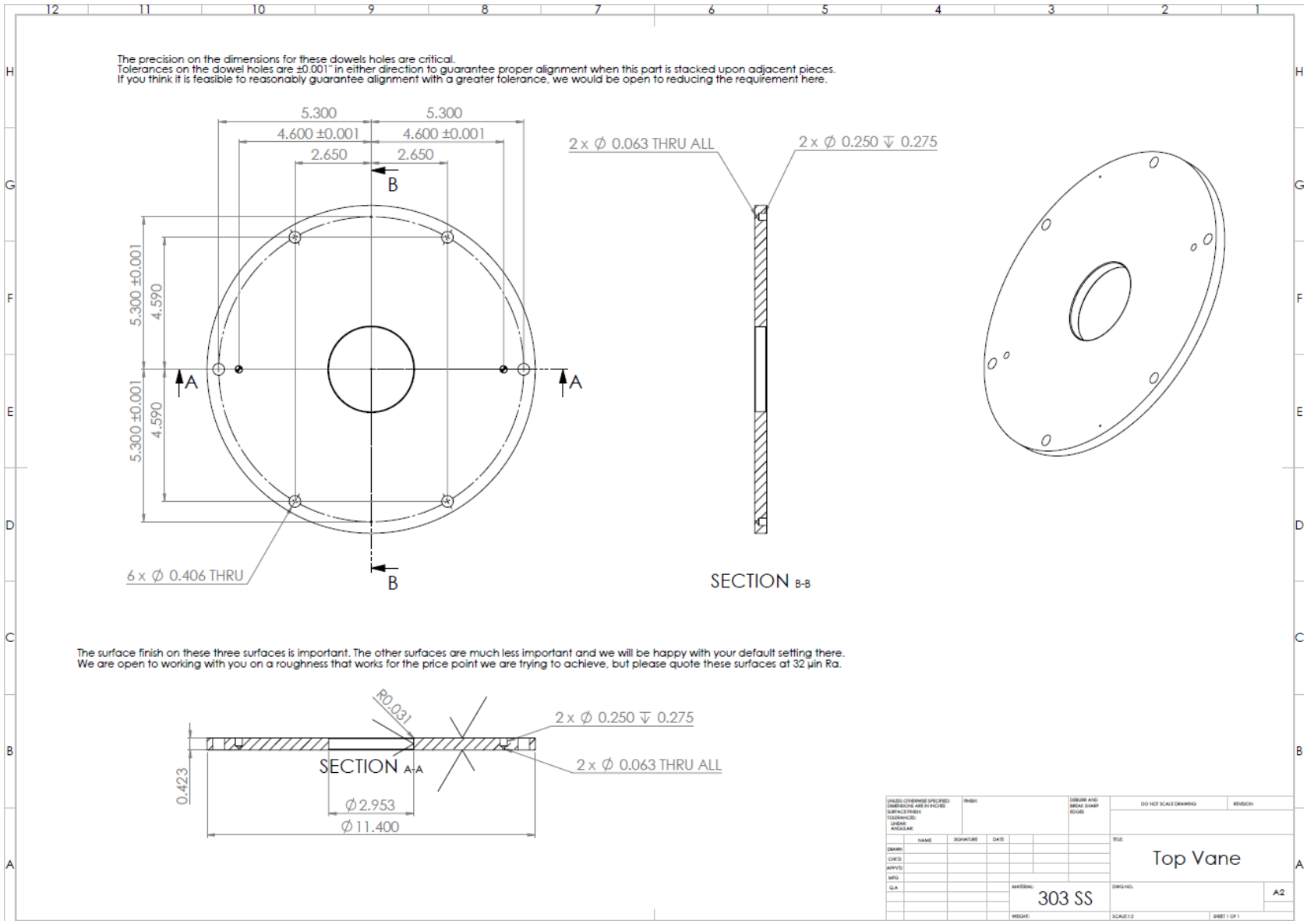

Figure B.4: Final vane that forms junction between cavities and extractor.

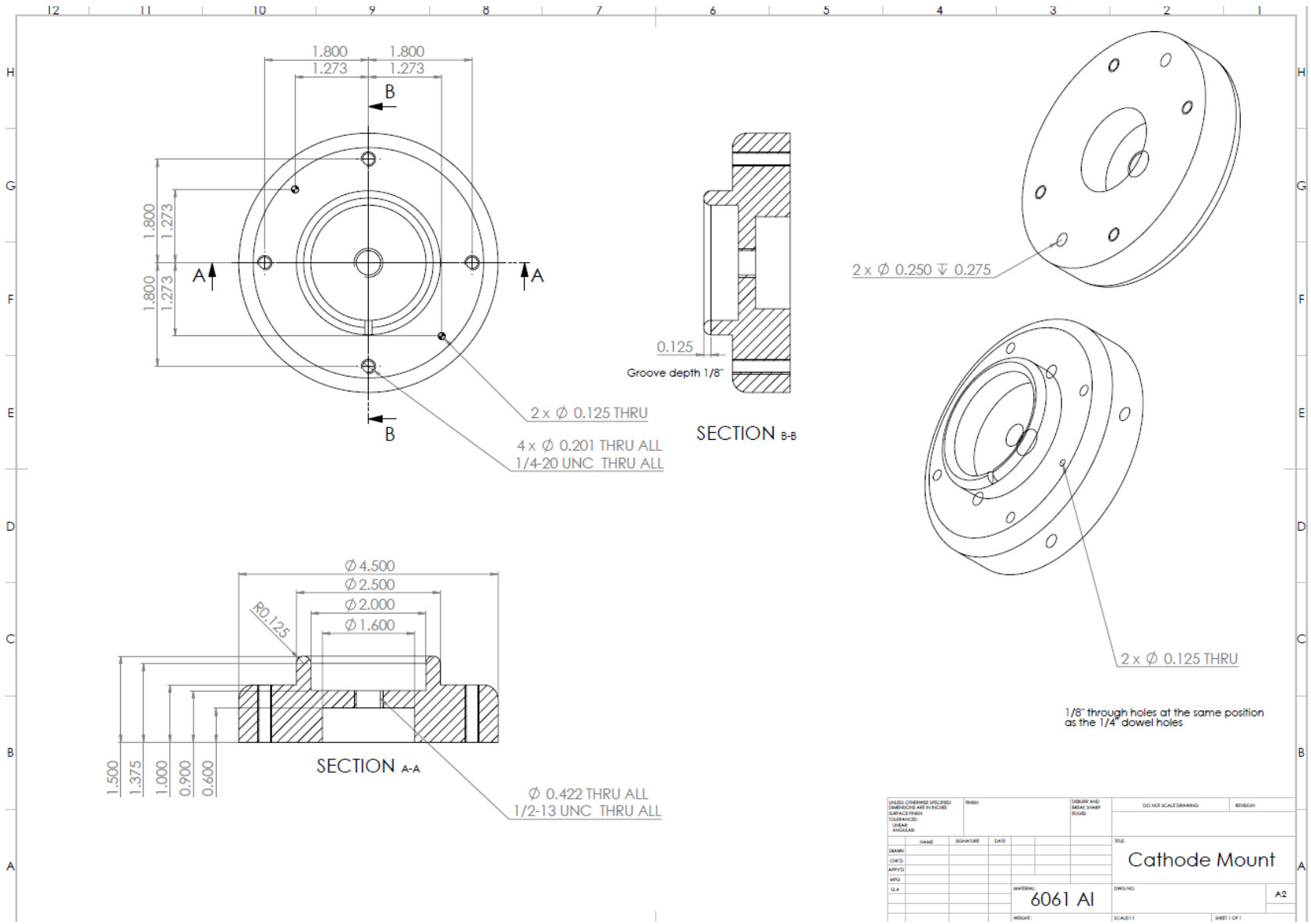

Figure B.5: Cathode mount that connected to MELBA output flange.

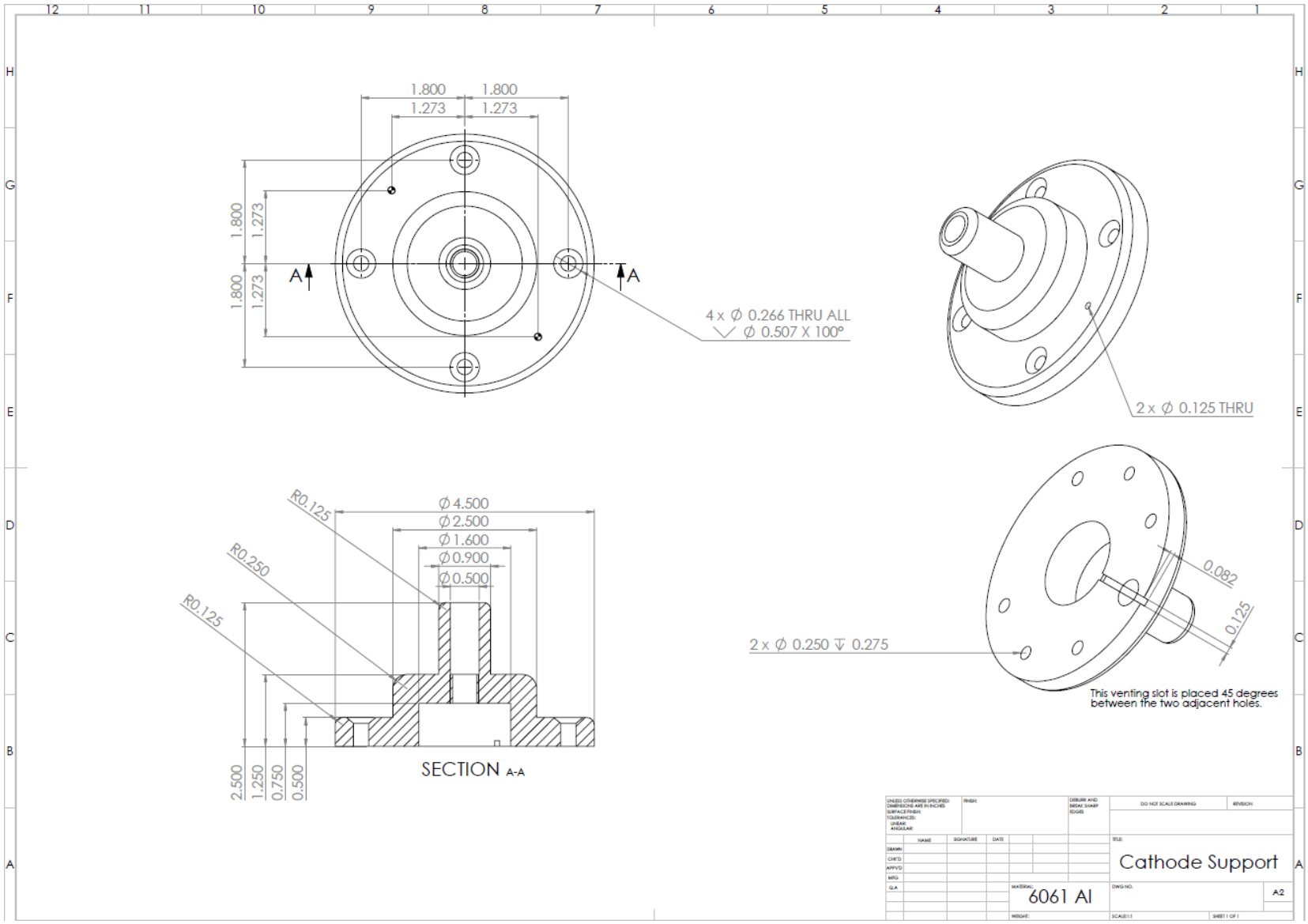

Figure B.6: Cathode support, which connects to the cathode mount, that mates to the cathode rod.

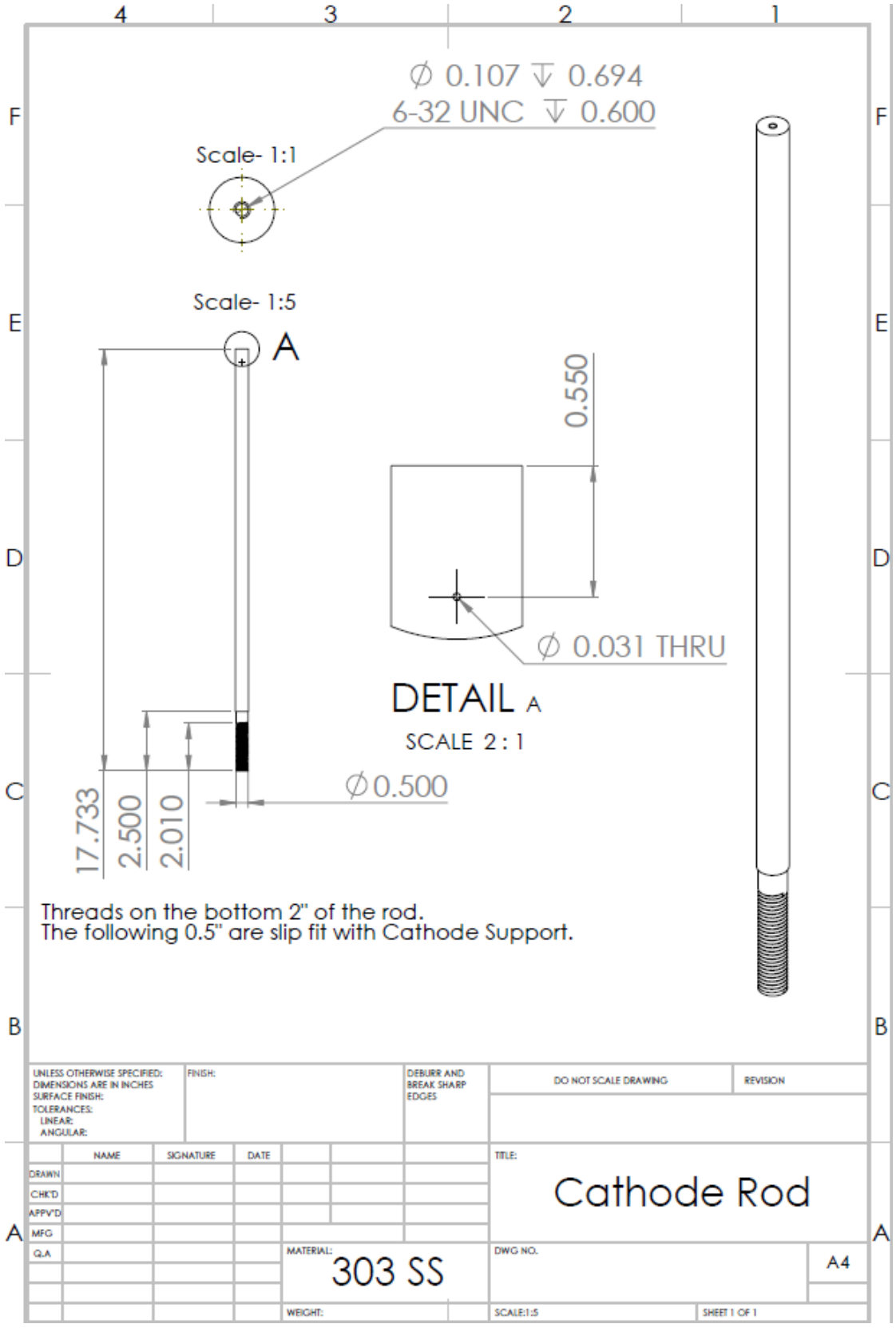

Figure B.7: MILO cathode rod.

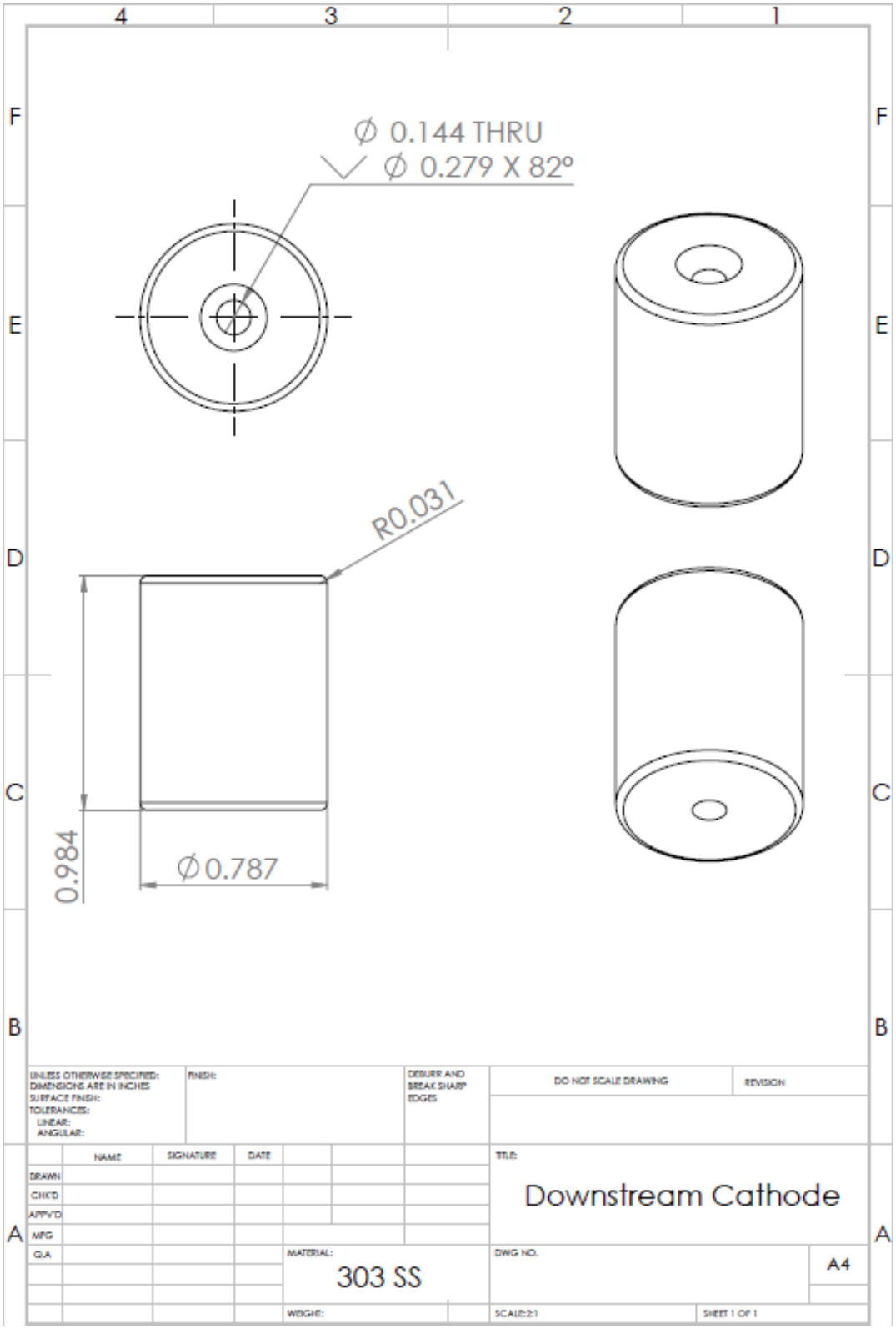

Figure B.8: Downstream cathode that was varied in radius over two experiments in Chapter 6.

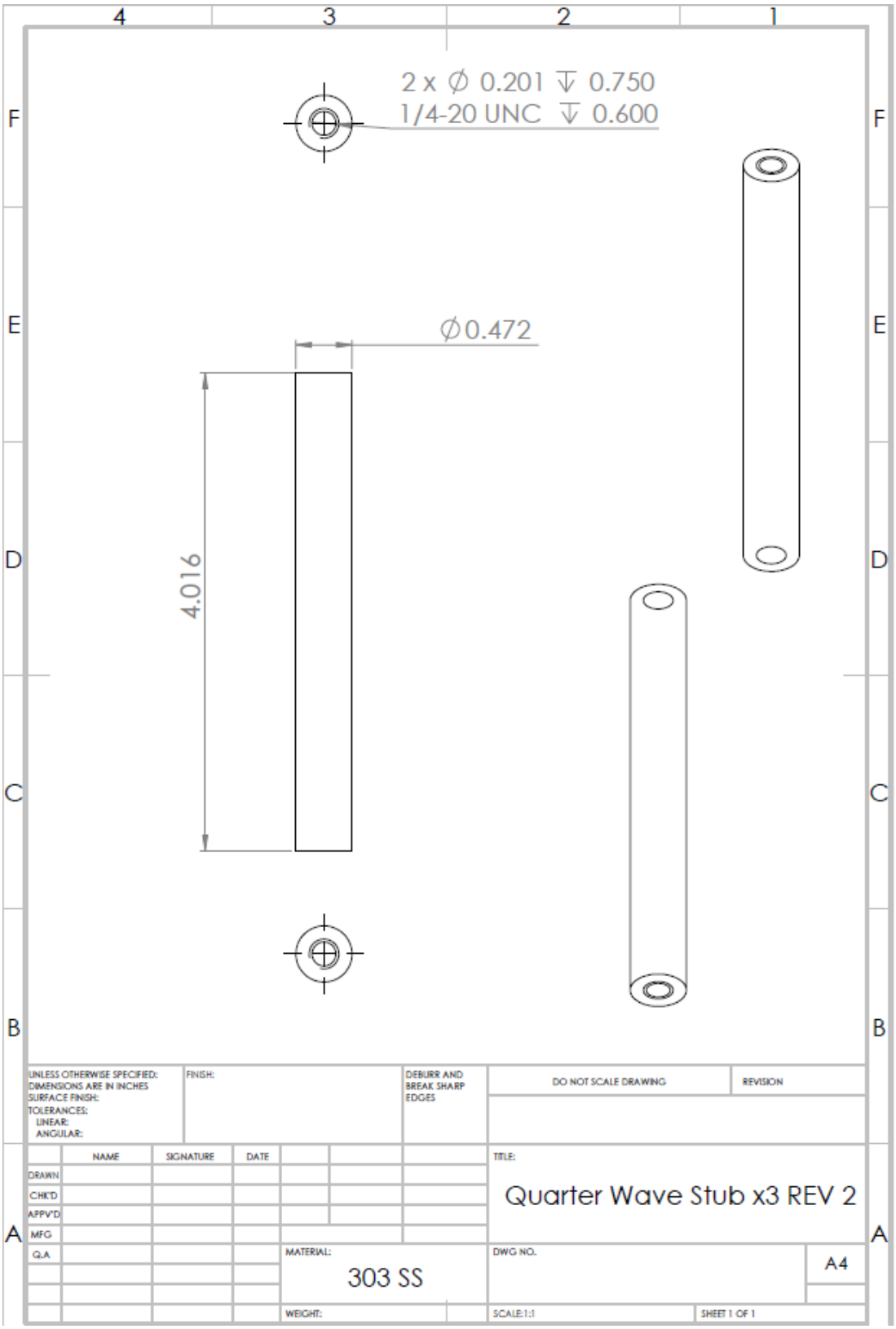

Figure B.9: Quarter wave transformer that electrically grounds the beam dump to the outer conductor of the output transmission line.

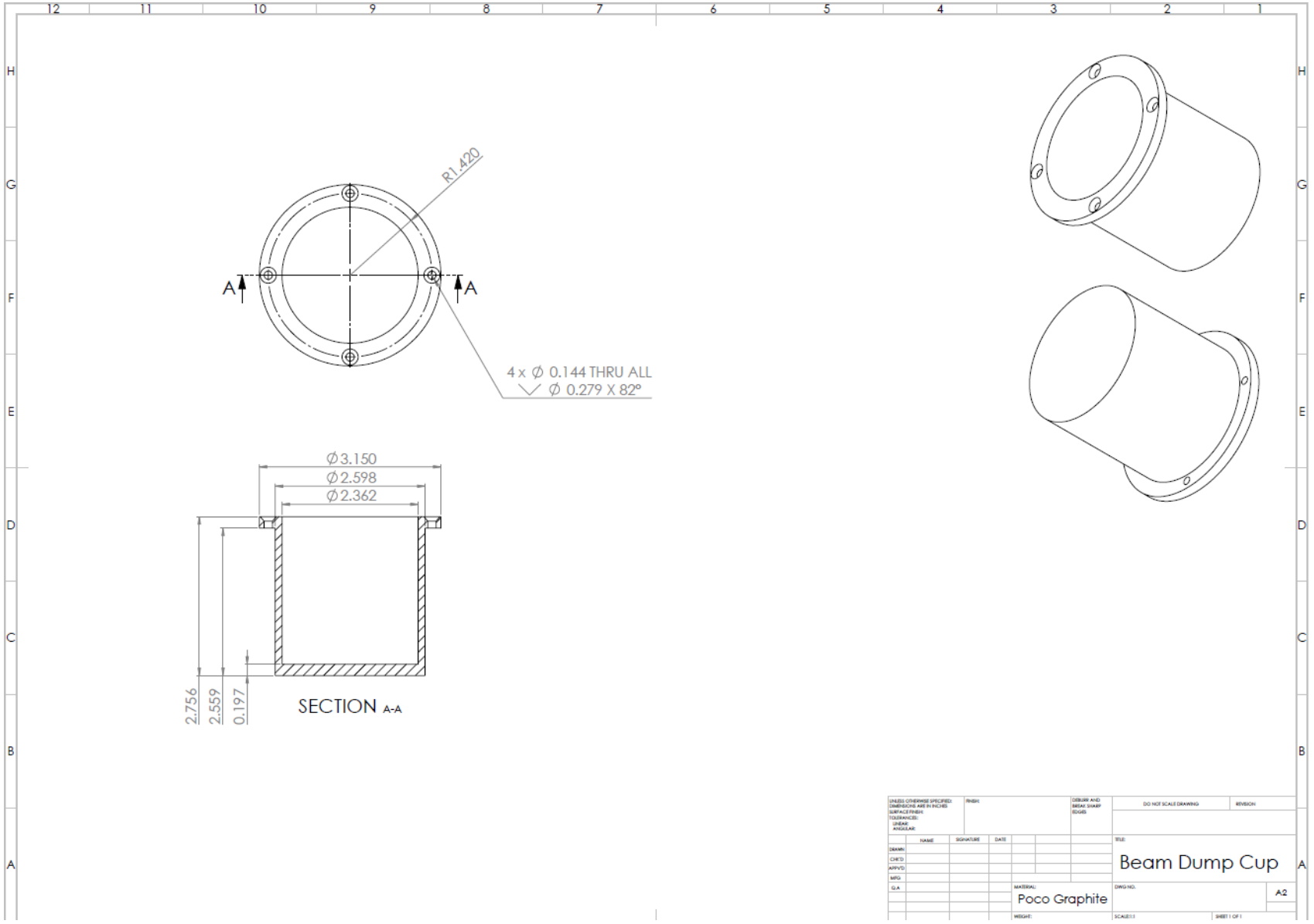

Figure B.10: Downstream anode, where the beam is dumped. This graphite anode is where electrons make impact.

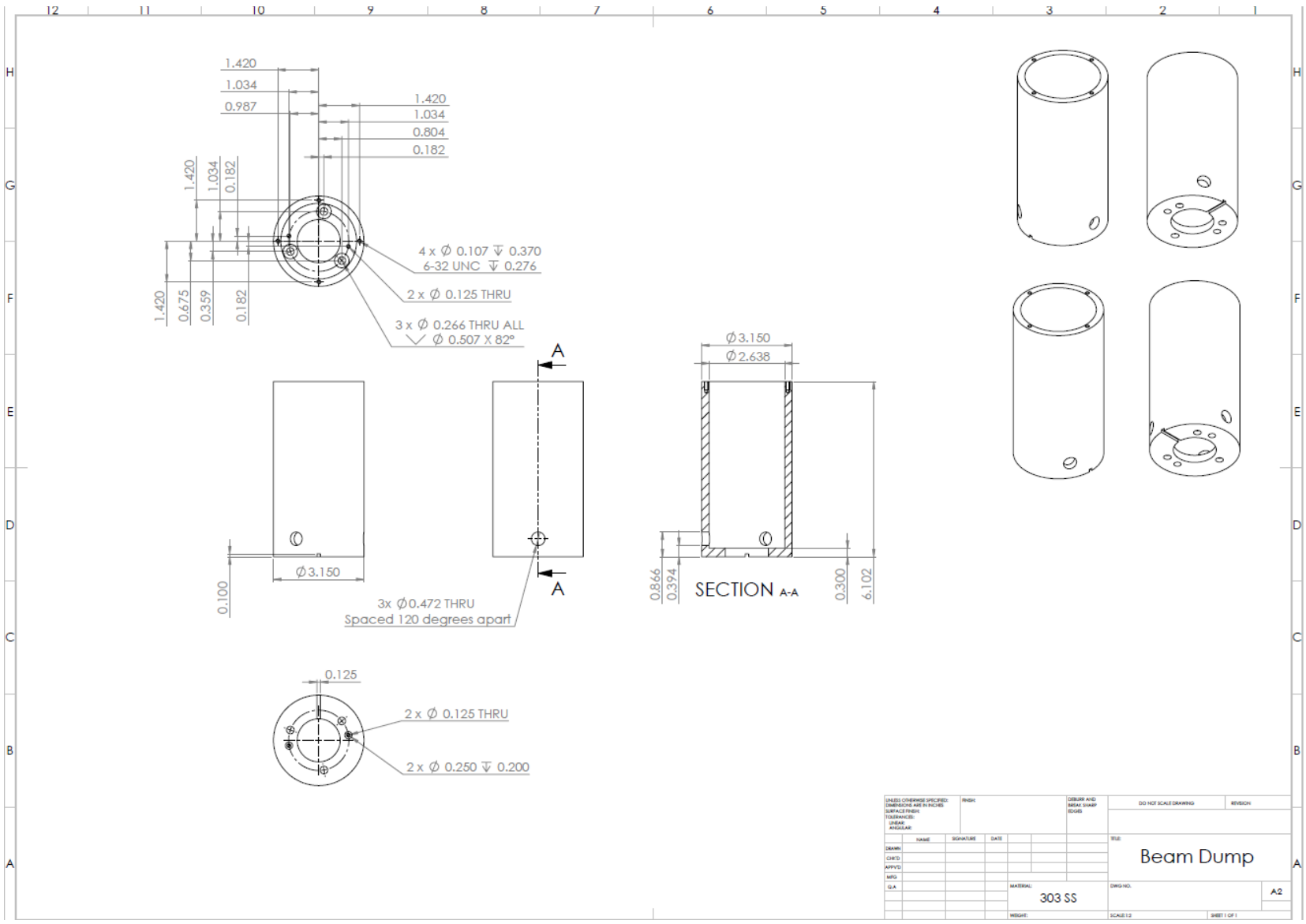

Figure B.11: Beam dump shell, that forms the inner conductor of the extractor. The graphite anode mates at the top of this piece.

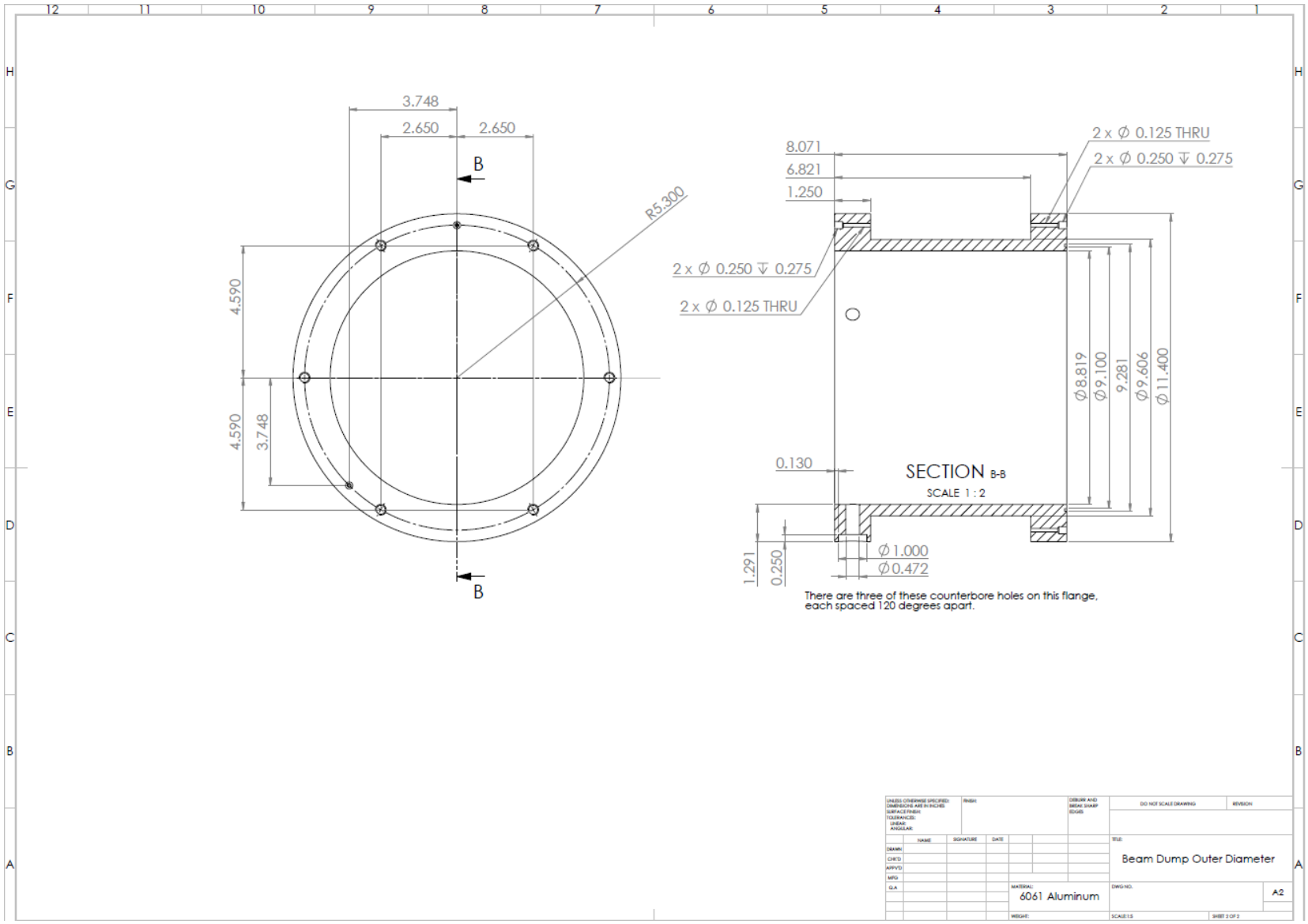

Figure B.12: Outer diameter of the output coax that connects the cavities to the tapered transmission line.

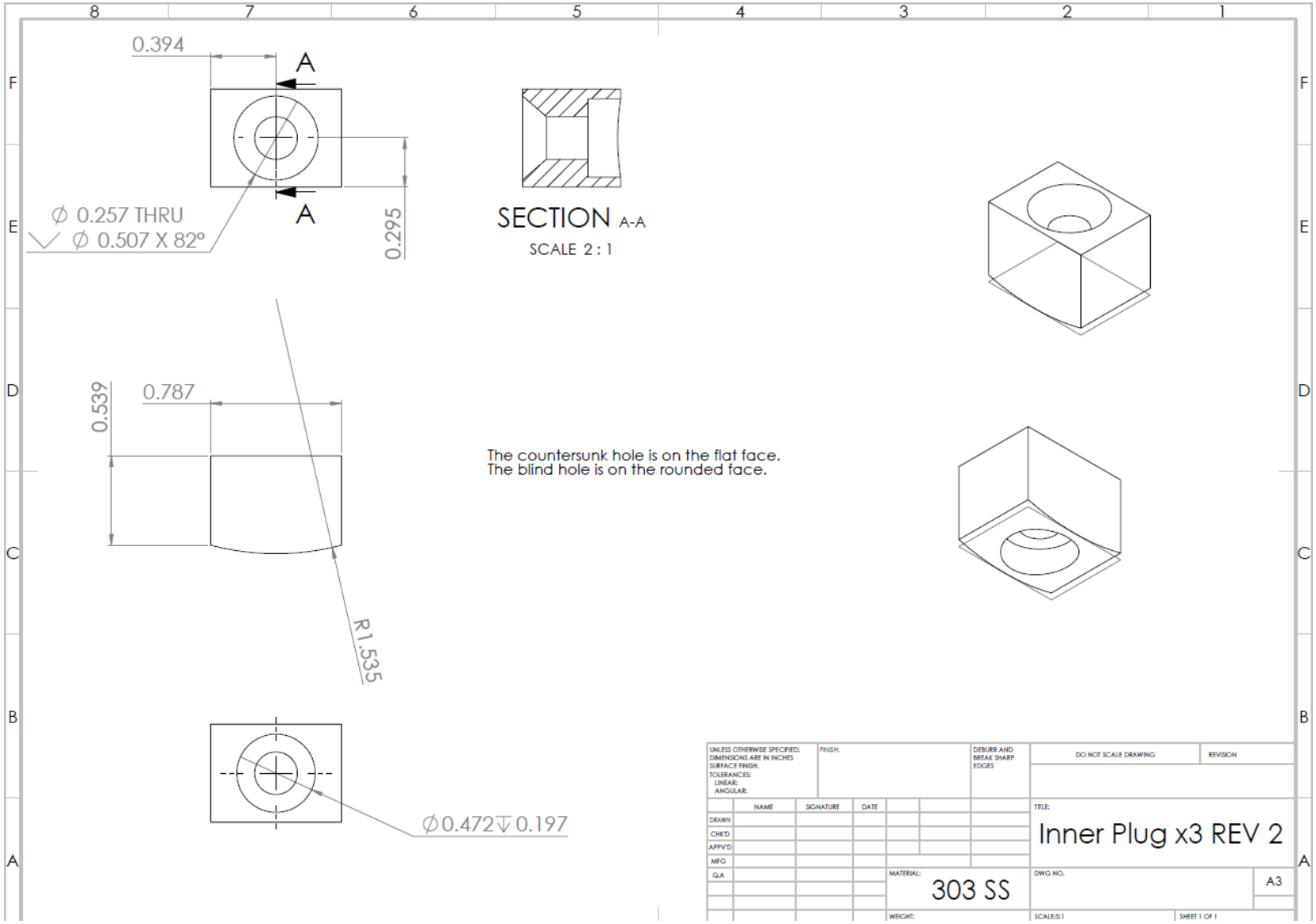

Figure B.13: Piece that mates the quarter-wave stubs to the beam dump.

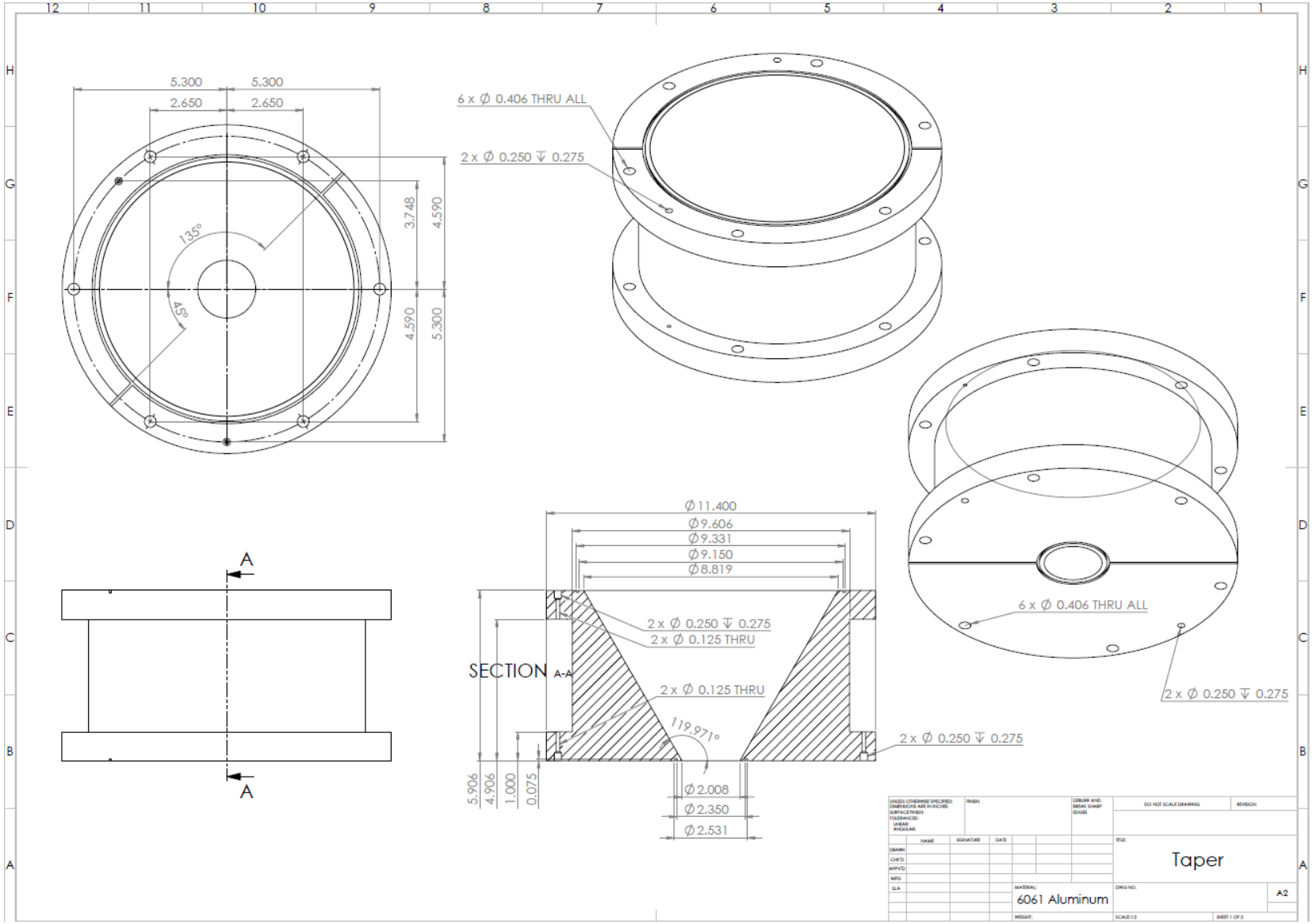

Figure B.14: Tapered outer conductor of the output coaxial transmission line.

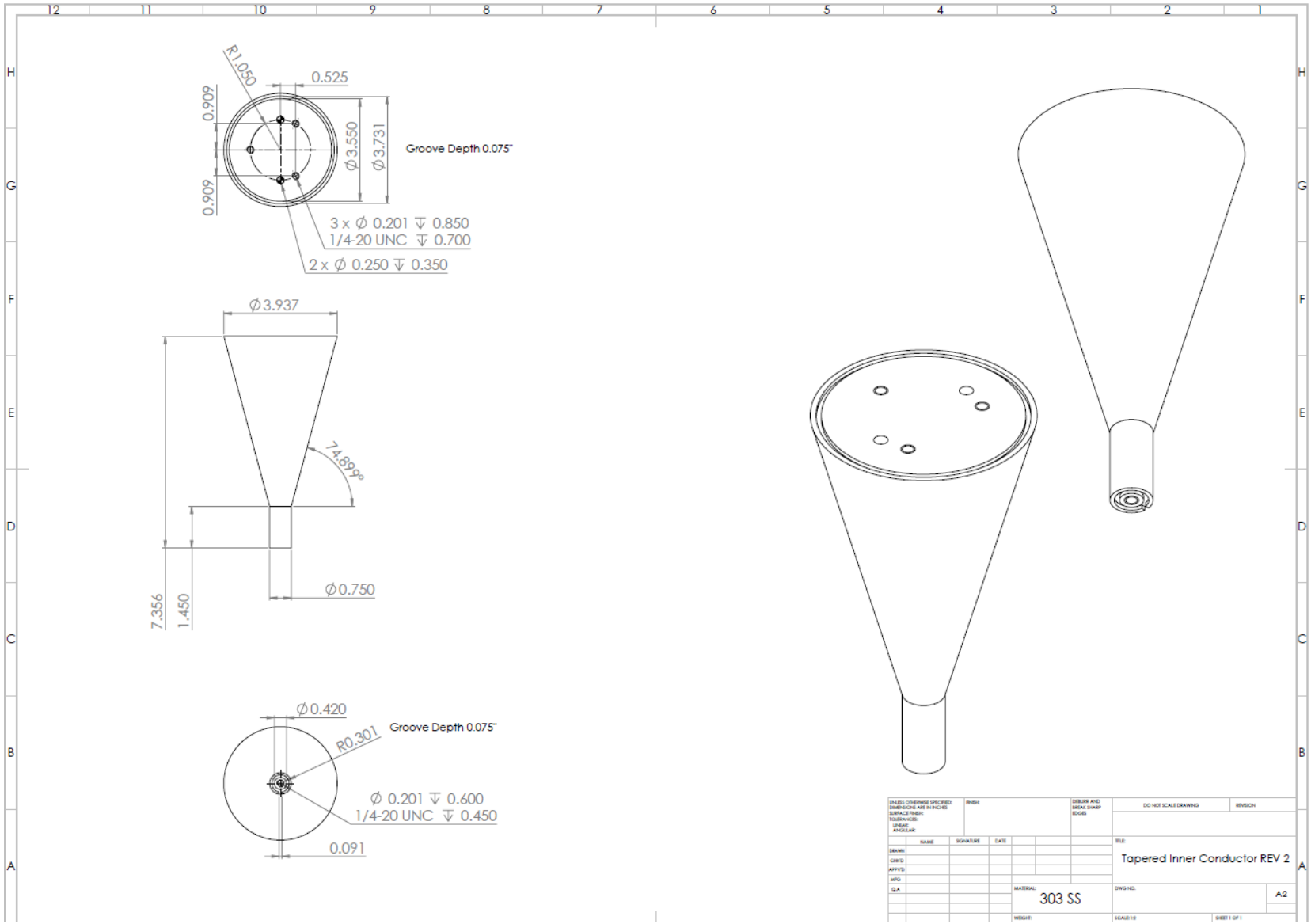

Figure B.15: Inner conductor of the tapered output transmission line.

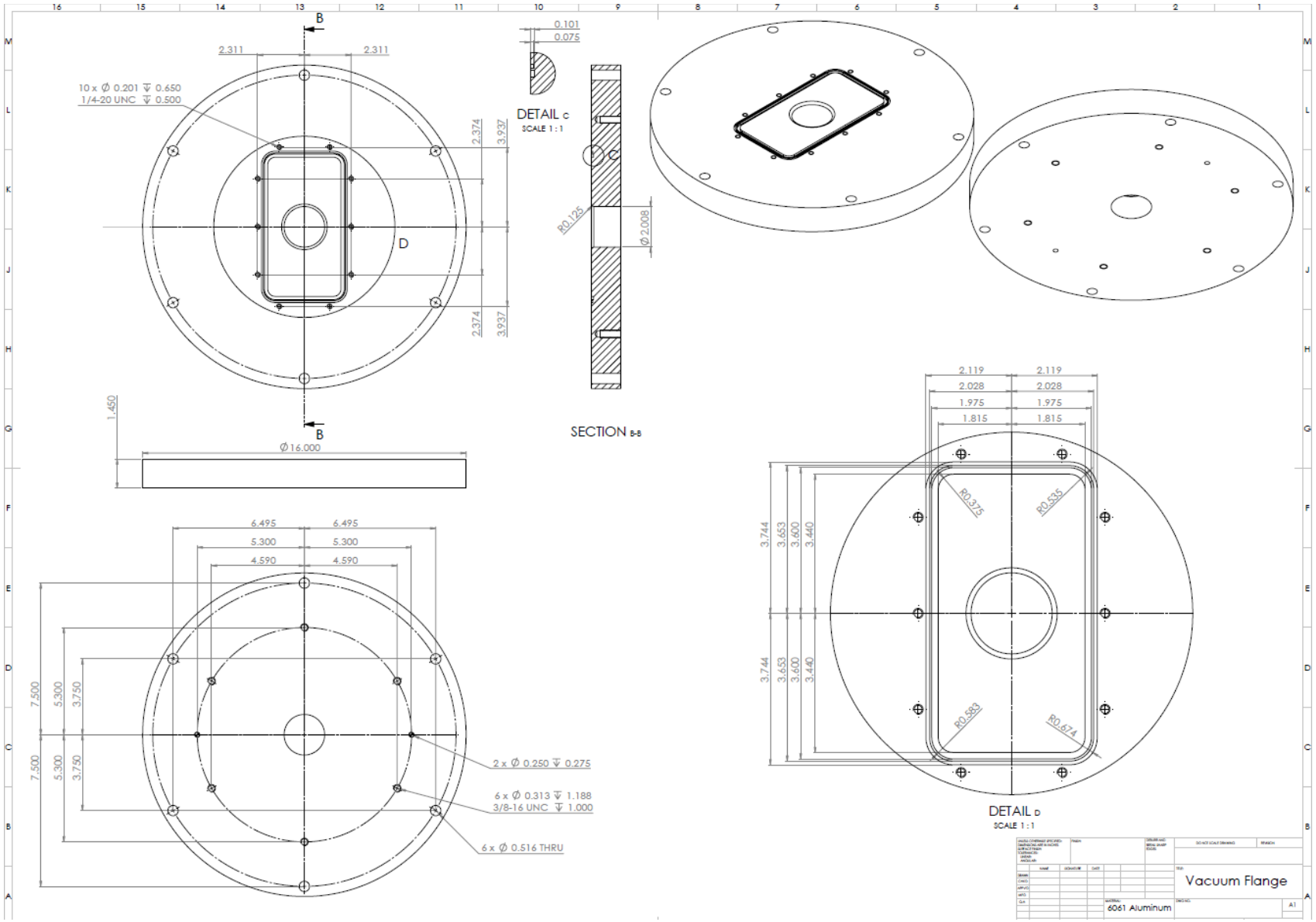

Figure B.16: Vacuum flange of the MILO assembly that mates to the MELBA test chamber.

Appendix C HRPM Experimental Post-processing Routine

The MATLAB post-processing script used to analyze the magnetron experiments is given here. With the raw traces collected during the experiments, the program will produce plots of the signals, Fourier transforms, voltage, current, and others. This program was used to analyze the low Q experiment, for which many of the input values are unique, such as the tuner position for each individual shot.

```
clear all
close all

%%%%%%%%%%% SHOT SERIES INFORMATION %%%%%%%%%%%%

first_shot = 17648;
last_shot = 17841;
num_shots = last_shot - first_shot + 1;
num_diode_traces = 4;
show_fig = 'off'; %This will plot and display figures if 'on', will not if 'off'
%The following string is where all the shot data is located
all_shots_dir = 'E:\HRPM_CACE_Experiments\36mmIrisHeight\StandardHRPM\HotTest\17648-17841\';
%Record tuner position
tuner_pos = zeros(num_shots,1);
tuner_pos = set_value(tuner_pos,first_shot,17648,17650,5.0);
tuner_pos = set_value(tuner_pos,first_shot,17651,17653,4.0);
tuner_pos = set_value(tuner_pos,first_shot,17654,17656,3.0);
tuner_pos = set_value(tuner_pos,first_shot,17657,17659,2.0);
tuner_pos = set_value(tuner_pos,first_shot,17660,17662,2.5);
tuner_pos = set_value(tuner_pos,first_shot,17663,17683,2.75);
tuner_pos = set_value(tuner_pos,first_shot,17684,17688,3.5);
tuner_pos = set_value(tuner_pos,first_shot,17689,17692,3.25);
tuner_pos = set_value(tuner_pos,first_shot,17693,17696,3);
tuner_pos = set_value(tuner_pos,first_shot,17697,17700,2.75);
tuner_pos = set_value(tuner_pos,first_shot,17701,17704,2.5);
tuner_pos = set_value(tuner_pos,first_shot,17705,17708,2.25);
tuner_pos = set_value(tuner_pos,first_shot,17709,17712,2.0);
tuner_pos = set_value(tuner_pos,first_shot,17713,17718,4.0);
tuner_pos = set_value(tuner_pos,first_shot,17719,17725,3.75);
tuner_pos = set_value(tuner_pos,first_shot,17726,17731,3.5);
tuner_pos = set_value(tuner_pos,first_shot,17732,17737,3.25);
```

```
tuner_pos = set_value(tuner_pos,first_shot,17738,17741,3.0);
tuner_pos = set_value(tuner_pos,first_shot,17742,17744,3.75);
tuner_pos = set_value(tuner_pos,first_shot,17745,17746,4.0);
tuner_pos = set_value(tuner_pos,first_shot,17747,17748,2.75);
tuner_pos = set_value(tuner_pos,first_shot,17749,17750,2.5);
tuner_pos = set_value(tuner_pos,first_shot,17751,17752,2.25);
tuner_pos = set_value(tuner_pos,first_shot,17753,17755,3.5);
tuner_pos = set_value(tuner_pos,first_shot,17756,17759,3.25);
tuner_pos = set_value(tuner_pos,first_shot,17760,17761,3.0);
tuner_pos = set_value(tuner_pos,first_shot,17762,17764,3.5);
tuner_pos = set_value(tuner_pos,first_shot,17765,17767,3.75);
tuner_pos = set_value(tuner_pos,first_shot,17768,17770,4.0);
tuner_pos = set_value(tuner_pos,first_shot,17771,17773,3.25);
tuner_pos = set_value(tuner_pos,first_shot,17774,17779,3.0);
tuner_pos = set_value(tuner_pos,first_shot,17780,17785,2.75);
tuner_pos = set_value(tuner_pos,first_shot,17786,17788,3.25);
tuner_pos = set_value(tuner_pos,first_shot,17789,17791,3.5);
tuner_pos = set_value(tuner_pos,first_shot,17792,17794,3.75);
tuner_pos = set_value(tuner_pos,first_shot,17795,17797,4.0);
tuner_pos = set_value(tuner_pos,first_shot,17798,17815,3.5);
tuner_pos = set_value(tuner_pos,first_shot,17816,17820,1.75);
tuner_pos = set_value(tuner_pos,first_shot,17821,17826,1.5);
tuner_pos = set_value(tuner_pos,first_shot,17827,17831,1.25);
tuner_pos = set_value(tuner_pos,first_shot,17832,17836,1.0);
tuner_pos = set_value(tuner_pos,first_shot,17837,17841,0.0);

tuner_pos = tuner_pos + 1; %All of these shots were taken with the short rods in the chamber

%Record magnetic field direction. Set to 1 if in the forward direction
field_dir = ones(num_shots,1);
field_dir = set_value(field_dir,first_shot,17648,17761,1);
field_dir = set_value(field_dir,first_shot,17762,17797,0);
field_dir = set_value(field_dir,first_shot,17798,17836,1);

%Create vector to skip shots for postprocessing. Set to one if you want to
%skip.
skip_analysis = zeros(num_shots,1);
%skip_analysis = set_value(skip_analysis,first_shot,17648,17685,1);

%Create a vector for TFA analysis. There are numerous signals for each shot
%on both LBO and SBO, so this may take a while to run. Set to 1 to perform
%analysis for each individual shot. This will only work if skip_analysis is
%also set to 1, because it controls whether the signals are downloaded.
plot_TFA = ones(num_shots,1);
%plot_TFA = set_value(skip_analysis,first_shot,17744,17744,1);
show_tfa = 'off'; %This will plot and display tfa figures if 'on', will not if 'off'
save_tfa = 1; %Set to 1 to save all TFA plots generated

%%%%%%%%%% SCOPE AND CHANNEL INFORMATION %%%%%%%%%%%%%
```

```
%================== Shot Plot Information ==================
%Set the following to 1 to plot voltage, current, and diode information
make_shot_plot = 1;
analyze_SBO_pow = ones(num_shots,3);%Assume every shot and waveguide requires analysis

%GPIB address is not idenitified for power scope, because it is always 7
%Identify the scope number for each SBO wg
%Columns are scope numbers for SBO wg 1, 2, and 3, respectively
sbo_pow_ch_id = zeros(num_shots,3);
sbo_pow_ch_id(:,1) = 1; %WG 1 was always connected to ch 1
sbo_pow_ch_id(:,2) = 2; %WG 2 was always connected to ch 2
sbo_pow_ch_id(:,3) = 3; %WG 3 was always connected to ch 3
plot_lbo_power = 1; %Set this boolean to 1 to include the LBO in the shot plot
lbo_pow_ch_id = 4*ones(num_shots,1); %LBO Channel is always channel 4
%================== SBO WG Freq Information ==================
%Set to 1 to analyze SBO waveguide output
perform_SBO_wgfreq_analysis = 1; %Analyze waveguide signals from SBO
analyze_SBO_wgfreq = ones(num_shots,3); %Assume every shot requires analysis, and then correct in the
following lines
analyze_SBO_wgfreq(38,:) = 0; %Fast scope information not collected on shot 17686
analyze_SBO_wgfreq(17800 - first_shot + 1,:) = 0; %Fast scope information not collected on shot 17800

%Identify the fast scope number for each sbo waveguide
%Columns are scope numbers for SBO wg 1, 2, and 3, respectively
sbo_wgfreq_scope_id = zeros(num_shots,3);
sbo_wgfreq_scope_id(:,1) = 6; %WG1 was always connected to GPIB6
sbo_wgfreq_scope_id(:,2) = 6; %WG2 was always connected to GPIB6
sbo_wgfreq_scope_id(:,3) = 6; %WG3 was always connected to GPIB6

%Identify the scope number for each SBO wg
%Columns are scope numbers for SBO wg 1, 2, and 3, respectively
sbo_wgfreq_ch_id = zeros(num_shots,3);
sbo_wgfreq_ch_id(:,1) = 1; %WG 1 was always connected to ch 1
sbo_wgfreq_ch_id(:,2) = 2; %WG 2 was always connected to ch 2
sbo_wgfreq_ch_id(:,3) = 3; %WG 3 was always connected to ch 3

%================== LBO B-Dot Information ==================

%Analyze B-Dot signals from the LBO. Columns are for LBO cavities 1, 2, and 3, respectively
perform_LBO_analysis = 1;
analyze_LBO = ones(num_shots,3); %Assume every shot requires analysis, and then correct in the following lines
analyze_LBO(38,:) = 0; %Fast scope information not collected on shot 17686
analyze_LBO(17800 - first_shot + 1,:) = 0; %Fast scope information not collected on shot 17800

%Identify the scope number for each cavity on a shot by shot basis
%Columns are scope numbers for LBO cavities 1, 2, and 3, respectively
lbo_scope_id = zeros(num_shots,3);
lbo_scope_id(:,1) = 3; %Cavity 1 is connected to GPIB3 for every shot
lbo_scope_id(:,2) = 6; %Cavity 2 is connected to GPIB6 for every shot
```

```
lbo_scope_id(:,3) = 3; %Cavity 3 is connected to GPIB3 for every shot

%Identify the channel number for each cavity on a shot by shot basis
%Columns are channel numbers for LBO cavities 1, 2, and 3, respectively
lbo_ch_id = zeros(num_shots,3);
lbo_ch_id(:,1) = 1; %Cavity 1 is connected to channel 1
lbo_ch_id(:,2) = 4; %Cavity 2 is connected to channel 4
lbo_ch_id(:,3) = 2; %Cavity 3 is connected to channel 2

%================== SBO B-Dot Information ==================

%Analyze B-Dot signals from the SBO. Columns are for SBO cavities 1, 3, and 5, respectively
perform_SBO_BDot_analysis = 1;
analyze_SBO_BDot = ones(num_shots,3); %Assume every shot requires analysis, and then correct in the following
lines
analyze_SBO_BDot(:,3) = 0; %Cavity 5 was never connected to a scope
analyze_SBO_BDot(38,:) = 0; %Fast scope information not collected on shot 17686
analyze_SBO_BDot(17800 - first_shot + 1,:) = 0; %Fast scope information not collected on shot 17800

%Identify the scope number for each cavity for SBO Bdots
%Columns are scope numbers for SBO cavities 1, 3, and 5, respectively
sbo_bdot_scope_id = zeros(num_shots,3);
sbo_bdot_scope_id(:,1) = 3; %Cavity 1 was always connected to GPIB3
sbo_bdot_scope_id(:,2) = 3; %Cavity 3 was always connected to GPIB3

%Identify the scope number for each cavity for SBO Bdots
%Columns are scope numbers for SBO cavities 1, 3, and 5, respectively
sbo_bdot_ch_id = zeros(num_shots,3);
sbo_bdot_ch_id(:,1) = 4; %Cavity 1 was always connected to ch 4
sbo_bdot_ch_id(:,2) = 3; %Cavity 3 was always connected to ch 3

%%%%%%%%%%% DIODE INFORMATION %%%%%%%%%%%
%The values below represent the diode used for each channel. The four
%entries are for the first, second, and third waveguides, and the last is
%for the LBO power trace (if present), respectively.
diode_inputs = zeros(num_shots,num_diode_traces);
diode_inputs(:,1) = 2;
diode_inputs(:,2) = 4;
diode_inputs(:,3) = 1;
diode_inputs(:,4) = 3;

%%%%%%%%%%% ATTENUATION %%%%%%%%%%%
%Provide values of line attenuation for waveguide output for shots 16894-17110
CA_inline = zeros(num_shots,1);%Initialize additional attenuation to cable A
CA_inline(1:end) = 20.3;

CD_inline = zeros(num_shots,1);%Initialize additional attenuation to cable D
CD_inline(1:end) = 20.1;
```

```
CE_inline = zeros(num_shots,1);%Initialize additional attenuation to cable E
CE_inline(1:end) = 20.7;

CC_inline = zeros(num_shots,1);%Initialize additional attenuation to cable C
CC_inline(1:end) = 42.2; %Check that this is right

dir_coupler_loss = 53; %Loss due to the waveguide directional coupler
splitter_loss = 3.1; %Loss due to splitter

%Calculate cable loss. These attenuation values are taken at 2.195 GHz
C1 = 17.7; %Attenuation of Cable A + D in dB
C2 = 17.7; %Attenuation of Cable A + E in dB
C3 = 20.1; %Attenuation of Cable D + E in dB
cable_A = C2-((C3-C1+C2)/2);
cable_D = C1-C2+((C3-C1+C2)/2);
cable_E = (C3-C1+C2)/2;
cable_C = 10; %THIS WAS NOT ACTUALLY MEASURED, JUST AN APPROXIMATION

%Calculate total loss
WG1_atten = CA_inline + cable_A + dir_coupler_loss + splitter_loss;
WG2_atten = CD_inline + cable_D + dir_coupler_loss + splitter_loss;
WG3_atten = CE_inline + cable_E + dir_coupler_loss + splitter_loss;
LBO_atten = CC_inline + cable_C + dir_coupler_loss + splitter_loss;
Total_attenuation = [WG1_atten,WG2_atten,WG3_atten,LBO_atten];

%%%%%%%%%% MISCELLANEOUS %%%%%%%%%%
%Perform operations on the fourier transform plots
filter_fft_DC = 1; %Remove DC element of FFT (boolean)
filter_cutoff = 0.001;
%Specify frequency ranges for FFT plots
lbo_fft_fmin = 0.1;
lbo_fft_fmax = 4;
sbo_bdot_fft_fmin = 0.1;
sbo_bdot_fft_fmax = 5;
sbo_wgfreq_fft_fmin = 0.1;
sbo_wgfreq_fft_fmax = 5;
%Define number of points used for moving average in each plot of raw signals
sig_plot_movmean_npts = 25;
%Set this to 1 if you want to immediately remove any DC offset from a trace
%when it is retreived from the data file.
remove_signal_DC_offset = 1;

%Booleans for saving and overwriting files. Set to 1 if you want to save or
%write out, set to 0 to not.
save_plots = zeros(num_shots,1); %Write plots out as png file
%save_plots = set_value(save_plots,first_shot,17760,17761,1);
compile_master_key_metrics = 0; %Iterate through the key metric files and compile them all into one file

%This is the slope used to convert from max measured bank voltage to magnetic field.
```

```
%This cal factor converts from bank voltage to kilogauss to tesla
magnetic_field_cal = 0.0578;

%%%%%%%%% BEGIN ITERATING THROUGH SHOTS %%%%%%%%%
first_index = 1;
last_index = num_shots;
for i=first_index :last_index
   if skip_analysis(i) == 1
      shot_num = first_shot + i - 1;
      output_str = strcat(num2str(i),{', '},num2str(shot_num));
      disp(output_str)
      continue
   end

   shot_num = first_shot + i - 1;
   output_str = strcat(num2str(i),{', '},num2str(shot_num));
   disp(output_str)
   data_dir = strcat(all_shots_dir,num2str(shot_num),'\traces\');

   %Calculate magnetic field
   filename = strcat(data_dir,num2str(shot_num),'_000_001_Magnet.txt');
   pearson_data = csvread(filename);
   pearson_baseline = mean(pearson_data(1:200,2));
   pearson_corrected = pearson_data(:,2) - pearson_baseline;
   movmean_num_pts = floor(length(pearson_data)/500);
   pearson_corrected_avg = movmean(pearson_corrected,movmean_num_pts);
   magnetic_field = magnetic_field_cal*max(abs(pearson_corrected_avg));

   %Create directory for key metrics to be saved
   key_file_directory = strcat(strcat(pwd,'\AnalyzedData\',num2str(shot_num),'\'));
   if ~exist(key_file_directory,'dir')
      mkdir(key_file_directory)
   end
   %Create variable for location of key metric file
   key_metric_path = strcat(key_file_directory,'key_metrics.csv');
   %Print the shot number
   fileID_ind = fopen(key_metric_path,'w');
   fprintf(fileID_ind,'%s%i\n','Shot Number,',shot_num);
   fclose(fileID_ind);

   %Print magnetic field, stub length, and field direction
   print_metric(key_metric_path,'Magnetic Field (T),',magnetic_field)
   print_metric(key_metric_path,'Stub Length (cm),',tuner_pos(i))
   print_metric(key_metric_path,'Field Dir,',field_dir(i))

   %Create title for each figure
   if field_dir(i) == 1
      b_str = 'Forward';
   elseif field_dir(i) == 0
```

```
    b_str = 'Reverse';
end
title_str = strcat({'Shot '},num2str(shot_num),...
    {', Stub Len '},num2str(tuner_pos(i)),{' cm, B = '},...
    num2str(round(magnetic_field,4)),{' T '},b_str);

%Analyze LBO B-Dots
if perform_LBO_analysis == 1
    %Determine number of LBO traces collected on this shot
    num_traces = sum(analyze_LBO(i,:)==1);
    lbo_signals = cell(1,size(analyze_LBO,2));
    %Iterate through the three cavities and pull down the traces
    for j=1:size(analyze_LBO,2)
        %Generate filename for this cavity
        filename = strcat(num2str(shot_num),'_GPIB0',num2str(lbo_scope_id(i,j)),...
            '_00',num2str(lbo_ch_id(i,j)),'_Signal',...
            num2str(lbo_ch_id(i,j)),'.txt');
        fdir = strcat(data_dir,filename);
        %If the file exists, step in
        if exist(fdir,'file') == 2
            %Download the file into this vector
            lbo_signals{j} = csvread(fdir);
            if remove_signal_DC_offset == 1
                dc_offset = mean(lbo_signals{j}(1:2500,2));
                lbo_signals{j}(:,2) = lbo_signals{j}(:,2) - dc_offset;
            end
        end
    end
    %With the traces downloaded, plot them
    if num_traces > 0
        %Create the figures
        lbo_f1  = figure('visible',show_fig,'position',[25 25 750 750]);
        lbo_f1_all  = figure('visible',show_fig,'position',[25 25 750 750]);
        lbo_fft  = figure('visible',show_fig,'position',[25 25 2400 750]);
        lbo_fft_all = figure('visible',show_fig,'position',[25 25 750 750]);
        lbo_sbo_signals_all = figure('visible',show_fig,'position',[25 25 750 750]);
        subplot_index = 0;
        %Determine plotting ranges for each signal plot
        tstart = zeros(size(analyze_LBO,2),1);
        tfinish = zeros(size(analyze_LBO,2),1);
        for j=1:size(analyze_LBO,2)
            %Retrieve start and finish time values for each trace.
            %Apply the function only if the signal was downloaded for
            %that cavity.
            if size(lbo_signals{j},1) > 1 && size(lbo_signals{j},2) == 2
                [tstart(j),tfinish(j)] = find_time_range(lbo_signals{j});
                lbo_signals_avg = zeros(size(lbo_signals{j},1),size(analyze_LBO,2));
            end
        end
```

```
%Now find the nonzero minimum and the maximum of tfinish
tstart_final_lbo = min(tstart(tstart>0));
tfinish_final_lbo = max(tfinish(tfinish>0));
%Iterate through each cavity
dom_freq_lbo = zeros(1,size(analyze_LBO,2));
for j=1:size(analyze_LBO,2)
   %If there was data taken for this cavity on this shot,
   %enter the statement
   if analyze_LBO(i,j) == 1
      %Plot the signals
      set(0, 'CurrentFigure', lbo_f1);
      subplot_index = subplot_index + 1;
      subplot(num_traces,1,subplot_index);
      baseline = mean(lbo_signals{j}(:,2));
      ordinate = movmean(lbo_signals{j}(:,2),2) - baseline;
      plot(lbo_signals{j}(:,1)*1E9,ordinate)
      ylabel(strcat({'LBO Cavity '},num2str(j)))
      %xlim([650 800])
      xlim([tstart_final_lbo*(1E9) tfinish_final_lbo*(1E9)])
      if subplot_index == 1
         title(title_str)
         %title('Shot 17744')
      elseif subplot_index == num_traces
         xlabel('t (ns)')
      end
      hold on
      lbo_signals_avg(:,j) = movmean(abs(ordinate),sig_plot_movmean_npts);
      plot(lbo_signals{j}(:,1)*1E9,lbo_signals_avg(:,j),'r')
      set(findall(gcf,'-property','FontSize'),'FontSize',18)

      %Plot all signals on the same axes
      if subplot_index == 1
         lbo_all_fft_legend = cell(num_traces,1);
         lbo_all_fft_plot_type = {'-.r','--k',':b'};
      end
      set(0, 'CurrentFigure', lbo_f1_all);
      ordinate = movmean(lbo_signals{j}(:,2),2) - baseline;
      ordinate = ordinate./max(abs(ordinate));
      plot(lbo_signals{j}(:,1)*1E9,ordinate,lbo_all_fft_plot_type{subplot_index})
      ylabel('LBO Signals')
      xlim([tstart_final_lbo*(1E9) tfinish_final_lbo*(1E9)])
      if subplot_index == 1
         title(title_str)
      elseif subplot_index == num_traces
         xlabel('t (ns)')
      end
      hold on
      set(findall(gcf,'-property','FontSize'),'FontSize',18)
```

```
%Plot an LBO and SBO signal on the same axes
if subplot_index == 2
    set(0, 'CurrentFigure', lbo_sbo_signals_all);
    ordinate = movmean(lbo_signals{j}(:,2),2) - baseline;
    ordinate = ordinate./max(abs(ordinate));
    plot(lbo_signals{j}(:,1)*1E9,ordinate,'r')
    ylabel('S/S_0')
    xlim([tstart_final_lbo*(1E9) tfinish_final_lbo*(1E9)])
    if subplot_index == 1
        title(title_str)
    elseif subplot_index == num_traces
        xlabel('t (ns)')
    end
    hold on
    set(findall(gcf,'-property','FontSize'),'FontSize',18)
end

set(0, 'CurrentFigure', lbo_fft);
%Perform FFT
[freq,FFT_signal] = perform_FFT(lbo_signals{j},filter_fft_DC,filter_cutoff);
FFT_signal = movmean(FFT_signal,50); %Smooth the plot
noise_floor = mean(FFT_signal);
FFT_signal = FFT_signal - noise_floor; %Remove noise floor, if any
indexmax = max(FFT_signal) == FFT_signal; %Find index of maximum peak
dom_freq = freq(indexmax); %Find dominant frequency
dom_freq_lbo(j) = dom_freq;
ymax = FFT_signal(indexmax); %Find value of dominant peak
FFT_signal = FFT_signal./ymax; %Normalize the FFT
subplot(1,num_traces,subplot_index); %Plot and format FFT's
plot(freq,FFT_signal)
xlabel(strcat({'f (GHz), LBO Cav '},num2str(j)))
xlim([lbo_fft_fmin lbo_fft_fmax])
ylim([0 1.1])
if subplot_index == 1
    ylabel('A/A_0')
end
hold on
strmax = [num2str(dom_freq), ' GHz'];
text(dom_freq, 1, strmax, 'HorizontalAlignment' , 'center', 'VerticalAlignment', 'bottom', 'FontSize', 10);
plot(dom_freq, 1, '*')
if num_traces == 1 || num_traces == 2
    if subplot_index == 1
        title(title_str)
    end
elseif num_traces == 3
    if subplot_index == 2
        title(title_str)
    end
end
```

```
            set(findall(gcf,'-property','FontSize'),'FontSize',28)
            %Print dominant frequency
            left_col = strcat({'LBO B-Dot '},num2str(j),{' Dom Freq (GHz),'});
            print_metric(key_metric_path,char(left_col),dom_freq)

            %Superimpose all FFT's on one figure
            set(0, 'CurrentFigure', lbo_fft_all);
            plot(freq,FFT_signal,lbo_all_fft_plot_type{subplot_index})
            if subplot_index == 1
               set(findall(gcf,'-property','FontSize'),'FontSize',16)
               ylabel('A/A_0','FontSize',24)
               xlabel('f (GHz)','FontSize',24)
            end
            lbo_all_fft_legend{subplot_index} = char(strcat({'LBO Cav '},num2str(j),{', f = '},strmax));
            xlim([1 1.1])
            ylim([0 1.1])
            hold on
            if subplot_index == num_traces
               fft_all_leg = legend(lbo_all_fft_legend,'Location','best');
               fft_all_leg.FontSize = 12;
            end

         end
      end %Stop iterating through cavities
   end %Plots are complete

   if num_traces > 0
      %Save plots to individual folder
      traces_filename = strcat(key_file_directory,'LBO_signals_',num2str(shot_num),'.png');
      save_png(save_plots(i),lbo_f1,char(traces_filename))
      fft_filename = strcat(key_file_directory,'LBO_FFT_',num2str(shot_num),'.png');
      save_png(save_plots(i),lbo_fft,char(fft_filename))

      %Save to 'AllShots' LBO folder
      file_dir_sig = strcat(strcat(pwd,'\AnalyzedData\AllShots\LBO\Signals\'));
      if ~exist(file_dir_sig,'dir')
         mkdir(file_dir_sig)
      end
      file_dir_fft = strcat(strcat(pwd,'\AnalyzedData\AllShots\LBO\FFTs\'));
      if ~exist(file_dir_fft,'dir')
         mkdir(file_dir_fft)
      end
      traces_filename = strcat(file_dir_sig,num2str(shot_num),'_LBO_signals.png');
      save_png(save_plots(i),lbo_f1,char(traces_filename))
      fft_filename = strcat(file_dir_fft,num2str(shot_num),'_LBO_FFT.png');
      save_png(save_plots(i),lbo_fft,char(fft_filename))
   end

end %LBO analysis complete
```

```
%Analyze SBO Waveguide signals
if perform_SBO_wgfreq_analysis == 1
   %Determine number of SBO Waveguide traces collected on this shot
   num_traces = sum(analyze_SBO_wgfreq(i,:)==1);
   sbo_wgfreq_signals = cell(1,size(analyze_SBO_wgfreq,2));
   %Iterate through the three waveguides and pull down the traces
   for j=1:size(analyze_SBO_wgfreq,2)
      %Generate filename for this waveguide
      filename = strcat(num2str(shot_num),'_GPIB0',num2str(sbo_wgfreq_scope_id(i,j)),...
         '_00',num2str(sbo_wgfreq_ch_id(i,j)),'_Signal',...
         num2str(sbo_wgfreq_ch_id(i,j)),'.txt');
      fdir = strcat(data_dir,filename);
      %If the file exists, step in
      if exist(fdir,'file') == 2
         sbo_wgfreq_signals{j} = csvread(fdir);
         if remove_signal_DC_offset == 1
            dc_offset = mean(sbo_wgfreq_signals{j}(1:2500,2));
            sbo_wgfreq_signals{j}(:,2) = sbo_wgfreq_signals{j}(:,2) - dc_offset;
         end
      end
   end
   %With the traces downloaded, plot them
   if num_traces > 0
      %Create the figures
      sbo_wgfreq_f1  = figure('visible',show_fig,'position',[25 25 750 750]);
      sbo_wgfreq_f1_all  = figure('visible',show_fig,'position',[25 25 750 750]);
      sbo_wgfreq_fft  = figure('visible',show_fig,'position',[25 25 2400 750]);
      sbo_wgfreq_fft_all  = figure('visible',show_fig,'position',[25 25 750 750]);
      subplot_index = 0;
      %Determine plotting ranges for each signal plot
      tstart = zeros(size(analyze_SBO_wgfreq,2),1);
      tfinish = zeros(size(analyze_SBO_wgfreq,2),1);
      for j=1:size(analyze_SBO_wgfreq,2)
         %Retrieve start and finish time values for each trace.
         %Apply the function only if the signal was downloaded for
         %that cavity.
         if size(sbo_wgfreq_signals{j},1) > 1 && size(sbo_wgfreq_signals{j},2) == 2
            [tstart(j),tfinish(j)] = find_time_range(sbo_wgfreq_signals{j});
            sbo_wgfreq_signals_avg = zeros(size(sbo_wgfreq_signals{j},1),size(analyze_SBO_wgfreq,2));
         end
      end
      %Now find the nonzero minimum and the maximum of tfinish
      tstart_final_sbowg = min(tstart(tstart>0));
      tfinish_final_sbowg = max(tfinish(tfinish>0));
      %Iterate through each cavity
      dom_freq_sbo = zeros(1,size(analyze_SBO_wgfreq,2));
      for j=1:size(analyze_SBO_wgfreq,2)
         %If there was data taken for this cavity on this shot,
```

```
%enter the statement
if analyze_SBO_wgfreq(i,j) == 1
   %Plot the signals
   set(0, 'CurrentFigure', sbo_wgfreq_f1);
   subplot_index = subplot_index + 1;
   subplot(num_traces,1,subplot_index);
   baseline = mean(sbo_wgfreq_signals{j}(:,2));
   ordinate = movmean(sbo_wgfreq_signals{j}(:,2),2) - baseline;
   plot(sbo_wgfreq_signals{j}(:,1)*1E9,ordinate)
   ylabel(strcat({'SBO WG '},num2str(j)))
   [tstart,tfinish] = find_time_range(sbo_wgfreq_signals{j});
   %xlim([650 760])
   xlim([tstart_final_sbowg*(1E9) tfinish_final_sbowg*(1E9)])
   if subplot_index == 1
      title(title_str)
      %title('Shot 17744')
   elseif subplot_index == num_traces
      xlabel('t (ns)')
   end
   hold on
   sbo_wgfreq_signals_avg(:,j) = movmean(abs(ordinate),sig_plot_movmean_npts);
   plot(sbo_wgfreq_signals{j}(:,1)*1E9,sbo_wgfreq_signals_avg(:,j),'r')
   set(findall(gcf,'-property','FontSize'),'FontSize',18)

   %Plot all signals on the same axes
   if subplot_index == 1
      sbo_all_signals_legend = cell(num_traces,1);
      sbo_all_signals_plot_type = {'-.r','--k',':b'};
   end
   set(0, 'CurrentFigure', sbo_wgfreq_f1_all);
   hold on
   ordinate = movmean(sbo_wgfreq_signals{j}(:,2),2) - baseline;
   ordinate = ordinate./max(abs(ordinate));
   plot(sbo_wgfreq_signals{j}(:,1)*1E9,ordinate,sbo_all_signals_plot_type{subplot_index})
   if subplot_index == 1
      title(title_str)
      ylabel('SBO Signals')
      xlim([tstart_final_sbowg*(1E9) tfinish_final_sbowg*(1E9)])
   elseif subplot_index == num_traces
      xlabel('t (ns)')
   end
   hold on
   set(findall(gcf,'-property','FontSize'),'FontSize',18)

   %Plot one LBO and one SBO signal on the same axes
   if subplot_index == 2
      set(0, 'CurrentFigure', lbo_sbo_signals_all);
      hold on
      ordinate = movmean(sbo_wgfreq_signals{j}(:,2),2) - baseline;
```

```
    ordinate = ordinate./max(abs(ordinate));
    plot(sbo_wgfreq_signals{j}(:,1)*1E9,ordinate,'b')
    xlim([tstart_final_sbowg*(1E9) tfinish_final_sbowg*(1E9)])
    hold on
    ax = gca;
    ax.FontSize = 16;
    xlabel('t (ns)','FontSize',24)
    ylabel('S/S_0','FontSize',24)
    leg = legend('LBO B-dot 2','SBO WG 2');
    leg.FontSize = 12;
    xlim([650 760])
end

set(0, 'CurrentFigure', sbo_wgfreq_fft);
%Perform FFT
[freq,FFT_signal] = perform_FFT(sbo_wgfreq_signals{j},filter_fft_DC,filter_cutoff);
FFT_signal = movmean(FFT_signal,50); %Smooth the plot
noise_floor = mean(FFT_signal);
FFT_signal = FFT_signal - noise_floor; %Remove noise floor, if any
indexmax = max(FFT_signal) == FFT_signal; %Find index of maximum peak
dom_freq = freq(indexmax); %Find dominant frequency
dom_freq_sbo(j) = dom_freq;
ymax = FFT_signal(indexmax); %Find value of dominant peak
FFT_signal = FFT_signal./ymax; %Normalize the FFT
subplot(1,num_traces,subplot_index); %Plot and format FFT's
plot(freq,FFT_signal)
xlabel(strcat({'f (GHz), SBO WG '},num2str(j)))
xlim([sbo_wgfreq_fft_fmin sbo_wgfreq_fft_fmax])
ylim([0 1.1])
if subplot_index == 1
    ylabel('A/A_0')
end
hold on
strmax = [num2str(dom_freq), ' GHz'];
text(dom_freq, 1, strmax, 'HorizontalAlignment' , 'center', 'VerticalAlignment', 'bottom', 'FontSize', 10);
plot(dom_freq, 1, '*')
if num_traces == 1 || num_traces == 2
    if subplot_index == 1
        title(title_str)
    end
elseif num_traces == 3
    if subplot_index == 2
        title(title_str)
    end
end
set(findall(gcf,'-property','FontSize'),'FontSize',28)
%Print dominant frequency
left_col = strcat({'SBO WG '},num2str(j),{' Dom Freq (GHz),'});
print_metric(key_metric_path,char(left_col),dom_freq)
```

```
%Superimpose all FFT's on one figure
set(0, 'CurrentFigure', sbo_wgfreq_fft_all);
if subplot_index == 1
    sbo_all_fft_legend = cell(num_traces,1);
    sbo_all_fft_plot_type = {'-.k','--b',':r'};
end
plot(freq,FFT_signal,sbo_all_fft_plot_type{subplot_index})
if subplot_index == 1
    ylabel('A/A_0')%,'FontSize',32)
    xlabel('f (GHz)')%,'FontSize',32)
    set(findall(gcf,'-property','FontSize'),'FontSize',32)
end
sbo_all_fft_legend{subplot_index} = char(strcat({'WG '},num2str(j),{', f = '},strmax));
xlim([1.8 2.2])
ylim([0 1.1])
hold on
ax = gca;
ax.FontSize = 16;
ylabel('A/A_0','FontSize',32)
xlabel('f (GHz)','FontSize',32)
if subplot_index == num_traces
    cell_all_plot = [lbo_all_fft_legend;sbo_all_fft_legend];
    fft_all_leg = legend(sbo_all_fft_legend,'Location','best');
    fft_all_leg.FontSize = 12;
end

%Superimpose all FFT's from lbo and sbo on one figure
set(0, 'CurrentFigure', lbo_fft_all);
if subplot_index == 1
    sbo_all_fft_legend = cell(num_traces,1);
    sbo_all_fft_plot_type = {'-.k','--b',':r'};
end
plot(freq,FFT_signal,sbo_all_fft_plot_type{subplot_index})
if subplot_index == 1
    ylabel('A/A_0')%,'FontSize',32)
    xlabel('f (GHz)')%,'FontSize',32)
    set(findall(gcf,'-property','FontSize'),'FontSize',32)
end
sbo_all_fft_legend{subplot_index} = char(strcat({'WG '},num2str(j),{', f = '},strmax));
xlim([1.03 2.15])
ylim([0 1.1])
hold on
ax = gca;
ax.FontSize = 16;
ylabel('A/A_0','FontSize',32)
xlabel('f (GHz)','FontSize',32)
if subplot_index == num_traces
```

```
                cell_all_plot = [lbo_all_fft_legend;sbo_all_fft_legend];
                fft_all_leg = legend(cell_all_plot,'Location','northoutside','NumColumns',2);
                fft_all_leg.FontSize = 12;
                breakxaxis([1.08 2.07]);
            end

        end
    end %Iteration through cavities is now complete
end %Plots are complete

if num_traces > 0
    %Save plots to individual folder
    traces_filename = strcat(key_file_directory,'SBO_WG_signals_',num2str(shot_num),'.png');
    save_png(save_plots(i),sbo_wgfreq_f1,char(traces_filename))
    fft_filename = strcat(key_file_directory,'SBO_WG_FFT_',num2str(shot_num),'.png');
    save_png(save_plots(i),sbo_wgfreq_fft,char(fft_filename))

    %Save to 'AllShots' SBO WG folder
    file_dir_sig = strcat(strcat(pwd,'\AnalyzedData\AllShots\SBO_WG\Signals\'));
    if ~exist(file_dir_sig,'dir')
        mkdir(file_dir_sig)
    end
    file_dir_fft = strcat(strcat(pwd,'\AnalyzedData\AllShots\SBO_WG\FFTs\'));
    if ~exist(file_dir_fft,'dir')
        mkdir(file_dir_fft)
    end
    traces_filename = strcat(file_dir_sig,num2str(shot_num),'_SBO_WG_signals.png');
    save_png(save_plots(i),sbo_wgfreq_f1,char(traces_filename))
    fft_filename = strcat(file_dir_fft,num2str(shot_num),'_SBO_WG_FFT.png');
    save_png(save_plots(i),sbo_wgfreq_fft,char(fft_filename))
end

end %SBO WG freq analysis complete

%With all of the signals downloaded, perform TFA
if plot_TFA(i) == 1

    tfa_lbo_sbo = figure('visible',show_tfa,'position',[0 0 1500 1000]);
    lbo_freq_avg = (1E9)*mean(dom_freq_lbo);
    lbo_freq_narrow_bds = [0.8*lbo_freq_avg, 1.2*lbo_freq_avg];
    sbo_freq_avg = (1E9)*mean(dom_freq_sbo);
    sbo_freq_narrow_bds = [0.8*sbo_freq_avg, 1.2*sbo_freq_avg];

    %Perform TFA routine for LBO B-Dot signals
    num_lbo_sigs = length(lbo_signals);
    lbo_tfa = figure('visible',show_tfa,'position',[0 0 1500 1000]);
    lbo_t_window = 300;
    for k=1:num_lbo_sigs
        dt_sig = (1E9)*(lbo_signals{k}(2,1)-lbo_signals{k}(1,1));
```

```
        num_tsteps = round(lbo_t_window/dt_sig);
        t1 = (1E9)*lbo_signals{k}(:,1);
        Fs = (1E9)/dt_sig;
        max_index = find(lbo_signals{k}(:,2) == max(lbo_signals{k}(:,2)));
        first_index = max_index - num_tsteps/2;
        last_index = max_index + num_tsteps/2;
        %t = t1(first_index:last_index) - t1(first_index);
        t = t1(first_index:last_index);
        sig_norm = lbo_signals{k}(:,2)./max(abs(lbo_signals{k}(:,2)));
        sig = sig_norm(first_index:last_index);
        subplot(3,2,2*k-1)
        pspectrum(sig,Fs,'Leakage',1,'FrequencyLimits',[5E8, 5E9])
        title_str = strcat({'Shot '},num2str(shot_num),...
            {', Stub Len '},num2str(tuner_pos(i)),{' cm, B = '},...
            num2str(round(magnetic_field,4)),{' T '},b_str);
        title_txt = strcat({'LBO B-Dot '},num2str(k),{', F_d_o_m = '},num2str(round(dom_freq_lbo(k),4)),{' GHz,
F_h_a_r_m = '},num2str(round(2*dom_freq_lbo(k),4)),{' GHz'});
        title(title_txt)
        subplot(3,2,2*k)
        pspectrum(sig,Fs,'spectrogram','Leakage',1,'OverlapPercent',0,'MinThreshold',-40,'FrequencyLimits',[0,
3E9],'Reassign',true,'FrequencyResolution',1e7,'OverlapPercent',99)
        title_txt = strcat({'LBO B-Dot '},num2str(k),{', B='},num2str(round(magnetic_field,3)),{'T, Stub Len
'},num2str(tuner_pos(i)),{'cm'});
        title(title_txt)

        set(0, 'CurrentFigure', tfa_lbo_sbo);
        subplot(3,2,2*k-1)
        pspectrum(sig,Fs,'spectrogram','Leakage',1,'OverlapPercent',0,'MinThreshold',-
40,'FrequencyLimits',lbo_freq_narrow_bds,'Reassign',true,'FrequencyResolution',1e7,'OverlapPercent',99)
        title_txt = strcat({'LBO B-Dot '},num2str(k),{', F_D = '},num2str(round(dom_freq_lbo(k),4)),{' GHz, F_H =
'},...
            num2str(round(2*dom_freq_lbo(k),4)),{' GHz, B='},num2str(round(magnetic_field,3)),{'T, Stub Len
'},num2str(tuner_pos(i)),{'cm'});
        title(title_txt)

        set(0, 'CurrentFigure', lbo_tfa);
    end
    %Save to individual folder
    lbo_tfa_filename = strcat(key_file_directory,'lbo_tfa_wide_',num2str(shot_num),'.png');
    save_png(save_tfa,lbo_tfa,char(lbo_tfa_filename))
    %Save to 'AllPlots'
    lbo_tfa_file_dir_sp = strcat(strcat(pwd,'\AnalyzedData\AllShots\LBO_TFA_Wide\'));
    if ~exist(lbo_tfa_file_dir_sp,'dir')
        mkdir(lbo_tfa_file_dir_sp)
    end
    lbo_tfa_filename = strcat(lbo_tfa_file_dir_sp,num2str(shot_num),'_lbo_tfa.png');
    save_png(save_tfa,lbo_tfa,char(lbo_tfa_filename))

    %Perform TFA routine for SBO WG signals
```

```
    num_sbo_sigs = length(sbo_wgfreq_signals);
    sbo_tfa = figure('visible',show_tfa,'position',[0 0 1500 1000]);
    sbo_t_window = 300;
    for k=1:num_sbo_sigs
        dt_sig = (1E9)*(sbo_wgfreq_signals{k}(2,1)-sbo_wgfreq_signals{k}(1,1));
        num_tsteps = round(sbo_t_window/dt_sig);
        t1 = (1E9)*sbo_wgfreq_signals{k}(:,1);
        Fs = (1E9)/dt_sig;
        if k==1
            max_index = find(sbo_wgfreq_signals{k}(:,2) == max(sbo_wgfreq_signals{k}(:,2)));
        end
        first_index = max_index - num_tsteps/2;
        last_index = max_index + num_tsteps/2;
        %t = t1(first_index:last_index) - t1(first_index);
        t = t1(first_index:last_index);
        sig_norm = sbo_wgfreq_signals{k}(:,2)./max(abs(sbo_wgfreq_signals{k}(:,2)));
        sig = sig_norm(first_index:last_index);
        subplot(3,2,2*k-1)
        pspectrum(sig,Fs,'Leakage',1,'FrequencyLimits',[5E8, 6.5E9])
        title_txt = strcat({'SBO WG '},num2str(k),{', F_d_o_m = '},num2str(round(dom_freq_sbo(k),4)),{' GHz,
2*F_L_B_O_,_A_V_G = '},num2str(round(2*lbo_freq_avg/(1E9),4)),{' GHz'});
        title(title_txt)
        subplot(3,2,2*k)
        pspectrum(sig,Fs,'spectrogram','Leakage',1,'OverlapPercent',0,'MinThreshold',-40,'FrequencyLimits',[1.5E9,
3.5E9],'Reassign',true,'FrequencyResolution',1e7,'OverlapPercent',99)
        title_txt = strcat({'SBO WG '},num2str(k),{', B='},num2str(round(magnetic_field,3)),{'T, Stub Len
'},num2str(tuner_pos(i)),{'cm'});
        title(title_txt)

        set(0, 'CurrentFigure', tfa_lbo_sbo);
        subplot(3,2,2*k)
        pspectrum(sig,Fs,'spectrogram','Leakage',1,'OverlapPercent',0,'MinThreshold',-
40,'FrequencyLimits',sbo_freq_narrow_bds,'Reassign',true,'FrequencyResolution',1e7,'OverlapPercent',99)
        title_txt = strcat({'SBO WG '},num2str(k),{', F_d_o_m = '},num2str(round(dom_freq_sbo(k),4)),{' GHz,
2*F_L_B_O_,_A_V_G = '},num2str(round(2*lbo_freq_avg/(1E9),4)),{' GHz'});
        title(title_txt)

        set(0, 'CurrentFigure', sbo_tfa);
    end
    %Save to individual folder
    sbo_tfa_filename = strcat(key_file_directory,'sbo_tfa_wide_',num2str(shot_num),'.png');
    save_png(save_tfa,sbo_tfa,char(sbo_tfa_filename))
    %Save to 'AllPlots'
    sbo_tfa_file_dir_sp = strcat(strcat(pwd,'\AnalyzedData\AllShots\SBO_TFA_Wide\'));
    if ~exist(sbo_tfa_file_dir_sp,'dir')
        mkdir(sbo_tfa_file_dir_sp)
    end
    sbo_tfa_filename = strcat(sbo_tfa_file_dir_sp,num2str(shot_num),'_sbo_tfa.png');
    save_png(save_tfa,sbo_tfa,char(sbo_tfa_filename))
```

```
    %Save figure with SBO and LBO TFA
    set(0, 'CurrentFigure', tfa_lbo_sbo);
    lbo_sbo_tfa_filename = strcat(key_file_directory,'tfa_narrow_',num2str(shot_num),'.png');
    save_png(save_tfa,tfa_lbo_sbo,char(lbo_sbo_tfa_filename))
    %Save to 'AllPlots'
    lbo_sbo_tfa_file_dir_sp = strcat(strcat(pwd,'\AnalyzedData\AllShots\TFA_Narrow\'));
    if ~exist(lbo_sbo_tfa_file_dir_sp,'dir')
        mkdir(lbo_sbo_tfa_file_dir_sp)
    end
    lbo_sbo_tfa_filename = strcat(lbo_sbo_tfa_file_dir_sp,num2str(shot_num),'_tfa_narrow.png');
    save_png(save_tfa,tfa_lbo_sbo,char(lbo_sbo_tfa_filename))

end

%Make shot plot
if make_shot_plot == 1

    %Determine number of SBO Waveguide traces collected on this shot
    num_traces = sum(analyze_SBO_pow(i,:)==1);
    sbo_pow_raw = cell(1,size(analyze_SBO_pow,2));
    sbo_pow = cell(1,size(analyze_SBO_pow,2));
    %Iterate through the three waveguides and pull down the traces,
    %then use them to calculate the output power
    for j=1:size(analyze_SBO_pow,2)
        %Generate filename for this waveguide
        filename = strcat(num2str(shot_num),'_002_00',...
            num2str(sbo_pow_ch_id(i,j)),'_Power',...
            num2str(sbo_pow_ch_id(i,j)),'.txt');
        fdir = strcat(data_dir,filename);
        %If the file exists, step in
        if exist(fdir,'file') == 2
            sbo_pow_raw{j} = csvread(fdir);
            %Remove DC offset
            if remove_signal_DC_offset == 1
                dc_offset = mean(sbo_pow_raw{j}(1:500,2));
                sbo_pow_raw{j}(:,2) = sbo_pow_raw{j}(:,2) - dc_offset;
            end
            %Calculate power
            movmean_npts = floor(size(sbo_pow_raw{j},1)/1000);
            %Calculate diode voltage in mV
            diode_data_input = (1E3)*abs(movmean(sbo_pow_raw{j}(:,2),movmean_npts));
            sbo_pow{j}(:,1) = sbo_pow_raw{j}(:,1);
            sbo_pow{j}(:,2) = Power_Calculation(diode_data_input,...
                diode_inputs(i,j),Total_attenuation(i,j));
            %Calculate total power by iteratively adding the traces
            if j==1
                sbo_pow_tot = sbo_pow{j};
            else
```

```
            sbo_pow_tot(:,2) = sbo_pow_tot(:,2) + sbo_pow{j}(:,2);
        end
    end
end

%Download the voltage and rogowski waveforms
v_fname = strcat(num2str(shot_num),'_001_002_VOLN.txt');
v_fdir = strcat(data_dir,v_fname);
r_fname = strcat(num2str(shot_num),'_001_003_MEC2.txt');
r_fdir = strcat(data_dir,r_fname);
if exist(v_fdir,'file') == 2 %&& exist(r_fdir,'file') == 2
    vol_raw = csvread(v_fdir);
    melba_voltage = zeros(size(vol_raw,1),size(vol_raw,2));
    movmean_npts = floor(size(vol_raw,1)/500);
    melba_voltage(:,1) = vol_raw(:,1);
    melba_voltage(:,2) = -1*movmean(vol_raw(:,2),movmean_npts);
    [voltage_rise1,voltage_rise2] = voltage_rise_time(melba_voltage);
    left_col = strcat({'Voltage Rise 1 (ns),'});
    print_metric(key_metric_path,char(left_col),voltage_rise1*(1E9))
    left_col = strcat({'Voltage Rise 2 (ns),'});
    print_metric(key_metric_path,char(left_col),voltage_rise2*(1E9))
    rog_raw = csvread(r_fdir);
    melba_current = calc_current(rog_raw);
end
%Download the LBO power trace, if desired
if plot_lbo_power == 1
    %Generate filename
    filename = strcat(num2str(shot_num),'_002_00',...
        num2str(lbo_pow_ch_id(i)),'_Power',...
        num2str(lbo_pow_ch_id(i)),'.txt');
    fdir = strcat(data_dir,filename);
    %If the file exists, step in
    if exist(fdir,'file') == 2
        lbo_pow_raw = csvread(fdir);
        if remove_signal_DC_offset == 1
            dc_offset = mean(lbo_pow_raw(1:500,2));
            lbo_pow_raw(:,2) = lbo_pow_raw(:,2) - dc_offset;
        end
        %movmean_npts = floor(size(sbo_pow_raw{j},1)/100);
        diode_data_input = (1E3)*abs(movmean(lbo_pow_raw(:,2),50));
        lbo_pow = zeros(size(lbo_pow_raw,1),size(lbo_pow_raw,2));
        lbo_pow(:,1) = sbo_pow_raw{j}(:,1);
        lbo_pow(:,2) = Power_Calculation(diode_data_input,...
            diode_inputs(i,4),Total_attenuation(i,4));
        left_col = strcat({'LBO B-Dot Power (kW),'});
        print_metric(key_metric_path,char(left_col),max(lbo_pow(:,2)))
        lbo_max_pow_index = min(find( lbo_pow(:,2) == max(lbo_pow(:,2)) ));
        time_at_lbo_pkpow = lbo_pow(lbo_max_pow_index,1);
        left_col = strcat({'LBO Pow Peak time (ns),'});
```

```
        print_metric(key_metric_path,char(left_col),time_at_lbo_pkpow*(1E9))
        %Print the times at which LBO power reaches FWHM. Create
        %new vector where the LBO power is normalized to 1 at
        %maximum
        lbo_pow_fwhm = zeros(length(lbo_pow(:,1)),2);
        lbo_pow_fwhm(:,1) = lbo_pow(:,1);
        lbo_pow_fwhm(:,2) = lbo_pow(:,2)/max(lbo_pow(:,2));
        [lbopower_fwhm1,lbopower_fwhm2] = power_fwhm(lbo_pow_fwhm);
        left_col = strcat({'LBO Power FWHM 1 (ns),'});
        print_metric(key_metric_path,char(left_col),lbopower_fwhm1*(1E9))
        left_col = strcat({'LBO Power FWHM 2 (ns),'});
        print_metric(key_metric_path,char(left_col),lbopower_fwhm2*(1E9))
    end
end

%With the voltage, current, and power downloaded and calculated,
%plot them all
if num_traces > 0
    %Create the figures
    shot_plot  = figure('visible',show_fig);
    if plot_lbo_power == 1
        legend_entries = cell(7,1);
    else
        legend_entries = cell(6,1);
    end

    %Iterate through each waveguide
    legend_plot_style = {'-.k','--k',':k'};
    for j=1:size(analyze_SBO_pow,2)
        %Plot voltage and current on the first time iterating
        %through the loop
        if j==1
            plot(melba_voltage(:,1)*1E9,melba_voltage(:,2),...
                melba_current(:,1)*1E9,melba_current(:,2),'LineWidth',2)
            hold on
            legend_entries{j} = 'Voltage, x100kV';
            legend_entries{2*j} = 'Current, kA';
        end
        %If there was data taken for this waveguide on this shot,
        %enter the statement
        if analyze_SBO_pow(i,j) == 1
            %Plot the signals
            plot(sbo_pow{j}(:,1)*1E9,sbo_pow{j}(:,2)/10000,legend_plot_style{j},'LineWidth',1.25)
            hold on
            %Print output power in each waveguide
            power_out = max(sbo_pow{j}(:,2))/1000;
            left_col = strcat({'SBO WG '},num2str(j),{' Pow (MW),'});
            print_metric(key_metric_path,char(left_col),power_out)
            wg_max_pow_index = min(find( (sbo_pow{j}(:,2))/1000 == power_out));
```

```
time_at_wg_pkpow = sbo_pow{j}(wg_max_pow_index,1);
left_col = strcat({'SBO WG '},num2str(j),{' Peak time (ns),'});
print_metric(key_metric_path,char(left_col),time_at_wg_pkpow*(1E9))
%Plot total SBO power and LBO power if desired
if j == size(analyze_SBO_pow,2)
   %Calculate and print total power
   plot(sbo_pow_tot(:,1)*1E9,sbo_pow_tot(:,2)/10000,'k','LineWidth',2)
   hold on
   power_out_tot = max(sbo_pow_tot(:,2))/1000;
   left_col = strcat({'SBO Max Inst. Pow (MW),'});
   print_metric(key_metric_path,char(left_col),power_out_tot)
   %Print total Energy
   left_col = strcat({'SBO Total Energy (J),'});
   print_metric(key_metric_path,char(left_col),max(tot_energy))
   %Print the times at which SBO power reaches FWHM
   [power_fwhm1,power_fwhm2] = power_fwhm(sbo_pow_tot);
   left_col = strcat({'SBO Power FWHM 1 (ns),'});
   print_metric(key_metric_path,char(left_col),power_fwhm1*(1E9))
   left_col = strcat({'SBO Power FWHM 2 (ns),'});
   print_metric(key_metric_path,char(left_col),power_fwhm2*(1E9))
   %Find voltage, time, and current at peak power
   indexmax_sbopow = find(sbo_pow_tot(:,2)==max(sbo_pow_tot(:,2))); %Find index of maximum
peak

   %The time step for sbo_pow_tot is not the same for every shot.
   dt_sbo_power_tot = sbo_pow_tot(2,1)-sbo_pow_tot(1,1);
   dt_sbo_vol = melba_voltage(2,1)-melba_voltage(1,1);
   indexmax = floor((dt_sbo_power_tot/dt_sbo_vol)*indexmax_sbopow);
   left_col = strcat({'Voltage at Pk. Power (x100kV),'});
   print_metric(key_metric_path,char(left_col),melba_voltage(indexmax,2))
   left_col = strcat({'Current at Pk. Power (kA),'});
   print_metric(key_metric_path,char(left_col),melba_current(indexmax,2))
   left_col = strcat({'Time at Pk. Power (ns),'});
   print_metric(key_metric_path,char(left_col),(1E9)*sbo_pow_tot(indexmax_sbopow,1))
   %Find, print, and plot the SBO turn on and shut off time
   [t_on_SBO_WG,t_off_SBO_WG] = power_time_on_off_WG(sbo_pow_tot);
   left_col = strcat({'SBO Startup Time WG (ns),'});
   print_metric(key_metric_path,char(left_col),t_on_SBO_WG)
   left_col = strcat({'SBO Shutoff Time WG (ns),'});
   print_metric(key_metric_path,char(left_col),t_off_SBO_WG)
   %Find, print, and plot the LBO turn on and shut off
   %time from the B-Dot diode trace
   [t_on_LBO_diode,t_off_LBO_diode] = power_time_on_off_LBO_BDot(lbo_pow);
   left_col = strcat({'LBO Startup Time Diode (ns),'});
   print_metric(key_metric_path,char(left_col),t_on_LBO_diode)
   left_col = strcat({'LBO Shutoff Time Diode (ns),'});
   print_metric(key_metric_path,char(left_col),t_off_LBO_diode)
   if plot_lbo_power == 1
      hold on
      plot(lbo_pow(:,1)*1E9,...
```

```
                lbo_pow(:,2)*(max(sbo_pow_tot(:,2))/10000)/max(lbo_pow(:,2)),'g','LineWidth',1.25)
            end
            yvec = linspace(-0.5,0,10);
            xvec_on = t_on_SBO_WG*ones(length(yvec),1);
            xvec_off = t_off_SBO_WG*ones(length(yvec),1);
            plot(xvec_on,yvec,'k',xvec_off,yvec,'k')
            xvec_on = t_on_LBO_diode*ones(length(yvec),1);
            xvec_off = t_off_LBO_diode*ones(length(yvec),1);
            plot(xvec_on,yvec,'g',xvec_off,yvec,'g')
            if exist('t_on_LBO_waveform','var') == 1
               plot(t_on_LBO_waveform*ones(length(yvec),1),yvec,'--m',...
                  t_on_SBO_waveform*ones(length(yvec),1),yvec,'m',...
                  t_off_LBO_waveform*ones(length(yvec),1),yvec,'--m',...
                  t_off_SBO_waveform*ones(length(yvec),1),yvec,'m')
            end
         end
      end
   end %Iteration through cavities is now complete
   set(findall(gcf,'-property','FontSize'),'FontSize',14)
   xlabel('t (ns)')
   [tstart_sp,tfinish_sp] = find_time_range(sbo_pow_tot);
   xlim([tstart_sp tfinish_sp])
   title(title_str)
   if plot_lbo_power == 1
      legend_entries{3} = 'WG 1, x10MW';
      legend_entries{4} = 'WG 2, x10MW';
      legend_entries{5} = 'WG 3, x10MW';
      legend_entries{6} = 'Total P_S_B_O, x10MW';
      legend_entries{7} = 'LBO, uncalibrated';
   else
      legend_entries{3} = 'WG 1, MW';
      legend_entries{4} = 'WG 2, MW';
      legend_entries{5} = 'WG 3, MW';
      legend_entries{6} = 'Total P_S_B_O, MW';
   end
   legend(legend_entries,'Location','Northwest','FontSize',8)
end %Plots are complete

%Save to individual folder
traces_filename = strcat(key_file_directory,'shotplot_',num2str(shot_num),'.png');
save_png(save_plots(i),shot_plot,char(traces_filename))
%Save to 'AllPlots'
file_dir_sp = strcat(strcat(pwd,'\AnalyzedData\AllShots\ShotPlot\'));
if ~exist(file_dir_sp,'dir')
   mkdir(file_dir_sp)
end
traces_filename = strcat(file_dir_sp,num2str(shot_num),'_shotplot.png');
save_png(save_plots(i),shot_plot,char(traces_filename))
```

```
    end %Shot plot is complete

    %The existence of this variable is checked for plotting purposes, so it
    %must be cleared on a shot by shot basis
    if exist('t_on_LBO_waveform','var') == 1
        clearvars('t_on_LBO_waveform')
    end

end

first_index = 1;
last_index = num_shots;
for i=first_index :last_index
    shot_num = first_shot + i - 1;

    key_file_directory = strcat(strcat(pwd,'\AnalyzedData\',num2str(shot_num),'\'));
    %Create variable for location of key metric file
    key_metric_path = strcat(key_file_directory,'key_metrics.csv');

    %Compile key metrics file that contains all shots
    if compile_master_key_metrics==1
        %Read in the key metric file for this shot
        fileID = fopen(key_metric_path,'r');
        key_metric_store = textscan(fileID,'%s %f','Delimiter',',');
        fclose(fileID);

        %Create directory for master key metrics to be saved
        master_key_metric_directory = strcat(strcat(pwd,'\AnalyzedData\'));
        if ~exist(master_key_metric_directory,'dir')
            mkdir(master_key_metric_directory)
        end
        %Create variable for location of key metric file
        master_key_metric_path = strcat(master_key_metric_directory,'master_key_metrics.csv');
        %Iteratively add to master key metrics
        for q=1:length(key_metric_store{2})
            if q==1 && i==first_index
                fileID_ind = fopen(master_key_metric_path,'w');
            else
                fileID_ind = fopen(master_key_metric_path,'a');
            end
            string_in = char(strcat(key_metric_store{1}{q},','));
            fprintf(fileID_ind,'%s%i\n',string_in,key_metric_store{2}(q));
            fclose(fileID_ind);
        end
    end
end

%%%%%%%%%% FUNCTIONS %%%%%%%%%%
```

```
function [f, signal] = perform_FFT(input,filter_fft_DC,filter_cutoff)
    time = input(:,1);
    signal_input = input(:,2);
    dt = time(2)-time(1);
    fs = 1 / dt* 10^-9;
    fft_signal_input = fft(signal_input) * 10^-6;
    ABS_fft_signal_input = abs(fft_signal_input);
    Length_array = length(signal_input);
    f = ((1:Length_array/2)/(Length_array/2))*fs/2;
    signal = ABS_fft_signal_input(1:Length_array/2);
    if filter_fft_DC == 1
        for j=1:length(f)
            if f(j) < filter_cutoff
                signal(j) = 0;
            end
        end
    end
end

function PC = Power_Calculation(signal,diode_code,total_attenuation)
%signals must be entered in mV and will be returned in kW

if (diode_code == 1) %diode HM01
    A = 5.05e-9;
    B = -2.39E-6;
    C = 1.66E-3;
    D = 3.61E-2;
    E = 0;
    power_to_diode = A.*signal.^4 + B.*signal.^3 + C.*signal.^2 + D.*signal + E;
    Power_in_signal_HM01 = power_to_diode*10^(total_attenuation/10-6);
    PC = Power_in_signal_HM01;

    elseif (diode_code == 2) %diode HM02
    A = 4.75E-9;
    B = -1.96E-6;
    C = 1.56E-3;
    D = 4.35E-2;
    E = 0;
    power_to_diode = A.*signal.^4 + B.*signal.^3 + C.*signal.^2 + D.*signal + E;
    Power_in_signal_HM02 = power_to_diode*10^(total_attenuation/10-6);
    PC = Power_in_signal_HM02;

    elseif (diode_code == 3) %diode ML01
    A = 5.14e-9;
    B = -2.06E-6;
    C = 1.64E-3;
    D = 4.47E-2;
    E = 0;
    power_to_diode = A.*signal.^4 + B.*signal.^3 + C.*signal.^2 + D.*signal + E;
```

```
    Power_in_signal_ML01 = power_to_diode*10^(total_attenuation/10-6);
    PC = Power_in_signal_ML01;

    elseif (diode_code == 4) %diode ML03
    A = 3.99e-9;
    B = -2.07E-6;
    C = 1.47e-3;
    D = 2.82E-2;
    E = 0;
    power_to_diode = A.*signal.^4 + B.*signal.^3 + C.*signal.^2 + D.*signal + E;
    Power_in_signal_ML03 = power_to_diode*10^(total_attenuation/10-6);
    PC = Power_in_signal_ML03;

    else
        error('invalid diode code. diode code can be (1,2,3,4) corresponding to (HM01, HM02, ML01, ML03)')
end

end

%This function will accept an input NX1 vector and change the vector indices to
%an appropriate value based on the shot number. Shot1 is the very first
%shot in the series, shile first_shot is the first shot in the range and
%last_shot is the last shot in the range.
function vector = set_value(vector,shot1,first_shot,last_shot,value)
    bottom_range_index = first_shot-shot1+1;
    top_range_index = last_shot-shot1+1;
    vector(bottom_range_index:top_range_index) = value;
end

%Create function to write out key metrics, to make code shorter
%This function will only append, so make sure the file has already been
%created before using this function
function print_metric(dir_out,str,value)
    fileID_ind = fopen(dir_out,'a');
    fprintf(fileID_ind,'%s%f\n',str,value);
    fclose(fileID_ind);
end

%Function to save a png. Will only execute if save_plots is set to 1. Must
%provide the name of the figure and the full save location as a character
function save_png(save_plots,fig_name,save_loc)
    %Save signal plots
    if save_plots == 1
        saveas(fig_name, save_loc)
    end
end

%Write function to find time at which signal reaches its peak, and return a
%time range suitable for plotting. The variable signal must be an Nx2
```

```
%matrix, where the left column is time (in seconds) and the right column is the signal.
function [tstart,tfinish] = find_time_range(signal)
    indexmax = max(abs(signal(:,2))) == abs(signal(:,2)); %Find index of maximum peak
    t_peak = signal(indexmax,1);
    tstart = min(t_peak) - 75*(1E-9);
    tfinish = max(t_peak) + 110*(1E-9);
end

%This function accepts an Nx2 rogowski trace, where column 1 is time and
%column 2 is the rogowski signal, and integrates it to get current
function output = calc_current(input)

    time = input(:,1);
    raw_signal = input(:,2);
    dt = input(3,1)-input(2,1);
    %Calculate integrated signal
    int_sig = zeros(length(time),1);
    for inc = 2:length(time)
        int_sig(inc) = int_sig(inc-1) + raw_signal(inc)*dt;
    end
    %The next line is time in ns on scope before current pulse, used to
    %correct baseline
    t_limit = dt*400*ones(length(time),1);
    m = int_sig(400);
    IC = 1.229e10*(int_sig - (m*(time./t_limit)));
    current = 1e-3*IC;

    output = zeros(length(time),2);
    output(:,1) = time;
    movmean_npts = floor(length(time)/100);
    output(:,2) = movmean(current,movmean_npts);

end

%The following function accepts a Nx2 matrix where the first column is time
%and the second column is power. It will calculate the 10% oscillator start time
%and an oscillator off time.
function [t_on,t_off] = power_time_on_off_WG(input)

    time = input(:,1);
    dt = (1E9)*(time(3)-time(2)); %Calculate time step in nanoseconds
    signal = input(:,2);
    [M,indexmax] = max(signal);
    threshold_lvl = 0.1*signal(indexmax); %This is where I consider the oscillator not operational
    time_range = 400; %Time range to search for start and shutoff times (in ns)
    num_steps = floor(time_range/2/dt);
    index_lo = indexmax-num_steps;
    index_hi = indexmax+num_steps;
    %Choose default values for t_on and t_off in the event the program
```

```
    %fails to perform its objective
    t_on = time(index_lo);
    t_off = time(index_hi);
    %Determine index where the oscillator starts. This loop will begin
    %before the peak signal and will break the first time it
    for inc=index_lo:indexmax
        if signal(inc) > threshold_lvl && signal(inc-1) <= threshold_lvl
            t_on = (1E9)*time(inc);
        end
    end
    %Determine index where the oscillator shuts off
    for inc1=indexmax:index_hi
        inc2 = inc1-indexmax;
        inc = index_hi - inc2;
        if signal(inc) < threshold_lvl && signal(inc-1) >= threshold_lvl
            t_off = (1E9)*time(inc);
            break
        end
    end

end

%The following function accepts a Nx2 matrix where the first column is time in seconds
%and the second column is power. It will calculate the 10% oscillator start time
%and an oscillator off time. This is different from power_time_on_off_WG
%because to find the stop time, it iterates from peak power and onward in
%time, rather than starting at the end of the range and moving toward the
%peak.
function [t_on,t_off] = power_time_on_off_LBO_BDot(input)

    time = input(:,1);
    dt = (1E9)*(time(3)-time(2)); %Calculate time step in nanoseconds
    signal = input(:,2);
    [M,indexmax] = max(signal);
    threshold_lvl = 0.1*signal(indexmax); %This is where I consider the oscillator not operational
    time_range = 400; %Time range to search for start and shutoff times (in ns)
    num_steps = floor(time_range/2/dt);
    index_lo = indexmax-num_steps;
    index_hi = indexmax+num_steps;
    %Choose default values for t_on and t_off in the event the program
    %fails to perform its objective
    t_on = time(index_lo);
    t_off = time(index_hi);
    %Determine index where the oscillator starts. This loop will begin
    %before the peak signal and will break the first time it
    for inc=index_lo:indexmax
        if signal(inc) > threshold_lvl && signal(inc-1) <= threshold_lvl
            t_on = (1E9)*time(inc);
        end
```

```
    end
    %Determine index where the oscillator shuts off
    for inc=indexmax:index_hi
        if signal(inc) > threshold_lvl && signal(inc+1) <= threshold_lvl
            t_off = (1E9)*time(inc);
            break
        end
    end

end

%This function will return the point in time at which the voltage rises to
%10% and 90% of its maximum value. The time between t1 and t2 is the
%risetime. The input must be nx2, where the first column is time and the
%second column is the voltage.
function [t1,t2] = voltage_rise_time(input)

    time = input(:,1);
    voltage = abs(input(:,2));
    maxvolt = max(voltage);
    maxindex = find(voltage == maxvolt);
    t1 = 0;
    t2 = 0;
    for i=1:maxindex
        j = maxindex-i+1;
        if voltage(j+1) >= 0.9*maxvolt && voltage(j) <= 0.9*maxvolt
            t2 = time(j);
        elseif voltage(j+1) >= 0.1*maxvolt && voltage(j) <= 0.1*maxvolt
            t1 = time(j);
            break
        end
    end

end

%This function will return the point in time at which the power rises and
%falls to half of its maximum value. The time between t1 and t2 is the
%full width at half max (FWHM). The input must be nx2, where the first
%column is time and the second column is the voltage.
function [t1,t2] = power_fwhm(input)

    time = input(:,1);
    power = input(:,2);
    maxpow = max(power);
    maxindex = min(find(power == maxpow));
    t1 = 0;
    t2 = 0;
    %Find upper time limit
    for i=maxindex:length(power)
```

```
        if power(i+1) < 0.5*maxpow && power(i) >= 0.5*maxpow
            t2 = time(i);
            break
        end
    end
    %Find lower time limit
    for i=1:maxindex
        j = maxindex-i+1;
        if power(j+1) >= 0.5*maxpow && power(j) < 0.5*maxpow
            t1 = time(j);
            break
        end
    end

end
```

Appendix D MILO Experimental Post-processing Routine

The MATLAB post-processing script used to analyze the MILO experiments is given here. With the raw traces collected during the experiments, the program will produce plots of the signals, Fourier transforms, voltage, current, and others.

```
clear all
close all

%%%%%%%%%% SHOT SERIES INFORMATION %%%%%%%%%%
first_shot = 18084;
last_shot = 18208;
num_shots = last_shot - first_shot + 1;
num_diode_traces = 1;
show_fig = 'on'; %This will plot and display figures if 'on', will not if 'off'
%The following string is where all the shot data is located
all_shots_dir = 'E:\MILO\Experimental_Data\Cavity_Anode_Extraction\18084-18208\18084-18208\';

%Create vector to skip shots for postprocessing. Set to one if you want to
%skip.
skip_analysis = zeros(num_shots,1);
skip_analysis = set_value(skip_analysis,first_shot,18084,18174,1);
%skip_analysis = set_value(skip_analysis,first_shot,18147,18147,1);

%Create a vector for TFA analysis. There are numerous signals for each shot
%on both LBO and SBO, so this may take a while to run. Set to 1 to perform
%analysis for each individual shot. This will only work if skip_analysis is
%also set to 1, because it controls whether the signals are downloaded.
plot_TFA = zeros(num_shots,1);
show_tfa = 'off'; %This will plot and display tfa figures if 'on', will not if 'off'
save_tfa = 0; %Set to 1 to save all TFA plots generated

%%%%%%%%%% SCOPE AND CHANNEL INFORMATION %%%%%%%%%%
%================= Shot Plot Information ==================
%Set the following to 1 to plot voltage, current, and diode information
make_shot_plot = 1;
plot_fiber = 1;
analyze_pow = ones(num_shots,1);%Assume every shot and waveguide requires analysis

%GPIB address is not idenitified for power scope, because it is always 7
```

```
diode_ch_id = ones(num_shots,1); %Diode Channel is always channel 1

%================== WG Freq Information ==================

%Set to 1 to analyze waveguide output
perform_wgfreq_analysis = 1; %Analyze waveguide signals
analyze_wgfreq = ones(num_shots,1); %Assume every shot requires analysis, and then correct in the following lines
%No fast scope information on shot 18106, 18166, 18197
analyze_wgfreq = set_value(analyze_wgfreq,first_shot,18106,18106,0);
analyze_wgfreq = set_value(analyze_wgfreq,first_shot,18166,18166,0);
analyze_wgfreq = set_value(analyze_wgfreq,first_shot,18197,18197,0);

%Identify the fast scope number
wgfreq_scope_id = zeros(num_shots,1);
wgfreq_scope_id(:,1) = 6; %WG was always connected to GPIB6

%Identify the chanel number for each SBO wg
%Columns are scope numbers for SBO wg 1, 2, and 3, respectively
wgfreq_ch_id = zeros(num_shots,1);
wgfreq_ch_id(:,1) = 1; %WG was always connected to ch 1

%%%%%%%%%%% DIODE INFORMATION %%%%%%%%%%%

%The values below represent the diode used for each channel. The four
%entries are for the first, second, and third waveguides, and the last is
%for the LBO power trace (if present), respectively.
diode_inputs = zeros(num_shots,num_diode_traces);
diode_inputs(:,1) = 2;

%%%%%%%%%%% ATTENUATION %%%%%%%%%%%

%Provide values of line attenuation for waveguide output for shots 16894-17110
%CF_inline = 21.9*ones(num_shots,1);%Initialize additional attenuation to cable A
CF_inline = zeros(num_shots,1);
CF_inline = set_value(CF_inline,first_shot,18084,18165,21.9);
CF_inline = set_value(CF_inline,first_shot,18166,18208,24.8);

dir_coupler_loss = 52.9; %Loss due to the waveguide directional coupler
splitter_loss = 3.2; %Loss due to splitter

%Calculate cable loss. These attenuation values are taken at 2.195 GHz
C1 = 11; %Attenuation of Cable A + F in dB
C2 = 11.5; %Attenuation of Cable F + D in dB
C3 = 10.5; %Attenuation of Cable A + D in dB
cable_F = (C1+C2-C3)/2;
cable_A = (C1-C2+C3)/2;
cable_D = (-C1+C2+C3)/2;

%Calculate total loss
```

```
Diode_loss = CF_inline + cable_F + dir_coupler_loss + splitter_loss;
Total_attenuation = Diode_loss;

%%%%%%%%%% MISCELLANEOUS %%%%%%%%%%

%Define number of points used for moving average in each plot of raw signals
sig_plot_movmean_npts = 10;
%Perform operations on the fourier transform plots
filter_fft_DC = 1; %Remove DC element of FFT (boolean)
filter_cutoff = 0.05;
%Set frequency bounds for B-dot FFT plots
bdot_fft_fmin = 0.1;
bdot_fft_fmax = 5;
%Set this to 1 if you want to immediately remove any DC offset from a trace
%when it is retreived from the data file.
remove_signal_DC_offset = 1;

%Booleans for saving and overwriting files. Set to 1 if you want to save or
%write out, set to 0 to not.
save_plots = ones(num_shots,1);%ones(num_shots,1); %Write plots out as png file
compile_master_key_metrics = 0; %Iterate through the key metric files and compile them all into one file

%Store voltage and current so they can all be plotted on the same figure
vol_store = cell(1,num_shots);
cur_store = cell(1,num_shots);
imp_store = cell(1,num_shots);

%%%%%%%%%% BEGIN ITERATING THROUGH SHOTS %%%%%%%%%%

first_index = 1;
last_index = num_shots;
for i=first_index :last_index
    if skip_analysis(i) == 1
        shot_num = first_shot + i - 1;
        output_str = strcat(num2str(i),{', '},num2str(shot_num));
        disp(output_str)
        continue
    end

    shot_num = first_shot + i - 1;
    output_str = strcat(num2str(i),{', '},num2str(shot_num));
    disp(output_str)
    data_dir = strcat(all_shots_dir,num2str(shot_num),'\traces\');

    %Create directory for key metrics to be saved
    key_file_directory = strcat(strcat(pwd,'\AnalyzedData\',num2str(shot_num),'\'));
    if ~exist(key_file_directory,'dir')
        mkdir(key_file_directory)
    end
```

```
    %Create variable for location of key metric file
    key_metric_path = strcat(key_file_directory,'key_metrics.csv');
    %Print the shot number
    fileID_ind = fopen(key_metric_path,'w');
    fprintf(fileID_ind,'%s%i\n','Shot Number,',shot_num);
    fclose(fileID_ind);

    %Create title for each figure
    title_str = strcat({'Shot '},num2str(shot_num));

    %Analyze Waveguide signal
    if perform_wgfreq_analysis == 1
        %Determine number of SBO Waveguide traces collected on this shot
        num_traces = sum(analyze_wgfreq(i,:)==1);
        wgfreq_signals = cell(1,size(analyze_wgfreq,2));
        %Iterate through the three waveguides and pull down the traces
        for j=1:size(analyze_wgfreq,2)
            if shot_num == 18105 || 18106 || 18107 || 18108 || 18109 || 18110
                data_dir_temp = char(strcat({'E:\MILO\Experimental_Data\Cavity_Anode_Extraction\18084-
18208\18084-18208\'},...
                    num2str(shot_num),{'\traces\'}));
                sig_fname = strcat(num2str(shot_num),'_GPIB06_001_Signal1.txt');
                fdir = strcat(data_dir_temp,sig_fname);
            else
                %Generate filename for this waveguide
                filename = strcat(num2str(shot_num),'_GPIB0',num2str(wgfreq_scope_id(i,j)),...
                    '_00',num2str(wgfreq_ch_id(i,j)),'_Signal',...
                    num2str(wgfreq_ch_id(i,j)),'.txt');
                fdir = strcat(data_dir,filename);
            end
            %If the file exists, step in
            if exist(fdir,'file') == 2
                wgfreq_signals{j} = csvread(fdir);
                if remove_signal_DC_offset == 1
                    dc_offset = mean(wgfreq_signals{j}(1:2500,2));
                    wgfreq_signals{j}(:,2) = wgfreq_signals{j}(:,2) - dc_offset;
                end
            end
        end
        %With the traces downloaded, plot them
        if num_traces > 0
            %Create the figures
            wgfreq_f1  = figure('visible',show_fig,'position',[25 25 750 750]);
            wgfreq_fft  = figure('visible',show_fig,'position',[25 25 750 750]);
            wgfreq_fft_narrow = figure('visible',show_fig,'position',[25 25 750 750]);
            subplot_index = 0;
            %Determine plotting ranges for each signal plot
            tstart = zeros(size(analyze_wgfreq,2),1);
            tfinish = zeros(size(analyze_wgfreq,2),1);
```

```
for j=1:size(analyze_wgfreq,2)
   %Retrieve start and finish time values for each trace.
   %Apply the function only if the signal was downloaded for
   %that cavity.
   if size(wgfreq_signals{j},1) > 1 && size(wgfreq_signals{j},2) == 2
      [tstart(j),tfinish(j)] = find_time_range(wgfreq_signals{j});
      sbo_wgfreq_signals_avg = zeros(size(wgfreq_signals{j},1),size(analyze_wgfreq,2));
   end
end
%Now find the nonzero minimum and the maximum of tfinish
tstart_final_wg = min(tstart(tstart>0));
tfinish_final_wg = max(tfinish(tfinish>0));
%Iterate through each cavity
dom_freq_wg = zeros(1,size(analyze_wgfreq,2));
for j=1:size(analyze_wgfreq,2)
   %If there was data taken for this cavity on this shot,
   %enter the statement
   if analyze_wgfreq(i,j) == 1
      %Plot the signals
      set(0, 'CurrentFigure', wgfreq_f1);
      subplot_index = subplot_index + 1;
      subplot(num_traces,1,subplot_index);
      baseline = mean(wgfreq_signals{j}(:,2));
      ordinate = movmean(wgfreq_signals{j}(:,2),2) - baseline;
      plot(wgfreq_signals{j}(:,1)*1E9,ordinate)
      ylabel('SBO WG Output')
      [tstart,tfinish] = find_time_range(wgfreq_signals{j});
      if subplot_index == 1
         title(title_str)
         xlabel('t (ns)')
      end
      hold on
      sbo_wgfreq_signals_avg(:,j) = movmean(abs(ordinate),sig_plot_movmean_npts);
      xlim([tstart_final_wg*(1E9)/1.25 tfinish_final_wg*(1E9)*1.25])
      plot(wgfreq_signals{j}(:,1)*1E9,sbo_wgfreq_signals_avg(:,j),'r')
      set(findall(gcf,'-property','FontSize'),'FontSize',18)

      set(0, 'CurrentFigure', wgfreq_fft);
      %Perform FFT
      [freq,FFT_signal] = perform_FFT(wgfreq_signals{j},filter_fft_DC,filter_cutoff);
      FFT_signal = movmean(FFT_signal,50); %Smooth the plot
      noise_floor = mean(FFT_signal);
      FFT_signal = FFT_signal - noise_floor; %Remove noise floor, if any
      indexmax = max(FFT_signal) == FFT_signal; %Find index of maximum peak
      dom_freq = freq(indexmax); %Find dominant frequency
      dom_freq_wg(j) = dom_freq;
      ymax = FFT_signal(indexmax); %Find value of dominant peak
      FFT_signal = FFT_signal./ymax; %Normalize the FFT
      subplot(1,num_traces,subplot_index); %Plot and format FFT's
```

```
plot(freq,FFT_signal)
xlabel(strcat({'f (GHz), SBO WG '},num2str(j)))
%xlim([sbo_wgfreq_fft_fmin sbo_wgfreq_fft_fmax])
ylim([0 1.1])
if subplot_index == 1
   ylabel('A/A_0')
end
hold on
strmax = [num2str(dom_freq), ' GHz'];
text(dom_freq, 1, strmax, 'HorizontalAlignment' , 'center', 'VerticalAlignment', 'bottom', 'FontSize', 10);
plot(dom_freq, 1, '*')
if num_traces == 1 || num_traces == 2
   if subplot_index == 1
      title(title_str)
   end
elseif num_traces == 3
   if subplot_index == 2
      title(title_str)
   end
end
set(findall(gcf,'-property','FontSize'),'FontSize',28)

set(0, 'CurrentFigure', wgfreq_fft_narrow);
subplot(1,num_traces,subplot_index); %Plot and format FFT's
plot(freq,FFT_signal)
xlabel(strcat({'f (GHz), SBO WG '},num2str(j)))
xlim([0.8 1.2])
ylim([0 1.1])
if subplot_index == 1
   ylabel('A/A_0')
end
hold on
strmax = [num2str(dom_freq), ' GHz'];
text(dom_freq, 1, strmax, 'HorizontalAlignment' , 'center', 'VerticalAlignment', 'bottom', 'FontSize', 10);
plot(dom_freq, 1, '*')
if num_traces == 1 || num_traces == 2
   if subplot_index == 1
      title(title_str)
   end
elseif num_traces == 3
   if subplot_index == 2
      title(title_str)
   end
end
set(findall(gcf,'-property','FontSize'),'FontSize',28)

%Print dominant frequency
left_col = strcat({'WG Dom Freq (GHz),'});
print_metric(key_metric_path,char(left_col),dom_freq)
```

```
        end
    end %Iteration through cavities is now complete
end %Plots are complete

if num_traces > 0
    %Save plots to individual folder
    traces_filename = strcat(key_file_directory,'WG_signals_',num2str(shot_num),'.png');
    save_png(save_plots(i),wgfreq_f1,char(traces_filename))
    fft_filename = strcat(key_file_directory,'WG_FFT_',num2str(shot_num),'.png');
    save_png(save_plots(i),wgfreq_fft,char(fft_filename))
    fft_filename_narrow = strcat(key_file_directory,'WG_FFT_',num2str(shot_num),'_narrow.png');
    save_png(save_plots(i),wgfreq_fft_narrow,char(fft_filename_narrow))

    %Save to 'AllShots' WG folder
    file_dir_sig = strcat(strcat(pwd,'\AnalyzedData\AllShots\WG\Signals\'));
    if ~exist(file_dir_sig,'dir')
        mkdir(file_dir_sig)
    end
    file_dir_fft = strcat(strcat(pwd,'\AnalyzedData\AllShots\WG\FFTs\'));
    if ~exist(file_dir_fft,'dir')
        mkdir(file_dir_fft)
    end
    file_dir_fft_narrow = strcat(strcat(pwd,'\AnalyzedData\AllShots\WG\FFTs_Narrow\'));
    if ~exist(file_dir_fft_narrow,'dir')
        mkdir(file_dir_fft_narrow)
    end
    traces_filename = strcat(file_dir_sig,num2str(shot_num),'_WG_signals.png');
    save_png(save_plots(i),wgfreq_f1,char(traces_filename))
    fft_filename = strcat(file_dir_fft,num2str(shot_num),'_WG_FFT.png');
    save_png(save_plots(i),wgfreq_fft,char(fft_filename))
    fft_filename_narrow = strcat(file_dir_fft_narrow,num2str(shot_num),'_WG_FFT.png');
    save_png(save_plots(i),wgfreq_fft_narrow,char(fft_filename_narrow))
end

end %SBO WG freq analysis complete

%With all of the signals downloaded, perform TFA
if plot_TFA(i) == 1

    tfa_narrow = figure('visible',show_tfa,'position',[50 500 1000 500]);
    dom_freq_avg = (1E9)*mean(dom_freq);
    freq_narrow_bds = [5E8, 2.5E9];

    %Perform TFA routine for WG signals
    num_sigs = 1;
    wg_tfa = figure('visible',show_tfa,'position',[0 0 2000 750]);
    t_window = 750;
    for k=1:num_sigs
```

```
        dt_sig = (1E9)*(wgfreq_signals{k}(2,1)-wgfreq_signals{k}(1,1));
        num_tsteps = round(t_window/dt_sig);
        t1 = (1E9)*wgfreq_signals{k}(:,1);
        Fs = (1E9)/dt_sig;
        if k==1
           max_index = min(find(wgfreq_signals{k}(:,2) == max(wgfreq_signals{k}(:,2))));
        end
        first_index = max([1 (max_index - num_tsteps/2)]);
        last_index = max_index + 2*num_tsteps/4;
        t = t1(first_index:last_index);
        sig_norm = wgfreq_signals{k}(:,2)./max(abs(wgfreq_signals{k}(:,2)));
        sig = sig_norm(first_index:last_index);
        subplot(1,2,2*k-1)
        pspectrum(sig,Fs,'Leakage',1,'FrequencyLimits',[5E8, 5.5E9])
        ax = gca;
        ax.FontSize = 24;
        ax.LineWidth = 1.5;
        xlabel('Frequency (GHz)','FontSize',32)
        ylabel('Power Spectrum (dB)','FontSize',32)
        title_txt = strcat({'F_d_o_m = '},num2str(round(dom_freq_avg/(1E9),3)),{' GHz'});
        title(title_txt)
        subplot(1,2,2*k)
        pspectrum(sig,Fs,'spectrogram','FrequencyLimits',freq_narrow_bds,'TimeResolution',50E-
9,'Reassign',true,'MinThreshold',-30,'Overlap',95)
        ax = gca;
        ax.FontSize = 24;
        ax.LineWidth = 1.5;
        xlabel('Time (ns)','FontSize',32)
        ylabel('Frequency (GHz)','FontSize',32)
        %xlim([100 600])
        xlim([200 500])
        ylim([0.85 1.15])
        title_txt = strcat({'Shot '},num2str(shot_num));
        title(title_txt)

        set(0, 'CurrentFigure', tfa_narrow);
        %pspectrum(sig,Fs,'spectrogram','Leakage',0.4,'MinThreshold',-
40,'FrequencyLimits',freq_narrow_bds,'Reassign',true,'FrequencyResolution',2e7,'Overlap',95)
        pspectrum(sig,Fs,'spectrogram','FrequencyLimits',freq_narrow_bds,'TimeResolution',50E-
9,'Reassign',true,'MinThreshold',-30,'Overlap',95)
        ax = gca;
        ax.FontSize = 16;
        ax.LineWidth = 1.5;
        xlabel('Time (ns)','FontSize',24)
        ylabel('Frequency (GHz)','FontSize',24)
        xlim([100 600])
        ylim([0.85 1.15])
        yticks([0.85:0.05:1.15])
        title_txt = strcat({'F_d_o_m = '},num2str(round(dom_freq_avg/(1E9),3)),{' GHz'});
```

```
        title(title_txt)

        set(0, 'CurrentFigure', wg_tfa);
    end
    %Save to individual folder
    wg_tfa_filename = strcat(key_file_directory,'tfa_wide_',num2str(shot_num),'.png');
    save_png(save_tfa,wg_tfa,char(wg_tfa_filename))
    %Save to 'AllPlots'
    wg_tfa_file_dir_sp = strcat(strcat(pwd,'\AnalyzedData\AllShots\WG_TFA_Wide\'));
    if ~exist(wg_tfa_file_dir_sp,'dir')
        mkdir(wg_tfa_file_dir_sp)
    end
    wg_tfa_filename = strcat(wg_tfa_file_dir_sp,num2str(shot_num),'_wg_tfa.png');
    save_png(save_tfa,wg_tfa,char(wg_tfa_filename))

    %Save narrow figure
    set(0, 'CurrentFigure', tfa_narrow);
    tfa_narrow_fname = strcat(key_file_directory,'tfa_narrow_',num2str(shot_num),'.png');
    save_png(save_tfa,tfa_narrow,char(tfa_narrow_fname))
    %Save to 'AllPlots'
    tfa_narrow_file_dir_sp = strcat(strcat(pwd,'\AnalyzedData\AllShots\WG_TFA_Narrow\'));
    if ~exist(tfa_narrow_file_dir_sp,'dir')
        mkdir(tfa_narrow_file_dir_sp)
    end
    tfa_narrow_fname_sp = strcat(tfa_narrow_file_dir_sp,num2str(shot_num),'_tfa_narrow.png');
    save_png(save_tfa,tfa_narrow,char(tfa_narrow_fname_sp))

end

%Make shot plot
if make_shot_plot == 1

    %Download the voltage and rogowski waveforms
    if shot_num == 18105 || shot_num == 18106 || shot_num == 18107 || shot_num == 18108 || shot_num ==
18109 || shot_num == 18110
        data_dir_temp = char(strcat({'E:\MILO\Experimental_Data\Cavity_Anode_Extraction\18084-18208\18084-
18208\'},...
            num2str(shot_num),{'\traces\'}));
        v_fname = strcat(num2str(shot_num),'_GPIB08_002_Signal2.txt');
        v_fdir = strcat(data_dir_temp,v_fname);
        r_fname = strcat(num2str(shot_num),'_GPIB08_003_Signal3.txt');
        r_fdir = strcat(data_dir_temp,r_fname);
    else
        v_fname = strcat(num2str(shot_num),'_001_002_VOLN.txt');
        v_fdir = strcat(data_dir,v_fname);
        r_fname = strcat(num2str(shot_num),'_001_004_ENTC.txt');
        r_fdir = strcat(data_dir,r_fname);
    end
    if exist(v_fdir,'file') == 2 %&& exist(r_fdir,'file') == 2
```

```
        vol_raw = csvread(v_fdir);
        melba_voltage = zeros(size(vol_raw,1),size(vol_raw,2));
        movmean_npts = floor(size(vol_raw,1)/500);
        melba_voltage(:,1) = vol_raw(:,1);
        melba_voltage(:,2) = -1*movmean(vol_raw(:,2),movmean_npts);
        [voltage_rise1,voltage_rise2] = voltage_rise_time(melba_voltage);
        left_col = strcat({'Voltage Rise 10pct (ns),'});
        print_metric(key_metric_path,char(left_col),voltage_rise1*(1E9))
        left_col = strcat({'Voltage Rise 90pct (ns),'});
        print_metric(key_metric_path,char(left_col),voltage_rise2*(1E9))
        rog_raw = csvread(r_fdir);
        melba_current = calc_current(rog_raw);
    end
    vol_store{i} = melba_voltage;
    cur_store{i} = melba_current;

    %Download the directional coupler diode trace
    %Generate filename
    if shot_num == 18105 || shot_num == 18106 || shot_num == 18107 || shot_num == 18108 || shot_num ==
18109 || shot_num == 18110
        data_dir_temp = char(strcat({'E:\MILO\Experimental_Data\Cavity_Anode_Extraction\18084-18208\18084-
18208\'},...
            num2str(shot_num),{'\traces\'}));
        pow_fname = strcat(num2str(shot_num),'_GPIB08_001_Signal1.txt');
        fdir = strcat(data_dir_temp,pow_fname);
    else
        filename = strcat(num2str(shot_num),'_002_00',...
            num2str(diode_ch_id(i)),'_Power',...
            num2str(diode_ch_id(i)),'.txt');
        fdir = strcat(data_dir,filename);
    end
    %If the file exists, step in
    if exist(fdir,'file') == 2
        pow_raw = csvread(fdir);
        if remove_signal_DC_offset == 1
            dc_offset = mean(pow_raw(1:500,2));
            pow_raw(:,2) = pow_raw(:,2) - dc_offset;
        end
        %movmean_npts = floor(size(sbo_pow_raw{j},1)/100);
        diode_data_input = (1E3)*abs(movmean(pow_raw(:,2),50));
        pow = zeros(size(pow_raw,1),size(pow_raw,2));
        pow(:,1) = pow_raw(:,1);
        pow(:,2) = Power_Calculation(diode_data_input,...
            diode_inputs(i,1),Total_attenuation(i,1));
        left_col = strcat({'Output Power (MW),'});
        print_metric(key_metric_path,char(left_col),max(pow(:,2))/1000)
        max_power_index = min( find( pow(:,2) == max(pow(:,2)) ) );
        [power_fwhm1,power_fwhm2] = power_fwhm(pow);
        left_col = strcat({'Power FWHM Rise (ns),'});
```

```
    print_metric(key_metric_path,char(left_col),power_fwhm1*(1E9))
    left_col = strcat({'Power FWHM Fall (ns),'});
    print_metric(key_metric_path,char(left_col),power_fwhm2*(1E9))
end

%With the voltage, current, and power downloaded and calculated,
%plot them all
shot_plot  = figure('visible',show_fig);

if shot_num == 18044
    yvec_max = 120;
else
    yvec_max = 35;
end
yvec_vert = linspace(0,yvec_max,100);
diode_max_time_ind = find( pow(:,2) == max(pow(:,2)) );
xvec_val = pow(min(diode_max_time_ind),1)*1E9;
xvec_vert = xvec_val*ones(length(yvec_vert),1);
impedance = 100*melba_voltage(:,2)./melba_current(:,2);
imp_store{i} = [melba_voltage(:,1) impedance];
plot(melba_voltage(:,1)*1E9,10*melba_voltage(:,2),'b',...
    melba_current(:,1)*1E9,melba_current(:,2),'r',...
    melba_voltage(:,1)*1E9,impedance,':k',...
    pow(:,1)*1E9,pow(:,2)/1000,'k',...
    'LineWidth',2)
hold on
plot(xvec_vert,yvec_vert,'--k','LineWidth',0.5)
legend_entries{1} = 'Voltage (kV)/10kV';
legend_entries{2} = 'Current, kA';
legend_entries{3} = 'Impedance, Ohms';
legend_entries{4} = 'Power (MW)';

set(findall(gcf,'-property','FontSize'),'FontSize',14)
xlabel('t (ns)')
xlim([500 2000])
ylim([0 yvec_max])
grid on
title(title_str)
legend(legend_entries,'Location','Northeast','FontSize',8)

%%%%%%%%%%%%%%Write out metrics%%%%%%%%%%%%%%
%Peak power timing
time_at_pkpow = pow(max_power_index,1);
left_col = strcat({'Power Peak time (ns),'});
print_metric(key_metric_path,char(left_col),time_at_pkpow*(1E9))
%MILO startup and shutoff
[t_on_WG,t_off_WG] = power_time_on_off_WG(pow);
left_col = strcat({'MILO Startup Time (ns),'});
print_metric(key_metric_path,char(left_col),t_on_WG)
```

```
left_col = strcat({'MILO Shutoff Time (ns),'});
print_metric(key_metric_path,char(left_col),t_off_WG)
%Maximum voltage
max_voltage = max(melba_voltage(:,2));
left_col = strcat({'Maximum Voltage (kV),'});
print_metric(key_metric_path,char(left_col),100*max_voltage)
%Voltage at peak power
%The time step for sbo_pow_tot is not the same for every shot.
dt_pow = pow(2,1)-pow(1,1);
dt_vol = melba_voltage(2,1)-melba_voltage(1,1);
for vc=1:(length(melba_voltage(:,1))-1)
   if melba_voltage(vc,1) <= time_at_pkpow && melba_voltage(vc+1,1) > time_at_pkpow
      indexmax = vc;
   end
end
%indexmax = floor((dt_pow/dt_vol)*max_power_index);
pk_pow_volt = melba_voltage(indexmax,2);
left_col = strcat({'Voltage at Pk. Pow (kV),'});
print_metric(key_metric_path,char(left_col),pk_pow_volt*100)
%Maximum current
max_current = max(melba_current(:,2));
left_col = strcat({'Maximum Current (kA),'});
print_metric(key_metric_path,char(left_col),max_current)
%Current at peak power
pk_pow_cur = melba_current(indexmax,2);
left_col = strcat({'Current at Pk. Pow (kA),'});
print_metric(key_metric_path,char(left_col),pk_pow_cur)
%Impedance at peak power
pk_pow_imp = pk_pow_volt*100/pk_pow_cur;
left_col = strcat({'Impedance at Pk. Pow (Ohms),'});
print_metric(key_metric_path,char(left_col),pk_pow_imp)
%Cathode Power at peak microwave power in W
pk_cathode_pow = (pk_pow_cur*1000)*(pk_pow_volt*100*1000);
left_col = strcat({'Cathode Power at Pk. Microwave Gen (GW),'});
print_metric(key_metric_path,char(left_col),pk_cathode_pow/(1E9))
%Efficiency at peak power
pk_eff = 100*(1000*max( pow(:,2)) )/pk_cathode_pow;
left_col = strcat({'Peak Microwave Efficiency (%),'});
print_metric(key_metric_path,char(left_col),pk_eff)

%Save to individual folder
traces_filename = strcat(key_file_directory,'shotplot_',num2str(shot_num),'.png');
save_png(save_plots(i),shot_plot,char(traces_filename))
%Save to 'AllPlots'
file_dir_sp = strcat(strcat(pwd,'\AnalyzedData\AllShots\ShotPlot\'));
if ~exist(file_dir_sp,'dir')
   mkdir(file_dir_sp)
end
traces_filename = strcat(file_dir_sp,num2str(shot_num),'_shotplot.png');
```

```
save_png(save_plots(i),shot_plot,char(traces_filename))

%Step in to plot fiber optic signal overlaid with output power
if plot_fiber == 1

    if shot_num == 18105 || shot_num == 18106 || shot_num == 18107 || shot_num == 18108 || shot_num ==
18109 || shot_num == 18110
        data_dir_temp = char(strcat({'E:\MILO\Experimental_Data\Cavity_Anode_Extraction\18084-
18208\18084-18208\'},...
            num2str(shot_num),{'\traces\'}));
        fiber_fnames{1} = strcat(data_dir_temp,num2str(shot_num),{'_GPIB08_004_Signal4.txt'});
        fiber_data = cell(length(fiber_fnames),1);
    else
        fiber_fnames{1} = strcat(data_dir,num2str(shot_num),{'_003_001_PMT_5.txt'});
        fiber_fnames{2} = strcat(data_dir,num2str(shot_num),{'_003_002_PMT_6.txt'});
        fiber_fnames{3} = strcat(data_dir,num2str(shot_num),{'_003_003_PMT_7.txt'});
        fiber_data = cell(length(fiber_fnames),1);
    end

    fiber_plot  = figure('visible',show_fig,'Position',[50 300 800 800]);
    mv = max(10*melba_voltage(:,2));
    plot(pow(:,1)*1E9,pow(:,2)/1000,'k',...
        melba_voltage(:,1)*1E9,10*melba_voltage(:,2),'b',...
        melba_current(:,1)*1E9,melba_current(:,2),'r',...
        'LineWidth',2)
    hold on
    legend_entries{1} = 'Power (MW)';
    legend_entries{2} = 'Voltage (kV)/10kV';
    legend_entries{3} = 'Current (kA)';
    fc_color = {'--m','--b','--r'};
    for fc = 1:1%length(fiber_fnames)
        if exist(char(fiber_fnames{fc})) == 2
            fiber_data{fc} = readmatrix(char(fiber_fnames{fc}));
            fiber_ydata = -movmean(fiber_data{fc}(:,2),100);
            plot(fiber_data{fc}(:,1)*1E9,mv*fiber_ydata/max(fiber_ydata),fc_color{fc})
            hold on
            legend_entries{fc+3} = char(strcat({'PMT '},num2str(fc)));
        end
    end
    %plot(xvec_vert,yvec_vert,'--m','LineWidth',0.5)
    plot(xvec_vert,yvec_vert,'--k','LineWidth',0.5)

    set(findall(gcf,'-property','FontSize'),'FontSize',24)
    xlabel('t (ns)')
    xlim([000 3000])
    %ylim([0 yvec_max])
    ylim([0 30])
    grid on
    title(title_str)
```

```
            legend(legend_entries,'Location','NorthEast','FontSize',12,'NumColumns',1)

            %Save to individual folder
            traces_filename = strcat(key_file_directory,'fibers_',num2str(shot_num),'.png');
            save_png(save_plots(i),fiber_plot,char(traces_filename))
            %Save to 'AllPlots'
            file_dir_sp = strcat(strcat(pwd,'\AnalyzedData\AllShots\Fibers\'));
            if ~exist(file_dir_sp,'dir')
               mkdir(file_dir_sp)
            end
            traces_filename = strcat(file_dir_sp,num2str(shot_num),'_fibers.png');
            save_png(save_plots(i),fiber_plot,char(traces_filename))

        end

    end %Shot plot is complete

end

first_index = 1;
last_index = num_shots;
for i=first_index :last_index

    if skip_analysis(i) == 1
        shot_num = first_shot + i - 1;
        output_str = strcat(num2str(i),{', '},num2str(shot_num));
        continue
    end

    shot_num = first_shot + i - 1;

    key_file_directory = strcat(strcat(pwd,'\AnalyzedData\',num2str(shot_num),'\'));
    %Create variable for location of key metric file
    key_metric_path = strcat(key_file_directory,'key_metrics.csv');

    %Compile key metrics file that contains all shots
    if compile_master_key_metrics==1
        %Read in the key metric file for this shot
        fileID = fopen(key_metric_path,'r');
        key_metric_store = textscan(fileID,'%s %f','Delimiter',',');
        fclose(fileID);

        %Create directory for master key metrics to be saved
        master_key_metric_directory = strcat(strcat(pwd,'\AnalyzedData\'));
        if ~exist(master_key_metric_directory,'dir')
            mkdir(master_key_metric_directory)
        end
        %Create variable for location of key metric file
        master_key_metric_path = strcat(master_key_metric_directory,'master_key_metrics.csv');
```

```
        %Iteratively add to master key metrics
        for q=1:length(key_metric_store{2})
            if q==1 && i==first_index
                fileID_ind = fopen(master_key_metric_path,'w');
            else
                fileID_ind = fopen(master_key_metric_path,'a');
            end
            string_in = char(strcat(key_metric_store{1}{q},','));
            fprintf(fileID_ind,'%s%i\n',string_in,key_metric_store{2}(q));
            fclose(fileID_ind);
        end
    end
end

%%%%%%%%%%% FUNCTIONS %%%%%%%%%%%

function [f, signal] = perform_FFT(input,filter_fft_DC,filter_cutoff)
    time = input(:,1);
    signal_input = input(:,2);
    dt = time(2)-time(1);
    fs = 1 / dt* 10^-9;
    fft_signal_input = fft(signal_input) * 10^-6;
    ABS_fft_signal_input = abs(fft_signal_input);
    Length_array = length(signal_input);
    f = ((1:Length_array/2)/(Length_array/2))*fs/2;
    signal = ABS_fft_signal_input(1:Length_array/2);
    if filter_fft_DC == 1
        for j=1:length(f)
            if f(j) < filter_cutoff
                signal(j) = 0;
            end
        end
    end
end

function PC = Power_Calculation(signal,diode_code,total_attenuation)
%signals must be entered in mV and will be returned in kW

if (diode_code == 1) %diode HM01
    A = 5.05e-9;
    B = -2.39E-6;
    C = 1.66E-3;
    D = 3.61E-2;
    E = 0;
    power_to_diode = A.*signal.^4 + B.*signal.^3 + C.*signal.^2 + D.*signal + E;
    Power_in_signal_HM01 = power_to_diode*10^(total_attenuation/10-6);
    PC = Power_in_signal_HM01;

    elseif (diode_code == 2) %diode HM02
```

```
    A = 4.75E-9;
    B = -1.96E-6;
    C = 1.56E-3;
    D = 4.35E-2;
    E = 0;
    power_to_diode = A.*signal.^4 + B.*signal.^3 + C.*signal.^2 + D.*signal + E;
    Power_in_signal_HM02 = power_to_diode*10^(total_attenuation/10-6);
    PC = Power_in_signal_HM02;

    elseif (diode_code == 3) %diode ML01
    A = 5.14e-9;
    B = -2.06E-6;
    C = 1.64E-3;
    D = 4.47E-2;
    E = 0;
    power_to_diode = A.*signal.^4 + B.*signal.^3 + C.*signal.^2 + D.*signal + E;
    Power_in_signal_ML01 = power_to_diode*10^(total_attenuation/10-6);
    PC = Power_in_signal_ML01;

    elseif (diode_code == 4) %diode ML03
    A = 3.99e-9;
    B = -2.07E-6;
    C = 1.47e-3;
    D = 2.82E-2;
    E = 0;
    power_to_diode = A.*signal.^4 + B.*signal.^3 + C.*signal.^2 + D.*signal + E;
    Power_in_signal_ML03 = power_to_diode*10^(total_attenuation/10-6);
    PC = Power_in_signal_ML03;

    else
        error('invalid diode code. diode code can be (1,2,3,4) corresponding to (HM01, HM02, ML01, ML03)')
end

end

%This function will accept an input NX1 vector and change the vector indices to
%an appropriate value based on the shot number. Shot1 is the very first
%shot in the series, shile first_shot is the first shot in the range and
%last_shot is the last shot in the range.
function vector = set_value(vector,shot1,first_shot,last_shot,value)
    bottom_range_index = first_shot-shot1+1;
    top_range_index = last_shot-shot1+1;
    vector(bottom_range_index:top_range_index) = value;
end

%Create function to write out key metrics, to make code shorter
%This function will only append, so make sure the file has already been
%created before using this function
function print_metric(dir_out,str,value)
```

```
    fileID_ind = fopen(dir_out,'a');
    fprintf(fileID_ind,'%s%f\n',str,value);
    fclose(fileID_ind);
end

%Function to save a png. Will only execute if save_plots is set to 1. Must
%provide the name of the figure and the full save location as a character
function save_png(save_plots,fig_name,save_loc)
    %Save signal plots
    if save_plots == 1
        saveas(fig_name, save_loc)
    end
end

%Write function to find time at which signal reaches its peak, and return a
%time range suitable for plotting. The variable signal must be an Nx2
%matrix, where the left column is time (in seconds) and the right column is the signal.
function [tstart,tfinish] = find_time_range(signal)
    indexmax = max(abs(signal(:,2))) == abs(signal(:,2)); %Find index of maximum peak
    t_peak = signal(indexmax,1);
    tstart = min(t_peak) - 75*(1E-9);
    tfinish = max(t_peak) + 110*(1E-9);
end

%This function accepts an Nx2 rogowski trace, where column 1 is time and
%column 2 is the rogowski signal, and integrates it to get current
function output = calc_current(input)

    time = input(:,1);
    raw_signal = input(:,2);
    dt = input(3,1)-input(2,1);
    %Calculate integrated signal
    int_sig = zeros(length(time),1);
    for inc = 2:length(time)
        int_sig(inc) = int_sig(inc-1) + raw_signal(inc)*dt;
    end
    %The next line is time in ns on scope before current pulse, used to
    %correct baseline
    t_limit = dt*400*ones(length(time),1);
    m = int_sig(400);
    IC = 1.229e10*(int_sig - (m*(time./t_limit)));
    current = 1e-3*IC;

    output = zeros(length(time),2);
    output(:,1) = time;
    movmean_npts = floor(length(time)/100);
    output(:,2) = movmean(current,movmean_npts);

end
```

```
%The following function accepts a Nx2 matrix where the first column is time
%and the second column is power. It will calculate the 10% oscillator start time
%and an oscillator off time.
function [t_on,t_off] = power_time_on_off_WG(input)

    time = input(:,1);
    dt = (1E9)*(time(3)-time(2)); %Calculate time step in nanoseconds
    signal = input(:,2);
    [M,indexmax] = max(signal);
    threshold_lvl = 0.1*signal(indexmax); %This is where I consider the oscillator not operational
    time_range = 400; %Time range to search for start and shutoff times (in ns)
    num_steps = floor(time_range/2/dt);
    index_lo = indexmax-num_steps;
    index_hi = indexmax+num_steps;
    %Choose default values for t_on and t_off in the event the program
    %fails to perform its objective
    t_on = time(index_lo);
    t_off = time(index_hi);
    %Determine index where the oscillator starts. This loop will begin
    %before the peak signal and will break the first time it
    for inc=index_lo:indexmax
        if signal(inc) > threshold_lvl && signal(inc-1) <= threshold_lvl
            t_on = (1E9)*time(inc);
        end
    end
    %Determine index where the oscillator shuts off
    for inc1=indexmax:index_hi
        inc2 = inc1-indexmax;
        inc = index_hi - inc2;
        if signal(inc) < threshold_lvl && signal(inc-1) >= threshold_lvl
            t_off = (1E9)*time(inc);
            break
        end
    end

end

%This function will return the point in time at which the voltage rises to
%10% and 90% of its maximum value. The time between t1 and t2 is the
%risetime. The input must be nx2, where the first column is time and the
%second column is the voltage.
function [t1,t2] = voltage_rise_time(input)

    time = input(:,1);
    voltage = abs(input(:,2));
    maxvolt = max(voltage);
    maxindex = min(find(voltage == maxvolt));
    t1 = 0;
```

```
    t2 = 0;
    for i=1:maxindex
        j = maxindex-i+1;
        if voltage(j+1) >= 0.9*maxvolt && voltage(j) <= 0.9*maxvolt
            t2 = time(j);
        elseif voltage(j+1) >= 0.1*maxvolt && voltage(j) <= 0.1*maxvolt
            t1 = time(j);
            break
        end
    end

end

%This function will return the point in time at which the power rises and
%falls to half of its maximum value. The time between t1 and t2 is the
%full width at half max (FWHM). The input must be nx2, where the first
%column is time and the second column is the voltage.
function [t1,t2] = power_fwhm(input)

    time = input(:,1);
    power = input(:,2);
    maxpow = max(power);
    maxindex = min(find(power == maxpow));
    t1 = 0;
    t2 = 0;
    %Find upper time limit
    for i=maxindex:length(power)
        if power(i+1) < 0.5*maxpow && power(i) >= 0.5*maxpow
            t2 = time(i);
            break
        end
    end
    %Find lower time limit
    for i=1:maxindex
        j = maxindex-i+1;
        if power(j+1) >= 0.5*maxpow && power(j) < 0.5*maxpow
            t1 = time(j);
            break
        end
    end

end
```

Bibliography

[1] G. B. Collins, *Microwave Magnetrons*. New York, NY, USA: McGraw-Hill, 1948.

[2] J. Goerth, "Early magnetron development especially in Germany," in *2010 International Conference on the Origins and Evolution of the Cavity Magnetron*, Bournemouth, United Kingdom, Apr. 2010, pp. 17–22. doi: 10.1109/CAVMAG.2010.5565571.

[3] A. W. Hull, "The Effect of A Uniform Magnetic Field on the Motion of Electrons Between Coaxial Cylinders.," *Phys. Review*, vol. 18, no. 1, p. 32, Jul. 1921.

[4] Y. Blanchard, G. Galati, and P. van Genderen, "The Cavity Magnetron: Not Just a British Invention," *IEEE Antennas and Propagation Magazine*, vol. 55, no. 5, p. 11, 2013.

[5] M. A. Stuchly and S. S. Stuchly, "Industrial, scientific, medical and domestic applications of microwaves," *IEE Proc. A Phys. Sci. Meas. Instrum. Manage. Educ. Rev. UK*, vol. 130, no. 8, p. 467, 1983, doi: 10.1049/ip-a-1.1983.0076.

[6] J. M. Osepchuk, "Microwave power applications," *IEEE Trans. Microwave Theory Techn.*, vol. 50, no. 3, pp. 975–985, Mar. 2002, doi: 10.1109/22.989980.

[7] E. Schamiloglu, R. J. Barker, M. Gundersen, and A. A. Neuber, "Modern Pulsed Power: Charlie Martin and Beyond," *Proc. IEEE*, vol. 92, no. 7, pp. 1014–1020, Jul. 2004, doi: 10.1109/JPROC.2004.829058.

[8] J. C. Martin, "Nanosecond pulse techniques," *Proc. IEEE*, vol. 80, no. 6, pp. 934–945, Jun. 1992, doi: 10.1109/5.149456.

[9] R. J. Barker and E. Schamiloglu, *High-Power Microwave Sources and Technologies*. New York, NY, USA: IEEE Press, 2001.

[10] J. Benford, J. Swegle, and E. Schamiloglu, *High Power Microwaves*, Third Edition. Boca Raton, FL: CRC Press, 2016.

[11] S. H. Gold and G. S. Nusinovich, "Review of high-power microwave source research," *Review of Scientific Instruments*, vol. 68, no. 11, pp. 3945–3974, Nov. 1997, doi: 10.1063/1.1148382.

[12] J. A. Nation, "On the Coupling of an High-Current Relativistic Electron Beam to a Slow Wave Structure," *Appl. Phys. Lett.*, vol. 17, no. 11, pp. 491–494, Dec. 1970, doi: 10.1063/1.1653281.

[13] G. Bekefi and T. J. Orzechowski, "Giant Microwave Bursts Emitted from a Field-Emission, Relativistic-Electron-Beam Magnetron," *Phys. Rev. Lett.*, vol. 37, no. 6, pp. 379–382, Aug. 1976, doi: 10.1103/PhysRevLett.37.379.

[14] V. L. Granatstein, M. Herndon, P. Sprangle, Y. Carmel, and J. A. Nation, "Gigawatt microwave from an intense relativistic electron beam," *Plasma Phys.*, vol. 17, no. 1, pp. 23–28, Jan. 1975, doi: 10.1088/0032-1028/17/1/003.

[15] A. Feickert, “U.S. Army Weapons-Related Directed Energy (DE) Programs: Background and Potential Issues for Congress,” p. 35, Feb. 2018.

[16] A. Kumar, “Drone Proliferation and Security Threats,” *Indian Journal of Asian Affairs*, vol. 33, p. 21, 2021.

[17] G. C. P. Patil, “Counter-Electronics High-Powered Microwave Advanced Missile Project,” p. 4, 2015.

[18] E. Schamiloglu, “High power microwave sources and applications,” in *2004 IEEE MTT-S International Microwave Symposium Digest (IEEE Cat. No.04CH37535)*, Fort Worth, TX, USA, 2004, vol. 2, pp. 999–1002. doi: 10.1109/MWSYM.2004.1339150.

[19] B. W. Hoff, J. W. McConaha, Z. W. Cohick, M. A. Franzi, D. A. Enderich, D. Revelli, J. Cox, H. Irshad, H. H. Pohle, A. Schmitt-Sody, S. C. Schaub, A. E. Baros, N. C. Lewis, J. W. Luginsland, M. T. Lanagan, and S. Perini, “Apparatus for controlled microwave exposure of aerosolized pathogens,” *Review of Scientific Instruments*, vol. 92, no. 1, p. 014707, Jan. 2021, doi: 10.1063/5.0032823.

[20] J. Benford, “Space Applications of High-Power Microwaves,” *IEEE Trans. Plasma Sci.*, vol. 36, no. 3, pp. 569–581, Jun. 2008, doi: 10.1109/TPS.2008.923760.

[21] L. Bacon and L. Rinehart, “A Brief Technology Survey of High-Power Microwave Sources,” SAND2001-1155, 782595, Apr. 2001. doi: 10.2172/782595.

[22] Y. Y. Lau, “Chapter 9: Theory of Crossed-Field Devices and a Comparative Study of Other Radiation Sources,” in *High-Power Microwave Sources*, Norwood, MA: Edited by V. L. Granatstein and I. Alexeff, Artech House, 1987, pp. 309–349.

[23] R. M. Gilgenbach, Y. Y. Lau, H. L. McDowell, K. L. Cartwright, and T. A. Spencer, “Crossed-Field Devices,” in *Modern Microwave and Millimeter Wave Power Electronics*, Edited by R. J. Barker, N. C. Luhmann, J. H. Booske, and G. S. Nusinovich., Piscataway, NJ, USA: IEEE, 2005, p. Chap. 6.

[24] R. J. Barker, J. H. Booske, N. C. Luhmann Jr., and G. S. Nusinovich, *Modern Microwave and Millimeter-Wave Power Electronics*. Piscataway, NJ, USA: Wiley, 2005.

[25] D. Andreev, A. Kuskov, and E. Schamiloglu, “Review of the relativistic magnetron,” *Matter and Radiation at Extremes*, vol. 4, no. 6, p. 067201, Nov. 2019, doi: 10.1063/1.5100028.

[26] M. C. Clark, B. M. Marder, and L. D. Bacon, “Magnetically insulated transmission line oscillator,” *Appl. Phys. Lett.*, vol. 52, no. 1, pp. 78–80, Jan. 1988, doi: 10.1063/1.99330.

[27] S. Exelby Jr, “Recirculating Planar Crossed-Field Amplifiers,” Doctoral Dissertation, University of Michigan, Ann Arbor, MI, USA, 2019.

[28] V. Serlin and M. Friedman, “Development and optimization of the relativistic klystron amplifier,” *IEEE Trans. Plasma Sci.*, vol. 22, no. 5, pp. 692–700, Oct. 1994, doi: 10.1109/27.338284.

[29] Y. Y. Lau, M. Friedman, J. Krall, and V. Serlin, “Relativistic Klystron amplifiers driven by modulated intense relativistic electron beams,” *IEEE Trans. Plasma Sci.*, vol. 18, no. 3, pp. 553–569, Jun. 1990, doi: 10.1109/27.55927.

[30] A. V. Gunin, A. I. Klimov, S. D. Korovin, I. K. Kurkan, I. V. Pegel, S. D. Polevin, A. M. Roitman, V. V. Rostov, A. S. Stepchenko, and E. M. Totmeninov, "Relativistic X-band BWO with 3-GW output power," *IEEE Trans. Plasma Sci.*, vol. 26, no. 3, pp. 326–331, Jun. 1998, doi: 10.1109/27.700761.

[31] H. Johnson, "Backward-Wave Oscillators," *Proc. IRE*, vol. 43, no. 6, pp. 684–697, 1955, doi: 10.1109/JRPROC.1955.278054.

[32] Yanchao Shi, W. Song, Yuqun Den, and Meng Zhu, "A high efficiency relativistic traveling-wave tube with distributed feedback resonant," in *2016 Progress in Electromagnetic Research Symposium (PIERS)*, Shanghai, China, Aug. 2016, pp. 4805–4809. doi: 10.1109/PIERS.2016.7735755.

[33] V. A. Flyagin, A. V. Gaponov, I. Petelin, and V. K. Yulpatov, "The Gyrotron," *IEEE Trans. Microwave Theory Techn.*, vol. 25, no. 6, pp. 514–521, Jun. 1977, doi: 10.1109/TMTT.1977.1129149.

[34] D. A. G. Deacon, L. R. Elias, J. M. J. Madey, G. J. Ramian, H. A. Schwettman, and T. I. Smith, "First Operation of a Free-Electron Laser," *Phys. Rev. Lett.*, vol. 38, no. 16, pp. 892–894, Apr. 1977, doi: 10.1103/PhysRevLett.38.892.

[35] D. J. Sullivan, "High Power Microwave Generation from a Virtual Cathode Oscillator (Vircator)," *IEEE Trans. Nucl. Sci.*, vol. 30, no. 4, pp. 3426–3428, Aug. 1983, doi: 10.1109/TNS.1983.4336679.

[36] F. J. Agee, C. E. Baum, W. D. Prather, J. M. Lehr, J. P. O'Loughlin, J. W. Burger, J. S. H. Schoenberg, D. W. Scholfield, R. J. Torres, J. P. Hull, and J. A. Gaudet, "Ultra-wideband transmitter research," *IEEE Trans. Plasma Sci.*, vol. 26, no. 3, pp. 860–873, Jun. 1998, doi: 10.1109/27.700855.

[37] J. Gaudet, E. Schamiloglu, J. O. Rossi, C. J. Buchenauer, and C. Frost, "Nonlinear Transmission Lines for High Power Microwave Applications - A Survey," in *2008 IEEE International Power Modulators and High-Voltage Conference*, Las Vegas, NV, USA, May 2008, pp. 131–138. doi: 10.1109/IPMC.2008.4743597.

[38] J. Zhang, D. Zhang, Y. Fan, J. He, X. Ge, X. Zhang, J. Ju, and T. Xun, "Progress in narrowband high-power microwave sources," *Physics of Plasmas*, vol. 27, no. 1, p. 010501, Jan. 2020, doi: 10.1063/1.5126271.

[39] E. C. Okress, *Crossed-Field Microwave Devices*. New York, NY, USA: Academic Press, 1961.

[40] R. B. Miller, "Mechanism of explosive electron emission for dielectric fiber (velvet) cathodes," *Journal of Applied Physics*, vol. 84, no. 7, pp. 3880–3889, Oct. 1998, doi: 10.1063/1.368567.

[41] P. Zhang, Á. Valfells, L. K. Ang, J. W. Luginsland, and Y. Y. Lau, "100 years of the physics of diodes," *Applied Physics Reviews*, vol. 4, no. 1, p. 011304, Mar. 2017, doi: 10.1063/1.4978231.

[42] J. Benford, "History and future of the relativistic magnetron," in *2010 International Conference on the Origins and Evolution of the Cavity Magnetron*, Bournemouth, United Kingdom, Apr. 2010, pp. 40–45. doi: 10.1109/CAVMAG.2010.5565566.

[43] M. C. Jones, V. B. Neculaes, Y. Y. Lau, R. M. Gilgenbach, and W. M. White, "Cathode priming of a relativistic magnetron," *Appl. Phys. Lett.*, vol. 85, no. 26, pp. 6332–6334, Dec. 2004, doi: 10.1063/1.1841454.

[44] M. Fuks and E. Schamiloglu, "Rapid Start of Oscillations in a Magnetron with a 'Transparent' Cathode," *Phys. Rev. Lett.*, vol. 95, no. 20, p. 205101, Nov. 2005, doi: 10.1103/PhysRevLett.95.205101.

[45] M. I. Fuks and E. Schamiloglu, "70% Efficient Relativistic Magnetron With Axial Extraction of Radiation Through a Horn Antenna," *IEEE Transactions on Plasma Science*, vol. 38, no. 6, pp. 1302–1312, Jun. 2010, doi: 10.1109/TPS.2010.2042823.

[46] C. Leach, S. Prasad, M. I. Fuks, J. Buchenauer, J. W. McConaha, and E. Schamiloglu, "Experimental Demonstration of a High-Efficiency Relativistic Magnetron With Diffraction Output With Spherical Cathode Endcap," *IEEE Trans. Plasma Sci.*, vol. 45, no. 2, pp. 282–288, Feb. 2017, doi: 10.1109/TPS.2016.2644625.

[47] M. I. Fuks and E. Schamiloglu, "Application of a Magnetic Mirror to Increase Total Efficiency in Relativistic Magnetrons," *Phys. Rev. Lett.*, vol. 122, no. 22, p. 224801, Jun. 2019, doi: 10.1103/PhysRevLett.122.224801.

[48] B. W. Hoff, R. M. Gilgenbach, N. M. Jordan, Y. Y. Lau, E. J. Cruz, D. M. French, M. R. Gomez, J. C. Zier, T. A. Spencer, and D. Price, "Magnetic Priming at the Cathode of a Relativistic Magnetron," *IEEE Trans. Plasma Sci.*, vol. 36, no. 3, pp. 710–717, Jun. 2008, doi: 10.1109/TPS.2008.923732.

[49] V. B. Neculaes, R. M. Gilgenbach, Y. Y. Lau, M. C. Jones, and W. M. White, "Low-Noise Microwave Oven Magnetrons With Fast Start-Oscillation by Azimuthally Varying Axial Magnetic Fields," *IEEE Trans. Plasma Sci.*, vol. 32, no. 3, pp. 1152–1159, Jun. 2004, doi: 10.1109/TPS.2004.828806.

[50] V. B. Neculaes, R. M. Gilgenbach, and Y. Y. Lau, "Low-Noise, Crossed-Field Devices Such as a Microwave Magnetron, Microwave Oven Utilizing Same and Method of Converting a Noisy Magnetron into a Low-Noise Magnetron," US Patent No. 6,872,929 B2, Mar. 29, 2005

[51] V. B. Neculaes, R. M. Gilgenbach, and Y. Y. Lau, "Low-Noise, Crossed-Field Devices Such as a Microwave Magnetron Having an Azimuthally-Varying Axial Magnetic Field and Microwave Oven Utilizing Same," US Patent No. 6,921,890 B2, Jul. 26, 2005

[52] R. M. Gilgenbach, Y.-Y. Lau, D. M. French, B. W. Hoff, J. Luginsland, and M. Franzi, "CROSSED FIELD DEVICE," US Patent No. 8,841,867 B2, Sep. 23, 2014

[53] M. A. Franzi, "Relativistic Recirculating Planar Magnetrons," Doctoral Dissertation, University of Michigan, Ann Arbor, MI, USA, 2014.

[54] G. B. Greening, "Multi-Frequency Recirculating Planar Magnetrons," Doctoral Dissertation, University of Michigan, Ann Arbor, MI, USA, 2017.

[55] M. A. Franzi, R. M. Gilgenbach, B. W. Hoff, D. A. Chalenski, D. Simon, Y. Y. Lau, and J. Luginsland, "Recirculating-Planar-Magnetron Simulations and Experiment," *IEEE Trans. Plasma Sci.*, vol. 41, no. 4, pp. 639–645, Apr. 2013, doi: 10.1109/TPS.2013.2242493.

[56] G. B. Greening, N. M. Jordan, S. C. Exelby, D. H. Simon, Y. Y. Lau, and R. M. Gilgenbach, "Multi-frequency recirculating planar magnetrons," *Appl. Phys. Lett.*, p. 5, 2016.

[57] S. C. Exelby, G. B. Greening, N. M. Jordan, D. A. Packard, D. Simon, Y. Y. Lau, B. W. Hoff, and R. M. Gilgenbach, "High-Power Amplification Experiments on a Recirculating Planar Crossed-Field Amplifier," *IEEE Trans. Plasma Sci.*, vol. 48, no. 6, pp. 1917–1922, Jun. 2020, doi: 10.1109/TPS.2020.2996030.

[58] R. M. Gilgenbach, Y.-Y. Lau, D. M. French, B. W. Hoff, M. Franzi, and J. Luginsland, "Recirculating Planar Magnetrons for High-Power High-Frequency Radiation Generation," *IEEE Trans. Plasma Sci.*, vol. 39, no. 4, pp. 980–987, Apr. 2011, doi: 10.1109/TPS.2010.2099670.

[59] H. Zhou, T. Li, and S. Li, "L-band dual-frequency recirculating planar magnetron," *Journal of Electromagnetic Waves and Applications*, vol. 33, no. 8, pp. 991–1002, May 2019, doi: 10.1080/09205071.2019.1583137.

[60] T. A. Treado, W. O. Doggett, G. E. Thomas, R. S. Smith, J. Jackson-Ford, and D. J. Jenkins, "Operating modes of relativistic rising-sun and A6 magnetrons," *IEEE Trans. Plasma Sci.*, vol. 16, no. 2, pp. 237–248, Apr. 1988, doi: 10.1109/27.3820.

[61] J. S. Levine, B. D. Harteneck, and H. D. Price, "Frequency-agile relativistic magnetrons," San Diego, CA, Sep. 1995, pp. 74–79. doi: 10.1117/12.218536.

[62] Jin-Chuan Ju, Yu-Wei Fan, Hui-Huang Zhong, and Ting Shu, "A Novel Dual-Frequency Magnetically Insulated Transmission Line Oscillator," *IEEE Trans. Plasma Sci.*, vol. 37, no. 10, pp. 2041–2047, Oct. 2009, doi: 10.1109/TPS.2009.2027603.

[63] Jun Cai, Xianping Wu, and Jinjun Feng, "Traveling-Wave Tube Harmonic Amplifier in Terahertz and Experimental Demonstration," *IEEE Trans. Electron Devices*, vol. 62, no. 2, pp. 648–651, Feb. 2015, doi: 10.1109/TED.2014.2377914.

[64] A. M. Elfrgani, S. Prasad, M. I. Fuks, and E. Schamiloglu, "Dual-Band Operation of Relativistic BWO With Linearly Polarized Gaussian Output," *IEEE Trans. Plasma Sci.*, vol. 42, no. 8, pp. 2141–2145, Aug. 2014, doi: 10.1109/TPS.2014.2331334.

[65] D. A. Packard, S. C. Exelby, N. M. Jordan, C. J. Swenson, B. W. Hoff, Y. Y. Lau, and R. M. Gilgenbach, "Frequency and Power Measurements on the Harmonic Recirculating Planar Magnetron," *IEEE Trans. Plasma Sci.*, pp. 1–11, 2020, doi: 10.1109/TPS.2020.2991656.

[66] G. B. Greening, S. C. Exelby, D. A. Packard, N. M. Jordan, Y. Y. Lau, and R. M. Gilgenbach, "Harmonic Frequency Locking in the Multifrequency Recirculating Planar Magnetron," *IEEE Trans. Electron Devices*, vol. 65, no. 6, pp. 2347–2353, Jun. 2018, doi: 10.1109/TED.2018.2810240.

[67] O. Buneman, "A Toroidal Magnetron," *Proc. Phys. Soc. B*, vol. 63, no. 4, pp. 278–288, Apr. 1950, doi: 10.1088/0370-1301/63/4/304.

[68] L. Brillouin, "Theory of the Magnetron. I," *Phys. Rev.*, vol. 60, no. 5, pp. 385–396, Sep. 1941, doi: 10.1103/PhysRev.60.385.

[69] L. Brillouin, "Theory of the Magnetron II. Oscillations in a Split-Anode Magnetron," *Phys. Rev.*, vol. 62, no. 3–4, pp. 166–177, Aug. 1942, doi: 10.1103/PhysRev.62.166.

[70] L. Brillouin, "Theory of the Magnetron. III," *Phys. Rev.*, vol. 63, no. 3–4, pp. 127–136, Feb. 1943, doi: 10.1103/PhysRev.63.127.

[71] V. Nallasamy, S. K. Datta, S. U. Reddy, and P. K. Jain, “Advances and present trends in magnetically insulated line oscillator,” *Journal of Electromagnetic Waves and Applications*, vol. 31, no. 17, pp. 1864–1874, Nov. 2017, doi: 10.1080/09205071.2017.1338622.

[72] D. Chen, J. Wen, Z. Luo, A. Yu, and Y. Zhang, “A High-Efficiency Magnetically Insulated Transmission Line Oscillator,” *IEEE Trans. Plasma Sci.*, vol. 45, no. 7, pp. 1723–1725, Jul. 2017, doi: 10.1109/TPS.2017.2702640.

[73] H. Xu, X.-Y. Wang, Y.-W. Fan, A. Li, and Z. Liu, “A High-Efficiency Ridged Magnetically Insulated Transmission Line Oscillator,” *IEEE Trans. Electron Devices*, vol. 67, no. 10, pp. 4442–4446, Oct. 2020, doi: 10.1109/TED.2020.3013726.

[74] V. Nallasamy, S. K. Datta, S. Reddy, and P. K. Jain, “Efficiency Enhancemant of an S-Band Magnetically Insulated Line Oscillator,” *International Journal of Microwave and Optical Technology*, vol. 11, no. 5, pp. 324–331, Sep. 2016.

[75] G. Dixit, A. Kumar, and P. K. Jain, “Design analysis and simulation study of an efficiency enhanced L-band MILO,” *Phys. Plasmas*, vol. 24, no. 1, p. 013113, Jan. 2017, doi: 10.1063/1.4973929.

[76] R. D. McBride, W. A. Stygar, M. E. Cuneo, D. B. Sinars, M. G. Mazarakis, J. J. Leckbee, M. E. Savage, B. T. Hutsel, J. D. Douglass, M. L. Kiefer, B. V. Oliver, G. R. Laity, M. R. Gomez, D. A. Yager-Elorriaga, S. G. Patel, B. M. Kovalchuk, A. A. Kim, P.-A. Gourdain, S. N. Bland, S. Portillo, S. C. Bott-Suzuki, F. N. Beg, Y. Maron, R. B. Spielman, D. V. Rose, D. R. Welch, J. C. Zier, J. W. Schumer, J. B. Greenly, A. M. Covington, A. M. Steiner, P. C. Campbell, S. M. Miller, J. M. Woolstrum, N. B. Ramey, A. P. Shah, B. J. Sporer, N. M. Jordan, Y. Y. Lau, and R. M. Gilgenbach, “A Primer on Pulsed Power and Linear Transformer Drivers for High Energy Density Physics Applications,” *IEEE Trans. Plasma Sci.*, vol. 46, no. 11, pp. 3928–3967, Nov. 2018, doi: 10.1109/TPS.2018.2870099.

[77] D. A. Packard, A. Cooleybeck, N. M. Jordan, B. J. Sporer, A. E. Mazarakis, Y. Y. Lau, R. M. Gilgenbach, and R. D. McBride, “HFSS and CST Simulations of a GW-Class MILO,” *IEEE Trans. Plasma Sci.*, pp. 1–8, 2020, doi: 10.1109/TPS.2020.2990163.

[78] S. E. Calico, M. C. Clark, R. W. Lemke, and M. C. Scott, “Experimental and theoretical investigations of a magnetically insulated line oscillator (MILO),” in *Proc. SPIE*, San Diego, CA, Sep. 1995, pp. 50–59. doi: 10.1117/12.218591.

[79] R. W. Lemke, J. W. Luginsland, and M. D. Haworth, “Evidence of a new pulse-shortening mechanism in a load-limited MILO,” *IEEE Trans. Plasma Sci.*, vol. 28, no. 3, pp. 511–516, Jun. 2000, doi: 10.1109/27.887660.

[80] M. D. Haworth, G. Baca, J. Benford, T. Englert, K. Hackett, K. J. Hendricks, D. Henley, M. LaCour, R. W. Lemke, D. Price, D. Ralph, M. Sena, D. Shiffler, and T. A. Spencer, “Significant pulse-lengthening in a multigigawatt magnetically insulated transmission line oscillator,” *IEEE Trans. Plasma Sci.*, vol. 26, no. 3, pp. 312–319, Jun. 1998, doi: 10.1109/27.700759.

[81] D. E. T. F. Ashby, J. W. Eastwood, J. Allen, K. C. Hawkins, and L. M. Lea, “Comparison between experiment and computer modeling for simple MILO configurations,” *IEEE Trans. Plasma Sci.*, vol. 23, no. 6, pp. 959–969, Dec. 1995, doi: 10.1109/27.476484.

[82] J. W. Eastwood, K. C. Hawkins, and M. P. Hook, "The tapered MILO," *IEEE Trans. Plasma Sci.*, vol. 26, no. 3, pp. 698–713, Jun. 1998, doi: 10.1109/27.700810.

[83] R. Cousin, J. Larour, J. Gardelle, B. Cassany, P. Modin, P. Gouard, and P. Raymond, "Gigawatt Emission From a 2.4-GHz Compact Magnetically Insulated Line Oscillator (MILO)," *IEEE Trans. Plasma Sci.*, vol. 35, no. 5, pp. 1467–1475, Oct. 2007, doi: 10.1109/TPS.2007.906122.

[84] S. Dwivedi and P. K. Jain, "Magnetically Insulated Line Oscillator (MILO) Performance Study and its Parameter Optimization," *IEEE Trans. Plasma Sci.*, vol. 41, no. 9, pp. 2532–2538, Sep. 2013, doi: 10.1109/TPS.2013.2277859.

[85] Y.-W. Fan, H.-H. Zhong, Z.-Q. Li, T. Shu, J.-D. Zhang, J.-L. Liu, J.-H. Yang, J. Zhang, C.-W. Yuan, and L. Luo, "Recent progress of the improved magnetically insulated transmission line oscillator," *Review of Scientific Instruments*, vol. 79, no. 3, p. 034703, Mar. 2008, doi: 10.1063/1.2894212.

[86] Y. Fan, X. Wang, G. Li, H. Yang, H. Zhong, and J. Zhang, "Experimental Demonstration of a Tunable Load-Limited Magnetically Insulated Transmission Line Oscillator," *IEEE Trans. Electron Devices*, vol. 63, no. 3, pp. 1307–1311, Mar. 2016, doi: 10.1109/TED.2016.2518744.

[87] M. Abide, T. Buntin, D. Barnett, J. Dickens, R. Joshi, A. Neuber, and J. Mankowski, "Low-Impedance S-Band MILO," in *2019 IEEE Pulsed Power & Plasma Science (PPPS)*, Orlando, FL, USA, Jun. 2019, pp. 1–5. doi: 10.1109/PPPS34859.2019.9009939.

[88] H. Zhou, T. Shu, and Z. Li, "Investigation of a high impedance magnetically insulated transmission line oscillator with hollow load," *Physics of Plasmas*, vol. 19, no. 9, p. 093113, Sep. 2012, doi: 10.1063/1.4752019.

[89] F. Yu-Wei, S. Ting, L. Yong-Gui, Z. Hui-Huang, L. Zhi-Qiang, W. Yong, Z. Yan-Song, and L. Ling, "A Compact Magnetically Insulated Line Oscillator with New-Type Beam Dump," *Chinese Phys. Lett.*, vol. 22, no. 1, pp. 164–167, Jan. 2005, doi: 10.1088/0256-307X/22/1/047.

[90] F. Yu-Wei, Z. Hui-Huang, L. Zhi-Qiang, S. Ting, Y. Han-Wu, Y. Jian-Hua, W. Yong, L. Ling, and Z. Yan-Song, "Investigation of an X-band magnetically insulated transmission line oscillator," *Chinese Phys. B*, vol. 17, no. 5, pp. 1804–1808, May 2008, doi: 10.1088/1674-1056/17/5/042.

[91] D.-B. Chen, D. Wang, F.-B. Meng, and Z.-K. Fan, "Bifrequency Magnetically Insulated Transmission Line Oscillator," *IEEE Trans. Plasma Sci.*, vol. 37, no. 1, pp. 23–29, Jan. 2009, doi: 10.1109/TPS.2008.2007731.

[92] J. Wen, D. Chen, D. Wang, and F. Qin, "Preliminary Experimental Research on Ku-Band MILO," *IEEE Trans. Plasma Sci.*, vol. 41, no. 9, p. 5, 2013.

[93] Y. Y. Lau, D. A. Packard, C. J. Swenson, J. W. Luginsland, D. Li, A. Jassem, N. M. Jordan, and R. M. Gilgenbach, "Explicit Brillouin flow solutions in magnetrons, magnetically insulated line oscillators, and radial magnetically insulated transmission lines," *IEEE Trans. Plasma Sci.*, Accepted for Publication 2021.

[94] G. D. Sims, “Preoscillation Phenomena in Space-Charge Clouds below the Main Oscillation Threshold,” in *Crossed-field Microwave Device*, Elsevier, 1961, pp. 179–208. doi: 10.1016/B978-0-12-395553-1.50023-6.

[95] O. Buneman, “Symmetrical States and Their Breakup,” in *Crossed-field Microwave Device*, Elsevier, 1961, pp. 209–233. doi: 10.1016/B978-0-12-395553-1.50024-8.

[96] P. J. Christenson, D. P. Chernin, A. L. Garner, and Y. Y. Lau, “Resistive destabilization of cycloidal electron flow and universality of (near-) Brillouin flow in a crossed-field gap,” *Physics of Plasmas*, vol. 3, no. 12, pp. 4455–4462, Dec. 1996, doi: 10.1063/1.872064.

[97] P. J. Christenson and Y. Y. Lau, “One-Dimensional Modulational Instability in a Crossed-Field Gap,” *Phys. Rev. Lett.*, vol. 76, no. 18, pp. 3324–3327, Apr. 1996, doi: 10.1103/PhysRevLett.76.3324.

[98] A. L. Garner, Y. Y. Lau, and D. Chernin, “Collapse of cycloidal electron flows induced by misalignments in a magnetically insulated diode,” *Physics of Plasmas*, vol. 5, no. 6, pp. 2447–2453, Jun. 1998, doi: 10.1063/1.872921.

[99] A. Palevsky, “Generation of intense microwave radiation by the relativistic e-beam magnetron (experiment and numerical simulation),” Doctoral Dissertation, Massachusetts Institute of Technology, 1980.

[100] Y. Y. Lau, J. W. Luginsland, K. L. Cartwright, D. H. Simon, W. Tang, B. W. Hoff, and R. M. Gilgenbach, “A re-examination of the Buneman–Hartree condition in a cylindrical smooth-bore relativistic magnetron,” *Physics of Plasmas*, vol. 17, no. 3, p. 033102, Mar. 2010, doi: 10.1063/1.3328804.

[101] R. C. Davidson, G. L. Johnston, K. T. Tsang, and A. T. Drobot, “Cylindrical Brillouin Flow In Relativistic Smooth-Bore Magnetrons,” in *Proc. SPIE*, Los Angeles, CA, United States, Jul. 1989, p. 186. doi: 10.1117/12.951796.

[102] D. H. Simon, Y. Y. Lau, J. W. Luginsland, and R. M. Gilgenbach, “An unnoticed property of the cylindrical relativistic Brillouin flow,” *Physics of Plasmas*, vol. 19, no. 4, p. 043103, Apr. 2012, doi: 10.1063/1.3701705.

[103] J. R. M. Vaughan, “A model for calculation of magnetron performance,” *IEEE Trans. Electron Devices*, vol. 20, no. 9, pp. 818–826, Sep. 1973, doi: 10.1109/T-ED.1973.17750.

[104] J. Slater, *Microwave Electronics*. D. Van Norstrand Company, 1950.

[105] M. C. Balk, “Simulation possibilities of vacuum electronic devices with CST PARTICLE STUDIO,” in *2008 IEEE International Vacuum Electronics Conference*, Monterey, CA, USA, May 2008, pp. 459–460. doi: 10.1109/IVELEC.2008.4556402.

[106] R. E. Peterkin and J. W. Luginsland, “A virtual prototyping environment for directed-energy concepts,” *Comput. Sci. Eng.*, vol. 4, no. 2, pp. 42–49, Apr. 2002, doi: 10.1109/5992.988646.

[107] M. Franzi, R. Gilgenbach, Y. Y. Lau, B. Hoff, G. Greening, and P. Zhang, “Passive mode control in the recirculating planar magnetron,” *Physics of Plasmas*, vol. 20, no. 3, p. 033108, Mar. 2013, doi: 10.1063/1.4794967.

[108] M. Franzi, R. M. Gilgenbach, B. Hoff, G. Greening, Y. Y. Lau, N. M. Jordan, D. Simon, D. French, and J. Luginsland, "Coaxial all cavity extraction in the Recirculating Planar Magnetron," in *IEEE International Vacuum Electronics Conference*, Apr. 2014, pp. 89–90. doi: 10.1109/IVEC.2014.6857504.

[109] X. Gao, Z. Yang, Y. Xu, L. Qi, D. Li, Z. Shi, F. Lan, and Z. Liang, "Dispersion characteristics of a slow wave structure with metal photonic band gap cells," *Nuclear Instruments and Methods in Physics Research Section A: Accelerators, Spectrometers, Detectors and Associated Equipment*, vol. 592, no. 3, pp. 292–296, Jul. 2008, doi: 10.1016/j.nima.2008.04.059.

[110] B. McCowan, "Calculating slow-wave circuit parameters with HFSS," in *Abstracts. International Vacuum Electronics Conference 2000 (Cat. No.00EX392)*, Monterey, CA, USA, 2000, p. 2. doi: 10.1109/OVE:EC.2000.847482.

[111] C. B. Wilsen, J. W. Luginsland, Yue Ying Lau, T. M. Antonsen, D. P. Chernin, P. M. Tchou, Student, M. W. Keyser, R. M. Gilgenbach, and L. D. Ludeking, "A simulation study of beam loading on a cavity," *IEEE Trans. Plasma Sci.*, vol. 30, no. 3, pp. 1160–1168, Jun. 2002, doi: 10.1109/TPS.2002.801623.

[112] E. L. Ginzton, *Microwave Measurements*. New York, NY, USA: McGraw-Hill, 1957.

[113] A. Hernandez, E. Martin, J. Margineda, and J. M. Zamarro, "Resonant cavities for measuring the surface resistance of metals at X-band frequencies," *J. Phys. E: Sci. Instrum.*, vol. 19, no. 3, pp. 222–225, Mar. 1986, doi: 10.1088/0022-3735/19/3/013.

[114] D. A. D. Greenwood, "An ICEPIC Convergence Study Using a Relativistic Magnetron," *AFRL Technical Memorandum*, no. AFRL-DE-PS-M-2005-1005, p. 18, 2005.

[115] J. C. Borghetti, "Inline Waveguide to Coaxial Transition," US3023382 A, Feb. 1962

[116] R. Levy and L. W. Hendrick, "Analysis and synthesis of in-line coaxial-to-waveguide adapters," in *2002 IEEE MTT-S International Microwave Symposium Digest (Cat. No.02CH37278)*, Seattle, WA, USA, 2002, pp. 809–811. doi: 10.1109/MWSYM.2002.1011754.

[117] E. Guerin, "Personal Communication," Apr. 2021.

[118] R. W. Lemke, S. E. Calico, and M. C. Clark, "Investigation of a load-limited, magnetically insulated transmission line oscillator (MILO)," *IEEE Trans. Plasma Sci.*, vol. 25, no. 2, pp. 364–374, Apr. 1997, doi: 10.1109/27.602513.

[119] R. Cousin, J. Larour, P. Gouard, and P. Raymond, "Evidence of the $3\pi/4$ interaction mode in a compact magnetically insulated line oscillator process," *Journal of Applied Physics*, vol. 100, no. 8, p. 084512, Oct. 2006, doi: 10.1063/1.2357645.

[120] R. M. Gilgenbach, L. D. Horton, R. F. Lucey, S. Bidwell, M. Cuneo, J. Miller, and L. Smutek, "Microsecond Electron Beam Diode Closure Experiments," in *Invited Talk, Proceedings of the IEEE Pulsed Power Conference*, Crystal City, VA, 1985, p. 7.

[121] Lucey, "Long-pulse relativistic electron beam generation and propagation in gases and in UV laser ionized channels," University of Michigan, Ann Arbor, MI, USA, 1988.

[122] C. L. Enloe, “Ultraviolet-Induced Flashover of Highly Angled Polymeric Insulators in Vacuum,” Doctoral Dissertation, University of Michigan, Ann Arbor, MI, USA, 1988.

[123] C. Waters, “Current Transformers Provide Accurate, Isolated Measurements.” 1986.

[124] R. K. Cacak and J. R. Craig, “Magnetic Field Uniformity around Near-Helmholtz Coil Configurations,” *Review of Scientific Instruments*, vol. 40, no. 11, pp. 1468–1470, Nov. 1969, doi: 10.1063/1.1683829.

[125] B. W. Hoff, A. D. Greenwood, P. J. Mardahl, and M. D. Haworth, “All Cavity-Magnetron Axial Extraction Technique,” *IEEE Transactions on Plasma Science*, vol. 40, no. 11, pp. 3046–3051, Nov. 2012, doi: 10.1109/TPS.2012.2217758.

[126] A. D. Greenwood, “All Cavity Magnetron Axial Extractor,” US 7106004 B1, Sep. 12, 2006

[127] C. Leach, S. Prasad, M. I. Fuks, and E. Schamiloglu, “Suppression of Leakage Current in a Relativistic Magnetron Using a Novel Design Cathode Endcap,” *IEEE Trans. Plasma Sci.*, vol. 40, no. 8, pp. 2089–2093, Aug. 2012, doi: 10.1109/TPS.2012.2199136.

[128] T. A. Treado, R. S. Smith, C. S. Shaughnessy, and G. E. Thomas, “Temporal study of long-pulse relativistic magnetron operation,” *IEEE Trans. Plasma Sci.*, vol. 18, no. 3, pp. 594–602, Jun. 1990, doi: 10.1109/27.55932.

[129] D. Price, J. S. Levine, and J. N. Benford, “Diode Plasma Effects on the Microwave Pulse Length from Relativistic Magnetrons,” *IEEE Trans. Plasma Sci.*, vol. 26, no. 3, p. 6, 1998.

[130] D. Price and J. N. Benford, “General Scaling of Pulse Shortening in Explosive-Emission-Driven Microwave Sources,” *IEEE Trans. Plasma Sci.*, vol. 26, no. 3, p. 7, 1998.

[131] D. A. Packard, G. B. Greening, N. M. Jordan, S. C. Exelby, P. Y. Wong, Y. Y. Lau, R. M. Gilgenbach, B. W. Hoff, and J. F. Hammond, “Harmonic-frequency locking in planar magnetrons,” in *2018 IEEE International Vacuum Electronics Conference (IVEC)*, Monterey, CA, Apr. 2018, pp. 253–254. doi: 10.1109/IVEC.2018.8391498.

[132] R. Adler, “A study of locking phenomena in oscillators,” *Proc. IEEE*, vol. 61, no. 10, pp. 1380–1385, 1973, doi: 10.1109/PROC.1973.9292.

[133] T. Treado, “Generation and Diagnosis of Long-and-Short-Pulse, High-Power Microwave Radiation from Relativistic Rising-Sun and A6 Magnetrons,” Doctoral Dissertation, North Carolina State University, Raleigh, NC, 1989.

[134] J. S. Herd and M. D. Conway, “The Evolution to Modern Phased Array Architectures,” *Proc. IEEE*, vol. 104, no. 3, pp. 519–529, Mar. 2016, doi: 10.1109/JPROC.2015.2494879.

[135] J. Benford, H. Sze, W. Woo, R. R. Smith, and B. Harteneck, “Phase Locking of Relativistic Magnetrons,” *Phys. Rev. Lett.*, vol. 62, no. 8, pp. 969–971, Feb. 1989, doi: 10.1103/PhysRevLett.62.969.

[136] Fen Qin, Dong Wang, Dai-Bing Chen, and Zhi-Kai Fan, “Simulation Investigation of L-Band Ladder Cathode MILO,” *IEEE Trans. Plasma Sci.*, vol. 37, no. 10, pp. 1921–1924, Oct. 2009, doi: 10.1109/TPS.2009.2023126.

[137] T. Jiang, J. He, J. Zhang, Z. Li, and J. Ling, “An Improved Ku-band MILO With Tapered Choke Cavity and Enlarged First Interaction Cavity,” *IEEE Trans. Electron Devices*, vol. 64, no. 1, pp. 286–292, Jan. 2017, doi: 10.1109/TED.2016.2623943.

[138] Y.-W. Fan, C.-W. Yuan, H.-H. Zhong, T. Shu, and L. Luo, “Simulation Investigation of an Improved MILO,” *IEEE Trans. Plasma Sci.*, vol. 35, no. 2, p. 5, 2007.

[139] T. A. Treado, P. D. Brown, and D. Aiguier, “New experimental results at long pulse and high repetition rate, from Varian’s phase-locked magnetron array program,” in *Proc. SPIE*, Los Angeles, CA, Jul. 1993, pp. 241–251. doi: 10.1117/12.147464.

[140] M. D. Haworth, K. L. Cartwright, J. W. Luginsland, D. A. Shiffler, and R. J. Umstattd, “Improved electrostatic design for milo cathodes,” *IEEE Trans. Plasma Sci.*, vol. 30, no. 3, pp. 992–997, Jun. 2002, doi: 10.1109/TPS.2002.801550.

[141] M. D. Haworth, K. E. Allen, G. Baca, J. N. Benford, T. J. Englert, K. E. Hackett, K. J. Hendricks, D. M. Henley, R. W. Lemke, D. Price, D. R. Ralph, M. D. Sena, D. A. Shiffler, and T. A. Spencer, “Recent progress in the hard-tube MILO experiment,” in *Proc. SPIE*, San Diego, CA, Oct. 1997, pp. 28–39. doi: 10.1117/12.279433.